SORPTION ENHANCED REFORMING OF ETHANOL OVER NOVEL CATALYSTS AND MICROWAVE REACTOR APPLICATION

A THESIS SUBMITTED TO
THE GRADUATE SCHOOL OF NATURAL AND APPLIED SCIENCES
OF
MIDDLE EAST TECHNICAL UNIVERSITY

BY

MERVE SARIYER

IN PARTIAL FULFILLMENT OF THE REQUIREMENTS
FOR
THE DEGREE OF MASTER OF SCIENCE
IN
CHEMICAL ENGINEERING

AUGUST 2018

Approval of the thesis:

SORPTION ENHANCED REFORMING OF ETHANOL OVER NOVEL CATALYSTS AND MICROWAVE REACTOR APPLICATION

submitted by **MERVE SARIYER** in partial fulfillment of the requirements for the degree of **Master of Science in Chemical Engineering Department, Middle East Technical University** by,

Prof. Dr. Halil Kalıpçılar
Dean, Graduate School of **Natural and Applied Sciences**

Prof. Dr. Pınar Çalık
Head of Department, **Chemical Engineering**

Prof. Dr. Naime Aslı Sezgi
Supervisor, **Chemical Engineering Dept., METU**

Prof. Dr. Timur Doğu
Co-Supervisor, **Chemical Engineering Dept., METU**

Examining Committee Members:

Prof. Dr. Deniz Üner
Chemical Engineering Dept., METU

Prof. Dr. Naime Aslı Sezgi
Chemical Engineering Dept., METU

Assoc. Prof. Dr. Erhan Bat
Chemical Engineering Dept., METU

Assoc. Prof. Dr. Levent Değirmenci
Chemical Engineering Dept., Bilecik Şeyh Edebali Uni.

Asst. Prof. Dr. Harun Koku
Chemical Engineering Dept., METU

Date: 29.08.18

I hereby declare that all information in this document has been obtained and presented in accordance with academic rules and ethical conduct. I also declare that, as required by these rules and conduct, I have fully cited and referenced all material and results that are not original to this work.

Name, Last name : MERVE SARIYER

Signature :

ABSTRACT

SORPTION ENHANCED REFORMING OF ETHANOL OVER NOVEL CATALYSTS AND MICROWAVE REACTOR APPLICATION

Sarıyer, Merve
M.Sc., Department of Chemical Engineering
Supervisor: Prof. Dr. Naime Aslı Sezgi
Co-Supervisor: Prof. Dr. Timur Doğu

August 2018, 175 pages

Environmental concerns and fast depletion of fossil fuel resources increased the research activities for the production of hydrogen from renewable sources. Hydrogen production through ethanol steam reforming reaction (SRE) has the potential to be used for its on board production on vehicles and with the sorption enhanced process (SESRE), use of CaO for in-situ removal of produced CO_2 increases hydrogen production, decreasing the carbon dioxide and carbon monoxide amount.

In this study nickel impregnated SBA-15, silica aerogel, commercial mesoporous carbon, the mesoporous carbon by METU were synthesized, characterized and tested in both the SRE and SESRE reactions. In addition to this, for the SESRE reaction, the effect of the divided section packing concept on the hydrogen purity was also investigated.

All catalysts gave good catalytic activity in the SRE reaction. The best one was the 10Ni-SA catalyst with the high yield, stable product distribution and low coke formation compared to other catalysts at 600°C. In all the packing concepts, in the pre-breakthrough period, the mole percentage of the hydrogen was nearly 90 % for all catalysts. In the breakthrough period, decrease of hydrogen and increase of CO and CO_2 mole fractions were observed, due to saturation of CaO with CO_2. Moreover, in the SESRE-M experiments in post-breakthrough period, the mole percentage of the products reached the same values with the SRE results for the only 10Ni-SA and 10Ni-P123-SBA-15 catalysts. For the other catalysts, the physical interaction between catalyst and sorbent affects the catalytic activity of the catalyst. The best packing configuration of catalyst and sorbent in the SESRE reaction is three ordered packing concept.

Activity test results showed that in-situ removal of CO_2 with CaO significantly enhanced hydrogen production by minimizing equilibrium limitations. Results proved the advantages of sorption enhanced process for the production of high purity hydrogen from ethanol.

With use of microwave heating system for the 10Ni-SBA-15 catalyst, the coke formation in the spent catalysts for the SRE was decreased from 56% to 3% compared to conventionally heated system.

Keywords: Hydrogen, Ethanol, Steam Reforming and Sorption Enhanced Steam Reforming, Mesoporous Materials, Microwave Reactor

ÖZ

ETANOLÜN YENİ KATALİZÖRLERLE ADSORPSİYON DESTEKLİ BUHARLI REFORMLANMASI VE MİKRODALGA REAKTÖR UYGULAMASI

Sarıyer, Merve
Yüksek Lisans, Kimya Mühendisliği Bölümü
Tez Yöneticisi: Prof. Dr. Naime Aslı Sezgi
Ortak Tez Yöneticisi: Prof. Dr. Timur Doğu

Ağustos 2018, 175 sayfa

Çevresel kaygılar ve fosil yakıt kaynaklarının hızlı tüketimi, yenilenebilir kaynaklardan hidrojen üretimi için yapılan araştırma faliyetlerini hızlandırmıştır. Etanolün buharlı reformlanması ile hidrojen üretimi motorlu araçlarda yerinde hidrojen üretimi için kullanılma potansiyeline sahiptir ve etanolün adsorpsiyon destekli reformlanmasında CaO kullanılmasıyla üretilen CO_2'in yerinde uzaklaştırılmasıyla karbon dioksit ve karbon monoksit miktarları azaltılarak hidrojen üretimi artar.

Bu çalışmada, nikel emdirilmiş SBA-15, silika aerojel, ticari mezogözenekli karbon ve METU tarafından sentezlenen mezogözenekli karbon katalizörler, sentezlenmiş, karakterize edilmiş ve SRE ve SESRE reaksiyonlarında test edilmişlerdir. Bunlara ek olarak, SESRE reaksiyonunda, ayrılmış bölmeli konseptin hidrojen saflığına olan etkisi araştırılmıştır.

Bütün katalizörler SRE reaksiyonunda yüksek aktivite vermişlerdir. Diğer katalizörlerle karşılaştırıldığında 600 °C' de en iyi olan, yüksek hidrojen verimi, istikrarlı ürün dağılımı ve düşük kok oluşumuyla 10Ni-SA katalizörüdür. Bütün sıralama konseptlerinde, bütün katalizörler için doygunluk öncesi dönemi, hidrojen mol yüzdesi yaklaşık %90’ dır. Doygunluk periyodunda, CaO’in CO_2 ile doyması sebebiyle, hidrojen mol kesrinde azalma ve CO ve CO_2 mol kesirlerinde artma gözlemlenmiştir. Ek olarak, SESRE-M deneylerinde, doygunluk sonrası döneminde ürünlerin mol yüzdeleri, sadece 10Ni-SA ve 10Ni-P123-SBA-15 katalizörleri için, SRE deneylerinde elde edilen sonuçlara ulaşmıştır. Diğer katalizörler için, katalizör ve sorbent arasındaki fiziksel etkileşim katalizörün katalitik aktivitesini etkilemiştir. SESRE reaksiyonunda en iyi katalizör ve sorbent dizilimi üç sıralı konsepttir.

Aktivite sonuçları CaO ile CO_2’in yerinde uzaklaştırılmasıyla denge sınırlamalarını en aza indirerek, hidrojen üretiminde önemli derecede iyileştirdiğini göstermektedir. Sonuçlar adsorpsiyon destekli buharlı reformlanma prosesinin etanolden yüksek saflıkta hidrojen üretimi için avantajlarını kanıtlamaktadır.

10Ni-SBA-15 katalizöründe mikrodalga ısıtma sistemi kullanılmasıyla, geleneksel ısıtma sistemine göre, kullanılmış katalizördeki kok oluşumu % 56’dan % 3’e düşürülmüştür.

Anahtar Kelimeler: Hidrojen, Etanol, Buharlı Reformlanma ve Adsorpsiyon Destekli Buharlı Reformlanma, Mezogözenekli Malzemeler, Mikrodalga Reaktör

To my beloved family

ACKNOWLEDGMENTS

To start with, I am greatly appreciated to my supervisor Prof. Dr. Naime Aslı Sezgi for her endless contributions, patience, support and guidance at every time. She helped me at every time and situation I need without hesitation. I would like to present my greatest gratitude to my co-supervisor Prof. Dr. Timur Doğu for the guidance and endless support. Starting from my undergraduate years, he inspired me with his unique knowledge and attitude towards chemical reaction engineering.

I would like to thank Chemical Engineering Department and the professors for their support, education and limitless information about chemical engineering discipline.

I would like to offer my special thanks to my lab-mates Arzu Arslan Bozdağ and Mehmetali İlker Şener for their help and support. Working with them together at every day and their valuable friendship taught me many valuable things. I wish to thanks to my lab-mates Pınar Değirmencioğlu, Sohrab Nikazar, Abdul Rehman Habib and Saeed Khan for their friendship and support.

I would like to thank to Mihrican Açıkgöz and Doğan Akkuş and METU Central Lab personnel for my characterization results. I am also thankful for İsa Çağlar and Cemil Araçlı for their help at every hard time.

Financial support by METU through project no BAP-03-04-2017-006 and BAP-07-02-2014-007-718 is gratefully acknowledged.

I would like to thank my lovely neighbour Merve Özkutlu for the endless support and courage, limitless and valuable friendship. I also would like to present my sincere to my unique friends, Ezgi Yavuzyılmaz, Fatma Şahin, Seda Sivri and Zeynep Karakaş for their motivation, help and endless friendship. Moreover, I would like to thank my 19 year old friend Berna Acar Kasırga for their endless frienship and support.

I would like to thank my dear master friends, Aslı Karausta, Nisa Erişen, Nur Ber Emerce, Yağmur Çulhacıoğlu, Beril Dumanlılar, Almira Çaldıklıoğlu, Mehmet Soner Yaşar and Berkan Atman. I also would like to thank Atalay Çalışan for his help and valuable conversations at every time.

I am grateful to my little smurfette Şenel Çalgüner who fill my life with endless joy, happiness, and love.

Most importantly, I would like to express my gratitude to my family. I would be glad to thank to my lovely mother Melike Sarıyer for being so caring all the time and for giving endless love and support. I would like to thank to my dear father Mehmet Sarıyer for being there whenever I needed him. I would like to thank my brother Oğuzhan Sarıyer for his continuous support, endless love, patience, confidence, and courage throughout my life. I cannot express my gratitude enough for him.

TABLE OF CONTENTS

ABSTRACT....................v
ÖZ....................vii
ACKNOWLEDGMENTS....................x
TABLE OF CONTENTS....................xii
LIST OF TABLES....................xvii
LIST OF FIGURES....................xix

CHAPTERS

1. INTRODUCTION....................1
   1.1 Hydrogen Safety....................3
   1.2 Hydrogen Fuel Safety....................3
2. STEAM REFORMING OF ETHANOL....................7
   2.1 Steam Reforming of Ethanol....................7
   2.2 Thermodynamics of Steam Reforming of Ethanol Reaction....................11
   2.3 Sorption Enhanced Steam Reforming of Ethanol....................15
3. CATALYSTS FOR ETHANOL STEAM REFORMING REACTION....................19
   3.1 SBA-15....................19
   3.2 Silica Aerogel....................21
   3.3 CMK (Carbon Mesostructured by KAIST)....................26
4. MICROWAVE HEATING....................33
   4.1 Microwave Energy....................33
   4.2 Microwave Applicators....................34

4.2.1 Multi-mode Microwave Applicators 34

4.2.2 Single-mode (Mono-mode) Microwave Applicators............................34

4.3 Dielectric Property of the Material 35

4.4 The Advantages of the Microwave Heated Systems 36

5. EXPERIMENTAL 39

5.1 Synthesis of the Catalysts 39

5.1.1 Synthesis of SBA-15..39

5.1.2 Synthesis of Silica Aerogel...40

5.1.3 Synthesis of MCMT (Mesoporous Carbon by METU) 40

5.1.4 Nickel Impregnation to the Synthesized Supports and Commercial Mesoporous Carbon 41

5.1.4.1 Incipient Wet-impregnation Method 41

5.1.4.2 Surfactant-Assisted Impregnation Method 42

5.2 Characterization Techniques...42

5.2.1 X-Ray Diffraction (XRD)..43

5.2.2 Nitrogen Adsorption/Desorption Analysis (BET) 43

5.2.3 Temperature Programmed Ammonia Desorption (NH_3-TPD)............43

5.2.4 Scanning Electron Microscopy (SEM) 43

5.2.5 Raman Spectroscopy..44

5.2.6 Thermal Gravimetric Analysis (TGA)...44

5.2.7 Fourier Transform Infrared Spectroscopy (FTIR) 44

5.3 Naming of the Catalysts...44

5.4 The Reaction System and Experimental Procedure.....................................45

5.4.1 The Reaction System 45

5.4.2 Experimental Procedure...47

6. RESULTS AND DISCUSSION 51
6.1 Characterization and Activity Results of SBA-15 Supported Catalysts...... 51
6.1.1 X-Ray Diffraction (XRD) Results 51
6.1.2 N_2 Adsorption/Desorption Isotherms and Physical Properties of the Materials 54
6.1.3 Scanning Electron Microscopy (SEM) Results 56
6.1.4 Temperature Programmed Ammonia Desorption (NH_3 - TPD) Results 60
6.1.5 Activity Test Results for the SBA-15 Supported Catalysts................. 61
6.1.5.1 Effect of Temperature and Impregnation Method on Hydrogen Production 64
6.1.5.2 Effect of the Packing of Catalyst and Sorbent on Hydrogen Production 68
6.1.6 TGA Results of the Spent Catalysts 78
6.2 Characterization and Activity Results of Commercial Mesoporous Carbon Supported Catalysts 79
6.2.1 X-Ray Diffraction Results 79
6.2.2 N_2 Adsorption/Desorption Isotherms and Physical Properties of the Materials 80
6.2.3 Scanning Electron Microscopy (SEM) Results 82
6.2.4 Temperature Programmed Ammonia Desorption (NH_3 - TPD) Results. 86
6.2.5 Activity Test Results for Commercial Mesoporous Carbon Supported Catalysts.. 87
6.2.5.1 Effect of Reaction Temperature 87
6.2.5.2 Effect of Metal Loading on Hydrogen Production 89

6.2.5.3 Effect of the Packing of Catalyst and Sorbent on Hydrogen Production 91

6.2.6 TGA Results of the Spent Mesoporous Carbon Supported Catalysts ..96

6.3 Characterization and Activity Results of Silica Aerogel Supported Catalysts 97

6.3.1 X-Ray Diffraction Results of Silica Aerogel Supported Catalyst 97

6.3.2 N_2 Adsorption/Desorption Isotherms and Physical Properties of the Materials 98

6.3.3 Temperature Programmed Ammonia Desorption (NH_3 - TPD) Results 100

6.3.4 Activity Results of Silica Aerogel Supported Catalysts on Hydrogen Production 101

6.3.4.1 The Effect of the Reaction Temperature....................................101

6.3.4.2 Effect of the Packing of Catalyst and Sorbent on Hydrogen Production 103

6.3.5 TGA Results 107

6.4 Characterization and Activity Results for Silica Aerogel Templated Carbon Material Supported Catalyst 107

6.4.1 Characterization of Silica Aerogel Templates 108

6.4.1.1 Fourier Transform Infrared Spectroscopy (FTIR) 108

6.4.1.2 N_2 Adsorption/Desorption Isotherms and Physical Properties of the Silica Aerogel Materials 110

6.4.2 Characterization of Silica Aerogel Templated Carbon Materials.......114

6.4.2.1 X-Ray Diffraction Results of Mesoporous Carbon Supports 114

6.4.2.2 RAMAN Results...114

6.4.2.3 N_2 Adsorption/Desorption Isotherms and Physical Properties ...116

6.4.2.4 Thermal Gravimetric Analysis (TGA) Results...........................121

6.4.2.5 Scanning Electron Microscopy (SEM) Results 124
6.4.3 Characterization of Nickel Impregnated MCMT Type Catalysts 130
6.4.3.1 X-Ray Diffraction Results 130
6.4.3.2 N_2 Adsorption/Desorption Isotherms and Physical Properties of the Materials 131
6.4.3.3 Temperature Programmed Ammonia Desorption (NH_3-TPD) Results 135
6.4.4 Activity Results of the Synthesized Mesoporous Carbon Supported Catalysts 136
6.5 Comparison of the Synthesized Catalysts 140
6.6 Activity Results of Microwave Heated System for the 10Ni-SBA-15 Catalyst 146
7. CONCLUSIONS AND RECOMMENDATIONS 151
REFERENCES 155

APPENDICES

A. CALCULATION OF METAL LOADING AMOUNT TO CATALYST....161
B. XRD DATA OF NICKEL, NICKEL OXIDE AND CARBON...............................163
C. CALCULATION OF CRYSTALLITE SIZE OF METAL......................................165
D. CALCULATION OF TOTAL ACID CAPACITY OF CATALYSTS…...........…167
E. BETA FACTOR CALCULATION OF GASES...169
F. PRODUCT MOLE PERCENTAGES, HYDROGEN YIELD AND CONVERSION CALCULATIONS...171

LIST OF TABLES

TABLES

Table 1: Hydrogen production techniques and their advantages and disadvantages (FreedomCAR & Fuel Partnership 2009) 2
Table 2: Synthesized Catalysts 45
Table 3: GC parameters and their setting values 46
Table 4: Temperature program for liquid and gas analyses 46
Table 5: All parameters and catalysts tested in SRE and SESRE experiments 50
Table 6: Crystallite size of metallic Ni in the synthesized catalysts 53
Table 7: The physical properties of the SBA-15, 10Ni-SBA-15 and 10Ni-P123-SBA-15 catalysts 55
Table 8: Acid capacities of the Ni loaded catalysts 61
Table 9: Crystallite size of the synthesized materials obtained from the XRD pattern 80
Table 10: The physical properties of commercial carbon supported catalyst 81
Table 11: Acid capacities of the nickel loaded mesoporous carbon catalysts 87
Table 12: Crystallite size of the nickel loaded silica aerogel supported catalyst 98
Table 13: The physical properties of SA and 10Ni-SA 99
Table 14: Peak identification for all silica aerogel supports 110
Table 15: Physical properties of SA and SAwoTMCS templates............................ 111
Table 16: I_D/I_G band intensities obtained from Raman spectra 115
Table 17: Physical properties of silica aerogel templates and synthesized carbon materials 117
Table 18: Crystallite size of the nickel loaded MCMT supported catalysts 131
Table 19: The physical properties of MCMT type catalysts................................... 132
Table 20: Acid capacities of the Ni loaded catalysts 135
Table 21: Coke deposition for spent catalysts... 145
Table B.1 XRD Data of Nickel.. 163
Table B.2 XRD Data of Nickel Oxide... 163

Table B.3 XRD Data of Carbon..164
Table C.1 XRD Data for 10Ni-SBA-15 165
Table E.1 Calibration factors for gas compounds..169
Table E.2 Calibration factors for liquid compounds 170
Table F.1 Mole fractions of compounds in the liquid mixture.................................173

LIST OF FIGURES

FIGURES

Figure 1: Effect of molar steam (S) to ethanol (E) ratio on equilibrium hydrogen percentage........13

Figure 2: Effect of molar steam to ethanol ratio on equilibrium carbon monoxide percentage........13

Figure 3: Effect of molar steam to ethanol ratio on equilibrium methane percentage 14

Figure 4: Effect of molar steam to ethanol ratio on equilibrium carbon dioxide percentage........14

Figure 5: Hydrogen yield values for different steam to ethanol ratios at different temperatures 15

Figure 6: Schematic representation of typical sol-gel synthesis procedure (Maleki et al., 2014)........25

Figure 7: Schematic view of the template synthesis procedure a) Mesoporous silica molecular sieve of MCM-48 b) MCM-48 after completing carbonization within pores c) CMK-1 obtained by removing the silica wall after carbonization (Ryoo et al., 1999) 28

Figure 8: Schematic view of the synthesis procedure for CMK-3 (Nettelroth et al., 2016)........29

Figure 9: The reaction of the different materials to the microwave heating a) conductive material b) insulating material , and c) absorbing material (Durka et al., 2009) 34

Figure 10: a) Mono-mode and b) Single-mode microwave applicators (Hayes et al., 2002)........35

Figure 11: Heating mechanisms of conventional heating and microwave heating (Zhang et al., 2017) 37

Figure 12: A schematic diagram of the hydrogen production system 49

Figure 13: The schematic view of all the packing concepts: a) Mixed concept (SESRE-M) b) The concept of two divided sections (SESRE-1O) c) The concept of six divided sections (SESRE-3O) 49
Figure 14: Low angle XRD patterns of the 10Ni-SBA-15 and 10Ni-P123-SBA-15 catalysts 52
Figure 15: High angle XRD patterns of the 10Ni-SBA-15 and 10Ni-P123-SBA-15 catalysts 53
Figure 16: N_2 adsorption/desorption isotherms of the SBA-15, 10Ni-SBA-15 and 10Ni-P123-SBA-15 catalysts (Filled symbols: Desorption branch, Empty symbols: Adsorption Branch) 55
Figure 17: Pore size distributions of the SBA-15, 10Ni-SBA-15 and 10Ni-P123-SBA-15 catalysts 56
Figure 18: SEM images from different parts of the 10Ni-SBA-15 catalyst at 50000X magnification 56
Figure 19: EDX spectrum of the 10Ni-SBA-15 catalyst 57
Figure 20: SEM images of the 10Ni-SBA-15 catalyst at a) 100000X and b) 50000X magnifications by backscattering detector 57
Figure 21: SEM images of the 10Ni-SBA-15 catalyst at a) 100000X and b) 50000X magnifications by backscattering detector 58
Figure 22: SEM images of the 10Ni-P123-SBA-15 catalyst at a) 100000X and b) 50000X magnifications 58
Figure 23: EDX spectrum of the 10Ni-P123-SBA-15 catalyst 59
Figure 24: SEM images from another part of the 10Ni-P123-SBA-15 catalyst at a) 50000X and b) 25000X magnifications by backscattering detector 59
Figure 25: SEM images from another part of the 10Ni-P123-SBA-15 catalyst at a) 50000X and b) 50000X magnifications by backscattering detector 60
Figure 26: NH_3-TPD graphs of the Ni loaded SBA-15 catalysts 61
Figure 27: Repeatability results for SRE at 600°C (Catalyst: 10Ni-SBA-15) 62
Figure 28: Product distribution of SRE at 600°C without catalyst 63
Figure 29: The product distribution of SESRE at 600°C with only CaO 64

Figure 30: Comparison of the average mole percentage of the products for the 10Ni-SBA-15 and 10Ni-P123-SBA-15 catalysts at 500°C and 600°C (SRE reaction environment) 66
Figure 31: Product distribution of SRE at 500°C (Catalyst: 10Ni-SBA-15) 66
Figure 32: Product distribution of SRE at 600°C (Catalyst: 10Ni-SBA-15) 67
Figure 33: Product distribution of SRE at 500°C (Catalyst: 10Ni-P123-SBA-15).... 67
Figure 34: Product distribution of SRE at 600°C (Catalyst: 10Ni-P123-SBA-15).... 68
Figure 35: Product distribution of SESRE-M at 600°C (Catalyst: 10Ni-SBA-15).... 69
Figure 36: Product distribution of SESRE-1O at 600°C (Catalyst: 10Ni-SBA-15) .. 71
Figure 37: Product distribution of SESRE-3O at 600°C (Catalyst: 10Ni-SBA-15) .. 71
Figure 38: Comparison of mole percentages of the H_2 and CO_2 for the SRE and SESRE reactions at 600°C (Catalyst: 10Ni-SBA-15) 72
Figure 39: Product distribution of SESRE-M at 600°C (Catalyst: 10Ni-P123-SBA-15) 74
Figure 40: Product distribution of SESRE-3O at 600°C (Catalyst: 10Ni-P123-SBA-15)... 74
Figure 41: Comparison of mole percentages of H_2 and CO_2 at 600°C for the SRE and SESRE reactions (Catalyst: 10Ni-P123-SBA-15).................................. 75
Figure 42: Product distribution of SESRE-3O at 500°C (Catalyst: 10Ni-SBA-15) .. 76
Figure 43: Comparison of mole percentages of H_2 and CO_2 at 500°C for the SRE and SESRE reactions (Catalyst: 10Ni-SBA-15) 76
Figure 44: Product distribution of SESRE-3O at 500°C (Catalyst: 10Ni-P123-SBA-15)... 77
Figure 45: Comparison of mole percentages of H_2 and CO_2 at 500°C for the SRE and SESRE-3O reactions (Catalyst: 10Ni-P123-SBA-15) 78
Figure 46: TGA results of the spent 10Ni-SBA-15 and 10Ni-P123-SBA-15 catalysts at reaction temperature of 500°C and 600°C 79
Figure 47: XRD patterns of MC, 5Ni-MC and 10Ni-MC catalysts........................... 80
Figure 48: N_2 adsorption/desorption isotherms of the MC, 5Ni-MC and 10Ni-MC catalysts (Filled symbols: Desorption branch, Empty symbols: Adsorption Branch) 81

Figure 49: Pore size distributions of the MC, 5Ni-MC and 10Ni-MC catalysts 82
Figure 50: SEM images of MC at different magnifications: a,b) 200000X and c,d) 100000X 83
Figure 51: SEM images of 10Ni-MC at different magnifications: a) 100000X b) 50000X, and c) 25000X 84
Figure 52: SEM images of 10Ni-MC a) at 200000X magnification b) at 200000X magnification by backscattering detector 85
Figure 53: EDX spectrum of the 10Ni-MC catalyst 85
Figure 54: SEM images of 10Ni-MC a) at 20000X magnification b) at 20000X magnification by backscattering detector 86
Figure 55: NH_3-TPD graphs of the commercial carbon materials 87
Figure 56: Effect of reaction temperature on the product distribution for the 10Ni-MC (SRE reaction environment) 88
Figure 57: Product distribution at 500°C for SRE reaction (Catalyst: 10Ni-MC)..... 88
Figure 58: Product distribution at 600°C for SRE reaction (Catalyst: 10Ni-MC)..... 89
Figure 59: Product distribution at 600°C for the SRE reaction (Catalyst: MC) 90
Figure 60: Product distribution at 600°C for the SRE reaction (Catalyst: 5Ni-MC) 90
Figure 61: Effect of metal loading on hydrogen production for MC, 5Ni-MC and 10Ni-MC at 600°C (SRE reaction environment) 91
Figure 62: Product distribution at 600°C for the SESRE-M configuration (Catalyst: 10Ni-MC) 92
Figure 63: Product distribution with SESRE-1O configuration at 600°C (Catalyst: 10Ni-MC) 93
Figure 64: Product distribution with SESRE-3O configuration at 600°C (Catalyst: 10Ni-MC) 94
Figure 65: Comparison of mole percentages of H_2 and CO_2 for the SRE and SESRE reactions at 600°C (Catalyst: 10Ni-MC) 94
Figure 66: Product distribution at 600°C for the SESRE-M configuration (Catalyst: 5Ni-MC) 95

Figure 67: Comparison of mole percentages of H_2 and CO_2 for the SRE and the SESRE-M reactions at 600°C (Catalyst: 5Ni-MC) 96
Figure 68: TGA results of the spent and fresh 10Ni-MC catalyst 97
Figure 69: XRD pattern of the 10Ni-SA catalyst..98
Figure 70: N_2 adsorption/desorption isotherms of the SA support and 10Ni-SA catalyst (Filled symbols: Desorption branch, Empty symbols: Adsorption Branch) 99
Figure 71: Pore size distributions of SA and 10Ni-SA 100
Figure 72: NH_3-TPD graph of the 10Ni-SA catalyst 100
Figure 73: Product distribution of SRE at 500°C (Catalyst: 10Ni-SA) 101
Figure 74: Product distribution of SRE at 600°C (Catalyst: 10Ni-SA) 102
Figure 75: Effect of reaction temperature on the product distribution for the 10Ni-SA (SRE reaction environment)..102
Figure 76: Product distribution of SESRE-M at 600°C (Catalyst: 10Ni-SA)..........104
Figure 77: Product distribution of SESRE-3O at 600°C (Catalyst: 10Ni-SA) 104
Figure 78: Comparison of mole percentages of H_2 and CO_2 for the SRE and SESRE reactions at 600°C (Catalyst: 10Ni-SA) 105
Figure 79: Product distribution of SESRE-3O at 500°C (Catalyst: 10Ni-SA) 106
Figure 80: Comparison of mole percentages of H_2 and CO_2 for the SRE and SESRE reactions at 500°C (Catalyst: 10Ni-SA) 106
Figure 81: TGA results for the spent 10Ni-SA catalyst at different reaction temperatures 107
Figure 82: FTIR spectra for the silica aerogel support material 109
Figure 83: N_2 adsorption/desorption isotherms for the synthesized templates (Filled symbols: Desorption branch, Empty symbols: Adsorption Branch).....112
Figure 84: Pore size distributions for the SA-C450 and SA-C700 113
Figure 85: Pore size distributions of SA-NC, SAwoTMCS-NC and SAwoTMCS-C600 113
Figure 86: XRD patterns of mesoporous carbon supports......................................114
Figure 87: Raman spectra of the synthesized MCMT materials.............................115

Figure 88: N_2 adsorption/desorption isotherms of the synthesized mesoporous carbons with NaOH treatment (Filled symbols: Desorption branch, Empty symbols: Adsorption Branch) 118
Figure 89: Pore size distributions of the synthesized mesoporous carbons with NaOH treatment........ 119
Figure 90: N_2 adsorption/desorption isotherms of the synthesized mesoporous carbons with HF treatment 120
Figure 91: Pore size distributions of the synthesized mesoporous carbons with HF treatment........ 121
Figure 92: TGA graph of the synthesized silica aerogel templates under air flow.. 122
Figure 93: TGA graph of the synthesized silica templates under nitrogen flow 122
Figure 94: TGA graph of MCMT materials under air flow........ 123
Figure 95: TGA graph of MCMT materials under nitrogen flow........ 124
Figure 96: SEM images of MCMT-A-600-DH-NaOH at different magnifications: a) 50000X, b) 100000X, and c) 200000X........ 125
Figure 97: SEM images of MCMT-A-600-DH-NaOH at different magnifications: a) 10000X and b) 40000X........ 125
Figure 98: EDX spectrum of MCMT-A-600-DH-NaOH 126
Figure 99: SEM image of MCMT-A-600-DH-HF at 200000X magnification 126
Figure 100: SEM images of MCMT-A-600-DH-HF at different magnifications: a) 5000X, b) 10000X, and c) 25000X........ 127
Figure 101: EDX spectrum of MCMT-A-600-DH-HF 127
Figure 102: SEM images of MCMT-B-450-DH-HF at 200000X magnification.... 128
Figure 103: EDX spectrum of MCMT-B-450-DH-HF........ 128
Figure 104: SEM images of MCMT-B-700-DH-HF at different magnifications: a) 50000X and b) 100000X........ 129
Figure 105: SEM images of MCMT-B-700-DH-HF at different magnifications: a) 100000X and b) 200000X........ 129
Figure 106: EDX spectrum of MCMT-B-700-DH-HF........ 130
Figure 107: XRD patterns of 10Ni-MCMT-A-DH-NaOH and 10Ni-MCMT-A-DH-HF........ 131

Figure 108: N_2 adsorption/desorption isotherms of the MCMT-A-600-DH-NaOH support and 10Ni-MCMT-A-600-DH-NaOH catalyst (Filled symbols: Desorption branch, Empty symbols: Adsorption Branch) 133

Figure 109: N_2 adsorption/desorption isotherms of the MCMT-A-600-DH-HF support and 10Ni-MCMT-A-600-DH-HF catalyst (Filled symbols: Desorption branch, Empty symbols: Adsorption Branch) 133

Figure 110: Pore size distributions of the MCMT-A-600-DH-NaOH support and 10Ni-MCMT-A-600-DH-NaOH catalyst 134

Figure 111: Pore size distributions of the MCMT-A-600-DH-HF support and 10Ni-MCMT-A-600-DH-HF catalyst 134

Figure 112: NH_3-TPD graphs of the Ni loaded MCMT catalysts 135

Figure 113: Product distribution at 600°C for the SRE reaction (Catalyst: 10Ni-MCMT-A-600-DH-HF) 136

Figure 114: Product distribution at 600°C for the SRE reaction (Catalyst: 10Ni-MCMT-A-600-DH-NaOH) 138

Figure 115: Product distribution with the SESRE-M configuration at 600°C (Catalyst: 10Ni-MCMT-A-600-DH-NaOH) 138

Figure 116: Product distribution with the SESRE-3O configuration at 600°C (Catalyst: 10Ni-MCMT-A-600-DH-NaOH) 139

Figure 117: Comparison of mole percentages of H_2 and CO_2 for the SRE and the SESRE reactions at 600°C (Catalyst: 10Ni-MCMT-A-600-DH-NaOH) 139

Figure 118: The average mole percentages of the products for all catalysts in SRE experiments at 600°C 140

Figure 119: Hydrogen yield values for SRE experiments at 600°C 141

Figure 120: The mole percentages of H_2 for all catalysts in different sorbent-catalyst configurations in the SESRE reaction at 600°C...................................142

Figure 121: The mole percentages of CO for all catalysts in different sorbent-catalyst configurations in the SESRE reaction at 600°C...................................143

Figure 122: The mole percentages of CH_4 for all catalysts in different sorbent-catalyst configurations in the SESRE reaction at 600°C...................................144

Figure 123: The mole percentages of CO_2 for all catalysts in different sorbent-catalyst configurations in SESRE experiments at 600°C 145
Figure 124: Product distribution at 600°C for the SRE reaction in MWR (Catalyst: 10Ni-SBA-15) 147
Figure 125: Product distribution at 600°C for the SESRE-M reaction in MWR (Catalyst: 10Ni-SBA-15) 147
Figure 126: Comparison of H_2 and CO_2 compositions at 600°C for the SRE and SESRE in MWR... 148
Figure 127: Comparison of product distributions for SRE and SESRE in conventionally and microwave heated reactors at 600 °C at the 20th minute of the reaction... 149
Figure 128: Comparison of product distributions for SRE and SESRE in conventionally and microwave heated reactors at 600 °C at the 120th min of the reaction... 149
Figure 129: TGA analysis results for spent catalysts for the SRE in conventionally and microwave heated reactors... 150

NOMENCLATURE

A_i : Area of component i read from GC

B : Full width at half maximum, radian

c : Crystal shape factor

$C_{gas\ total}$: Total concentration of the gas at 20°C and 1 atm, mol/ml

F_{ETOH}^{o} : Initial molar flow rate of ethanol

$F_{ETOH,liquid}^{f}$: Final flow rate of the ethanol

F_i : Molar flow rate of species i, mol/s

MW_i : Molecular weight of species i, g/mol

N_i : Number of moles of species i

P : Pressure, atm

Q_{Ar} : Volumetric flow rate of argon, ml/s

Q_i : Volumetric flow rate of species i, ml/s

$Q_{gas\ products}$: Total volumetric flow rate of gas products, ml/s

R : Ideal gas constant, J/mol.K

T_{room} : Room temperature, °C

$t_{crystallite}$: Crystallite size, nm

V_{NH_3}: Volume of ammonia, ml

X_{ETOH} : Conversion of ethanol

$x_{i,L}$: Mole fraction of species i in the liquid

y_i : Mole fraction of species i

Greek Letters

βi : Beta factor of component i

ρ_i : Density of species i at 20°C, g/ml

λ : Wavelength of radiation, nm

θ : Bragg angle, °

Abbreviations

BET: Brunauer Emmett Teller

BJH: Barrett Joyner Halenda

CHR: Conventionally Heated Reactor

CMK: Carbon Mesostructured by KAIST

GC: Gas Chromatograph

KAIST: Korea Advanced Institute of Science and Technology

MWR: Microwave Reactor

MC: Mesoporous Carbon

MCMT: Mesoporous Carbon by METU

SA: Silica Aerogel

SAwoTMCS: Silica Aerogel without TMCS

SBA-15: Santa Barbara Amorphous-15

SEM: Scanning Electron Microscopy

SESRE: Sorption Enhanced Steam Reforming of Ethanol

SESRE-M: Sorption Enhanced Steam Reforming of Ethanol-Mixed Concept

SESRE-1O: Sorption Enhanced Steam Reforming of Ethanol-1O concept

SESRE-3O: Sorption Enhanced Steam Reforming of Ethanol-3O concept

SRE: Steam Reforming of Ethanol

TCD: Thermal Conductivity Detector

TEOS: Tetraethyl orthosilicate

TMCS: Trimethylchlorosilane

TGA: Thermogravimetric Analysis

TPD: Temperature Programmed Desorption

WGSR: Water Gas Shift Reaction

XRD: X-Ray Diffraction

CHAPTER 1

INTRODUCTION

In today’s world, fossil fuels such as hydrocarbons, natural gas, coal, and fuel oil are used as an energy sources. However, with an increase in world population, the demand for the energy sources is gradually increasing. The consumption of these energy sources has made a negative effect on the environmental issues such as global warming due to the emissions of pollutants such as CO_2 and SO_2. Moreover, these energy sources have been used for decades and the estimated lifetime of coal is about 300 years and that of natural gas is nearly 80 years. Therefore, they are not sustainable and renewable and nearly come to an end. At this point, the need of clean, less polluting and renewable energy sources or carriers has become important throughout the world. Solar and wind energies have appeared as alternative sources but they are not continuously available to meet the need of the entire world. Therefore, environmental concerns and fast depletion of fossil resources have accelerated the research activities for the production of fuels and energy carriers from bio-resources.

Hydrogen is considered as a new energy carrier and new studies about energy sources and carriers are focused on the improvement of hydrogen energy. Hydrogen has high energy content and it is nontoxic, clean and renewable energy carrier. Since it does not contain any C-C bond, the most important advantage of using hydrogen as an energy carrier is no release of carbon dioxide to the environment because it can combust cleanly without emitting environmental pollutants.

Hydrogen containing one proton and one electron is the simplest, most abundant and the lightest element among all elements. In spite of its simple form, it cannot exist in the nature in molecular form. It is combined with the other elements. Therefore, it should be produced from the compounds containing hydrogen. The compounds consisting of hydrogen are especially water, hydrocarbons, natural gas, gasoline, and alcohols.

There are many innovations on chemical processes for hydrogen production because it became important in the world energy sector of the world. Hydrogen can be produced from different sources such as hydrocarbons and alcohols via steam reforming, auto-thermal steam reforming and partial oxidation, coal and biomass by gasification, water through electrolysis etc. Hydrogen production techniques and their advantages and disadvantages are shown in Table 1. In steam reforming, hydrogen can be produced from the hydrocarbons and alcohols by applying heat. In electrolysis of water, an electric current is supplied in order to separate the hydrogen and oxygen from the water. In addition, in the photolytic processes, hydrogen can be produced from the algae and bacteria using the sunlight as an energy source (Momirlan et al., 2005).

Table 1: Hydrogen production techniques and their advantages and disadvantages (FreedomCAR & Fuel Partnership, 2009)

Production Technology	Method	Advantage	Disadvantage
Thermal Processes	• Reforming, auto-thermal reforming and partial oxidation of alcohols and hydrocarbons • Gasification of coal and biomass	• Clean, sustainable and renewable • Feedstock availability	• Cost effective reactor • High temperature resistant materials
Electrolytic Processes	• Electrolysis of water	• No pollutant gases • Feedstock availability at all times	• Low efficiency, high cost
Photolytic Processes	• Biological hydrogen production	• Clean and sustainable • Energy efficiency with low temperature operation	• Low efficiency, high cost • Very slow production rate

The considerable interest in the use of hydrogen as an energy carrier is increasing because there are many advantages of hydrogen. These are:

- It is potential for non-toxic, clean and quiet energy generation.
- It has high energy per mass content of 143 MJ/kg, which is three times higher than that of hydrocarbon based fuels (Mazloomi et al., 2012)
- It has long term maintainability due to the resource availability
- It has no C–C bond so there is no release of CO_2 to the environment

1.1 Hydrogen Safety

Despite the advantages of the hydrogen energy, there are some disadvantages of the hydrogen energy. The problematic properties of the hydrogen are:

Due to having high diffusivity and low molecular weight, hydrogen molecules are so small that they can easily escape through holes so open flames should be removed from the storage area of hydrogen. Moreover, being flammable and explosive, and having low minimum ignition energy. High pressure hydrogen gas may form explosive mixtures in the contact with air and it has low minimum ignition energy that hydrogen can ignite when even small amount of hydrogen is mixed with air.

In the liquefaction process of hydrogen, Joule Thomson cycle is used, allowing gas to expand through throttling device. However, in this process, temperature is decreasing; on the other hand, pressure is increasing, leading to an opposite sign of Joule Thomson cycle. This also brings about a dangerous situation for hydrogen.

1.2 Hydrogen Fuel Safety

While being a very clean and energy-dense fuel, hydrogen tends to disperse quickly under normal pressure, which causes the need for the higher pressure of hydrogen in the fuel transport system. Additionally, hydrogen molecules are so light that they can easily escape through holes and can even enter the molecular structure of some steels, making them brittle over time. In normal operation of the car, small amount of hydrogen leakage accumulating in the air may form flammable or even explosive mixtures (U.S. Department of Energy, 2011; Cadwallader et al., 1999).

The possible hydrogen storage approaches are physical storage of compressed hydrogen gas in the high pressure tanks and physical storage of cryogenic hydrogen with cooling to -253°C and at high pressure in the insulated tanks. Moreover, hydrogen can be stored in the form of advanced materials such as in the form of chemical compounds that reacts to produce hydrogen (U.S. Department of Energy, 2011).

Hydrogen has a very high energy content by weight; on the other hand, energy content per volume is low. This is the most important challenge for the hydrogen storage. Big storage tanks are needed for the hydrogen storage that limits the usage of hydrogen energy in the cars.

The transportation and storage problems of hydrogen restricted its usage as an energy carrier. While being a very clean and energy-dense fuel, it is also highly volatile and explosive so it tends to disperse quickly under normal pressure, which causes the need for the storage at high pressure. At this point, on board hydrogen production appears as an alternative way to the hydrogen storage.

Among the hydrogen production methods, steam reforming of alcohols is a promising way, considering the environmental concerns and hydrogen economy. Due to its high hydrogen content, non-toxicity and easy distribution possibilities, bio-ethanol which can be produced from the fermentation of cellulosic biomass is considered as a promising feedstock for hydrogen production at relatively low temperatures because ethanol is richer in terms of hydrogen.

One of the important applications of hydrogen is its use in fuel-cell derived car. Fuel cells (FC) have the potential to replace the internal combustion engine in vehicles because they are energy-efficient, and clean. Chemical energy is converted to the electrical energy in fuel cells. However, PEM fuel-cells are highly sensitive to the CO concentration of the feed stream. The amount of CO must not exceed 100 ppm (Fierro et al. 2005) in order not to deactivate the catalyst within the fuel-cell.

Sorption enhanced reforming of ethanol (SESRE) is a possible alternative to obtain high purity hydrogen, by reducing the CO and CO_2 concentrations in the gas mixture. Equilibrium limitations may also be eliminated by a SESRE process, according to Le Chatelier’s principle.

Steam reforming of ethanol is highly endothermic reaction so energy efficiency should be considered in order to make this process economically feasible. Recent research activities with microwave heated reactors showed more stable reactor performance, higher yields and lower coke formation than the conventionally heated reaction systems (Gündüz et al., 2015). Due to transfer of microwave energy directly to the catalyst particles more efficient energy utilization can be achieved.

In this study, the aim is to produce high purity hydrogen gas with the steam reforming and sorption enhanced steam reforming of ethanol reactions. With this aim, different catalyst supports which are SBA-15, silica aerogel, and mesoporous carbon were synthesized and nickel was impregnated to these catalyst supports. Nickel was also impregnated to the commercial mesoporous carbon. The activity tests were performed at 500°C and 600°C in steam reforming and sorption enhanced steam reforming of ethanol reactions. Different packing concepts were investigated in the sorption enhanced process to achieve hydrogen rich gas mixture. Finally, the best catalyst with the highest yield and highest coke formation was also tried in the microwave heated reactor system in both steam reforming and sorption enhanced steam reforming reaction.

CHAPTER 2

STEAM REFORMING OF ETHANOL

Alcohols are good candidates for the production of hydrogen with a steam reforming reaction. Ethanol is widely used because it possesses many advantages which are high hydrogen content, good availability, low production cost, safe storage and transportation, and non-toxicity. It can be produced from the fermentation of cellulosic biomass. Produced ethanol which consists of excess water can be used as a feed-stock for the steam reforming of ethanol reaction. Actually, pure ethanol can be directly used as a fuel for the internal combustion engines. However, separation of ethanol from water is expensive process.

Hydrogen can also be produced from ethanol with two other production methods, partial oxidation and oxidative steam reforming. For the partial oxidation of ethanol, ethanol and oxygen react with each other so pure ethanol is needed for the partial oxidation. Moreover, separation of oxygen from the air is an expensive process. On the other hand, in the auto-thermal reforming of ethanol, coke formation which is the main problem of the steam reforming of ethanol reaction can be eliminated because the feed contains ethanol, water and oxygen. However, the separation of oxygen from air still exists in this process.

When these three methods are compared with each other, steam reforming of ethanol is a suitable way in terms of energy efficiency.

2.1 Steam Reforming of Ethanol

In steam reforming, the desired reaction pathway contains steam reforming (R.1) and water gas shift reaction (R.2) in the presence of sufficient steam supply. The steam reforming (SRE) is an endothermic reaction whose products are hydrogen and carbon monoxide. The water gas shift reaction is an exothermic reaction which converts the carbon monoxide to carbon dioxide and increases the amount of hydrogen. The WGSR reduces the formation of coke and provides more H_2 production. Considering the desired overall steam reforming reaction, for 1 mole of ethanol, 6 moles of hydrogen can be produced in the case of no side reactions and coke formation.

SRE $C_2H_5OH + H_2O \leftrightarrow 2CO + 4H_2$ $\Delta H^\circ_{298} = 256.32$ kJ/mol (R.1)

WGSR $CO + H_2O \leftrightarrow CO_2 + H_2$ $\Delta H^\circ_{298} = -41.16$ kJ/mol (R.2)

Overall SRE $C_2H_5OH + 3H_2O \leftrightarrow 2CO_2 + 6H_2$ $\Delta H^\circ_{298} = 174$ kJ/mol (R.3)

However, equilibrium conditions also limit the hydrogen production. Moreover, there are many side reactions which reduce the hydrogen production due to important parameters such as water/ethanol ratio, reaction temperature and catalyst properties.

Insufficient steam supply results in a lower hydrogen production, eliminating the WGSR. R.1 and R.4 become important in the insufficient steam supply.

$C_2H_5OH + 2H_2 \leftrightarrow 2CH_4 + H_2O$ (R.4)

Dehydrogenation may occur in the presence of basic catalyts. Some possible side reactions during ethanol steam reforming reaction are given as follows:

Dehydrogenation $C_2H_5OH \leftrightarrow CH_3CHO + H_2$ (R.5)

Decarbonylation $CH_3CHO \leftrightarrow CH_4 + CO$ (R.6)

Acetaldehyde Steam Reforming $CH_3CHO + H_2O \leftrightarrow 3H_2 + 2CO$ (R.7)

Steam reforming of Methane $CH_4 + H_2O \leftrightarrow CO + 3H_2$ (R.8)

On the other hand, in the dehydration reaction ethylene is produced as an intermediate product which forms carbon (R.9). This carbon is deposited in the active site of the catalyst. Ethylene may also react with the water and produces carbon monoxide and hydrogen (R.11). In general, R.9, R.10 and R.11 are observed in the presence of acidic catalysts.

Dehydration $C_2H_5OH \leftrightarrow C_2H_4 + H_2O$ (R.9)

Ethylene decomposition $C_2H_4 \leftrightarrow 2C + 2H_2$ (R.10)

Ethylene Steam Reforming $C_2H_4 + 2H_2O \leftrightarrow 4H_2 + 2CO$ (R.11)

In addition to the above reactions, ethanol decomposition reactions may occur:

Decompositon

$C_2H_5OH \leftrightarrow CO + CH_4 + H_2$ (R.12)

$2C_2H_5OH \leftrightarrow C_3H_6O + CO + 3H_2$ (R.13)

$C_2H_5OH \leftrightarrow 0.5CO_2 + 1.5CH_4$ (R.14)

$C_2H_5OH \leftrightarrow CH_2O + CH_4$ (R.15)

Furthermore, some reactions occur with the formed products like H_2, CO_2 and CO. These reactions are shown as below:

CO Methanation $CO + 3H_2 \leftrightarrow CH_4 + H_2O$ (R.16)

CO_2 Methanation $CO_2 + 4H_2 \leftrightarrow CH_4 + 2H_2O$ (R.17)

Reverse dry reforming $2CO + 2H_2 \leftrightarrow CH_4 + CO_2$ (R.18)

The reactions which are the source of the coke formation are shown in R.18-21.

Methane decomposition $CH_4 \leftrightarrow 2H_2 + C$ (R.18)

Boudouard reaction $2CO \leftrightarrow CO_2 + C$ (R.19)

Ethylene decomposition $C_2H_4 \leftrightarrow 2C + 2H_2$ (R.20)

Carbon Gasification $C + H_2O \leftrightarrow H_2 + CO$ (R.21)

There are many studies related to the steam reforming of ethanol over different catalysts. Nowadays, different catalyst supports were studied for ethanol steam reforming reaction. Araiza et al. (2018) studied the effect of morphology of cerium metal on the coke formation. Three supports, ceria particle in the form of rod and cube, using different synthesis routes were synthesized and nickel was impregnated to all the catalyst supports. At the temperatures lower than 500°C the surface area, morphology of the catalyst and the dispersion of the nickel on the catalyst directly affected the ethanol steam reforming reaction. Nickel impregnated ceria rods gave high activity and hydrogen yield compared to other catalysts under 24 h activity test. For this catalyst, the coke deposition was very low and well dispersion of nickel on catalyst was achieved. On the other hand; at the temperatures higher than 600^oC there was no significant difference between the activity results of these catalysts.

Li et al. (2018) studied nickel and nickel-cerium impregnated montmorillonite catalysts for the ethanol steam reforming reaction. With the addition of ceria to the catalyst, the ethanol conversion increased from 84.5 % to 97.3 %. Moreover, for this catalyst, the coke formation was very low compared to other one. This was due to the small nickel crystal size of the Ni-Ce catalyst compared to Ni catalyst. Generally, catalysts having relatively small nickel crystal sizes showed excellent sintering resistance. Moreover, high oxygen storage and transport capacity of the CeO_2 reduced the coke formation due to reaction of carbon with mobile O_2. Due to these, the Ni-Ce catalyst gave highly stable product distribution in the long term activity experiment. In the ethanol steam reforming reaction different catalyst supports were used in the literature. He et al. (2017) studied the effect of different precursor for the nickel impregnation to the SBA-15 catalyst support. Nickel impregnated SBA-15 catalyst gave high activity towards ethanol steam reforming of ethanol reaction. Complete conversion was achieved at the temperatures higher than 450^oC with a water to ethanol ratio of 3/1. Moreover, the hydrogen yield increased with an increase in temperature. However, with an increase in the temperature from 650^oC to 700^oC the hydrogen yield remains nearly constant. Nearly same product distributions were obtained for all the catalysts synthesized with different precursors. On the other hand, the nickel dispersion on the catalyst was homogeneous with the use of the nickel citrate precursor and the catalyst synthesized with this precursor suppressed the coke formation.

Vizcaino et al. (2007) reported the effect of different supports and metals on the ethanol steam reforming reaction at a temperature of 600^oC with a steam to ethanol molar ratio of 3.7/1. Copper and nickel impregnated Al_2O_3 catalyst enhanced the ethanol dehydration reaction due to the acidic sites of this catalyst; therefore, the mole percentage of the hydrogen in the product distribution was lower compared to other supports. Moreover, ethanol dehydration promoted the coke deposition. All silica supports containing copper and nickel gave the best catalytic activity on ethanol steam reforming reaction due to the dispersion of nickel crystals were observed for these catalysts.

2.2 Thermodynamics of Steam Reforming of Ethanol Reaction

In the steam reforming of ethanol reaction, the selection of the catalyst, the operating temperature and the ratio of H_2O to C_2H_5OH are very critical points. Before the selection of the best catalyst for the reaction in order to examine the effect of different H_2O/ C_2H_5OH ratios on the product distribution and hydrogen yield, the first step is to perform thermodynamic analysis for the reaction. With the help of the thermodynamic analysis, the best operating conditions such as temperature, pressure and H_2O/ C_2H_5OH molar ratio can be determined.

Thermodynamic equilibrium analysis was performed using the ASPEN program which is based on the minimization of free energy method. Assuming that the reactor effluent stream composed of H_2, CO, CO_2, CH_4, C_2H_4, ethanol and water gases, equilibrium molar gas composition was determined for different temperatures and steam to ethanol ratios. Then, equilibrium product distribution in dry basis was plotted. All equilibrium product distribution graphs for H_2, CO, CO_2, and CH_4 gases for different steam to ethanol ratios are shown from Figures 1-4. Moreover, the graph of hydrogen yield for different steam to ethanol ratios at different temperatures is shown in Figure 5. As it can be seen from these figures, increase in the water to ethanol ratio favored the hydrogen production. In the case of low water to ethanol ratios and low temperatures, ethanol decomposition reaction to methane and carbon dioxide favored. Moreover, in the low water to ethanol ratios at high temperatures, ethanol decomposed to methane, carbon monoxide and hydrogen. In order to favor the steam reforming of ethanol reaction high temperatures and high water to ethanol ratios should be selected. In this way, water gas shift and methane steam reforming reactions became dominant. However, high ratios require more energy input for the evaporation of water-ethanol mixture.

Moreover, increase in the temperature favors the methane steam reforming. Therefore, high temperatures are reasonable for decrease in methane and increase in the hydrogen production. Furthermore, it can be seen that an increase in the temperature increases the formation of carbon monoxide whereas carbon dioxide amount decreases because the water gas shift is an exothermic reaction and high temperatures are not suitable for exothermic reactions.

Lima da Silva et al. (2009) studied the thermodynamic analysis of ethanol steam reforming reaction with considering the carbon deposition. According to Silva et al. at very low contact times, steam to ethanol ratios does not affect carbon deposition. At very low contact times, ethanol tends to be converted to ethylene which is the main source of coke formation. On the other hand, at high contact times, the carbon formation is directly proportional to steam to ethanol ratios. In conclusion, the ethylene production should be decreased to prevent the coke formation at low contact times. At high contact times, the temperature higher than 500°C and inlet steam to ethanol ratio, 3:1 is very proper to perform steam reforming of ethanol reaction with minimum coke formation. At lower temperatures high steam to ethanol ratio can prevent the coke formation at high contact times. Wang et al. (2008) reported that higher pressures limited the hydrogen production and coke formation decreased with an increase in steam to ethanol ratios. Moreover, the effect of inert gas on the thermodynamic analysis of ethanol was also investigated by Wang et al. High argon to ethanol ratio increased the hydrogen production. Alvarado et al. (2010) performed thermodynamic analysis and it was reported that when the steam to ethanol ratio was lower than 4, carbon deposits can be formed. Moreover, the reaction temperature defined the carbon type such as graphite of carbon nanotube. While the temperature lower than 400°C favored the graphite domains, the temperature higher than 400°C resulted in a multi walled carbon nanotubes. Addition to this, in order to achieve the highest hydrogen yield, high temperatures, high water to ethanol ratios can be selected.

Considering equilibrium product distributions for different feed ratios, optimization is needed to determine the best operating temperature of the reactor. Steam to ethanol ratio should be chosen above 3 in order to prevent the coke formation, minimize the methane formation and increase hydrogen production. Moreover, high feed ratios require more energy input. Therefore, the best feed ratio is chosen as 3.2.

Higher temperatures favor the hydrogen production but it also increases the formation of CO because water gas shift reaction, which is exothermic reaction, is not active at high temperatures. Moreover, high temperatures require more heat input. When optimization is performed, the best operating temperature was chosen as 600°C with a water to ethanol ratio 3.2/1 by mole.

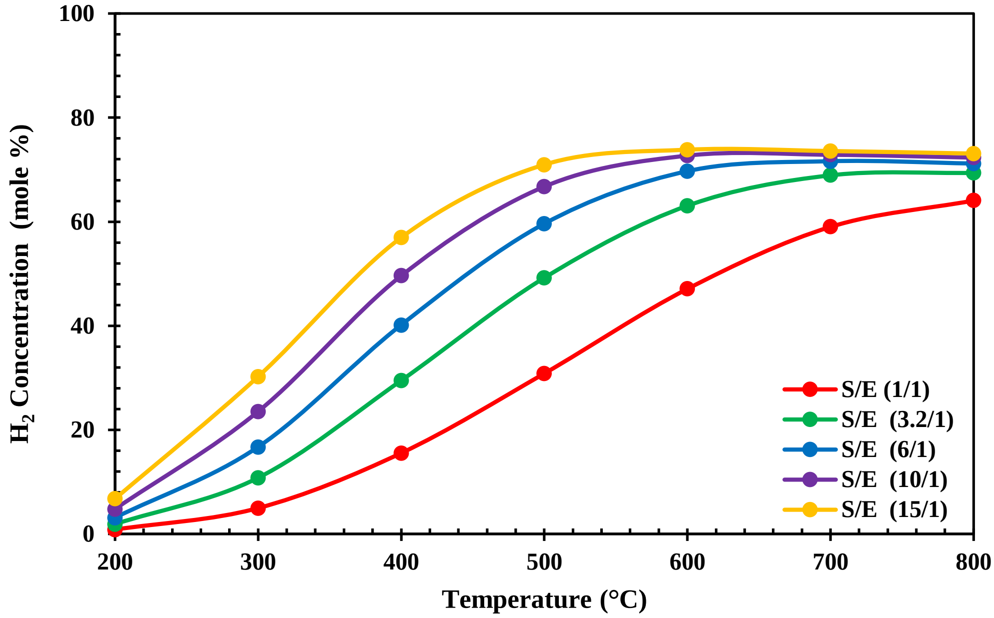

Figure 1: Effect of molar steam (S) to ethanol (E) ratio on equilibrium hydrogen percentage

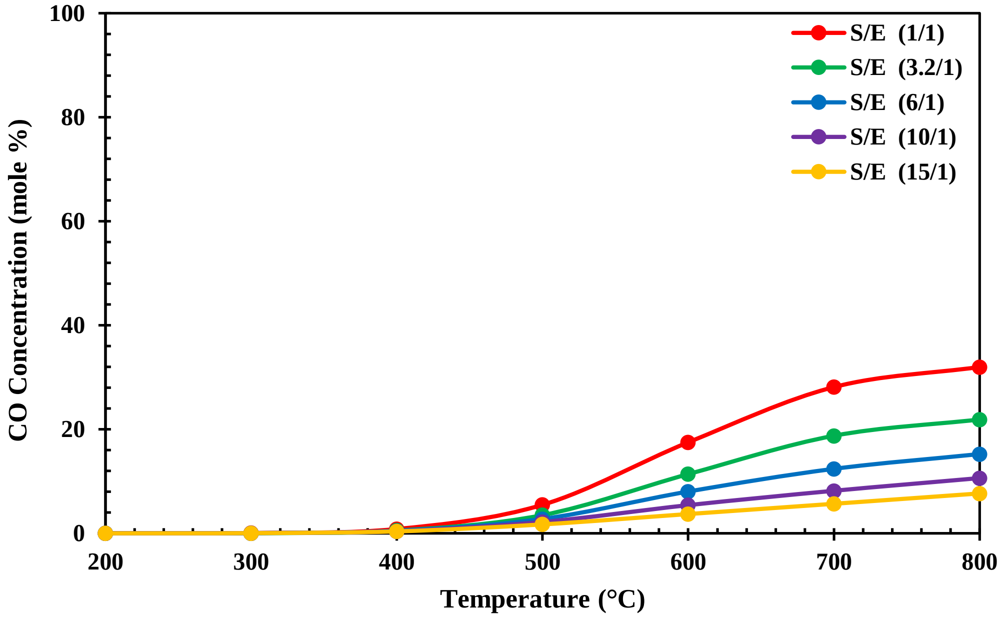

Figure 2: Effect of molar steam to ethanol ratio on equilibrium carbon monoxide percentage

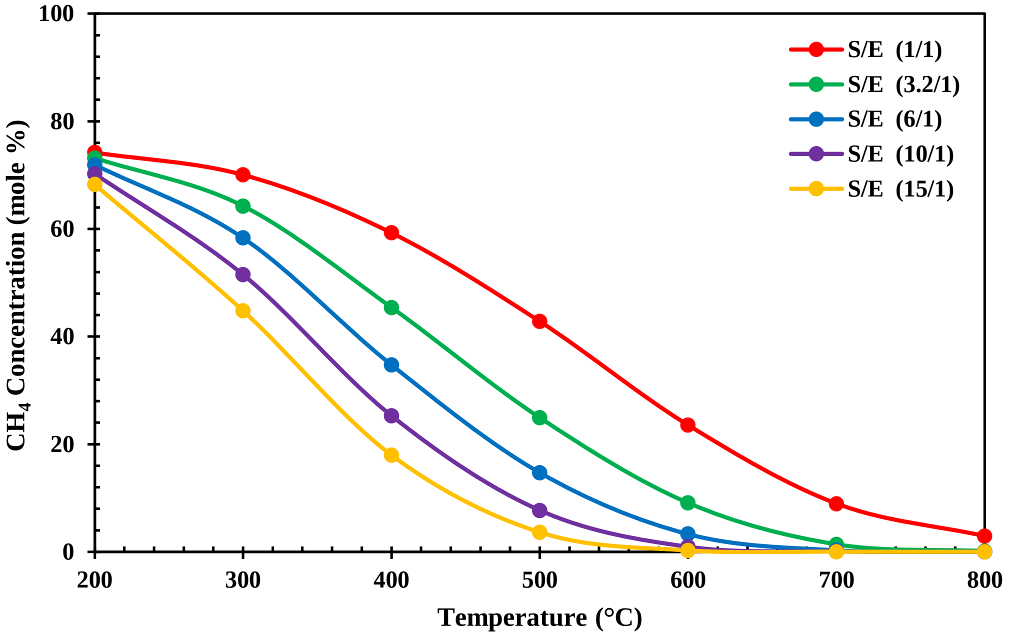

Figure 3: Effect of molar steam to ethanol ratio on equilibrium methane percentage

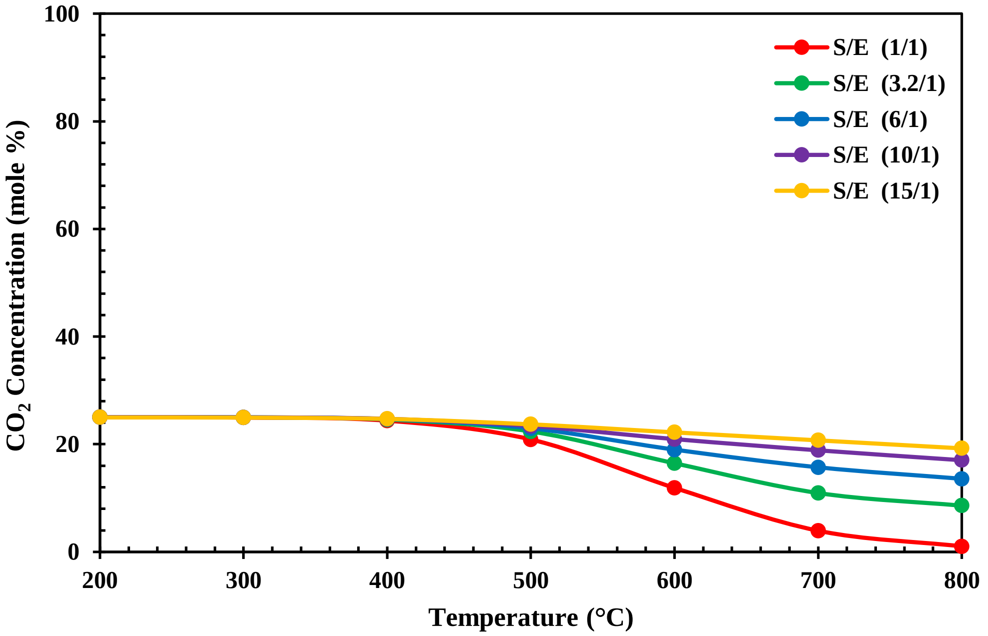

Figure 4: Effect of molar steam to ethanol ratio on equilibrium carbon dioxide percentage

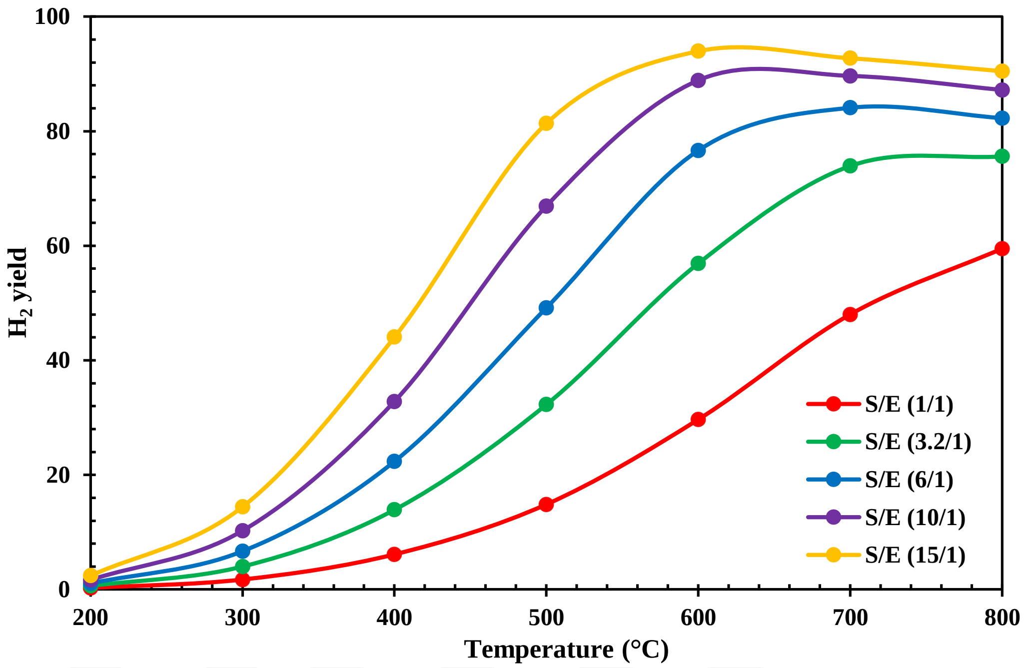

Figure 5: Hydrogen yield values for different steam to ethanol ratios at different temperatures

2.3 Sorption Enhanced Steam Reforming of Ethanol

The purity of the hydrogen is very important issue for fuel cell applications of hydrogen. PEM fuel-cells are highly sensitive to the CO concentration of the feed stream. The amount of CO must not exceed 100 ppm (Fierro et al., 2005), in order not to deactivate the catalyst within the fuel-cell. However, due to the formation of side reactions, the purity of the hydrogen decreased. There are many process intensification methods which improve the purity of the hydrogen. One of them is membrane reactor which can separate the hydrogen from the other gaseous species. However, high cost of the membrane reactors limits the usage of this method. Sorption enhanced reforming of ethanol (SESRE) is a possible alternative to increase the hydrogen yield and to obtain high purity hydrogen, by reducing the CO and CO_2 concentrations in the gas mixture. Equilibrium limitations may also be eliminated by a SESRE process according to Le Chatelier’s principle. This process is based on carbon dioxide capture by the sorbents. There are many sorbents which are used for the capture of carbon dioxide such as hydrotalcites, CaO based sorbents, huntite, and dolomite. CaO is a

promising candidate for the sorption of carbon gases during the steam reforming process. It is a low cost sorbent for CO_2 and can easily be obtained by calcination of $CaCO_3$. When CaO is mixed with catalyst within the reaction zone, CO_2 adsorbs onto CaO (R.23) and in this way the equilibrium shifts to the formation of more hydrogen (R.22). In this way, a decrease in the CO_2 amount also decreases the formation of CO through reverse water gas shift reaction. In WGSR, to eliminate CO_2 the equilibrium is shifted to the product side. In this way, hydrogen production increases and percentage of CO_2 in product stream decreases so purity of hydrogen increases.
The overall steam reforming reaction with CaO is shown below:

$$C_2H_5OH + 3H_2O + 2CaO \leftrightarrow 6H_2 + 2CaCO_3 \tag{R.22}$$

CO_2 capture with CaO is shown below:

$$CaO + CO_2 \leftrightarrow CaCO_3 \tag{R.23}$$

Gunduz et al. (2012) studied sorption enhanced steam reforming of ethanol over nickel and cobalt impregnated MCM-41 catalysts with CaO as a sorbent. In the SESRE experiments performed at 600^{o}C complete conversion and 94 % of the maximum hydrogen mole percentage were achieved. Moreover, high purity hydrogen was obtained with the carbon dioxide capture of CaO. Aceves Olivas et al. (2014) studied different sorbents, CaO, CaO*MgO, and Na_2ZrO_3, and investigated the effect of sorbent on ethanol conversion, capture time of carbon dioxide and hydrogen yield and purity with Ni/Al_2O_3 catalyst in the temperature range of 500°C and 600°C. Results showed that usage of adsorbent decreased the carbon formation over the catalyst surface. The usage of all sorbents increased the hydrogen production (nearly 95 % in mole percentage) and purity.

There are many reactor configurations which are studied in the literature for sorption enhanced steam reforming of ethanol. Lee et al. (2014) studied one-body hybrid solid pellets for the sorption-enhanced water gas shift reaction. Pellets composed of mixture of catalyst ($Cu/ZnO/Al_2O_3$) and adsorbent (K_2CO_3 promoted hydrotalcite) in different weight ratios. The usage of the pellet also decreased the pressure drop. The purity of the hydrogen increased with an increase in the adsorbent amount in the pellet. It was reported that when the catalyst bed was divided into two sections: in the first section pellets with high catalyst amount and in the second section, high adsorbent containing pellets. In this configuration, the hydrogen purity was increased more compared to the experiments only performed with high catalyst amount containing pellets or high adsorbent containing pellets. Moreover, the purity of the hydrogen can be increased with pressure swing adsorption. However, sometimes the nature of the catalyst and sorbent is not fit to each other in the pellet form or mixed form. Qi et al. (2018) studied sorption enhanced methanol reforming with a $CuO/ZnO/Al_2O_3$ catalyst and K-hydrotalcite sorbent. Two packing modes which were mixing of the catalyst and sorbent and pellet form of sorbent and catalyst were investigated in this study with a steam to methanol ratio as 3/1 and in the temperature range of 473K to 573K. Two packing modes did not give expected results of sorption enhanced reforming process. Methanol conversion in the mixed concept was higher than that of in the pellet form of the sorbent and catalyst. The catalyst loss its catalytic activity due to the alkaline property of K-hydrotalcites. At this point, many reactor configurations of catalyst and adsorbent can be investigated in order to increase the hydrogen purity and conversion. Lee et al. (2017) studied the different reactor configurations with $Cu/ZnO/Al_2O_3$ catalyst and Na-Mg double salt-based sorbent in water gas shift reaction. One-body hybrid solid pellets containing sorbent and catalyst gave poor catalytic activity and poor carbon dioxide sorption capacity due to change in the components of the catalyst and sorbent. Therefore, multi-section packing concept was investigated to achieve high purity hydrogen. In this concept, catalyst bed was divided into different sections and these sections were filled with the catalyst and sorbent in many different ways. In this way, interaction between catalyst and sorbent decreased. With the multi-section concept, the hydrogen purity can be increased.

CHAPTER 3

CATALYSTS FOR ETHANOL STEAM REFORMING REACTION

Selection of a proper catalyst support and metal is very important issue for the steam reforming and sorption enhanced steam reforming reactions. The properties of the catalyst such as acidity or basicity, high thermal and chemical stability, the interaction of the metal with support are very critical parameters. Moreover, the coke formation should be taken into consideration while selecting the proper catalyst support and metal because the dispersion of the metal over the catalyst support and the interaction between catalyst support and metal plays important role on the coke formation. Therefore, the metals and supports showing the highest activity towards ethanol steam reforming should be selected for the reaction in terms of hydrogen purity, less side products and coke formation.

3.1 SBA-15

High surface area mesoporous materials attract attention as catalyst in many reactions. These porous materials are classified according to their pore diameters. As stated in International Union of Pure and Applied Chemistry IUPAC notation, materials with pore diameters less than 2 nm are called microporous materials and materials with pore diameters greater than 50 nm are macroporous materials. Moreover, mesoporous materials have the pore diameters between 2 nm and 50 nm. Mesoporous materials break the diffusion limitations of microporous materials due to their pore size.

SBA-15 is the best known mesoporous silica based material with ordered pore structure. It has cylindrical two dimensional hexagonally ordered pores. The synthesis procedure is highly acidic; therefore, SBA-15 materials are acidic materials.

SBA-15 catalyst with high surface area, narrow pore size distribution, and larger pore diameter is widely used in ethanol reforming with incorporation of metals.

There are many studies related to the SBA-15 catalyst in the literature. Due to its low cost, low catalyst deactivation and high activity towards ethanol steam reforming reaction nickel is generally used with the incorporation of the SBA-15. He et al. (2015) studied the hydrogen production via ethanol steam reforming reaction over Ni/SBA-15 catalyst and the effect of addition of Au to the catalyst. SBA-15 with a uniform 2D hexagonal ordered mesopore channel structure, large pore volume, surface area and high thermal stability was the proper candidate for the steam reforming of ethanol reaction. In this study, catalysts were prepared with the wet impregnation method. 6Ni/SBA-15 showed high selectivity of hydrogen and Au was impregnated to this catalyst. 6Ni-1.2Au/SBA-15 catalyst gave high hydrogen selectivity. In time-on-stream tests of the 6Ni/SBA-15 and 6Ni-1.2Au/SBA-15, the activity of the 6Ni/SBA-15 catalyst started to decrease after 10 hour-experiment; on the other hand, for the 6Ni-1.2Au/SBA-15 catalyst, highly stable product distribution was achieved in 25 hour-activity test. Addition of the Au to the catalyst enhanced the stability towards catalytic deactivation.

Li et al. (2015) investigated Ni/SBA-15 catalyst and the addition of ceria to this catalyst on ethanol steam reforming reaction. Keeping the nickel loading same, the ceria amount was changed and surfactant assisted impregnation via CTAB was carried out. Highly dispersed nickel crystals were observed for all the catalysts. 1Ce-Ni/SBA-15 gave the higher hydrogen percentage compared to 0.5Ce-Ni/SBA-15 and 2Ce-Ni/SBA-15. The incorporation of ceria to the catalyst enhanced the stability of time-on stream test compared to Ni/SBA-15 catalyst. TGA analysis for the spent catalysts of long term activity tests showed that 25 % decrease in the coke formation was achieved with 1Ce-Ni/SBA-15 catalyst compared to Ni/SBA-15 catalyst.

The crystallite size of the nickel on the SBA-15 support can be changed with the surfactant impregnation method. Generally, two surfactants which were CTAB and P123 were used in the surfactant assisted impregnation method. In the nickel impregnation step, the surfactant assisted to impregnation with different surfactant to nickel ratios. The ratio is very important because it effects all the physical properties of the material. With the proper surfactant to nickel ratio, smaller crystallite size nickel in the catalyst can be achieved, lowering the coke formation and enhancing the catalytic activity. Tao et al. (2017) investigated the CO methanation with the highly dispersed nickel on the SBA-15 support. Changing the surfactant (CTAB) to nickel ratio, the nickel crystallite sizes are arranged. With the surfactant assisted impregnation method, nickel crystallites were uniformly distributed in the SBA-15 considering the TEM images. With the suitable molar ratio of surfactant to nickel as 3, the nickel crystallite size was decreased from 14.6 nm to 6.5 nm. The methane yield was increased from 60 % to 90 % changing the impregnation method from wet impregnation to surfactant assisted impregnation method.

Moreover, P123 was also studied in the surfactant assisted impregnation method. Yang et al. (2016) studied the Ni/SBA-15 catalyst prepared by P-123 assisted impregnation method in the carbon dioxide reforming of methane reaction. Changing the surfactant to nickel ratio from 0 to 750, different catalysts were synthesized with Type IV isotherm and H1 hysteresis loop. Same nickel crystallite size (nearly 17 nm) was achieved with the P123 assisted method. With decreasing the ratio, the nickel crystallite size also decreased. TEM images showed that highly dispersed nickel crystallites were clearly seen with the P123 assisted method. Lower coke formation and high catalytic activity were achieved with the catalyst synthesized with P123 assisted method with a surfactant to nickel ratio as 3.

3.2 Silica Aerogel

Since silica aerogel was firstly produced in the 1930s by Kistler et al., there are wide range of applications such as catalyst support, drug delivery, thermal insulation, adsorption, oil spill cleanup (Malfait et al. 2015). They are highly mesoporous materials with high surface area (500-1200 m^2/g), high porosity (nearly 80-99 %), low thermal conductivity (0.005 W/mK) and low density (nearly 0.003 g/cm^3). The pore sizes are changing between 5 and 100 nm, with an average pore diameter between 10 nm and 40 nm (Soleimani Dorcheh et al., 2008). They are generally synthesized by sol-gel process. The synthesis procedure has been modified with using different precursors, and synthesis parameters such as aging time, drying step, or solvent. There are three common step, gel preparation, aging of the gel and drying of the gel for the synthesis of the silica aerogel in all production methods. As a precursor, generally silicon alkoxides such as TMOS, TEOS and PEDS have been used. Solvents such as alcohols are generally used to form a homogeneous mixture of water and alkoxysilane. Moreover, alcohols participate in the esterification reaction which decreases the hydrolysis rate.

From the kinetic point of view, the rate of hydrolysis and condensation reactions is very slow so it takes very long time to reach completion, consequently cooperation of acid or base catalysis are needed to speed up the procedure. Sol-gels can be synthesized in the cooperation of three different catalytic cases which are acid catalyzed, base catalyzed and acid and base catalyzed methods. In the acid catalyzed method, silica molecules have a tendency to get hydrolyzed to produce straight chains with low-cross-link density. Therefore, randomly combined chains can be formed and then they can be readily resolubilized. At this method, gelation takes a long time. In the base catalyzed method, the number of uniform cross-links increases, which enhances polymerization and promote silica structure. In the acid-base catalyzed procedure, in the first hydrolysis procedure, acid catalysis like HCl is used to enhance the reaction. Then, basic catalysis such as ammonia is added to the first solution. With two-catalyzed method, the rate of condensation favors and the gelation time decreases (Maleki et al., 2014).

Sol-gel method consists of three main step, gel preparation, aging of the gel and drying. The schematic representation of the typical sol-gel method is shown in Figure 6. Gel preparation step contains the hydrolysis and water and alcohol condensation steps.

- **Gel Preparation**

Hydrolysis: Silicon alkoxide (TEOS or TMOS) reacts with water to form silanol groups in the presence of solvent (such as alcohols). Alcohols are generally used as a solvent for esterification reaction. Generally, acid is used as a catalyst to enhance the reaction. In order to go to the complete hydrolysis, Si/H_2O ratio is very important. (Soleimani Dorcheh et al., 2008). Hydrolysis generally takes place in the presence of acid or base catalysis.

During the hydrolysis step, the following reaction takes place:

$$\mathrm{Si(OR)_4 + H_2O \rightarrow HO - Si(OR)_3 + ROH}$$

If the hydrolysis reaction is completed,

$$\mathrm{Si(OR)_4 + 4H_2O \rightarrow Si(OH)_4 + 4ROH}$$

Condensation: Formed silanol groups form siloxane bridges (Si-O-Si). They can react with each other or react with alkoxides (Si-OR) by giving water or alcohol (Gurav et al. 2010). Condensation generally occurs in the presence of alcohols and basic catalysts accompany to the condensation. Two partially hydrolyzed molecules can link together in a condensation;

Water Condensation:

$$\mathrm{(OR)_3Si - OH + HO -} Si\mathrm{(OR)_3 \rightarrow (OR)_3Si - O - Si(OR)_3 + H_2O}$$

Alcohol Condensation:

$$\mathrm{(OR)_3Si - OR + HO -} Si\mathrm{(OR)_3 \rightarrow (OR)_3Si - O - Si(OR)_3 + ROH}$$

During the hydrolysis and condensation steps, the primary silica particles are formed and they combine into secondary particles with linking to each other. In this way, three-dimensional silica network can be established by the process of polymerization.

- **Aging of the Gel**

Aging is the important step to strengthen the silica network. With the aging step, pore shrinkage can be minimized. The gel was stored in the presence of alcohols to complete the reaction. After the completion of the reaction, silica aerogels are formed (Thapliyal et al., 2014). After the aging period, solvent exchange procedure can be applied to prevent the capillary stress. The water at the pores can be replaced with hexane.

- **Drying**

Due to the capillary pressure during the evaporation process, shrinkage of the gels may occur because siloxane bonds in the aerogels are not strong to stand the capillary pressure. In this way, the resulted dense and cracked aerogels can be synthesized.

In order to prevent formation of shrinked and cracked aerogels, one of the ways is to replace the some of the siloxane bonds (Si-O-Si) with the flexible bonds (Si-R). This organic group will help the aerogel to change back to its original wet size without any cracking and shrinkage in the gel. The other one is the surface modification. This method consists of changing the capillary force gaining by the silica network with surface modification of the aerogel with alkyl groups and giving a surface with deficient Si-OH groups. In this way, more hydrophobic surfaces can be produced by the reaction of the hydroxyl groups (-OH) with hydrophobic reagents such as TMCS, MTCS (Maleki et al., 2014). TMCS can react with the surface silanol groups and the water inside the pores. The reactions are given below. The first one is the removal of surface silanol groups and the second one is the reaction of the TMCS with the water in the pores.

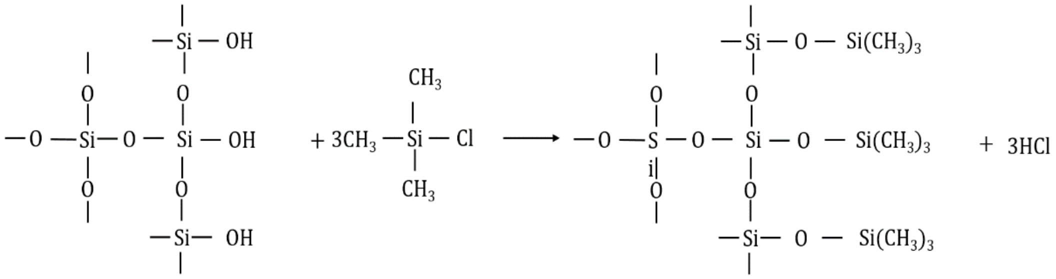

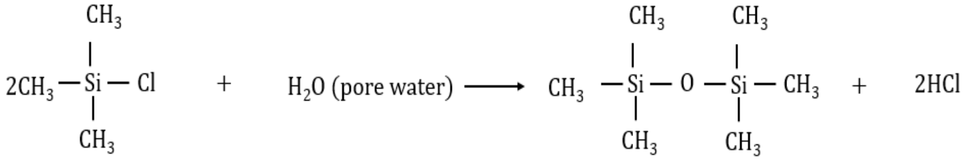

Third one uses the direct relation between the surface tension and capillary pressure. Evaporation of the solvent having a low surface tension decreases the capillary pressure compared to evaporation of alcohols or water. Generally, water (surface tension value of 72.80 mN/m at 20°C) in the pores is changed with hexane (surface tension value of 18.43 mN/m at 20°C) as a low surface tension solvent.

Drying process contains three different steps which are freeze-drying, evaporation at ambient pressure and supercritical drying. In freeze drying the solvent within the pores is frozen and sublimed under vacuum (Sinkó et al., 2010). In evaporation at ambient pressure the solvent can be removed with evaporation process under ambient pressure

(Liu et al., 2008). In supercritical drying, the solvent in the pores is taken above its supercritical temperature and pressure. In this way, no liquid-vapor interface occurs and capillary pressure gradients can be eliminated.

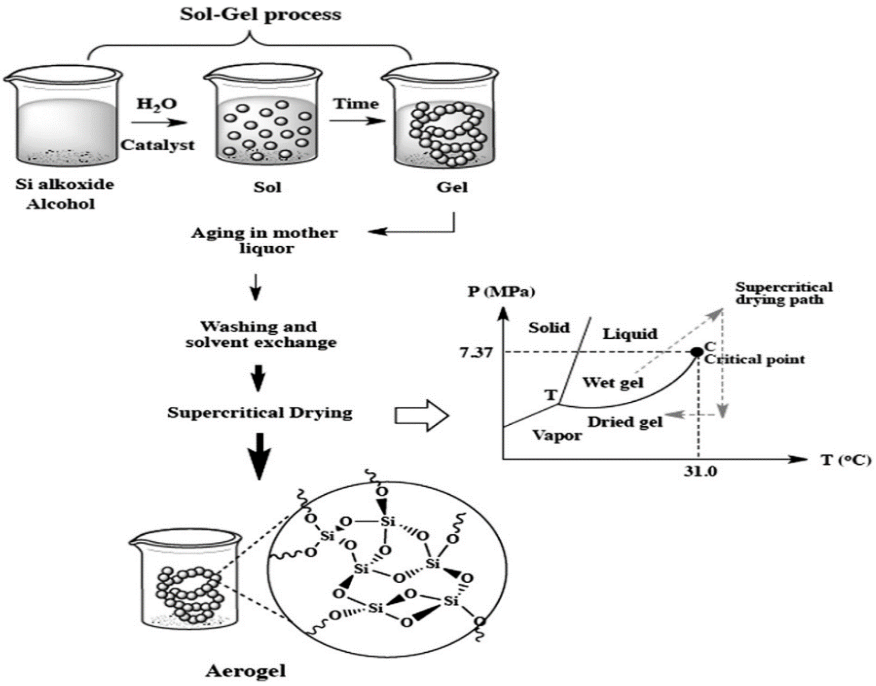

Figure 6: Schematic representation of typical sol-gel synthesis procedure (Maleki et al., 2014)

There are different studies related to the silica aerogel in the literature. Wu et al. (2011) studied the preparation and surface modification of the silica aerogels with the ambient pressure drying. Two consecutive surface modification with MTMS and TMCS/ethanol/hexane via ambient pressure drying was applied in the synthesis of the silica aerogel. With changing the TEOS/MTMS/EtOH/H_2O ratios, the effect on the surface area, pore diameter and pore volume was investigated. The surface area values for silica aerogels changed between 850 to 1000 m^2/g. With increasing the ethanol and water amounts keeping the other parameters constant, their surface area increased, but pore volume and pore diameter of the aerogels decreased. SEM & TEM images revealed that with an increase in MTMS/TEOS ratio, more Si-CH_3 groups were appeared in the surface of the aerogel with decreasing the surface tension of the gel, resulting in the less shrinkage in the pore structure.

Dominguez et al. (2008) studied the monoliths coated with Co-SiO_2 aerogel for the production of hydrogen from ethanol. The silica aerogel was synthesized with the sol-gel method and ceramic monoliths were impregnated into the sol and then removed and cobalt was immersed to the gel. Final products were evaporated under ambient pressure or supercritical conditions. Activity results showed that the material evaporated under supercritical conditions gave higher hydrogen yield and conversion in the temperature range of 473 K to 773 K compared to that of under atmospheric pressure. The aerogel evaporated under supercritical conditions was tested for 70 h and no catalyst deactivation and no change in the product distribution was observed at 623 K. Same catalyst support was also tested in the methanol steam reforming reaction by Amiri et al. (2015). With changing the copper amount and the calcination temperature of the catalysts, activity tests for methanol steam reforming were performed. With a calcination at 450°C and 700°C, the catalysts were converted to hydrophilic catalysts. At low calcination temperatures (300°C and 450°C), highly dispersed copper species were achieved because there were no characteristic peaks of copper species in their XRD patterns. At high calcination temperature (700°C), the characteristic peaks of CuO and copper-silicon were observed in the XRD pattern. With an increase in the copper content, hydrogen production rate increased. Moreover, with an increase in the calcination temperature, higher catalytic activity was achieved due to the existing of CuO primary species.

3.3 CMK (Carbon Mesostructured by KAIST)

Recent studies has been focused on the improvement of carbon structured materials. Carbon materials such as carbon nanotubes, carbon nanofibers, and mesoporous carbons take attention due to their high chemical stability, electrical and thermal conductivity and good availability (Nettelroth et al., 2016). Ordered mesoporous carbons are important materials among them due to their high surface area, optimal and uniform pore size and pore volume. They are widely used for the catalyst supports, electrode materials, adsorbents, and hydrogen storage materials. Moreover, for the microwave reactor applications, carbon support materials draw attention because carbon is the most important microwave adsorbent. When the other silica or alumina supported catalyst is used for the microwave reactor applications, the addition of the carbon based materials to the catalyst support is necessary to adsorb microwave. With the usage of the carbon based catalyst support, the extra additon of the carbon based materials is omitted.

Nowadays, hard template method is widely used in order to create ordered mesoporous carbons with well-defined pore sturucture. In recent years, for the preparation of mesoporous carbons, different templates such as MCM-41, SBA-1, SBA-15, partially disordered MCM-48, SBA-15 alumino silicate, SBA-16, KIT-6 have been used as an hard template and furfuryl alcohol, sucrose, naphthalene, acetonitrile, styrene and phenolic resin as an precursors. With changing the template, the pore structure, surface area and pore volume of the carbon materials have been changed so far. The silica template removal was generally achieved via NaOH solution or HF solution. The first ordered mesoporous carbon, CMK-1, was synthesized by Ryoo with the MCM-48 as an hard template and sucrose as an carbon source (Ryoo et al., 1999). The mesopores inside the silica template was filled with the sucrose in the solution containing sulfuric acid. The template removal was performed with NaOH solution. The material with surface area of 1380 m^2/g was successfully synthesized. The schematic view for the formation of CMK-1 is shown in Figure 7. The first picture represented the MCM-48 template and the second one showed that the pores inside the silica template were filled with the sucrose and the third one indicated final CMK-1 structure.

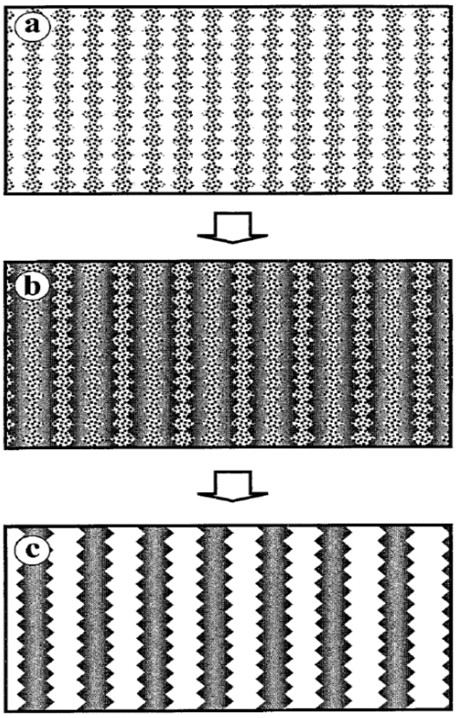

Figure 7: Schematic view of the template synthesis procedure a) Mesoporous silica molecular sieve of MCM-48 b) MCM-48 after completing carbonization within pores c) CMK-1 obtained by removing the silica wall after carbonization (Ryoo et al., 1999)

Moreover, SBA-1 was studied as an template for the CMK-2 (Jun et al., 2000). Then, using the SBA-15 as an silica template, CMK-3 was synthesized by Jun et al. (2000). The schematic view for the synthesis of CMK-3 is shown in Figure 8. Same procedure was also used for the synthesis of the CMK-3 with CMK-1. Sucrose was used as a precursor and it was impregnated to the SBA-15 pores. After pyrolysis, in order to remove the silica template, HF solution was used and the material with a surface area of 1520 m^2/g and pore volume of 1.3 cm^3/g was synthesized. Looking at the TEM images of the CMK-3 and SBA-15, the morphology of the CMK-3 is exactly an inverse replica of SBA-15 Due to the interconnections between the cylindrical pores, the carbon structure is not disordered. Looking at the XRD pattern of the CMK-3, (110), (110) and (200) characteristic diffraction peaks for the SBA-15 can be seen for the CMK-3 (Jun et al., 2000).

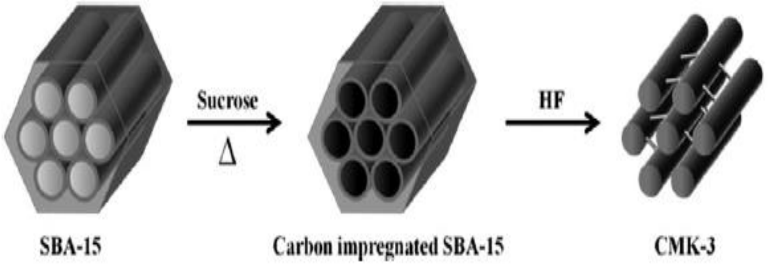

Figure 8: Schematic view of the synthesis procedure for CMK-3 (Nettelroth et al., 2016)

With the some modifications, SBA-15 alumino silicate, SBA-16, KIT-6 were used as an hard template for the CMK-5, CMK-6 and CMK-7, CMK-8 and CMK-9, respectively. For all the CMK types except for the CMK-5 and CMK-9, sucrose was used as an carbon source. For the CMK-5 and CMK-9, furfuryl alcohol was used as an carbon source. For the CMK-5, aluminosilicate SBA-15 was used as a silica template. The pores of the template were filled with the furfuryl alcohol and this material was heated to 80°C, giving the carbon only in the form of coated on the walls of the pores. The furfuryl alcohol in the other part of the pores which did not process polymerization was removed by evacuation. After, pyrolysis and silica removal procedures were completed. XRD analysis resulted in the insufficient atomic ordering of the synthesized materials (Joo et al., 2001).

Using the KIT-6 as a template, CMK-8 and CMK-9 were also synthesized (Kleitz et al., 2003). Same synthesis procedure of CMK-3 and CMK-5 was also performed for the synthesis of the nanotube type CMK-8 and rod type CMK-9, respectively. Carbonization of sucrose results in a rod type CMK-9 material; whereas, the use of furfuryl alcohol and pyrolysis under vacuum conditions gave nanotube or nanopipes CMK-8 material. Tube type material gave higher surface area and pore volume compared to nanopipe one. Due to the high pore size of the KIT-6, the coating of the pore walls with the carbon precursors was more effective compared to that of SBA-15 alumino silicate.

There are many studies related to the CMK materials. Lei et al. (2008) studied the chemical vapor deposition method in order to fill the pores of the SBA-15 with ferrocene and the effect of different graphitization temperatures on CMK-5. The ferrocene was heated and sublimed at 120°C in the first reactor and under argon flow its vapor was carried to the second reactor at 500°C and it was impregnated to the SBA-15 pores. SBA-15 was exposed to the ferrocene at different time intervals and it was found that with an increase in the contact time of ferrocene and SBA-15, pore volume, pore diameter and pore volume of CMK-5 decreased. With the graphitization temperature below 850°C, highly ordered mesoporous carbon was synthesized with low graphitization degree. On the other hand, with the graphitization temperature above 850°C, graphitization degree of CMK-5 was improved, destroying the ordered structure of the CMK-5.

There are many applications of the CMK type materials. Zhou et al. (2016) studied the enhance carbon dioxide capture via CMK-3. CMK-3 was synthesized with a surface area of 1115 m^2/g and a pore volume of 1.11 cm^3/g. The synthesized CMK-3 was tested in the sorption of carbon dioxide under different water amounts. With the incorporation of the water to the sorption process improved the carbon dioxide capture capacity of the CMK-3. Moreover, Xia et al. (2007) reported the hydrogen storage properties of the CMK-3 materials. CMK-3 was synthesized with the hard template method and it was treated with the carbon dioxide at different time intervals. With an increase in the contact time of carbon dioxide and CMK-3, the structure of the carbon was destroyed because the intensity of the characteristic diffraction peaks for the CMK-3 was decreased with an increase in the contact time of carbon dioxide and CMK-3 and the peaks were totally disappeared in the 8-hour contact time. On the other hand, with an increase in the contact time, the hydrogen uptake capacity was the highest at 77 K. The reason was the larger hydrogen uptake capacity of the materials with the pore size smaller than 1 nm. Therefore, disordered CMK-3 with low pore diameter was the effective one for the hydrogen uptake.

Roggenbuck et al. (2006) used the CMK-3 as a template in order to produce mesoporous magnesium oxide. $Mg(NO_3)_2$ was used as a magnesium oxide source. CMK-3 was dispersed into the aqueous solution and $Mg(NO_3)_2$ was inserted into this mixture. Then, after filtration and drying steps, under air atmosphere $Mg(NO_3)_2$ was converted to MgO at 573 K and then carbon was removed at 1023 K. The pore volume and surface area of the MgO (0.52 cm^3/g, 280 m^2/g) was smaller than that of SBA-15 (1.26 cm^3/g, 520 m^2/g). On the other hand, in low angle XRD pattern of MgO (100) reflection peak was observed; however, there were no (110) and (200) diffraction peaks, indicating a slight shrinkage in the structure of MgO.

Ezzeddine et al. (2016) studied the removal of methylene blue from water using the CMK-3 materials. CMK-3 material having a surface area of 885 m^2/g and a pore diameter of 4 nm was synthesized. CMK-3 was a promising candidate for the adsorbing of methylene blue from the water.

CHAPTER 4

MICROWAVE HEATING

In recent years, new heating processes take attention among the scientific studies. The new alternative heating way, microwave heating, appeared to provide energy to carry out the chemical reactions. With the faster energy absorption to the material, elimination of the cold spots through the catalyst bed and the selective heating, the disadvantages of the conventionally heated reactor system can be minimized.

Due to the highly endothermic nature of steam reforming of ethanol reaction and the possibility of catalyst deactivation with the side reactions in the cold spots, the need for the new heating types should be required in order to achieve efficient hydrogen production with less energy input. Microwave heating is an alternative heating process with eliminating the cold spots and giving less energy input compared to other heating types.

4.1 Microwave Energy

In the electromagnetic spectrum the microwaves are between radio waves and infrared radiation. The wavelength of the microwave changes from 1 mm to 1 m and the frequency range is between 300 and 300000 MHz (Durka et al., 2009). There are many application areas of the microwave heating. Microwaves are generally used in telecommunication systems. Moreover, microwaves can be used in the cooking of foods, processing of medical wastes, treatment of the wastes such as sewage sludge, regeneration of activated carbon, and chemical residues of petrol industries. In recent years, for the ceramics, polymers, metallic based materials, the microwave heating takes attention (Mishra et al., 2016).

The behavior of the different materials to the microwaves is shown in Figure 9. The first one is the conductive material so the microwaves are reflected from this material.

The second one which is called insulating material is highly transparent to the microwaves and the third one is the highly microwave absorbent material which absorbs microwaves with creating heat.

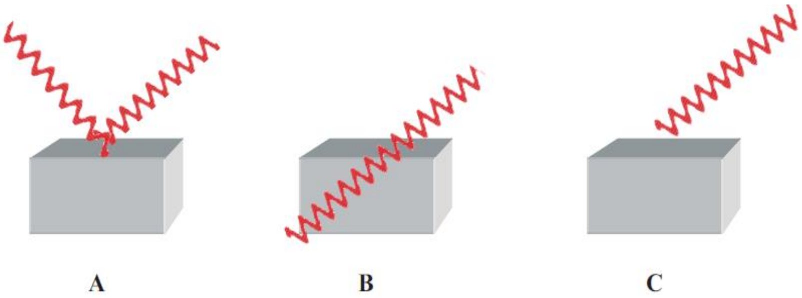

Figure 9: The reaction of the different materials to the microwave heating a) conductive material b) insulating material , and c) absorbing material (Durka et al., 2009)

4.2 Microwave Applicators

4.2.1 Multi-mode Microwave Applicators

The microwaves which are used in the house kitchens are the example of the simplest and cheapest multi-mode microwave applicator. These types of microwaves can also be used in the laboratories; however, there are some disadvantages. The experiments can be performed the microwave consisting of many holes in the microwave oven, causing a radiation leakage. Power and temperature control are not possible in the system because there is only on-off and there are some oscillations in the temperature (Will et al., 2004). Moreover, due to the formation of multiple modes of microwaves, hot spots and cold spots can be formed, causing a non-uniform temperature distribution.

4.2.2 Single-mode (Mono-mode) Microwave Applicators

In order to eliminate the disadvantages of the multi-mode system, the single-mode microwave applications are developed. With the adjustable electric field strength, the control of the temperature and energy input, mono-mode applicators focus the target material and homogeneous temperature profile can be achieved with single-mode heating. The schematic view of the multi-mode and single-mode applicators is shown in Figure 10.

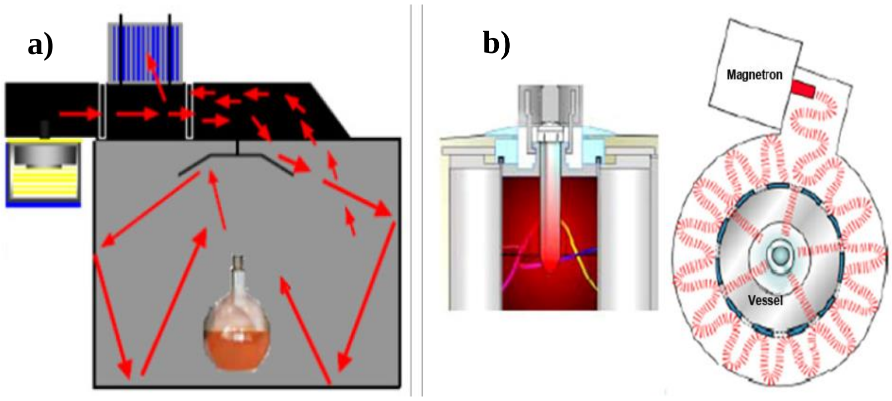

Figure 10: a) Mono-mode and b) Single-mode microwave applicators (Hayes et al., 2002)

4.3 Dielectric Property of the Material

When the carbon materials receive the microwaves, their delocalized π-electrons interact with changes in the electromagnetic field. The important part of the microwave energy can be converted to thermal energy due to the conductive loss caused by interfacial polarization (Maxwell-Wagner effect) (Li et al., 2014).

Unlike the conventional heating systems, in the microwave heating systems, the heat is generated by the direct conversion of electromagnetic energy (Guler et al., 2017; Varisli et al., 2017). With the interaction of the charged particles with microwave frequency waves, the material can be heated.

Microwave energy can be absorbed by a dielectric material. The dielectric properties of the materials can be explained with the complex permittivity of the material (ε^*). The below expression represents the relation for ε^*:

$$\varepsilon^* = \varepsilon' - j\varepsilon''$$

ε' is the dielectric constant, explained by a measure of the stored energy in the material in the form of electric field; on the other hand, ε'' is the dielectric loss factor, explained by a measure of the emitted energy in the material in the form of heat. Therefore, the complex permittivity term can be used the ability of to absorb microwave energy and convert from energy to heat (Li et al., 2014).

Dielectric loss tangent ($tan\delta$) value is the another explanation of the ability of the material to be heated in the presence of microwave heating. It can be described as the ratio of dielectric loss factor(ε'') to dielectric constant (ε'). The better the material absorbs microwaves, the higher the dielectric loss tangent value is. The equation for the dielectric loss tangent value is given below:

$$tan\delta = \frac{\varepsilon''}{\varepsilon'}$$

Carbon based materials having a high dielectric loss tangent values are strong microwave absorbers (Menéndez et al., 2010). Moreover, if the catalysts are transparent to the microwaves such as silica and alumina based catalyst, carbon materials should collaborate with the catalyst to heat the catalyst. Generally, the reactors made of quartz are transparent to the microwaves so there is no loss of microwave due to the quartz reactor while heating of the catalyst bed. Moreover, the dielectric loss factor and loss tangent values of the ethanol and water are high enough to absorb microwaves.

4.4 The Advantages of the Microwave Heated Systems

There are many advantages of the microwave heating mechanism compared to the conventional heating system. The schematic representation of the heating mechanisms for both conventional heating and microwave heating is shown in Figure 11. Firstly, in conventionally heated systems, heating starts from the walls of the reactor and then it is transferred to the material via convection and conduction mechanisms. Therefore, temperature near the wall was higher than that of the core of the material. Due to this, non-uniform temperature distribution is achieved with conventionally heated systems. On the other hand, in microwave heating, microwave energy is directly transferred to material so the heating starts from the interior of the material. Therefore, the formation of the cold spots can be eliminated and selective, uniform and volumetric heating can be achieved (Gündüz et al., 2015). In this way, higher yield, conversion and selectivity can be achieved and lower coke formation and highly stable product distributions can be observed via microwave heating. Moreover, the heating period to reach the desired temperature for the conventionally heated systems takes a long time. However, in the microwave system, the microwaves are focused to the material, resulted in the material to heat up quickly. Moreover, if the microwave power is switched off, there is only latent heat and so the thermal control of the system is very easy.

Hot spots formation in the microwave system in the active metal sides and carbon based catalysts also increase the reaction rate and so the conversion and yield values rise.

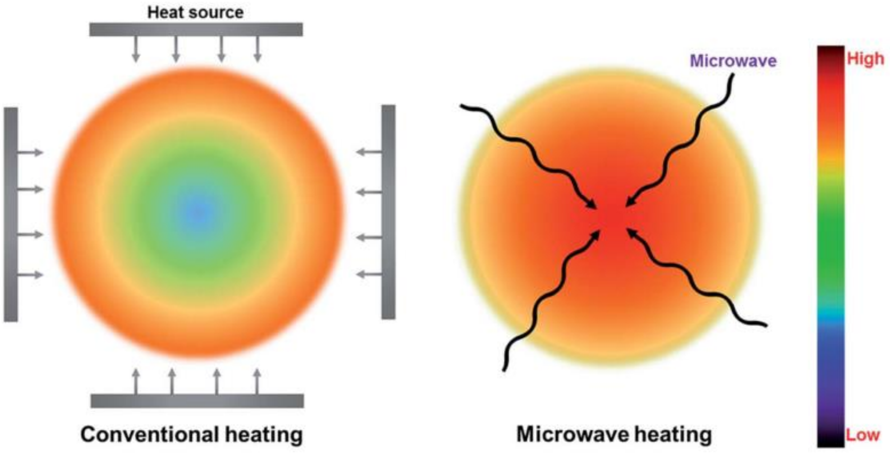

Figure 11: Heating mechanisms of conventional heating and microwave heating (Zhang et al., 2017)

There are many studies related with the microwave applications in the literature. Varisli et al. (2017) studied the ammonia decomposition reaction over iron incorporated mesoporous carbon catalysts. The mesoporous carbon is used not only as a catalyst support, but also as a microwave absorber and iron was impregnated to the catalyst support to enhance the catalytic activity of the catalyst and also the iron is a good microwave receptor. Activity results showed that higher ammonia conversion can be achieved in the microwave reactor system at lower temperatures compared to the conventionally heated system. Higher catalytic activity in the microwave heated system could be explained by the hot spot formation.

Durka et al. (2011) studied the methanol steam reforming reaction in microwave heated system with the catalyst of $CuZnO/Al_2O_3$ and $PdZnO/ Al_2O_3$. 10 % higher methanol conversion was achieved in the microwave heated system compared to the conventionally heated system at the same temperature. It was found that the product distribution graph was not effected by a heating types. Moreover, temperature distribution was also investigated for both heating types. As expected, in the microwave heating system, the temperature at the core was higher than that of in the wall. Moreover, reverse situation was observed for the conventionally heated system.

Fidalgo et al. (2008) studied the dry reforming of methane reaction in microwave assisted reactor system. A commercial activated carbon was used as a catalyst and microwave receptor. The quite increase in the methane and carbon dioxide was observed in the microwave heated system. Formation of the micro-plasmas under microwave heating enhanced the catalytic reactions.

Domínguez et al. (2007) investigated the catalytic deomposition of the methane over activated carbon in order to produce hydrogen. A commercial activated carbon, made from coconut shell and then activated with steam, was used as a catalyst. The catalytic activity tests were performd both conventionally heated and microwave heated reactor systems. It was found that activated carbon catalyst was selective to the methane decomposition reaction to produce hydrogen with high conversions. With microwave heating, higher methane conversions were achieved compared to conventional heating system in the first 30 min of the reaction time. However, after 120 min, the conversion of methane in microwave system was lower than that of in the conventionally hetaed system. Due to the blockage of the pores with the carbon formation, the activity of the catalyst decreased. In other words, with the efficient methane decomposition process with microwave heating, more carbon produced in the pores.

Gündüz et al. (2015) studied the ethanol steam reforming over novel mesoporous catalysts in microwave and conventionally heated systems. Cobalt and nickel were incorporated into the alumina support. Higher ethanol conversion was achieved in the microwave heated system. Coke formation was also eliminated in the microwave heated system with the elimination of cold-spots. Highly stable reactor performance was achieved in the long term activity test result.

CHAPTER 5

EXPERIMENTAL

The experimental portion of this study consists of three parts which are synthesis of the catalyst, catalyst characterization and its activity test. Different catalyst supports which are commercial and synthesized mesoporous carbons, SBA-15, and silica aerogel were impregnated with nickel. All catalysts were characterized using different characterization techniques. Activity tests for all the synthesized materials were performed at two different temperatures in SRE and SESRE reactions. For SESRE experiments, different packing concepts for the catalyst and CaO were also investigated. The best catalyst was also tested in the microwave system in both SRE and SESRE-M tests.

5.1 Synthesis of the Catalysts

5.1.1 Synthesis of SBA-15

Four grams of surfactant, Pluronic P-123 (P123, Poly(ethylene glycol)-block-poly(propylene glycol)-block-poly(ethylene glycol), Sigma Aldrich) was dissolved in the mixture of 125 ml deionized water and 25 ml hydrochloric acid (HCl, Hydrochloric acid fuming 37 %, Merck). The pH value of the mixture should be smaller than 1. After the mixture was well-mixed, the temperature of the mixture was set to 40°C. Then, 8.2 ml tetraethyl orthosilicate (TEOS, Merck) which is the silica source was added drop wise to the solution. After the solution was stirred for 37 minutes, it was taken into oven which was at 90°C. Hydrothermal synthesis was performed at 90°C for 24 h in a beaker. The final solid mixture was filtered and washed with deionized water and the solid product was dried. Finally, the solid product was calcined using dry air with a flow rate of 80 ml/min. The temperature of the furnace was arranged from ambient temperature to 600 °C with a heating rate of 1^{o}C/min and it was kept at 600 °C for 6 h. Calcination was performed to remove the surfactant from the support.

5.1.2 Synthesis of Silica Aerogel

In the synthesis of silica aerogel, 1.73 g water, 5.64 g ethanol and 10.01 g TEOS were mixed at room temperature. Then, 62 μL of 1M HCl solution was added dropwise to the mixed solution at room temperature. After two hours mixing, 3.85 g water and 9.92 g ethanol were added to the solution at room temperature. Then, 650 μL of 1M ammonia (NH_3, 25% v/v, Merck) and 800 μL of 1M ammonium floride (NH_4F, Merck) solutions were dropped to the solution separately to form gel. The formed gel was cut into small pieces and was stored in ethanol for 8 h at room temperature. Ethanol was replaced with 30 ml hexane (Sigma Aldrich) and the gel was put into the water bath at 45°C. After two hours, hexane was renewed with 30 ml hexane and trimethyl chlorosilane (TMCS, Merck) which is the silyating agent was added to the solution. The water formed after the addition of TMCS was removed from the solution and the new hexane was added in order to complete the hexane volume as 30 ml. Then, the gel containing hexane was put into the water bath at 45°C. Hexane was renewed two times at every five hours. Finally, the gel was filtered and put into the oven at 125°C for 2 h. For some of the sample preparation, TMCS was not added into the solution and these samples were named as SAwoTMCS (Silica aerogel without TMCS), on the other hand; the samples which contained TMCS was named as SA (Silica Aerogel).

5.1.3 Synthesis of MCMT (Mesoporous Carbon by METU)

MCMT was synthesized using a modified version of the hard-templating approach reported by Jun et al. (2000). For the SAwoTMCS, 1.25 g sugar (Torku, Turkey) was dissolved in the 5 ml distilled water. Then, 0.14 g sulfuric acid (95-98 %, Merck) was added to this solution. Then, 1 g of SAwoTMCS was added to the mixture and stirred for 1 h. The solution was put into the oven at 100°C for 6 h and at 160°C for another 6 h. In order to fill all pores with the sucrose, the same procedure was applied once more. 0.8 g sucrose was dissolved in the 5 ml distilled water. Then, 0.09 g sulfuric acid was added to the solution. Then, the obtained dark powder in the first step was ground and the powder was added to the solution slowly. After 1 h mixing, two different heating procedures were applied to the solution. In the first heating procedure, the solution was put into the oven at 100°C for 6 h and then at 160°C for another 6 h which was called double heating (DH). In the second procedure the solution was put into the oven at 160°C for 12 h, which was called single heating (SH). All the other steps were kept same. The obtained dark product was carbonized under helium gas with a flow rate of 80 ml/min at 900°C for 6 h with a heating rate of 5°C/min. Finally, the dark powder was treated with 1 M NaOH solution or 10 wt. % hydrofluoric acid for 45 min to remove the silica template. For the template removal step with NaOH, 1 M NaOH solution was prepared with a solution containing 24 g NaOH pellets, 300 ml ethanol and 300 ml distilled water. The solution was heated up to 100°C and the carbonized sample was put into the stirring solution. The sample was treated with the solution at 2 h. Then, the solution was renewed and the same procedure was repeated once more. Finally, the final sample was filtered and washed with 1 L boiling ethanol. For the template removal step with HF, 10 wt. % hydrofluoric acid solution was prepared using the 23 ml of 38-40 wt. % hydrofluoric acid and 100 ml distilled water. The carbonized sample was treated with the HF solution at room temperature for 45 min and then centrifuged and washed and filtered with the distilled water. Then, the final sample was dried at 100°C for 4 h. For the silica aerogel templates, only difference was the amount of distilled water and sulfuric acid used in the first sucrose addition. Silica aerogel has low density so 7 ml distilled water was used in order to dissolve the silica aerogel in the water and 0.196 g sulfuric acid was used. The other parameters were kept constant.

5.1.4 Nickel Impregnation to the Synthesized Supports and Commercial Mesoporous Carbon

5.1.4.1 Incipient Wet-impregnation Method

After the catalyst was synthesized, the nickel was impregnated to the catalyst supports. Nickel (10 wt.%) was incorporated to synthesized catalyst supports or commercial mesoporous carbon. As a nickel source, nickel nitrate ($Ni(NO_3)_2.6H_2O$, Acros Organics, 99 %) was used. The necessary amount of the nickel nitrate was dissolved in the 5 mL deionized water while the catalyst support was dissolved in the 10 mL of the deionized water. Calculation of nickel amount was given in Appendix A. After the solutions were well mixed, solution containing nickel was added to the catalyst solution drop wise. Then, the resulting solution was mixed for 24 h and then it was dried at 60°C. Finally, the solid product was calcined in a quartz tubular reactor heated using tubular furnace under dry air atmosphere with a flow rate of 80 ml/min. The temperature of the furnace was arranged from ambient temperature to 650 °C with a heating rate of 1^{o}C/min and it was kept at 650 °C for 6 h. Finally, the catalyst was reduced for 4 h with hydrogen with a flow rate of 60 ml/min at 650 °C to obtain metallic nickel with the reduction of nickel oxide. For MCMT catalyst support, same procedure was applied but instead of deionized water, ethanol was used.

5.1.4.2 Surfactant-Assisted Impregnation Method

Only for the SBA-15 catalyst support, the surfactant assisted impregnation method was also performed in order to obtain small crystallite size of metallic nickel. Ten weigh percent of nickel was incorporated to the synthesized SBA-15. P123 (0.09 g) (N_{P123}/N_{Ni}=1/100) was dissolved in the 25 ml of distilled water. After P123 was completely dissolved, 0.5 g of nickel was added to the solution. Then, 1 g of SBA-15 support was put into the solution. The resulting solution was mixed for 24 h and then it was dried at 60°C. Finally, the solid product was calcined in the quartz tubular reactor heated using the tubular furnace under dry air with a flow rate of 60 ml/min. The temperature of the furnace was arranged from ambient temperature to 650 °C with a heating rate of 1^{o}C/min and it was kept at 650 °C for 6 h. Finally, the catalyst was reduced for 4 h with hydrogen with a flow rate of 60 ml/min at 650 °C to obtain metallic nickel with the reduction of nickel oxide.

5.2 Characterization Techniques

The synthesized material was characterized using different techniques: X-Ray Diffraction (XRD), Nitrogen Adsorption/Desorption Analysis (BET), Temperature Programmed Ammonia Desorption (TPD), Temperature Programmed Reduction (TPR), Scanning Electron Microscopy (SEM), Fourier Transform Infrared Spectroscopy (FTIR), Raman Spectroscopy, and Thermal Gravimetric Analysis (TGA).

5.2.1 X-Ray Diffraction (XRD)

The crystal structure of the catalyst was analyzed using the X-ray diffractometer. The equipment used for the analysis was a Rigaku Ultima-IV diffractometer in METU Central Laboratory. For the high angle XRD pattern, Bragg angle values were set in the range of 10°-90° with a step size of 1°/min and for the low angle XRD pattern, Bragg angle values were set in the range of 1°-10° with a step size of 0.1°/min.

5.2.2 Nitrogen Adsorption/Desorption Analysis (BET)

In order to determine the multipoint Brunauer, Emmett and Teller (BET) surface area, pore volume, adsorption-desorption isotherms, and pore size distributions, Micromeritics Tristar II 3020 device at METU Department of Chemical Engineering was used. Before the BET analysis, materials were degassed at 110°C for 3h.

5.2.3 Temperature Programmed Ammonia Desorption (NH_3-TPD)

In order to determine the total acidity of the material, TPD analysis was performed. Firstly, the materials were dried at 200°C with argon gas at a flow rate of 50 ml/min. After the materials were cooled to the room temperature and they were saturated with 5 % NH_3 in helium gas with a flow rate of 50 ml/min at room temperature for an hour. Then, the samples were kept under 50 ml/min argon flow in order to purge ammonia. After, the materials were heated from room temperature to 125°C with a heating rate of 30°C/min under 30 ml/min helium flow. Then, the heating rate was lowered to 10°C/min and the materials were heated from 125°C to 650°C under 30 ml/min helium flow. The analyses were performed in the Kinetic Laboratory at Department of Chemical Engineering, METU using Micromeritics TPx System.

5.2.4 Scanning Electron Microscopy (SEM)

Morphology of the catalyst was determined using a QUANTA 400F field-emission scanning Electron microscope in the Central Laboratory. In order to prevent the interaction of electrons with the materials, the samples were covered with Au/Pd.

5.2.5 Raman Spectroscopy

Raman spectroscopy analysis was performed for MCMT type materials using FRA 106/S, Hyperion 1000, Ramanscope II equipped with a laser (532 nm) as excitation source.

5.2.6 Thermal Gravimetric Analysis (TGA)

For the used catalysts, thermal analysis technique (Shimadzu TA-60 WS) was used in order to determine the coke deposition amount. TGA analysis was performed under air atmosphere with a flow rate of 50 ml/min and a heating rate of 10°C/min in the temperature range of 25°C-900°C.

5.2.7 Fourier Transform Infrared Spectroscopy (FTIR)

FTIR Spectroscopy analysis gave us about the bond types of the materials. Analysis of materials were performed using a Perkin Elmer Spectrum One equipment. FTIR spectra of these samples were obtained at a wavenumber range of 400−4000 cm^{-1} with the resolution of 4 cm^{-1}.

5.3 Naming of the Catalysts

The synthesized SBA-15, SA and MC were named in format as AB-C where A referred to weight percentage of the metal, B was the type of metal and C indicated the support.

For MCMT type catalyst support, different silica templates, calcination temperatures, heating methods and washing procedures were applied. Therefore, the catalyst supports were named in the order of MCMT-X-Y-Z-T. X was the silica template: A for SAwoTMCS and B for SA. Y was referred to the calcination temperature of the silica template. Z was the heating methods: SH for the single heating procedure and DH for the double heating procedure. T was implied to the washing procedure: HF or NaOH.

The synthesized catalysts are given in Table 2.

Table 2: Synthesized Catalysts

Catalyst	Metal Loading (by wt.)	Support	Impregnation Method
10Ni-SBA-15	10	SBA-15	Incipient Wet Imp. Method
10Ni-P123-SBA-15			Surfactant Asst. Imp. Method
5Ni-MC	5	MC (Mesoporous Carbon)	Incipient Wet Imp. Method
10Ni-MC	10		
10Ni-SA	10	SA (Silica Aerogel)	Incipient Wet Imp. Method
10Ni-MCMT	10	MCMT (Mesoporous Carbon by METU)	Incipient Wet Imp. Method

5.4 The Reaction System and Experimental Procedure

5.4.1 The Reaction System

Catalytic activity tests for the SRE and SESRE reactions were performed both in a focused microwave (MWR) and conventionally heated tubular reactors (CHR). A schematic diagram of the reaction system installed with the conventionally and microwave heating units is given in Figure 12. The feed containing water and ethanol mixture was sent to the evaporator (THELCO, Model 15) at 130°C with the help of the syringe pump. The mixture was evaporated in the evaporator which was at 130°C. At the evaporator, the vaporized ethanol water mixture was mixed with the argon. Argon gas was used as a carrier gas for the vaporized ethanol water mixture. The flow rate of the argon was arranged using a mass flow controller located before the evaporator. After the evaporator, the gaseous mixture was sent to the tubular furnace (CARBOLITE, MTF 12/38/250). The pipeline between evaporator and reactor was heated with a heating tape at 130°C in order to prevent the condensation of the ethanol

& water vapors. Quartz reactor containing catalyst or catalyst and sorbent with a diameter of 13 mm diameter was placed into the tubular furnace. The water ethanol mixture carried by argon was fed to the catalyst bed and reactions took place. The exit stream of the reactor was sent to the condenser to separate the unreacted ethanol and water. The pipeline between reactor outlet and condenser was heated using heating tapes. The condenser temperature was adjusted by circulating water from water bath (NÜVE, BS 402) at a temperature of 1°C through the condenser. Reactor effluent stream was analyzed in a gas chromatograph (Agilent Technologies 6850, Porapak S column, TCD), which was connected on-line to the reactor. Liquid mixture was also analyzed using gas chromatograph with the same GC method. Argon gas was used as a carrier and reference gas for the gas chromatography. GC parameters and their values are shown in Table 3. The method information for gas and liquid analyses is shown in Table 4.

Table 3: GC parameters and their setting values

Parameter	Set Value
Inlet heater temperature (°C)	200
Total Flow (ml/min)	5
Detector Temperature (°C)	200
Reference Flow (ml/min)	40
Makeup Flow (ml/min)	5

Table 4: Temperature program for liquid and gas analyses

Initial Temperature (°C)	Final Temperature (°C)	Temperature ramp (°C/min)	Time (min)
38	38	--	3
38	175	24.1	
175	175	--	7
			15.68

In order to test the repeatability of the experiments, three experiments were performed at different times under same conditions for the 10Ni-SBA15 catalyst.

A similar system was used in the microwave experiments. The only difference was the replacement of conventionally heated tubular reactor with the microwave heated reactor. The microwave reactor experiments were performed in a microwave heated system, supplied by SAIREM Company, having a maximum working power of 2 KW and a frequency of 2.45 GHz. The microwave system consists of three main parts, generator, magnetron and applicator. Power was arranged from the generator. Then, generator sent to the direct current to the magnetron, where the direct current was turned to the microwave energy. Using the tuner part of the microwave heated reactor, the microwave is focused to the catalyst bed inserted into quartz reactor. The cooling water was used in order to take unabsorbed microwaves. The temperature of catalyst bed was arranged by changing the power in microwave system and measured with an infrared pyrometer (Raytek M13).

5.4.2 Experimental Procedure

Catalytic activity tests for the SRE and SESRE were performed both in a focused microwave (MWR) and conventionally heated tubular reactors (CHR) at 500°C and 600°C and at atmospheric pressure with a feed H_2O/C_2H_5OH ratio of 1:1 by volume. Activated carbon (0.05 g) was also used as a microwave receptor in all experiments of the SRE and SESRE reactions in order to keep the experimental parameters same for all experiments. In the case of the conventionally heated system, the reactor was heated to the desired reaction temperature (500°C and 600°C) in a tubular furnace. Moreover, the temperature of the heating tapes and evaporator was heated to 130°C and the condenser temperature was adjusted by circulating water at a temperature of 1°C through the condenser. When all the equipment was reached to desired parameters for the experiment, ethanol water mixture with a ratio of 1 to 1 by volume, was sent to the evaporator using a syringe pump with a flow rate of 0.9 ml/h. The feed was vaporized in evaporator which is at a temperature of nearly 130°C. The vaporized mixture which had a volumetric flow rate of 20 ml/min was mixed with argon having 30 ml/min volumetric flow rate at evaporator. Then, the feed was sent to the reactor tube with a total volumetric flow rate of 50 ml/min. Weight hourly space velocity (WHSV) of the reaction gas mixture was 4.8 h^{-1} in all 5-hour activity tests. The effluent stream of the reactor was sent to the condenser to separate liquid (unreacted water and ethanol).

Reactor effluent stream was analyzed in gas chromatograph (Agilent Technologies 6850, Porapak S column, TCD), which was connected on-line to the reactor.
In all experiments catalyst (0.15 g) was charged to the reactor. In the case of SESRE, three different packing concepts were investigated. In the first concept, the same amount of catalyst was physically mixed with 1.5 g CaO, as a sorbent for in-situ removal of CO_2 (SESRE-M). In the second case, firstly, CaO was inserted to the reactor and then catalyst was put into the reactor. This case was named as the concept of two divided sections (SESRE-1O). In the third case, placement of CaO and catalyst was in the order of 0.05 g catalyst and 0.50 g CaO keeping total amount of catalyst and CaO same. This case was named as the concept of six divided sections (SESRE-3O). CaO was obtained by the calcination of limestone (Dikmen limestone, Turkey) at 900°C for 6 h. The schematic view for the all of the packing concepts are shown in Figure 13.

In the microwave system, firstly the cooling water was arranged as 4 L/min. Then, the microwaves were focused to the catalyst bed in order to heat up the catalyst. The power was arranged from the generator and it was increased slowly until the catalyst took the required power in order to heat up the catalyst to desired temperature.

All parameters and catalysts tested in the SRE and SESRE experiments are given in Table 5.

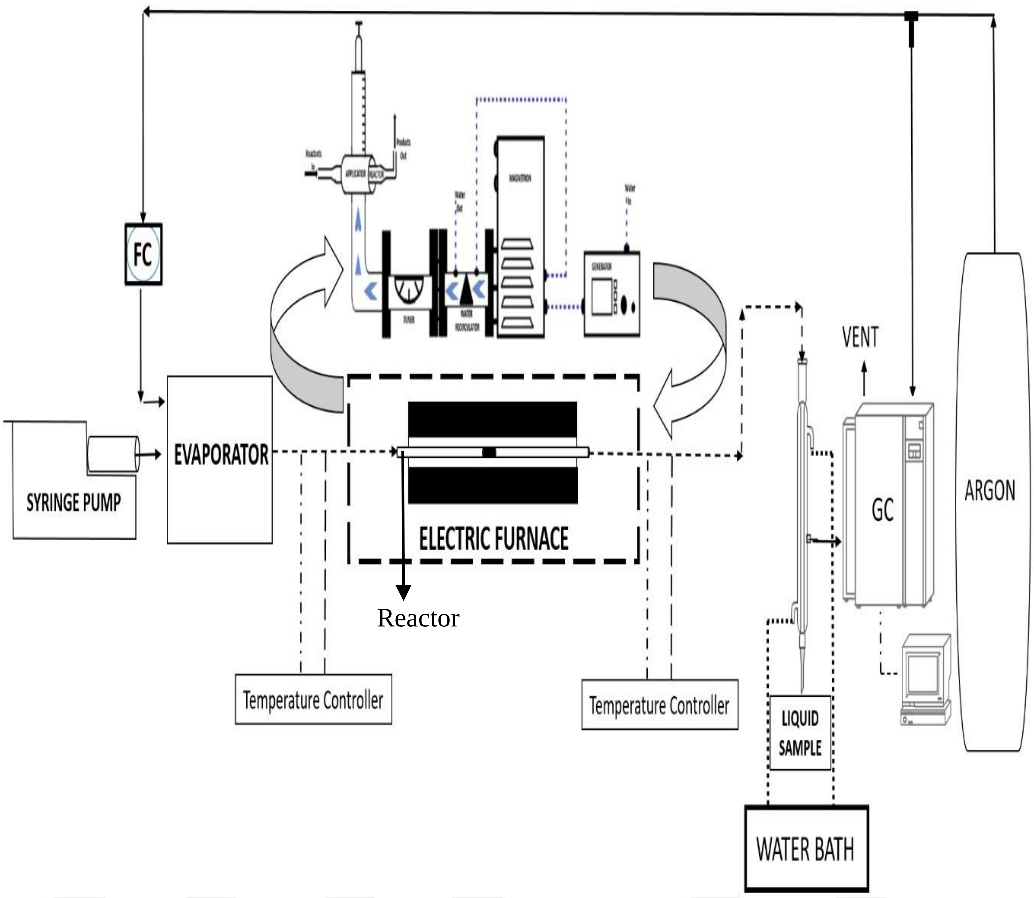

Figure 12: A schematic diagram of the hydrogen production system

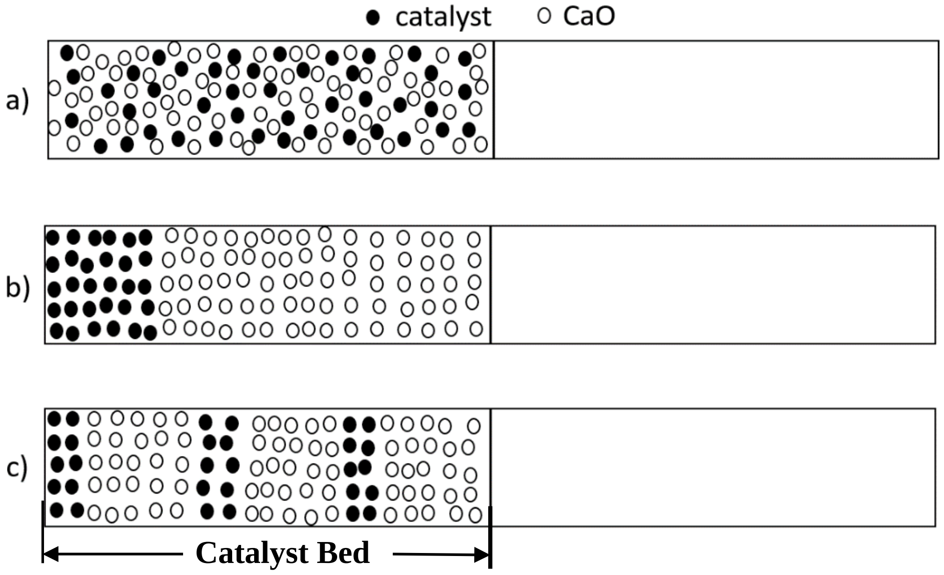

Figure 13: The schematic view of all the packing concepts: a) Mixed concept (SESRE-M) b) The concept of two divided sections (SESRE-1O) c) The concept of six divided sections (SESRE-3O)

Table 5: All parameters and catalysts tested in SRE and SESRE experiments

Catalysts	**Activity Test**	**Temperature (°C)**
No Catalyst	SRE	600
CaO	SESRE	
MC	SRE	
10Ni-SA	SRE	500
		600
	SESRE-M	600
	SESRE-3O	500
		600
10Ni-SBA-15	SRE	500
		600
	SESRE-M	600
	SESRE-1O	600
	SESRE-3O	500
		600
5Ni@MC	SRE	600
	SESRE-M	600
10Ni-MC	SRE	500
		600
	SESRE-M	600
	SESRE-1O	600
	SESRE-3O	600
10Ni-P123-SBA-15	SRE	500
		600
	SESRE-M	600
	SESRE-3O	500
		600
10Ni-MCMT-A-600-DH-HF	SRE	600
10Ni-MCMT-A-600-DH-NaOH	SRE	600
	SESRE-M	
	SESRE-3O	

CHAPTER 6

RESULTS AND DISCUSSION

In this study, different catalyst supports were synthesized and nickel was impregnated to these supports in two different weight ratios. Moreover, nickel impregnated commercial mesoporous carbon was also used as a catalyst for hydrogen production. In the steam reforming of ethanol reaction, the effects of the temperature, metal loading amount, the support, the packing section of catalyst and sorbent, and the reactor heating types on the hydrogen yield and purity and product distribution were investigated. Considering the thermodynamic analysis of the reactions, the temperature range and feed ratio (H_2O/C_2H_5OH) were chosen as 500°C-600°C and 1 to 1 by volume for all experiments, respectively. The effluent stream of the reactor consisted of H_2, CO, CH_4, CO_2, C_2H_4 and unreacted water and ethanol depending on the temperature and catalyst type. Liquid analysis was performed in order to find the ethanol conversion. Catalytic activities of the catalyst were examined according to ethanol conversion, hydrogen yield, hydrogen purity and coke formation.

In order to determine the physical and chemical properties of the supports, different characterization techniques, XRD, BET, TPD, TPR, SEM, DRIFTS, Raman Spectroscopy, and TGA were performed.

6.1 Characterization and Activity Results of SBA-15 Supported Catalysts

6.1.1 X-Ray Diffraction (XRD) Results

Low angle XRD patterns for 10Ni-SBA-15 and 10Ni-P123-SBA-15 catalysts are shown in Figure 14. In low angle XRD pattern, the peaks at the Bragg angle of 0.9°, 1.5° and 1.86° corresponded to the Miller crystal plate (1 0 0), (1 1 0) and (2 0 0), respectively. The presence of these three well resolved characteristic diffraction peaks showed that after impregnation of the nickel, the catalysts retained the ordered structure of support. Moreover, these peaks associated with hexagonal symmetry characteristic for SBA-15. High angle XRD patterns of these catalysts are shown in Figure 15. A broad diffraction peak at 22.5° was assigned to amorphous silica. The peaks at 2θ values of 44, 52, and 76° showed the presence of metallic nickel (JPDC-01-071-4653 given in Appendix B, Table B.1). There was no NiO peak in XRD pattern, which showed that all NiO was reacted with hydrogen in the reduction process.

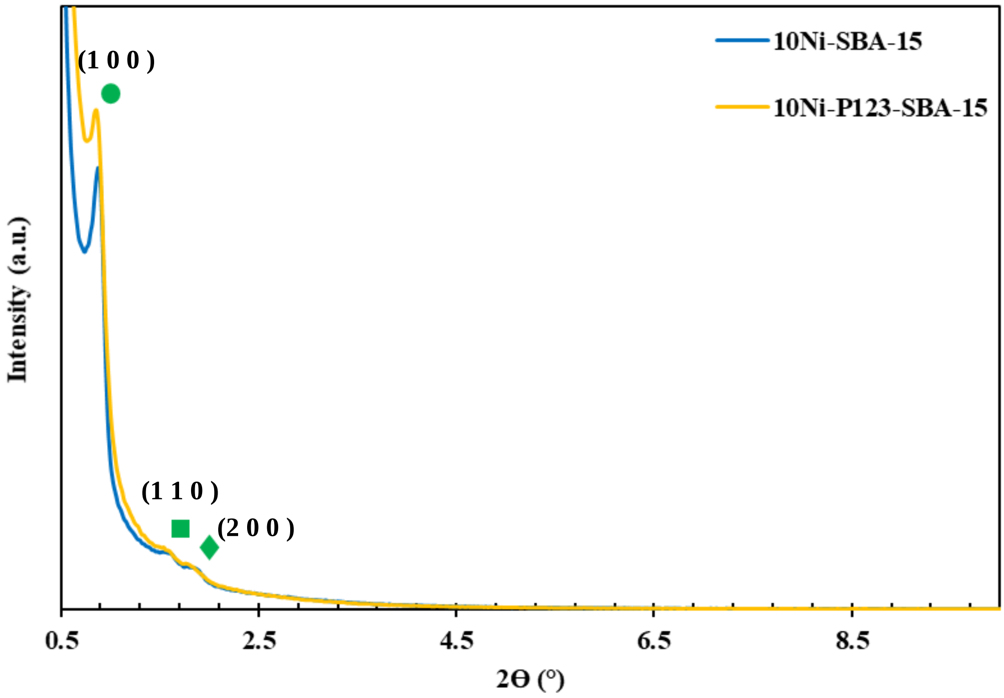

Figure 14: Low angle XRD patterns of the 10Ni-SBA-15 and 10Ni-P123-SBA-15 catalysts

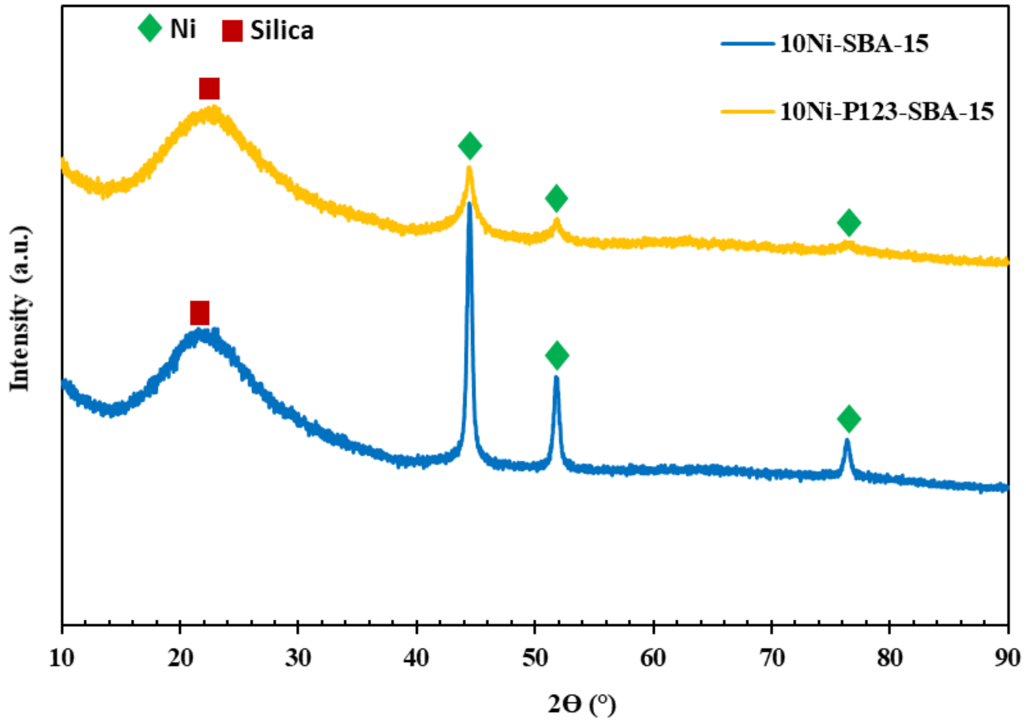

Figure 15: High angle XRD patterns of the 10Ni-SBA-15 and 10Ni-P123-SBA-15 catalysts

Using the metallic nickel d_{100} peak, the crystallite size of the nickel was calculated using Scherrrer equation and shown in Table 6 for all catalysts. Sample calculation was given in Appendix C. When the crystallite sizes of the metallic nickel of 10Ni-SBA15 and 10Ni-P123-SBA-15 catalysts were compared, the crystallite size of the 10Ni-P123-SBA15 was lower than that of 10Ni-SBA15. It showed that surfactant assisted impregnation method decreased the crystallite size of the nickel crystal compared to the wet impregnation method. This observation was in good agreement with the literature (Yang et al. 2016).

Table 6: Crystallite size of metallic Ni in the synthesized catalysts

Catalyst	2θ (°)	Metal	$t_{crystallite}$ (nm)
10Ni-SBA-15	44.43	Ni°	18.6
10Ni-P123-SBA-15	44.42	Ni°	7.9

6.1.2 N_2 Adsorption/Desorption Isotherms and Physical Properties of the Materials

Surface area, pore volume and diameter of the catalysts and microporosity of the catalysts were obtained from the N_2 adsorption-desorption analysis. The physical properties of the SBA-15, 10Ni-SBA-15 and 10Ni-P123-SBA-15 catalysts are shown in Table 7.

As seen in Table 7, SBA-15 had higher surface area than that of 10Ni-SBA-15 and 10Ni-P123-SBA-15. The BJH desorption average pore diameter of SBA-15 was 4.6 nm while that of 10Ni-SBA-15 was 4.16 nm and that of 10Ni-P123-SBA-15 was 3.88. With nickel loading to the support, the surface area and pore volume and pore diameter of catalysts decreased due to the blockage of the pores with nickel. Nickel particles were located into the micropores of the SBA-15 support, so the microporosity of the synthesized catalyst decreased.

Nitrogen adsorption/desorption isotherms of the SBA-15, 10Ni-SBA-15 and 10Ni-P123-SBA-15 catalysts are shown in Figure 16. According to IUPAC classification, SBA-15, 10Ni-SBA-15 and 10Ni-P123-SBA-15 showed Type IV isotherms with H1 hystheresis loops at a relative pressure range of 0.6 and 0.8. Moreover, formation of the hystheresis was due to the capillary condensation and so the difference between adsorption and desorption mechanisms. H1 hysteresis shows the presence of well-defined cylindrical pore channels. A steep increase in the adsorption branch, which was parallel to the desorption branch was observed. Sharp increase and decrease in the branches was the indication of narrow pore size distribution, which was consistent with pore size distribution shown in Figure 17. In other words, catalyst showed the characteristics of the ordered mesoporous material. Due to the blockage of the catalyst pores with nickel, adsorbed volume of nitrogen decreased.

Table 7: The physical properties of the SBA-15, 10Ni-SBA-15 and 10Ni-P123-SBA-15 catalysts

Catalyst	**Multipoint BET Surface Area (m^2/g)**	**BJH Desorption Pore Volume (cm^3/g)**	**BJH Desorption Average Pore Diameter (nm)**	**Microporosity (%)**
SBA-15	796	0.99	4.60	33
10Ni-SBA-15	388	0.62	4.16	17
10Ni-P123-SBA-15	414	0.60	3.88	19

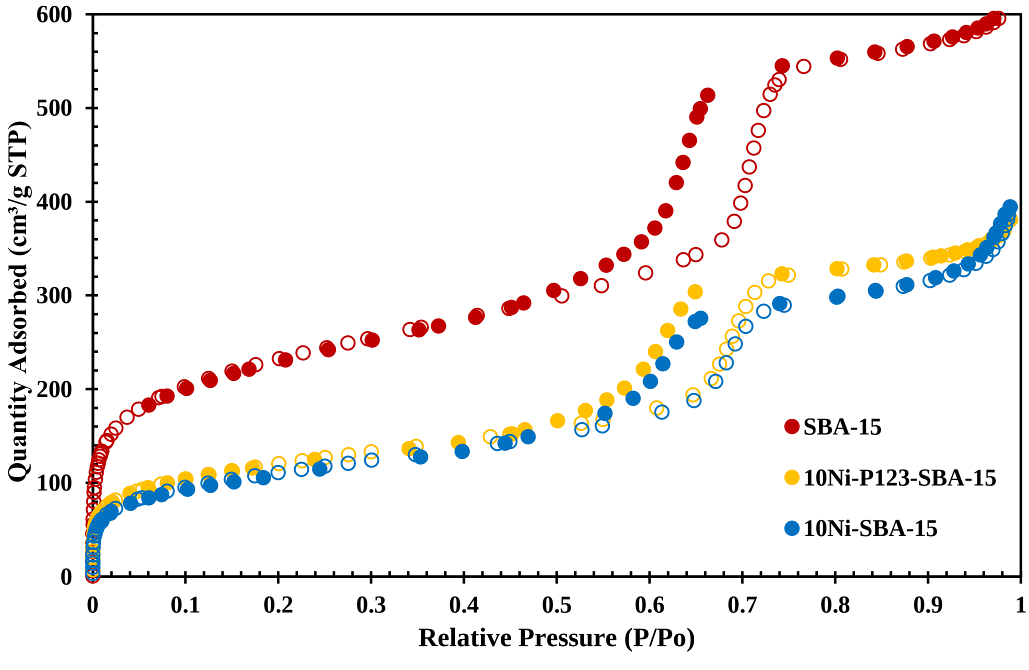

Figure 16: N_2 adsorption/desorption isotherms of the SBA-15, 10Ni-SBA-15 and 10Ni-P123-SBA-15 catalysts (Filled symbols: Desorption branch, Empty symbols: Adsorption Branch)

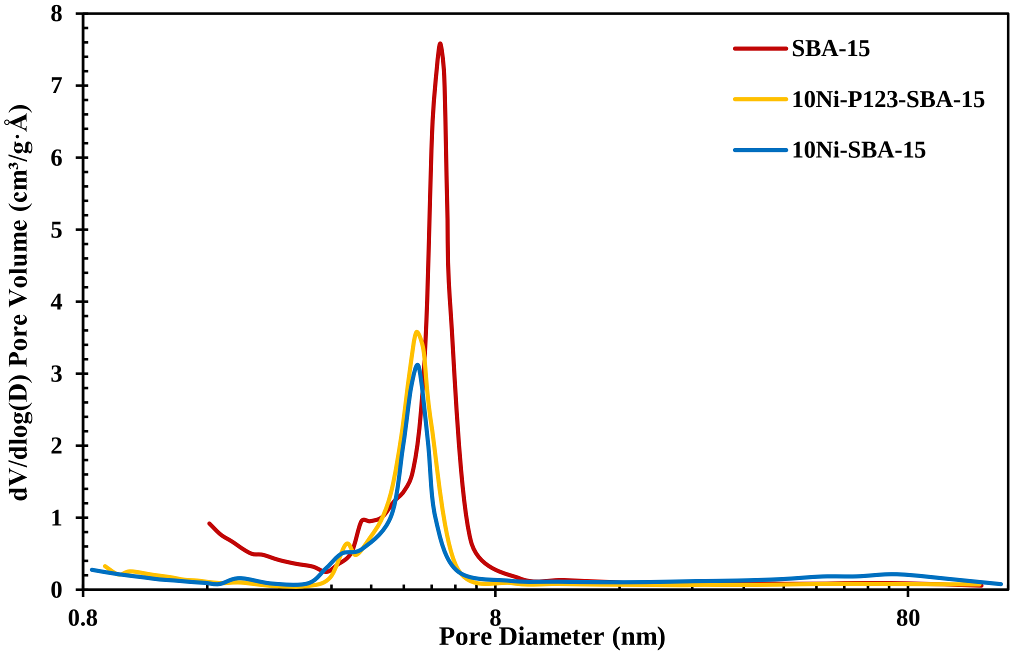

Figure 17: Pore size distributions of the SBA-15, 10Ni-SBA-15 and 10Ni-P123-SBA-15 catalysts

6.1.3 Scanning Electron Microscopy (SEM) Results

SEM images of 10Ni-SBA-15 catalyst are shown in Figure 18. It was evident that the morphology of SBA-15 was preserved after the impregnation of nickel. Small nickel particles in SEM image can be seen. EDX result of the first image (Figure 19) in Figure 18 showed that the nickel amount in the catalyst was 10 % by weight. The presence of the Au and Pd in the EDX spectra was due to the coating of catalyst with those metals.

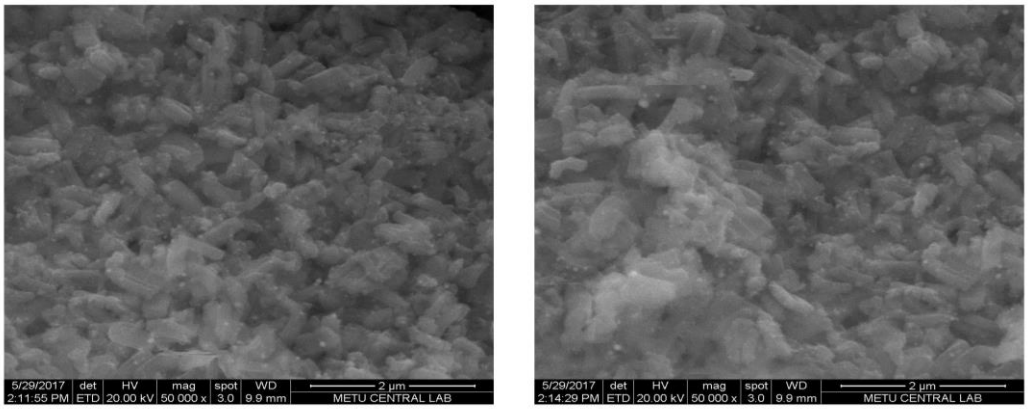

Figure 18: SEM images from different parts of the 10Ni-SBA-15 catalyst at 50000X magnification

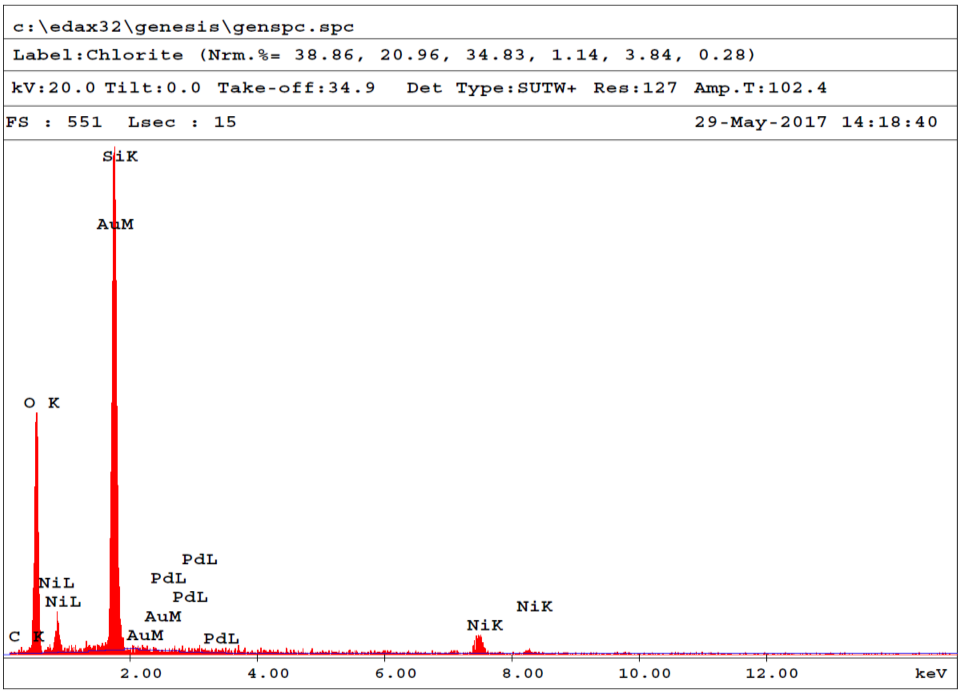

Figure 19: EDX spectrum of the 10Ni-SBA-15 catalyst

The presence of the nickel particles was verified with the back scattering images. SEM images and back scattering of these SEM images are shown in Figures 20-21. Morphology of the catalyst was preserved after the impregnation of the nickel. The white and small nickel crystals were clearly seen from the SEM images. Homogeneous distribution of the nickel particles was achieved for this catalyst. The nickel was successfully loaded into the catalyst. In view of the SEM images, nickel was well dispersed in the catalyst.

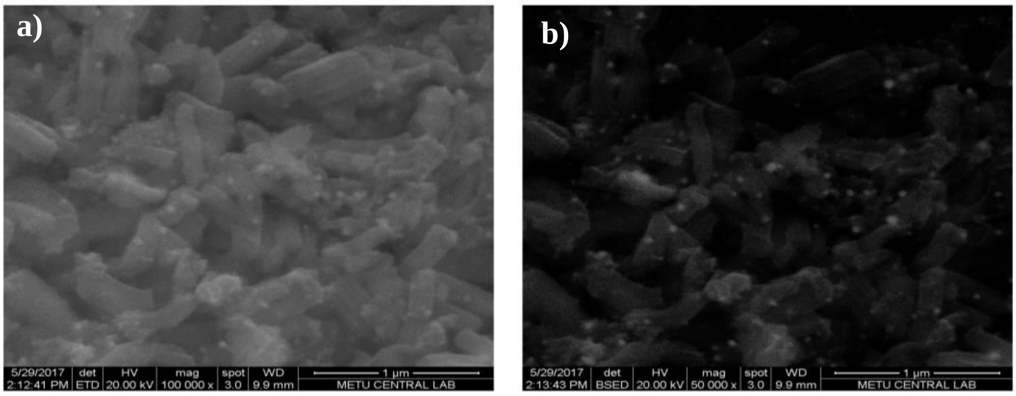

Figure 20: SEM images of the 10Ni-SBA-15 catalyst at a) 100000X and b) 50000X magnifications by backscattering detector

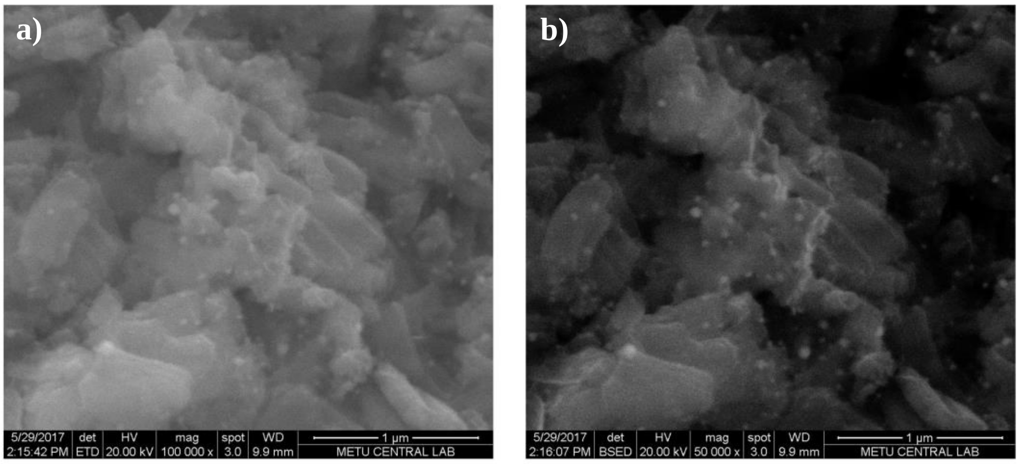

Figure 21: SEM images of the 10Ni-SBA-15 catalyst at a) 100000X and b) 50000X magnifications by backscattering detector

SEM images of 10Ni-P123-SBA-15 catalyst are represented in Figure 22. With the surfactant assisted impregnation method, the structure and morphology of the SBA-15 was preserved. However, some agglomerations can be seen from the SEM image in the structure of SBA-15. EDX result (Figure 23) for the first image of Figure 22, the weight percentage of the nickel in the catalyst was 7.

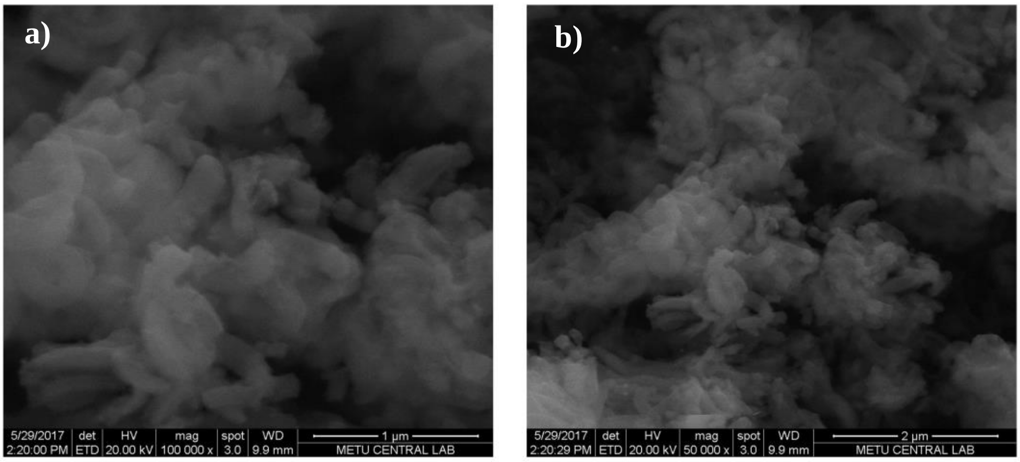

Figure 22: SEM images of the 10Ni-P123-SBA-15 catalyst at a) 100000X and b) 50000X magnifications

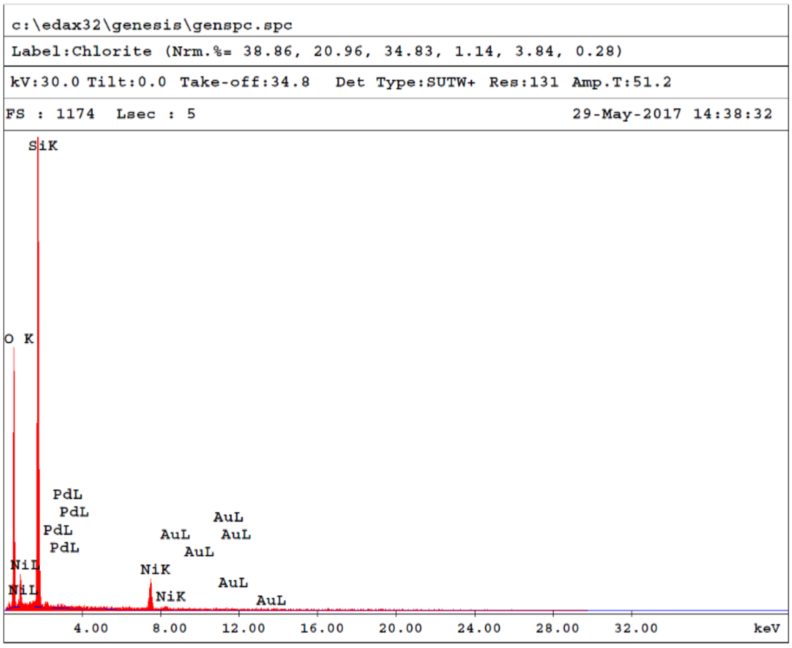

Figure 23: EDX spectrum of the 10Ni-P123-SBA-15 catalyst

SEM image and backscattering image from another part of the 10Ni-P123-SBA-15 catalyst are given in Figures 24-25. Backscattering images proved the presence of nickel crystals in the catalyst with looking at the white and shiny particles in the backscattering image. With looking at Figure 25, nickel particles were well dispersed on the catalyst as tiny particles. With looking at XRD and SEM results, it was proved that surfactant assisted impregnation method decreased the nickel crystal sizes and well dispersion of nickel crystals was achieved with this method.

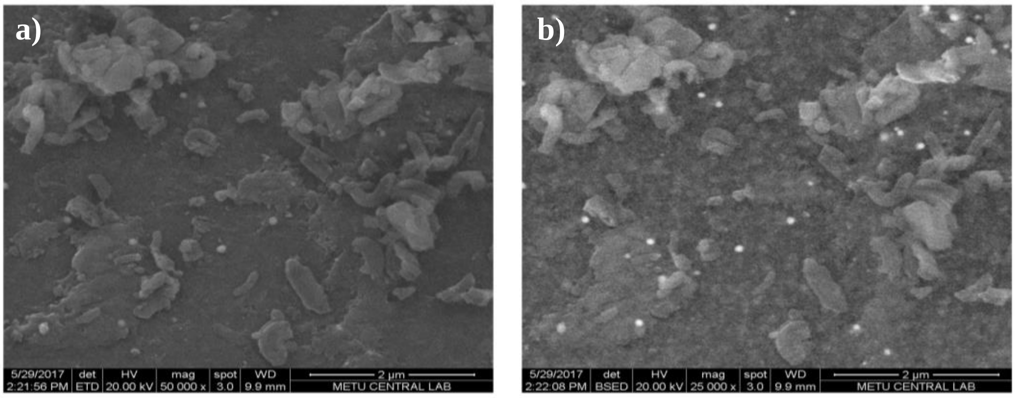

Figure 24: SEM images from another part of the 10Ni-P123-SBA-15 catalyst at a) 50000X and b) 25000X magnifications by backscattering detector

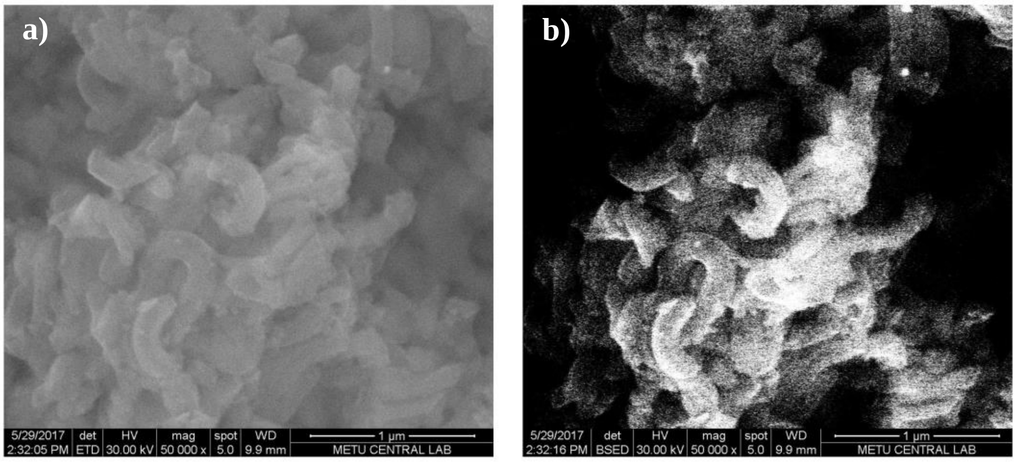

Figure 25: SEM images from another part of the 10Ni-P123-SBA-15 catalyst at a) 50000X and b) 50000X magnifications by backscattering detector

6.1.4 Temperature Programmed Ammonia Desorption (NH_3-TPD) Results

NH_3-TPD results of the synthesized materials are shown in Figure 26. Two peaks at 84°C and 325°C were observed for all catalysts. The first peak, physisorption peak of NH_3, which appeared for all the catalysts assigned to the weakly held ammonia. The other peaks after 125°C showed the moderate and strong acidities of the catalysts. The peaks at high temperatures showed high strength of the acidity. Total acidity calculations are given in Appendix D. The 10Ni-P123-SBA-15 catalyst had higher intensity peaks compared to 10Ni-SBA-15 catalyst, indicating the highest acidity of the catalyst. Total acid capacities of the catalysts were calculated from the areas under the curve due to the desorption mechanisms of the catalysts and the results are tabulated in Table 8. The 10Ni-P123-SBA-15 catalyst had the highest acid capacity compared to 10Ni-SBA-15.

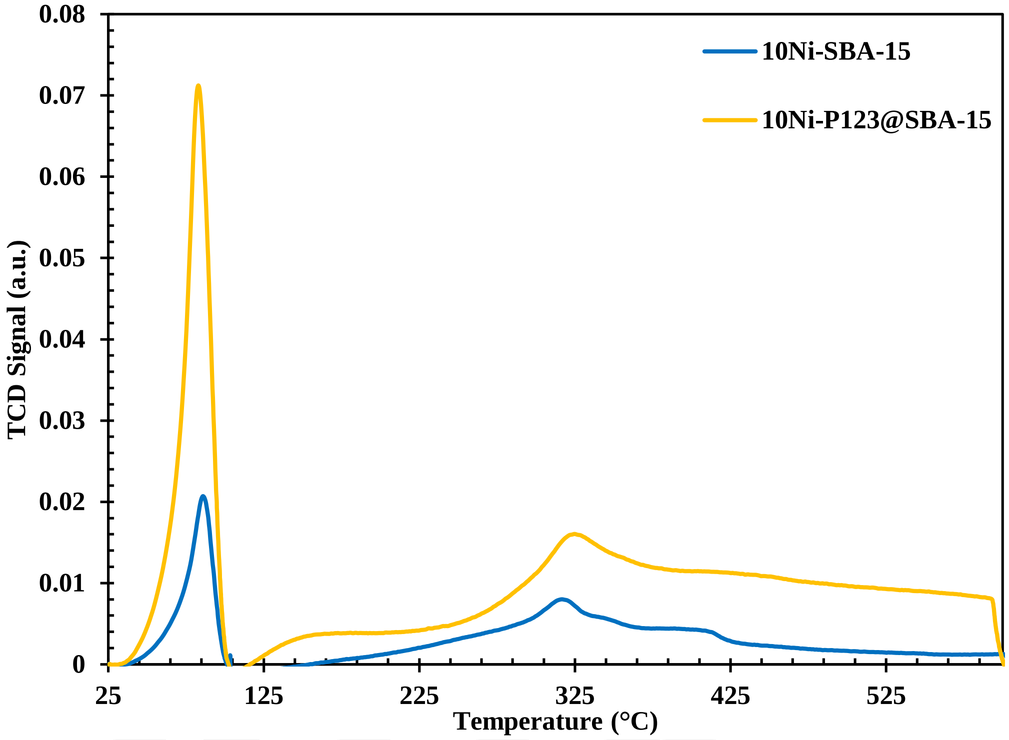

Figure 26: NH_3-TPD graphs of the Ni loaded SBA-15 catalysts

Table 8: Acid capacities of the Ni loaded catalysts

Catalyst	Total acid capacity (mmol/g)
10Ni-SBA-15	0.270
10Ni-P123-SBA-15	1.10

6.1.5 Activity Test Results for the SBA-15 Supported Catalysts

The 10Ni-SBA-15 and 10Ni-P123-SBA-15 catalysts were tested in a continuous fixed bed tubular reactor for the SRE and SESRE reactions at different experimental conditions. Composition of the reactor effluent stream was determined using a gas chromatography. The areas under the curves were multiplied with the beta factors in order to find the moles and then mole percentages of each gas in dry basis. Beta factor calculation was given in Appendix E. Then, ethanol conversion, the percentage of hydrogen yield and mole percentages of each gas were calculated and the activity of the catalysts were examined using these concepts. The sample calculation is given in

Appendix F. The reaction time was 5 hours for each experiment. Firstly, in order to check the reliability of the experiments, three experiments were performed in the same reaction environment (SRE) for the different 10Ni-SBA-15 batches. The product distributions are given in Figure 27. The reactor outlet stream consisted of H_2, CO, CO_2 and CH_4 gases. The product distributions were drawn according to the average of three experiment runs with the standard deviation value calculated using the three experiment data. The results were compatible with each other. Complete conversion was achieved for all experiments. The percentages of the hydrogen yields were 87 % (5.22 out of 6), 86 % (5.16 out of 6), and 76 % (4.56 out of 6). The following reactions may take place in the reactor according to the reactor effluent stream composition.

SRE	$C_2H_5OH + H_2O \leftrightarrow 2CO + 4H_2$
WGSR	$CO + H_2O \leftrightarrow CO_2 + H_2$
Overall SRE	$C_2H_5OH + 3H_2O \leftrightarrow 2CO_2 + 6H_2$
Methane Reforming	$CH_4 + 3H_2O \leftrightarrow CO + 3H_2$
Decompositon	$C_2H_5OH \leftrightarrow CO + CH_4 + H_2$

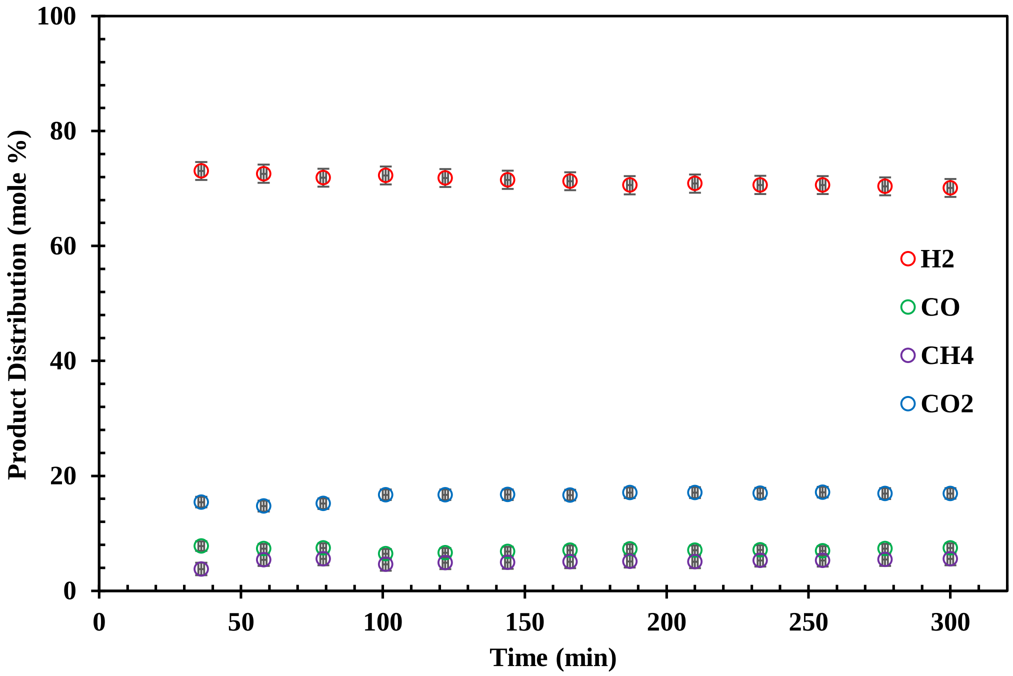

Figure 27: Repeatability results for SRE at 600°C (Catalyst: 10Ni-SBA-15)

In order to see the effect of the presence of the catalyst, the SRE activity test was performed in the absence of catalyst. The product distribution of SRE experiment without catalyst is given in Figure 28. In addition to H_2, CO, CO_2 and CH_4 gases, C_2H_4 gas was observed in the absence of catalyst. The average product distribution contained 70.8 % H_2, 10.9 % CO, 5 % CH_4, 10.4 % CO_2 and 2.9 % C_2H_4. The ethylene gas may be formed due to the dehydration reaction of ethanol.

$$\text{Dehydration} \qquad C_2H_5OH \leftrightarrow C_2H_4 + H_2O$$

The ethanol conversion was only 54 % and the percentage of the hydrogen yield was only 40 %. These results were pretty lower than the results obtained in the presence of catalyst. It was proved that the presence of catalyst favored the activity of the reaction in terms of ethanol conversion and hydrogen yield.

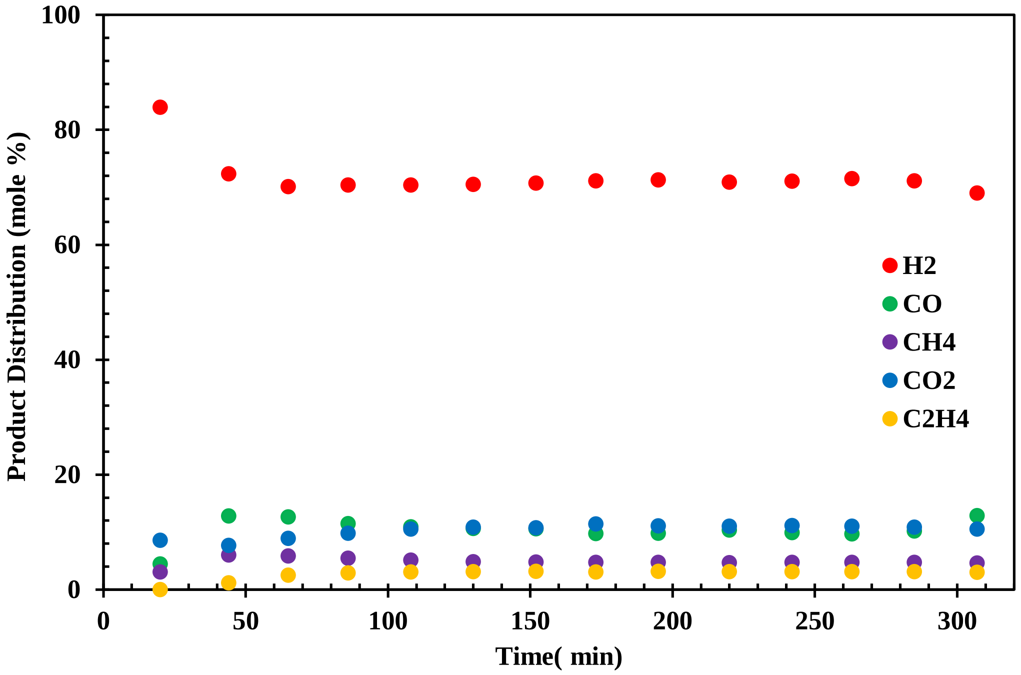

Figure 28: Product distribution of SRE at 600°C without catalyst

The product distribution only in the presence of CaO is shown in Figure 29. In the first 170 min, ethanol decomposition and reverse dry reforming of methane reactions took place in together. With ethanol decomposition, carbon monoxide and methane were produced. On the other hand, with a decrease in carbon dioxide favored the reverse dry reforming of methane reaction. With a decrease in the carbon dioxide amount, the reaction shifted to the methane side. In this way, the produced carbon monoxide was used up. After 170 min, carbon dioxide began to emerge in the product stream, saturating all the CaO. After this time, carbon dioxide mole percentage increased and with an increase in the carbon dioxide amount, the methane dry reforming reaction took place and the mole percentage of the methane decreased compared to first period.

Moreover, for all experiments, in order to keep all the parameters constant, the activated carbon was used for all experiments. In order to check whether carbon is reacted with water at 500°C and 600°C, the experiments were performed with only water. There were no products in the gas stream at 500°C and 600°C so it can be said that at these temperatures water and carbon did not react with each other.

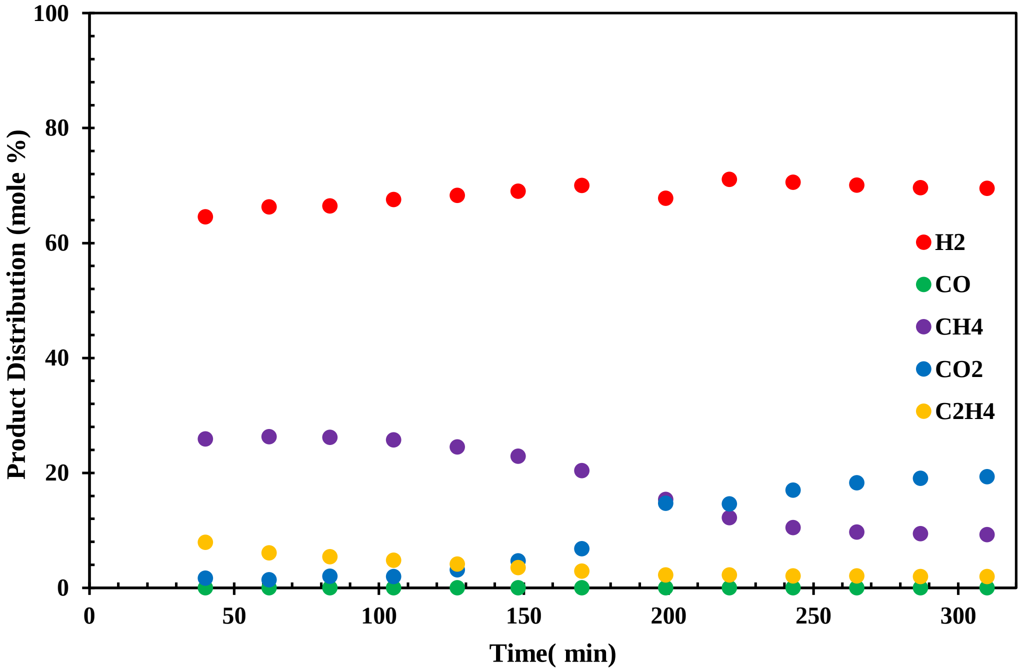

Figure 29: The product distribution of SESRE at 600°C with only CaO

6.1.5.1 Effect of Temperature and Impregnation Method on Hydrogen Production

Steam reforming of ethanol experiments were performed at 500°C and 600°C for 10Ni-SBA-15 and 10Ni-P123-SBA-15 catalysts. The average mole percentages of the products are given in Figure 30. The percentage of hydrogen yield value for the 10Ni-SBA-15 catalyst at 500°C was 55 %; on the other hand, it was 76 % at 600°C. With an increase in temperature, hydrogen yield enhancement was achieved. The mole percentage of the hydrogen increased with an increase in temperature because steam reforming of ethanol reaction is an endothermic reaction and at high temperature steam reforming of ethanol reaction became crucial with accelerating the production of hydrogen. Water gas shift reaction became important at 500°C so the mole percentage of the carbon dioxide increases and the mole percentage of the carbon monoxide decreases compared to results of the experiment performed at 600°C. With an increase in reaction temperature from 500°C to 600°C, steam reforming of methane reaction started to take place therefore the methane composition decreased with an increase in temperature. The formation of methane at 500°C and 600°C can be due to the ethanol decomposition reaction. This reaction became important at low temperatures. Decrease in the crystallite size of the nickel with the use of surfactant assisted impregnation method did not affect the product distribution. Both catalysts at same temperature gave nearly same product distribution in the SRE experiments.

Product distributions for the 10Ni-SBA-15 and 10Ni-P123-SBA-15 catalysts at different temperatures are given in Figures 31-34. The product distributions were stable throughout the experiment. Complete conversion was achieved for all experiments.

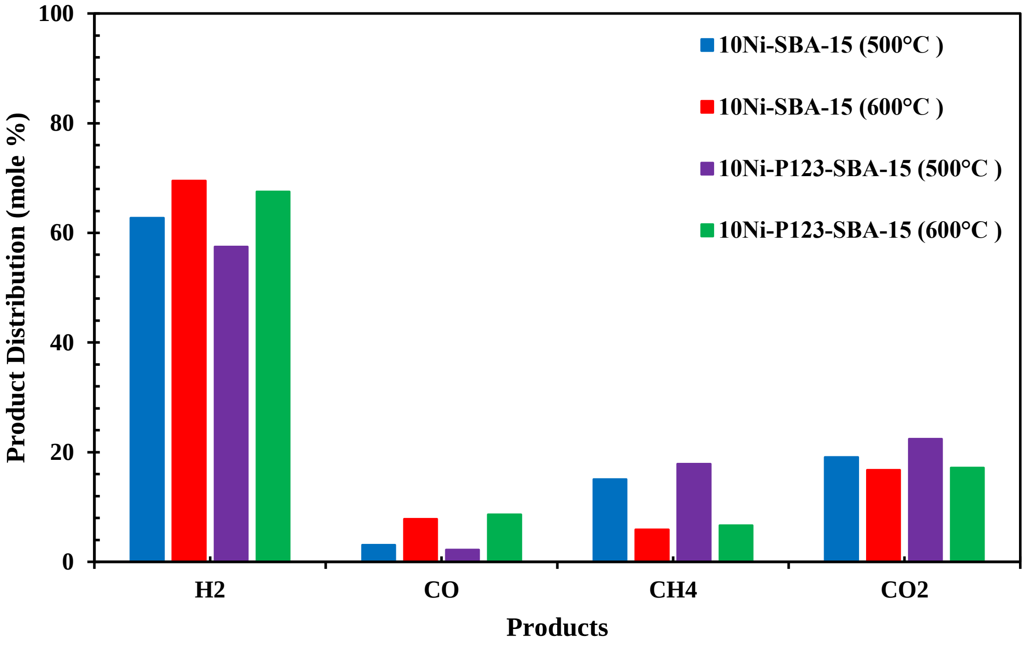

Figure 30: Comparison of the average mole percentage of the products for the 10Ni-SBA-15 and 10Ni-P123-SBA-15 catalysts at 500°C and 600°C (SRE reaction environment)

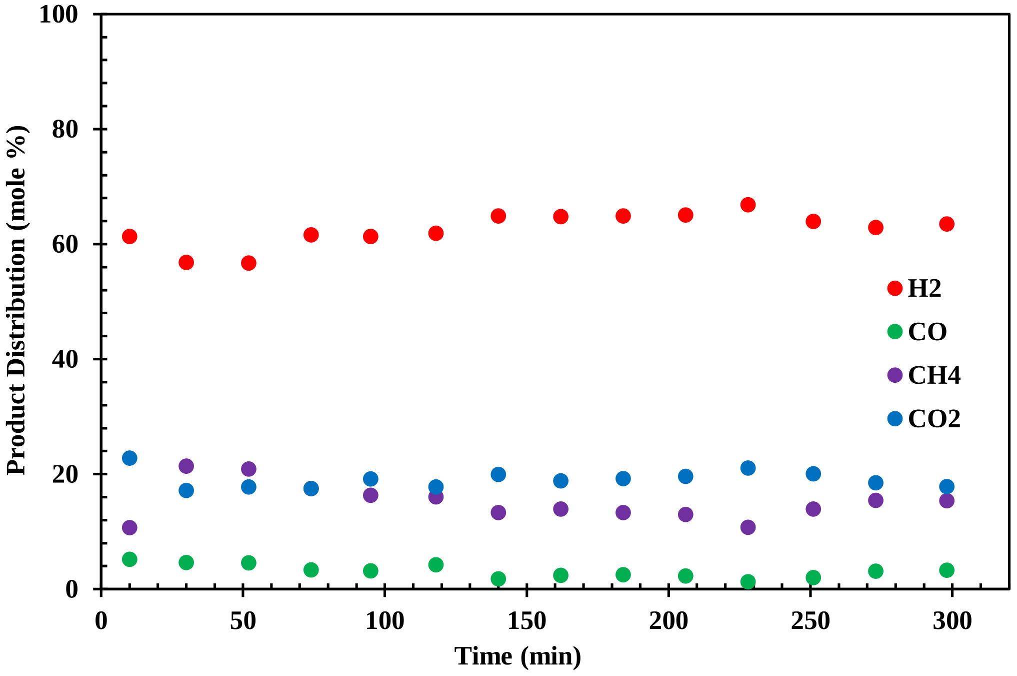

Figure 31: Product distribution of SRE at 500°C (Catalyst: 10Ni-SBA-15)

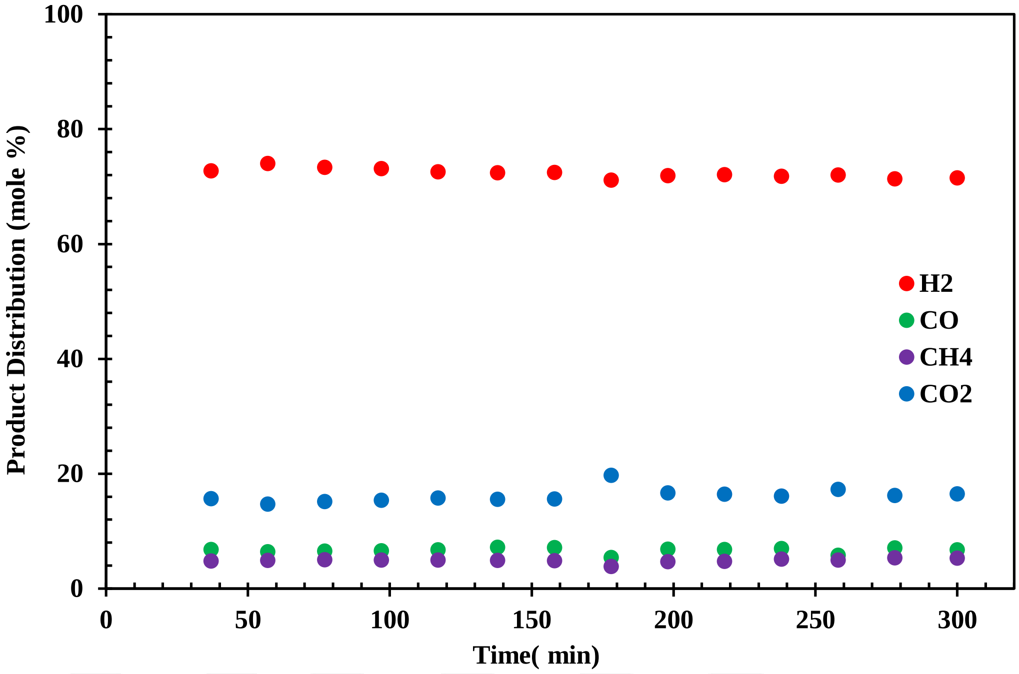

Figure 32: Product distribution of SRE at 600°C (Catalyst: 10Ni-SBA-15)

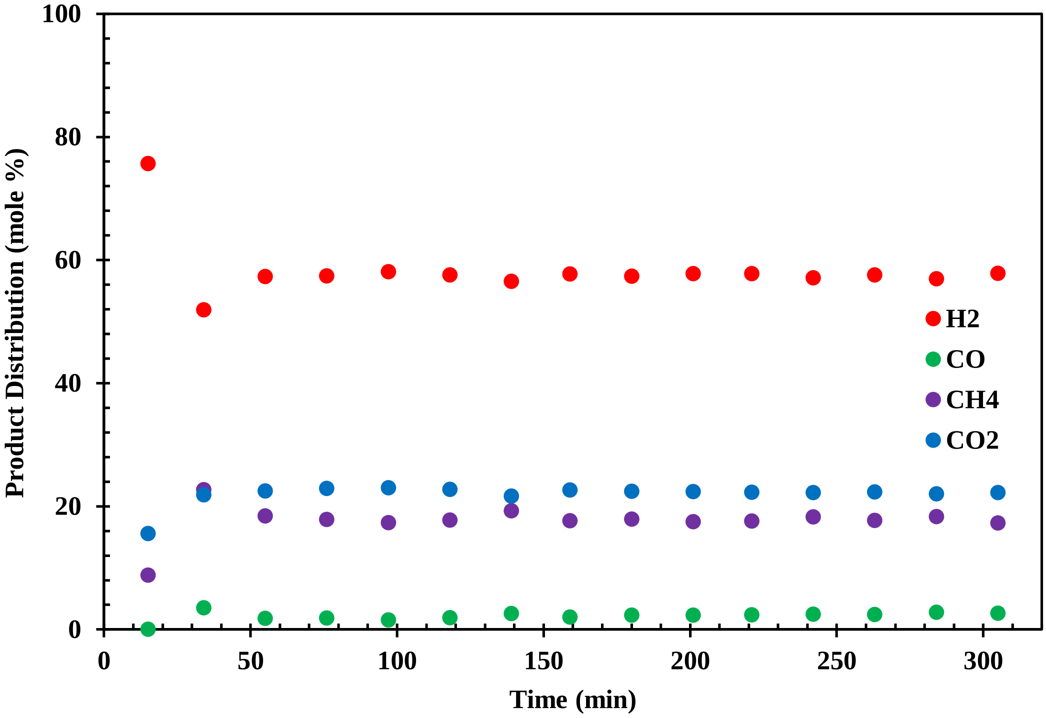

Figure 33: Product distribution of SRE at 500°C (Catalyst: 10Ni-P123-SBA-15)

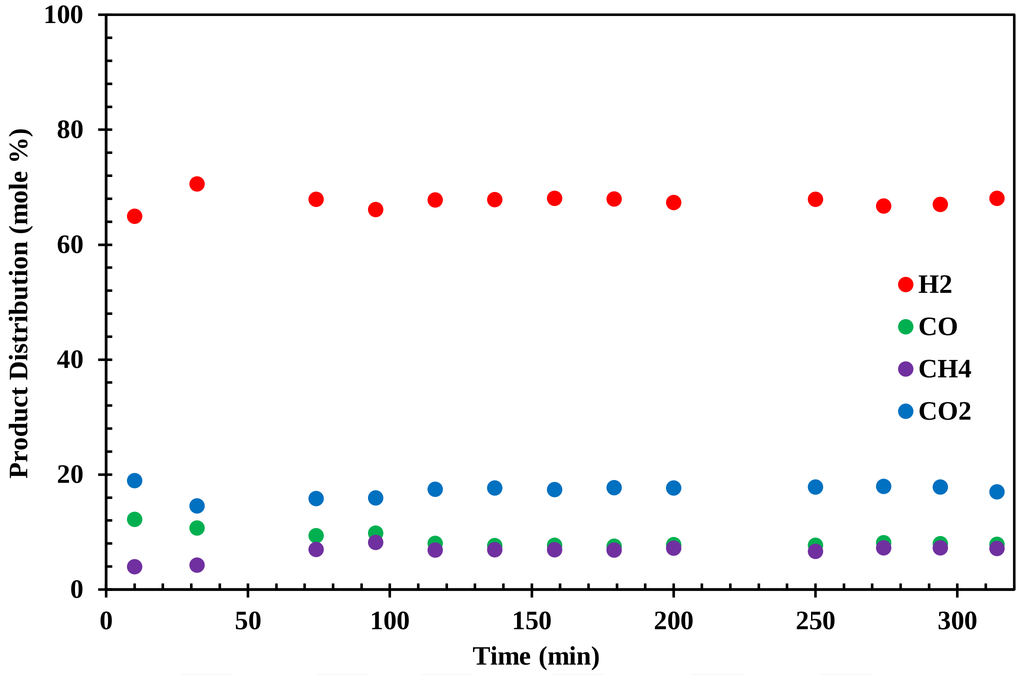

Figure 34: Product distribution of SRE at 600°C (Catalyst: 10Ni-P123-SBA-15)

6.1.5.2 Effect of the Packing of Catalyst and Sorbent on Hydrogen Production

In the SESRE CaO was used as a sorbent with different catalyst-sorbent configurations. Firstly, 10Ni-SBA-15 catalyst and CaO was physically mixed and tested in the reaction set-up. The product distribution for the mixed configuration at 600°C is given in Figure 35. In the first 55 minutes, all carbon dioxide was captured by CaO and with a decrease in carbon dioxide amount water gas shift reaction shifted to the products. In this way, carbon monoxide amount also decreased. The expected result for the SESRE experiment was that after the saturation of the CaO with CO_2, the mole percentage of the hydrogen in the SESRE test should be same with the mole percentage of the hydrogen in the SRE test. This situation should be also valid for carbon dioxide percentage. However, the mole percentage of the carbon dioxide in the SRE test was 17 %; on the other hand, after the saturation of CaO with CO_2, the mole percentage of the carbon dioxide was 7 % in the SESRE-M. Moreover, the mole percentage of the hydrogen in the SRE test was 69 %; on the other hand, after the saturation of CaO with CO_2, the mole percentage of the hydrogen was 62 %. Moreover, in the SESRE-M reaction, the mole percentages of methane and carbon monoxide were high in the post-breakthrough period compared to the SRE experiment results, indicating the occurrence of ethanol decomposition reaction. In the mixed concept of the catalyst and CaO, the catalyst may lose their activity due to the alkaline nature of the CaO. Moreover, the acidity of the 10Ni-SBA-15 was low and so it cannot stay stable in the CaO environment. In other words, the ethanol decomposition reaction became crucial in the mixed concept. Therefore, the mole percentage of the hydrogen and carbon dioxide decreased in the post breakthrough period. Moreover, the methane mole percentage in the SRE test was nearly 4 %; on the other hand, in the SESRE-M test the methane mole percentage reached to nearly 20 % in the first 100 minutes. This was due to the favor of the reverse dry reforming of methane reaction due to a decrease in carbon dioxide amount. With a decrease in carbon dioxide amount, the dry reverse methane reaction became important and the mole percentage of the methane increased. However, after 100 minutes, with an increase in carbon dioxide amount, the importance of this reaction disappeared. Due to the activity loss of the catalyst in the mixed concept, different catalyst and CaO configurations were tested in the SESRE tests.

Reverse dry reforming of methane	$2CO + 2H_2 \leftrightarrow CH_4 + CO_2$

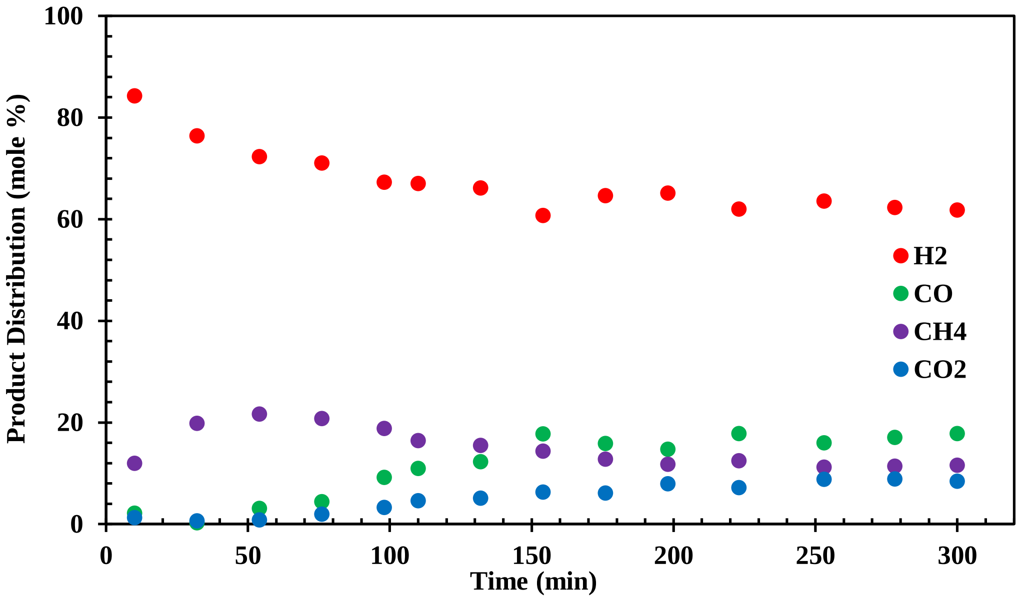

Figure 35: Product distribution of SESRE-M at 600°C (Catalyst: 10Ni-SBA-15)

Catalyst and CaO configurations in the one order was tested in the reaction set-up and the product distribution for SESRE-1O is given in Figure 36. In the first 20 min, the percentage of the hydrogen reached to 95 %, with a very little amount CO and CO_2. In the first 70 minutes, there was no carbon dioxide and carbon monoxide in the product distribution. After 70 minutes, carbon dioxide began to appear in product stream because all CaO was saturated with carbon dioxide. The mole percentage of the carbon dioxide in the SRE test was 17 %; on the other hand, after the saturation of CaO with CO_2, the mole percentage of the carbon dioxide was 16 % in the SESRE-1O. Moreover, the mole percentage of the hydrogen in the SRE test was 69 %; on the other hand, after the saturation of CaO with CO_2, the mole percentage of the hydrogen was 71 %. These results were logical. With this configuration, the small amount of the catalyst was contacted with the CaO so it did not lose their activity. In order to test the divided section packing concept, SESRE-3O concept was also tested. The product distribution is shown in Figure 37. Comparison of these three packing concept is shown in Figure 38. With an increase in the divided section, the mole percentage of the hydrogen increased in 20 min and reached to 100 % in SESRE-3O concept. The mole percentage of the methane in SESRE-1O was nearly 5 %; on the other hand, the mole percentage of the methane in SESRE-3O was nearly 7.5 %. Moreover, after the saturation of the CaO with carbon dioxide, the mole percentage of the carbon monoxide in SESRE-1O was nearly 8 %; on the other hand, the mole percentage of the carbon monoxide in SESRE-3O was nearly 13 %. The increase in the methane and carbon monoxide mole percentage may be due to the occurrence of ethanol decomposition reaction with an increase in contact of catalyst and CaO. The capture time of carbon dioxide was nearly same for all the packing concepts. After 180 minutes, the mole percentages of hydrogen were same for SRE and SESRE-1O. In all the packing concepts, for the 10Ni-SBA-15 catalyst, the less contact with the catalyst and sorbent had, the more active the catalyst was. Therefore, SESRE-1O was the best SESRE concept for the 10Ni-SBA-15 catalyst.

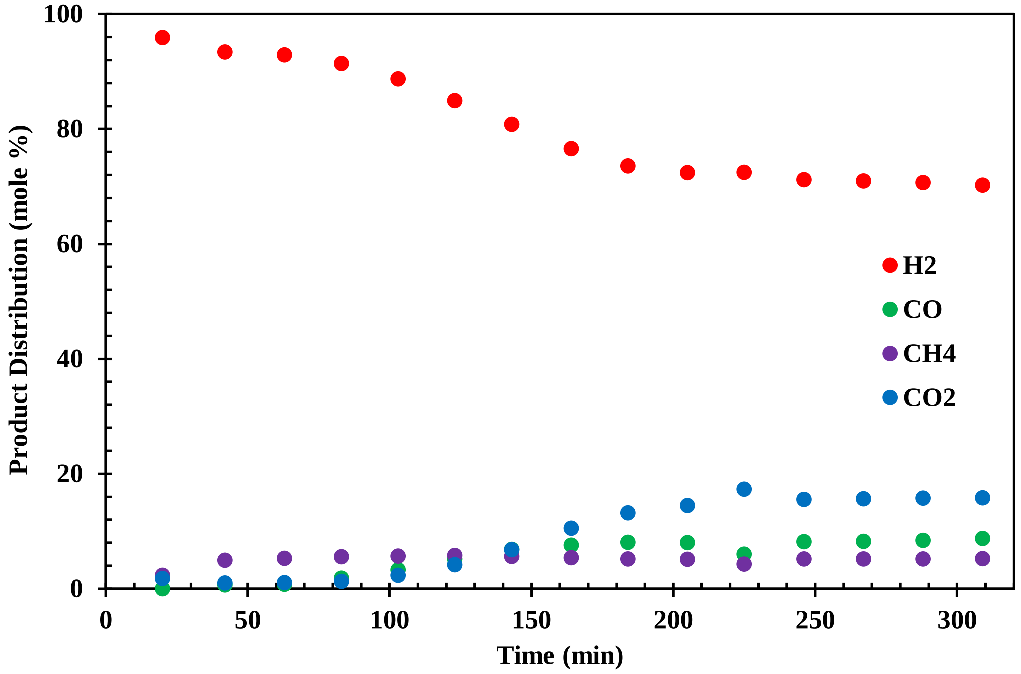

Figure 36: Product distribution of SESRE-1O at 600°C (Catalyst: 10Ni-SBA-15)

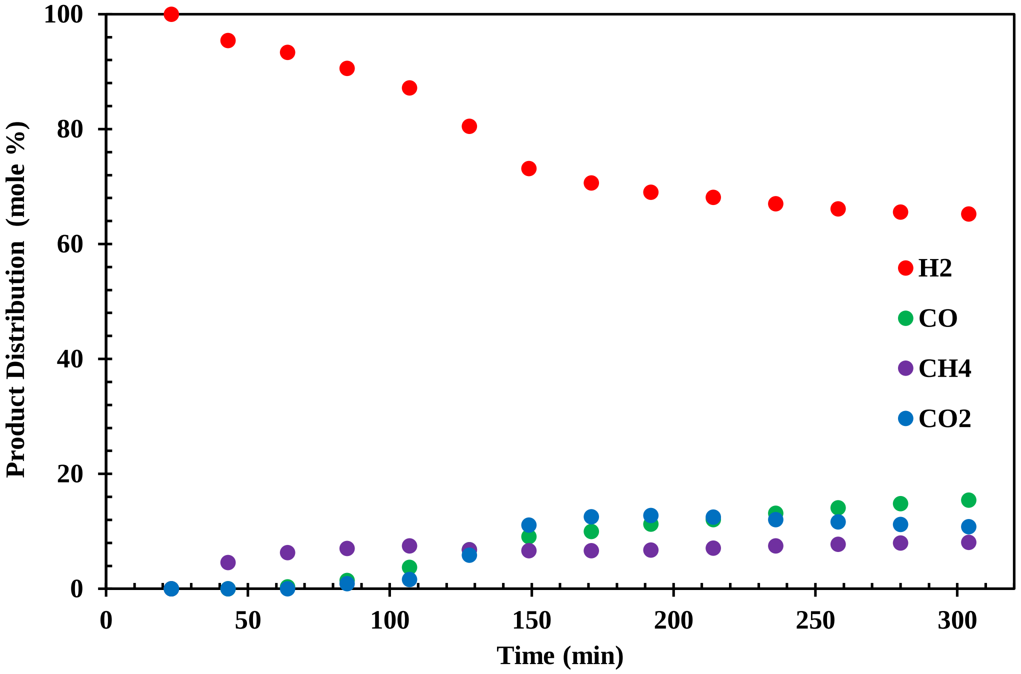

Figure 37: Product distribution of SESRE-3O at 600°C (Catalyst: 10Ni-SBA-15)

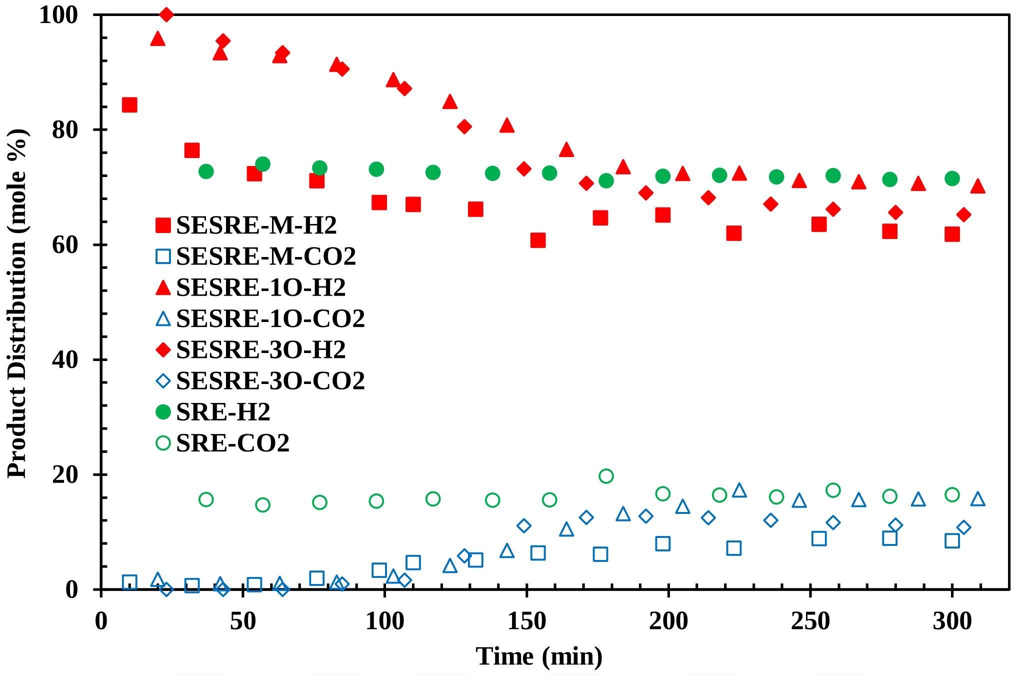

Figure 38: Comparison of mole percentages of the H_2 and CO_2 for the SRE and SESRE reactions at 600°C (Catalyst: 10Ni-SBA-15)

In order to check the different catalyst in the mixed concept, the 10Ni-P123-SBA-15 catalyst was also tested in SESRE-M at 600°C in order to determine whether this catalyst was lost their activity or not towards mixing concept. The product distribution of SESRE-M at 600°C is given in Figure 39. The average product distribution in SRE at 600°C was 67.5 % H_2, 8.6 % CO, 6.6 % CH_4 and 17.2 % CO_2. In the first 80 min, the purity of the hydrogen reached to 86 %. The mole percentage of the carbon dioxide decreased from 17.2 % to nearly 0 % in the first 100 min. The slight increase in methane with SESRE-M may be due to the reverse dry reforming reaction. Compared to 10Ni-SBA-15 catalyst, 10Ni-P123-SBA-15 catalyst gave better catalytic activity in the presence of the CaO in mixed concept. The carbon dioxide amount after saturation period was nearly same with the carbon dioxide amount in the SRE test, meaning that it showed good catalytic activity in the presence of sorbent. The presence of sorbent did not completely favor the ethanol decomposition reaction. This may be due to the acidity difference between the catalysts. The acidity of the 10Ni-SBA-15 catalyst was 0.270 mmol/g catalyst; on the other hand, that of 10Ni-P123-SBA-15 was 1.1 mmol/g catalyst. Due to the high acidic property of the 10Ni-P123-SBA-15 catalyst, it may not lose their activity in the SESRE-M concept. Three ordered packing concept was also investigated in the presence of the 10Ni-P123-SBA-15 catalyst at 600°C and product distribution is given in Figure 40. In the first 80 min, the purity of the hydrogen reached to 90 %.

The mole percentage of the methane in SESRE-M was nearly 9 %; on the other hand, the mole percentage of the methane in SESRE-3O was nearly 5 %. Moreover, after the saturation of the CaO with carbon dioxide, the mole percentage of the carbon monoxide in SESRE-M was nearly 13 %; on the other hand, the mole percentage of the carbon monoxide in SESRE-3O was nearly 10 %. The decrease in the methane and carbon monoxide mole percentage may be due to the elimination of ethanol decomposition reaction with a decrease in contact of catalyst and CaO.

The comparison graph is also shown in Figure 41. The mole percentage of the hydrogen in SESRE-3O was higher than that in SESRE-M throughout the experiment. The contact between catalyst and sorbent with SESRE-3O can be minimized and this situation also favored the hydrogen production.

The production rate of carbon dioxide in SESRE-M concept was slightly lower compared to that of carbon dioxide in SESRE-3O case due to little catalytic activity loss. Therefore, the breakthrough time of CO_2 for SESRE-M concept was higher than compared to SESRE-3O case.

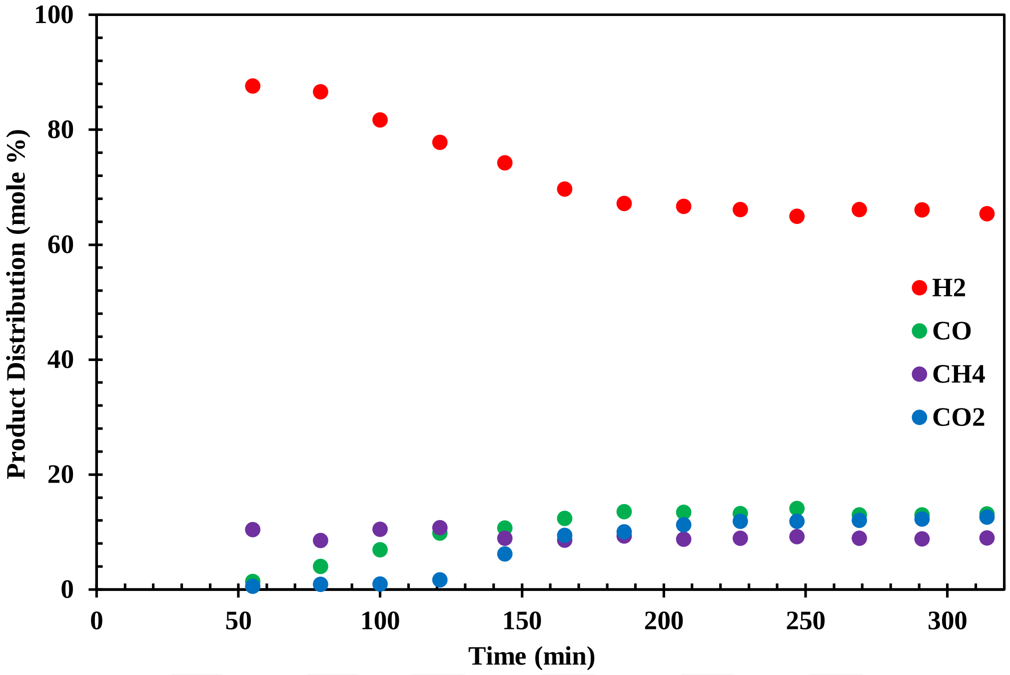

Figure 39: Product distribution of SESRE-M at 600°C (Catalyst: 10Ni-P123-SBA-15)

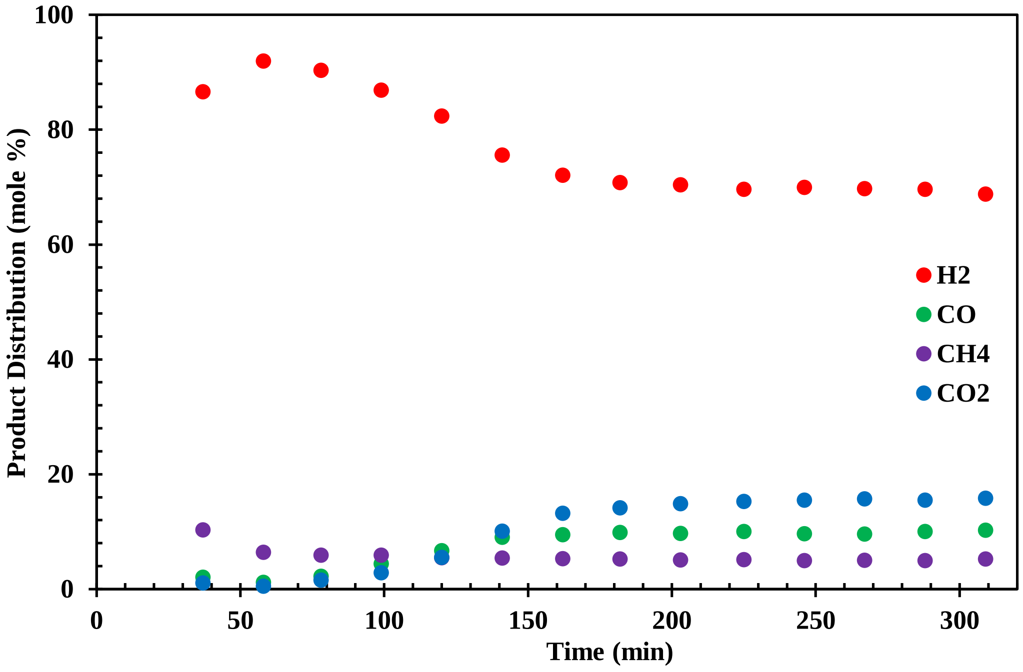

Figure 40: Product distribution of SESRE-3O at 600°C (Catalyst: 10Ni-P123-SBA-15)

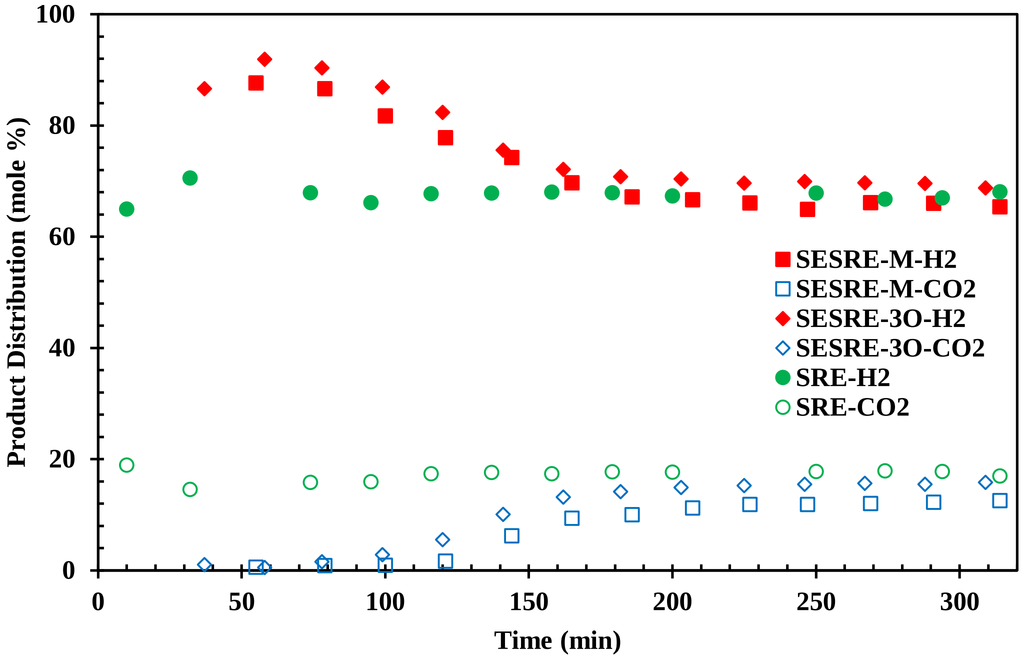

Figure 41: Comparison of mole percentages of H_2 and CO_2 at 600°C for the SRE and SESRE reactions (Catalyst: 10Ni-P123-SBA-15)

The effect of temperature on the capture time of CaO was also investigated. 10Ni-SBA-15 catalyst was tested in SESRE-3O at 500°C and product distribution is given in Figure 42 and comparison graph for the SRE and SESRE-3O experiments at 500°C is shown in Figure 43. The capture capacity of the CaO was also good at 500°C. The mole percentage of the hydrogen at 500°C was a little bit lower compared to SESRE-3O at 600°C. In the first 80 min, there was no CO and CO_2 in the product distribution. The carbon monoxide amount was too low due to water gas shift reaction at lower temperatures.

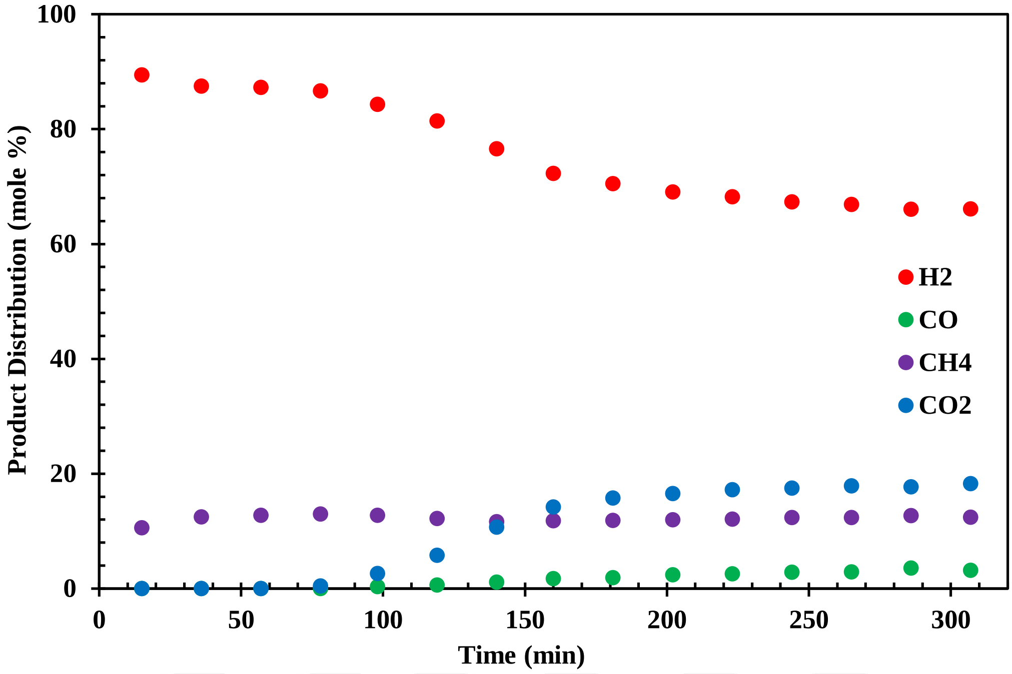

Figure 42: Product distribution of SESRE-3O at 500°C (Catalyst: 10Ni-SBA-15)

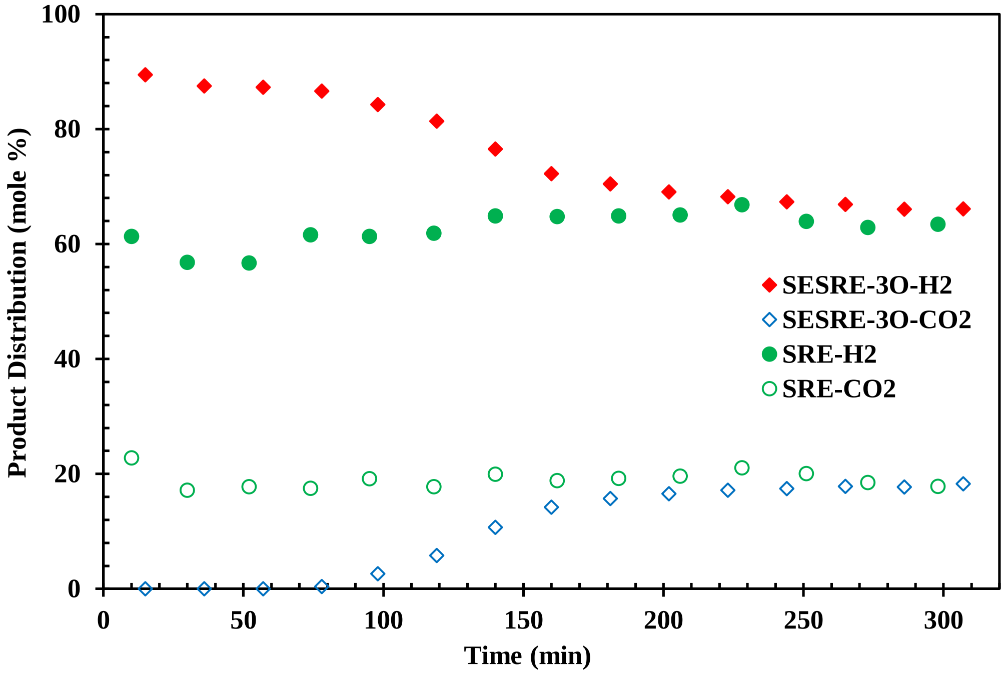

Figure 43: Comparison of mole percentages of H_2 and CO_2 at 500°C for the SRE and SESRE reactions (Catalyst: 10Ni-SBA-15)

10Ni-P123-SBA-15 catalyst was tested in SESRE-3O at 500°C and product distribution is given in Figure 44 and comparison graph for SRE and SESRE-3O experiments is shown in Figure 45. The average product distribution of SRE at 500°C was 57 % H_2, 3 % CO, 18 % CH_4 and 22 % CO_2. In the reaction time of 20 min in SESRE-3O at 500°C, the mole percentage of the hydrogen reached to 100 %. Hydrogen purity was enhanced with sorption enhanced process throughout the experiment. The mole percentage of the carbon dioxide decreased from 22 % to 0 % in the first 80 min compared to SRE experiment results.

The mole percentage of the methane in SESRE-3O at 500°C was nearly 12 %; on the other hand, the mole percentage of the methane in SESRE-3O at 600°C was nearly 5 % because high temperatures favored the methane steam reforming reaction.

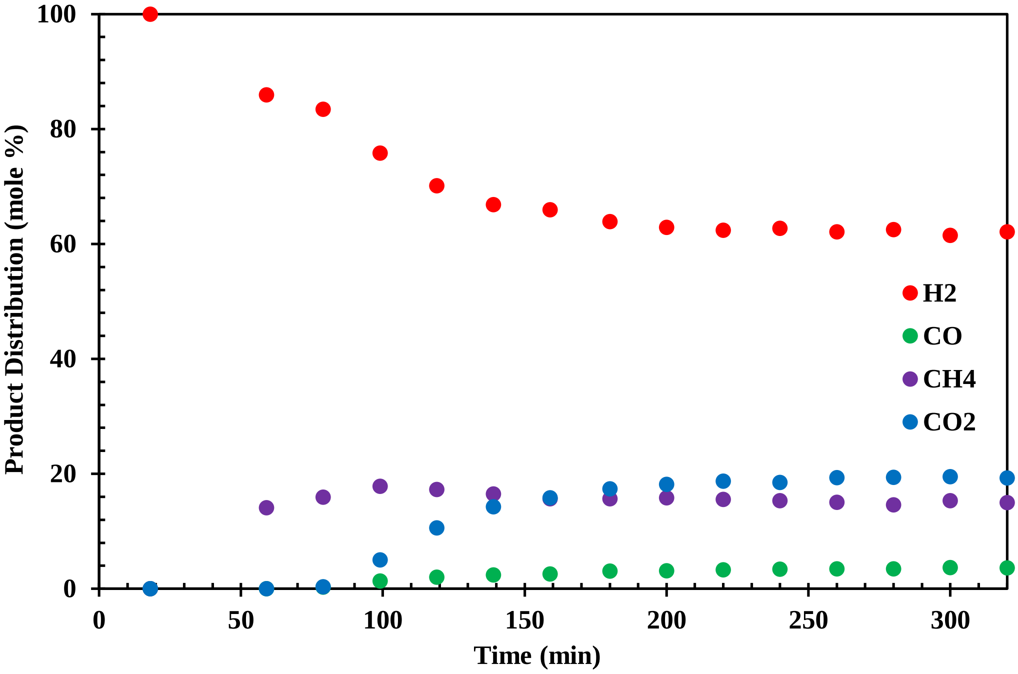

Figure 44: Product distribution of SESRE-3O at 500°C (Catalyst: 10Ni-P123-SBA-15)

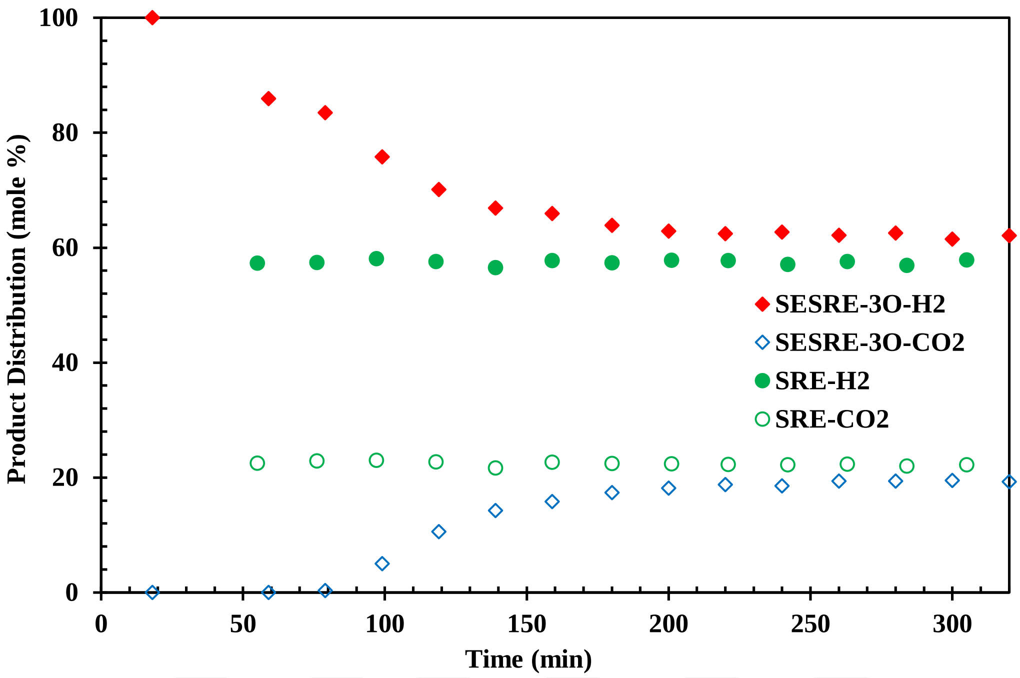

Figure 45: Comparison of mole percentages of H_2 and CO_2 at 500°C for the SRE and SESRE-3O reactions (Catalyst: 10Ni-P123-SBA-15)

6.1.6 TGA Results of the Spent Catalysts

TGA results for the spent catalysts are given in Figure 46. The weight loss between 25°C and 100°C was due to the moisture content in the catalyst. The weight loss between 500°C and 600°C was due to the carbon deposition in the catalyst.

In the 10Ni-SBA-15 catalyst 56 % coke deposition was observed. When the catalyst synthesized with the surfactant assisted impregnation method was used, the coke formation decreased from 56 % to 37 % due to the smaller nickel crystals at 600°C and decreased from 37 % to 5 % at 500°C. Moreover, with an increase in reaction temperature, the coke deposition increased. The less coke formation was obtained with 10Ni-P123-SBA-15 catalyst at 500°C.

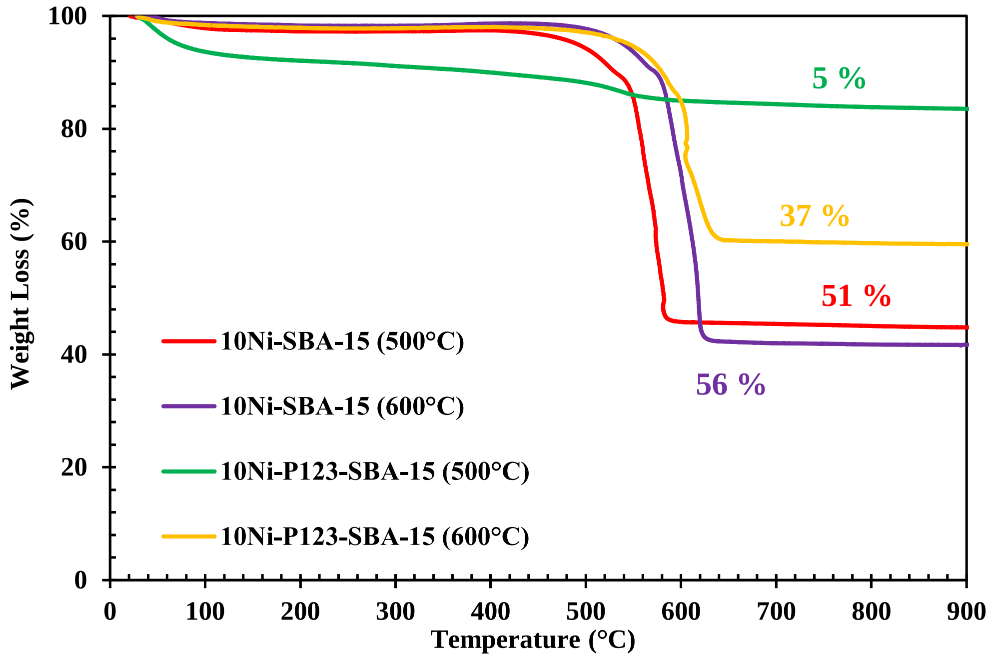

Figure 46: TGA results of the spent 10Ni-SBA-15 and 10Ni-P123-SBA-15 catalysts at reaction temperature of 500°C and 600°C

6.2 Characterization and Activity Results of Commercial Mesoporous Carbon Supported Catalysts

6.2.1 X-Ray Diffraction Results

XRD patterns of commercial mesoporous carbon and nickel impregnated mesoporous carbons are shown in Figure 47. The peaks at 2θ values of 44.4, 51.8 and 76.2° showed the presence of metallic nickel (JPDC-01-071-4653 given in Appendix B). As seen from Figure 47, the peaks at 2θ values of 25.94, 42.55, 54.5° and 78° belonged to the mesoporous carbon (JPDC-00-041-1487 given in Appendix B, Table B3). Moreover, after impregnation of nickel to the catalyst support, the intensity of carbon peaks decreased and the intensity of nickel peaks increased with an increase in nickel loading. Nickel crystallite size of the catalysts were tabulated in Table 9. Both catalysts had nearly same nickel crystallite sizes.

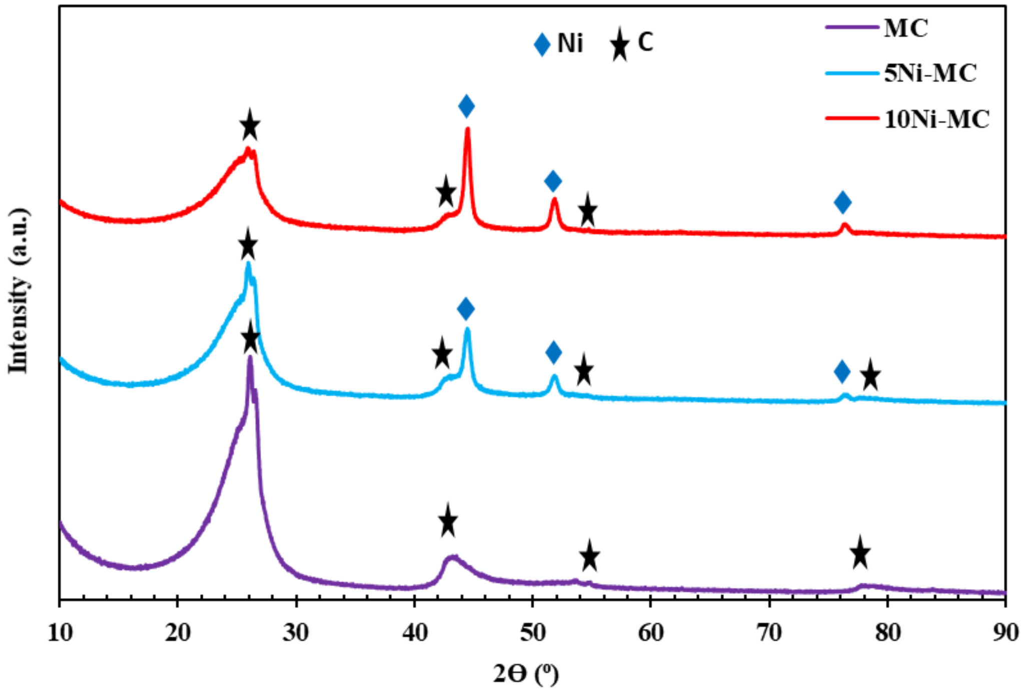

Figure 47: XRD patterns of MC, 5Ni-MC and 10Ni-MC catalysts

Table 9: Crystallite size of the synthesized materials obtained from the XRD pattern

Catalyst	**2θ (°)**	**$t_{\text{crystallite size}}$ (nm)**
5Ni-MC	44.44	14.2
10Ni-MC	44.43	15.4

6.2.2 N_2 Adsorption/Desorption Isotherms and Physical Properties of the Materials

The physical properties of the MC, 5Ni-MC and 10Ni-MC catalysts are given in Table 10. Nitrogen adsorption/desorption isotherms and pore size distributions for the MC, 5Ni-MC and 10Ni-MC catalysts are shown in Figures 48-49. Microporosity of the catalysts decreased with nickel loading because of the location of the nickel particles into the micropores. Moreover, due to the location of the nickel particles into the micropores, which can be seen from Figure 49, pore volume and pore diameter of the catalysts increased. According to IUPAC classification, MC, 5Ni-MC and 10Ni-MC catalysts showed Type IV isotherms with H2 hystheresis loops. MC, 5Ni-MC and 10Ni-MC catalysts had bimodal pore size distributions with two peaks at nearly 2.5 nm and 11.7 nm. With nickel loading the micropores of the mesoporous carbon disappeared and the mesopores increased.

Table 10: The physical properties of commercial carbon supported catalyst

Catalyst	Multipoint BET Surface Area (m^2/g)	BJH Desorption Pore Volume (cm^3/g)	BJH Desorption Average Pore Diameter (nm)	Microporosity (%)
MC	211	0.45	6.42	15
5Ni-MC	236	0.63	9.40	14
10Ni-MC	241	0.66	10.6	13

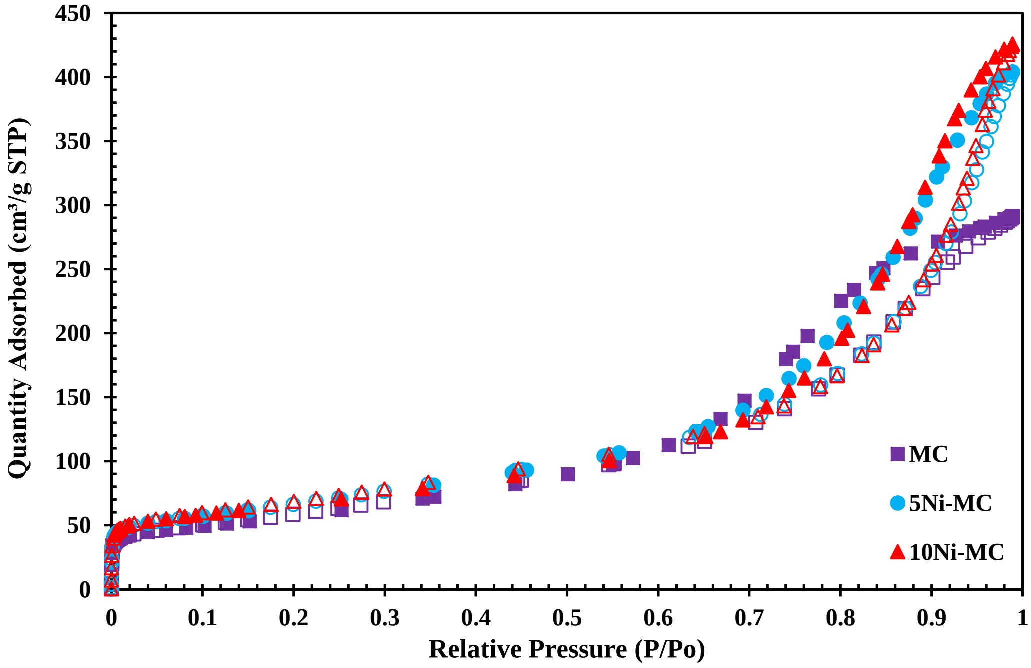

Figure 48: N_2 adsorption/desorption isotherms of the MC, 5Ni-MC and 10Ni-MC catalysts (Filled symbols: Desorption branch, Empty symbols: Adsorption Branch)

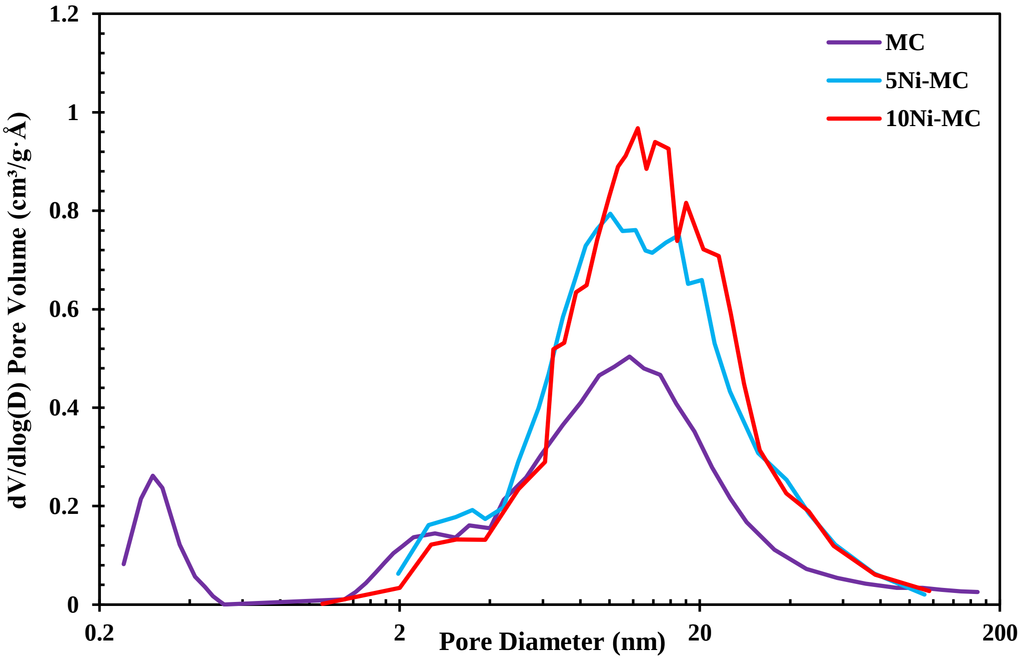

Figure 49: Pore size distributions of the MC, 5Ni-MC and 10Ni-MC catalysts

6.2.3 Scanning Electron Microscopy (SEM) Results

For the commercial mesoporous carbon, images at different magnifications can be seen in Figure 50. From the SEM images it was concluded that the mesoporous carbon had wide pore diameter range. Blue arrows show different pore sizes in Figure 50a in the commercial carbon. This was compatible with the pore size distribution of mesoporous carbon. Moreover, EDX analysis showed that mesoporous carbon did not contain any impurities.

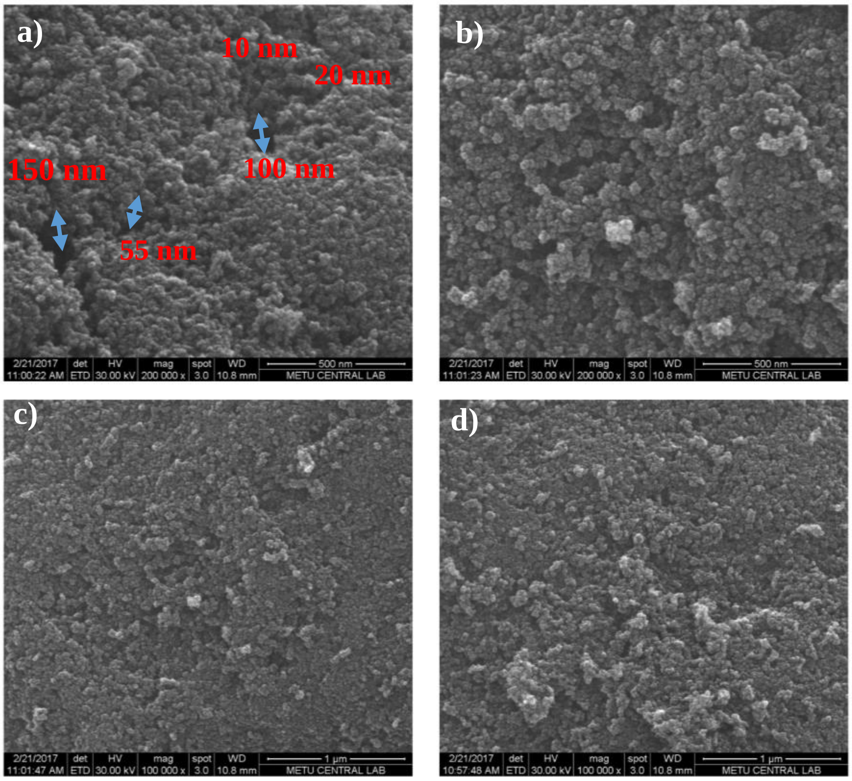

Figure 50: SEM images of MC at different magnifications: a,b) 200000X and c,d) 100000X

SEM images of nickel impregnated mesoporous carbon at different magnifications were shown in Figure 51. From the figure, it can be seen that nickel was located to the pores of the mesoporous carbon in different crystal sizes. Moreover, impregnation of nickel to the catalyst support did not affect the morphology of the support.

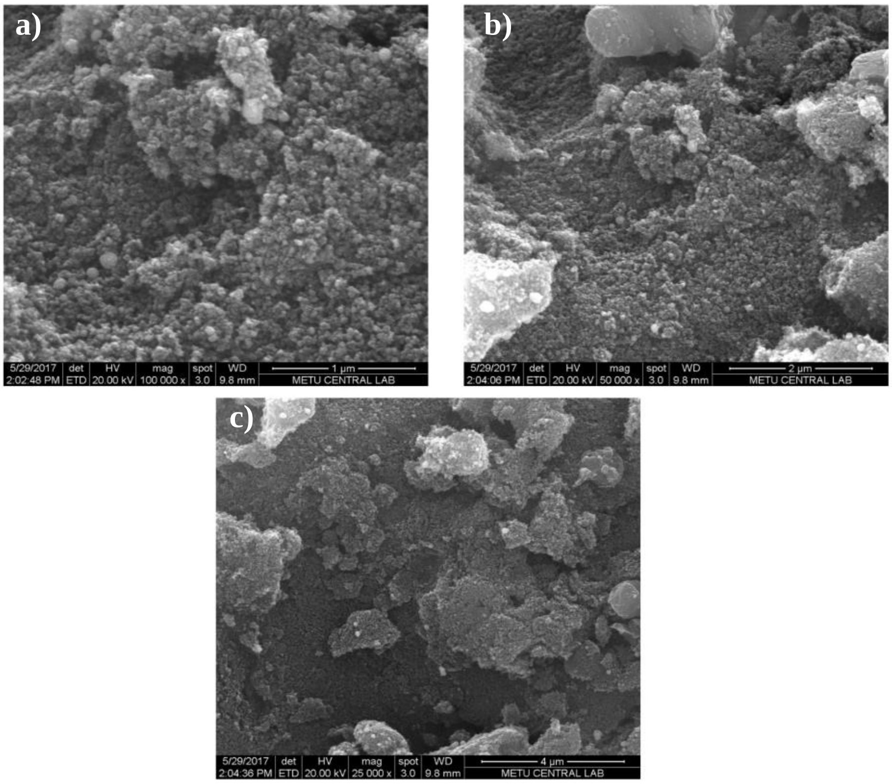

Figure 51: SEM images of 10Ni-MC at different magnifications: a) 100000X b) 50000X, and c) 25000X

SEM image and back scattering of this image for the 10Ni-MC catalyst can be seen in Figure 52. EDX spectrum for this image is given in Figure 53. The EDX result showed that the weight percentage of the nickel was nearly 15 % in this region of the catalyst. The existence of the Au and Pd elements was due to the coating of the samples before analysis. White and shiny region were thought to be nickel particles. The size of the largest nickel particle in the SEM image was nearly 200 nm. This indicated that nickel might be agglomerated in the catalyst.

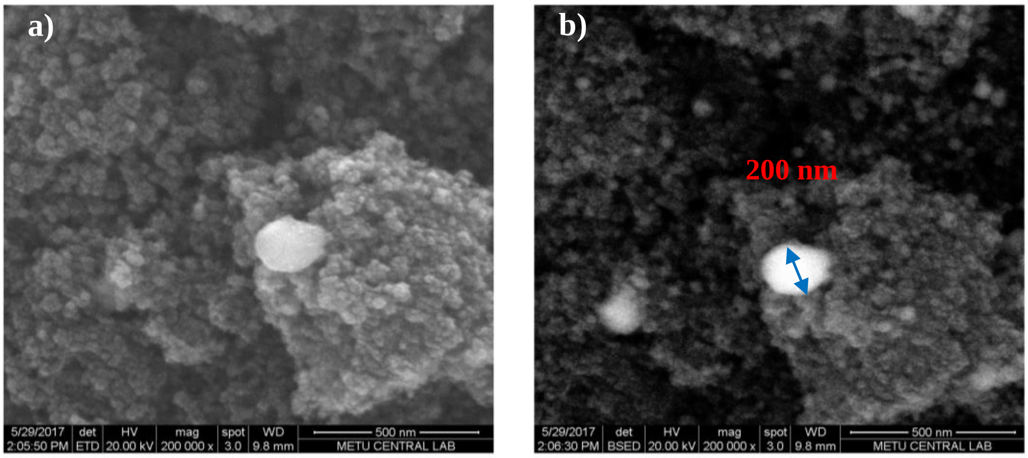

Figure 52: SEM images of 10Ni-MC a) at 200000X magnification b) at 200000X magnification by backscattering detector

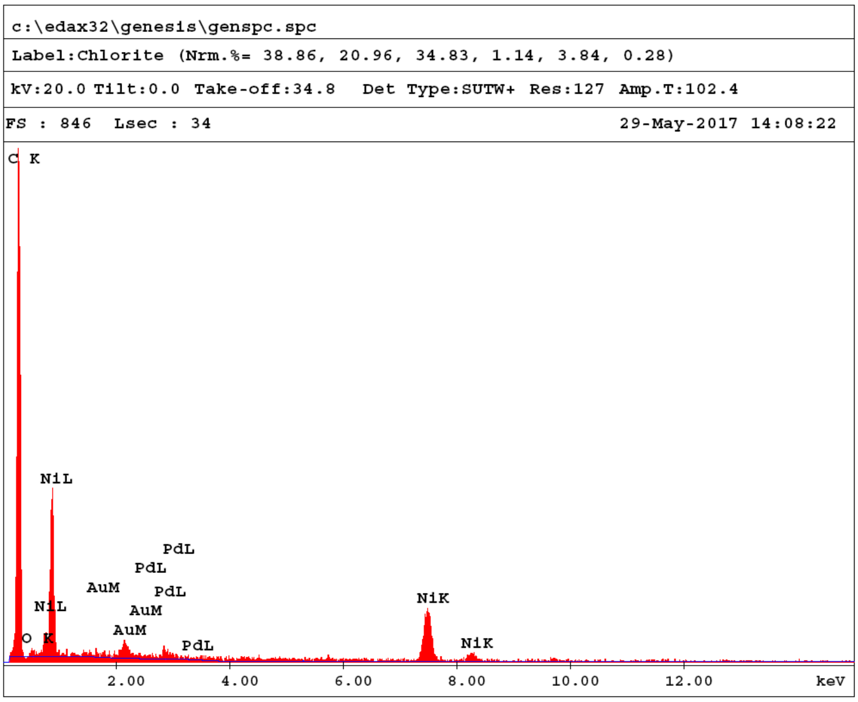

```
c:\edax32\genesis\genspc.spc
Label:Chlorite (Nrm.%= 38.86, 20.96, 34.83, 1.14, 3.84, 0.28)
kV:20.0 Tilt:0.0  Take-off:34.8   Det Type:SUTW+  Res:127  Amp.T:102.4
FS : 846   Lsec : 34                                 29-May-2017 14:08:22
```

Figure 53: EDX spectrum of the 10Ni-MC catalyst

SEM image and back scattering from another part of the 10Ni-MC catalyst can be seen in Figure 54. The EDX result showed that the weight percentage of the nickel was nearly 11 % in this region of the catalyst. Back scattering image proved the existence of nickel particles.

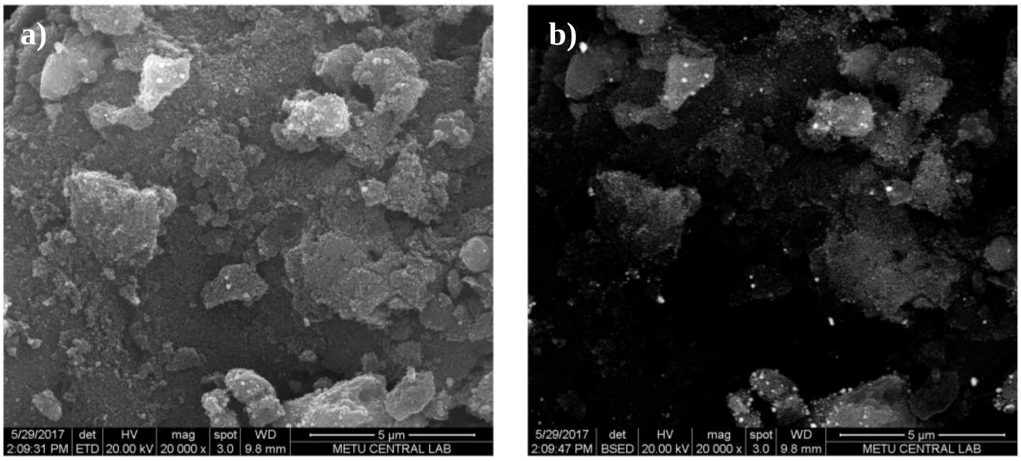

Figure 54: SEM images of 10Ni-MC a) at 20000X magnification b) at 20000X magnification by backscattering detector

6.2.4 Temperature Programmed Ammonia Desorption (NH_3-TPD) Results

NH_3-TPD results of the synthesized materials are shown in Figure 55. Total acid capacity of the catalysts are tabulated in Table 11. Two peaks at 286°C and 382°C were observed for the 5Ni-MC catalyst; on the other hand, two peaks at 314°C and 382°C were seen for the 10Ni-MC catalyst. There was a peak shift between 10Ni-MC and 5Ni-MC catalyst. The shift between the peak locations can be due to the location of the thermocouple. Acidity of the 10Ni-MC catalyst was higher than that of 5Ni-MC catalyst. This may be due to the difference in nickel loading amount.

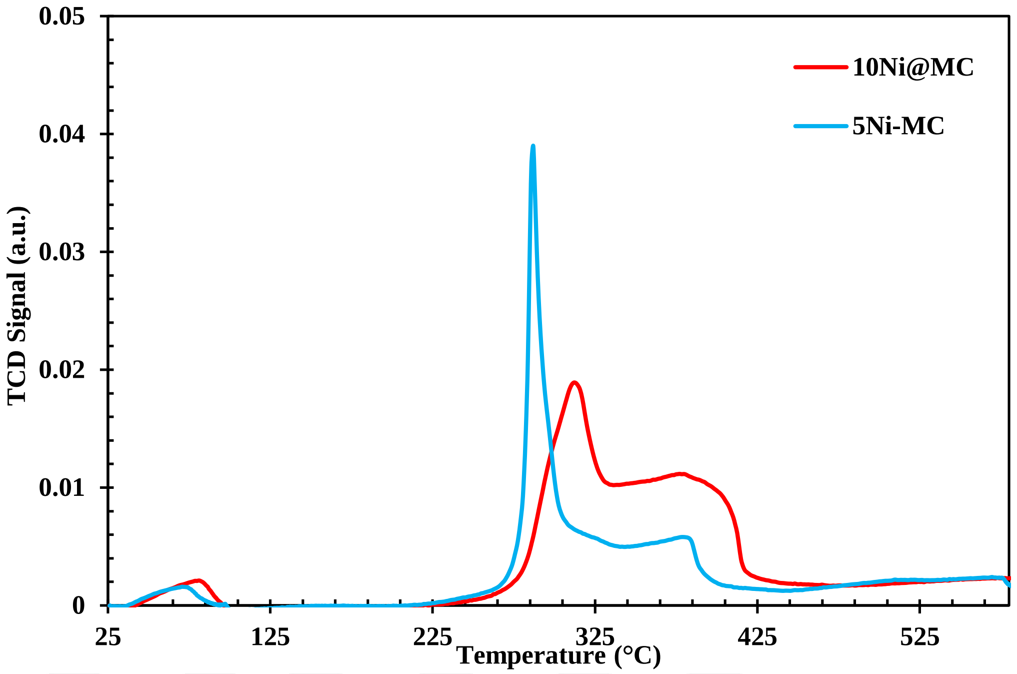

Figure 55: NH_3-TPD graphs of the commercial carbon materials

Table 11: Acid capacities of the nickel loaded mesoporous carbon catalysts

Catalyst	Total acid capacity (mmol/g)
5Ni-MC	0.145
10Ni-MC	0.209

6.2.5 Activity Test Results for Commercial Mesoporous Carbon Supported Catalysts

6.2.5.1 Effect of Reaction Temperature

Steam reforming of ethanol experiments were investigated on hydrogen production at 500°C and 600°C for 5Ni-MC and 10Ni-MC catalysts. For the 10Ni-MC catalyst, the average mole percentages of the products at different temperatures are given in Figure 56. At 600°C, the carbon monoxide amount increased with suppressing water gas shift reaction and the methane amount decreased with favoring the methane steam reforming reaction. The percentage of the hydrogen yield was 51 % at 500°C; on the other hand, that of hydrogen yield was 78 % at 600°C. Hydrogen yield enhancement was achieved with an increase in temperature. The product distributions are also given in Figures 57-58.

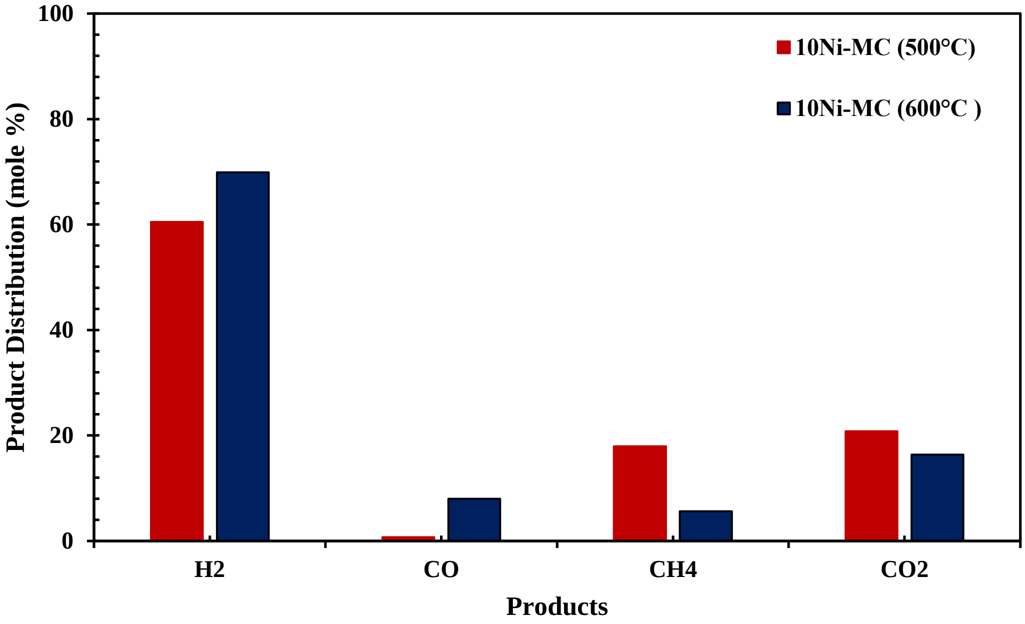

Figure 56: Effect of reaction temperature on the product distribution for the 10Ni-MC (SRE reaction environment)

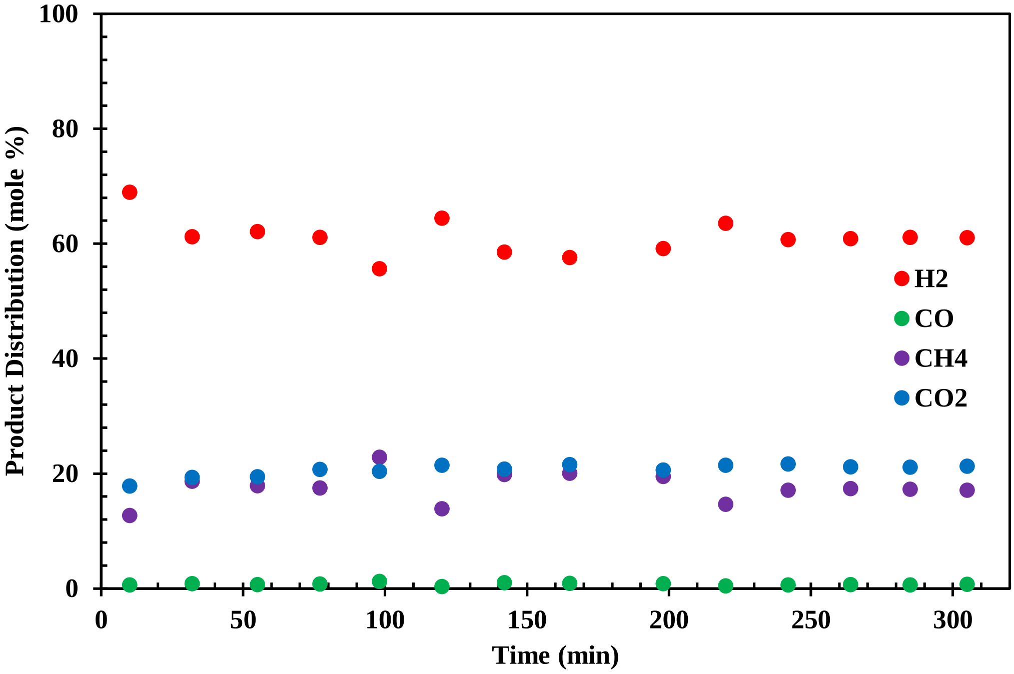

Figure 57: Product distribution at 500°C for SRE reaction (Catalyst: 10Ni-MC)

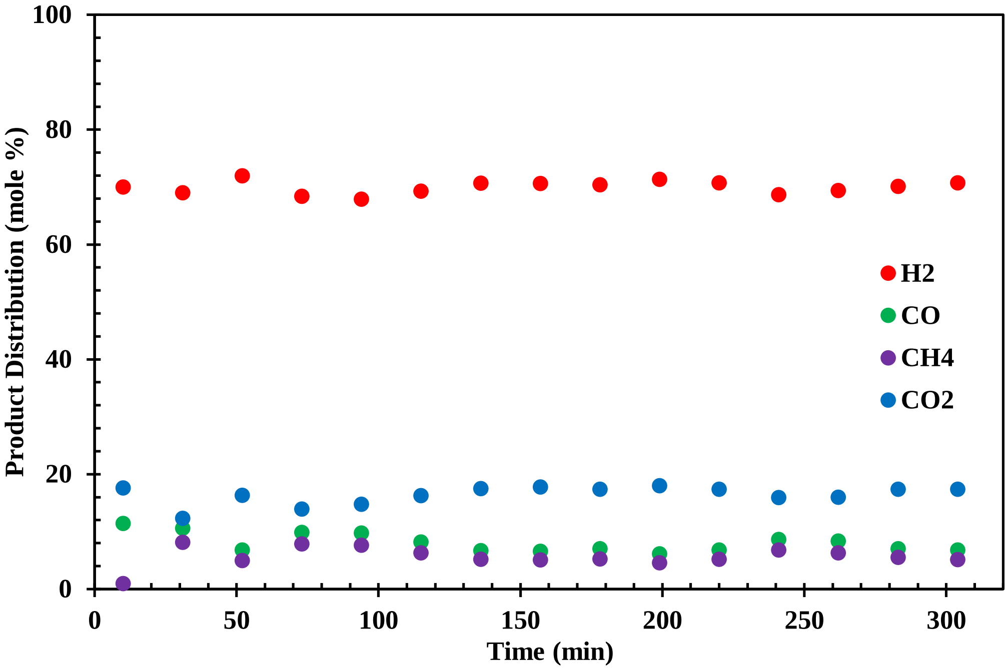

Figure 58: Product distribution at 600°C for SRE reaction (Catalyst: 10Ni-MC)

6.2.5.2 Effect of Metal Loading on Hydrogen Production

In order to investigate the amount of metal loading on the mesoporous carbon support, different amounts of the nickel by weight were impregnated to the mesoporous carbon. Moreover, only MC was also tested in the steam reforming of ethanol reaction. The product distribution for the MC and 5Ni-MC catalyst at 600°C are given in Figures 59-60. The average product distribution of the MC was 43 % H_2, 1.7 % CO, 4.5 % CH_4, and 51 % C_2H_4. The reason of high ethylene mole percentage may be due to the formation of dehydration reaction. The effect of steam reforming of ethanol reaction was very low in the presence of MC support because there was a very small amount of carbon dioxide in the product distribution. MC gave only 70 % ethanol conversion and 9 % of hydrogen yield. The catalytic activity of the MC support for the ethanol steam reforming reaction was enhanced with the nickel loading. Same product distributions were achieved with different amount of metal loaded catalysts (Figure 61) because approximately same characterization results were found for 5Ni-MC and 10Ni-MC catalysts. The percentage of the hydrogen yield was 78 % for the both catalysts.

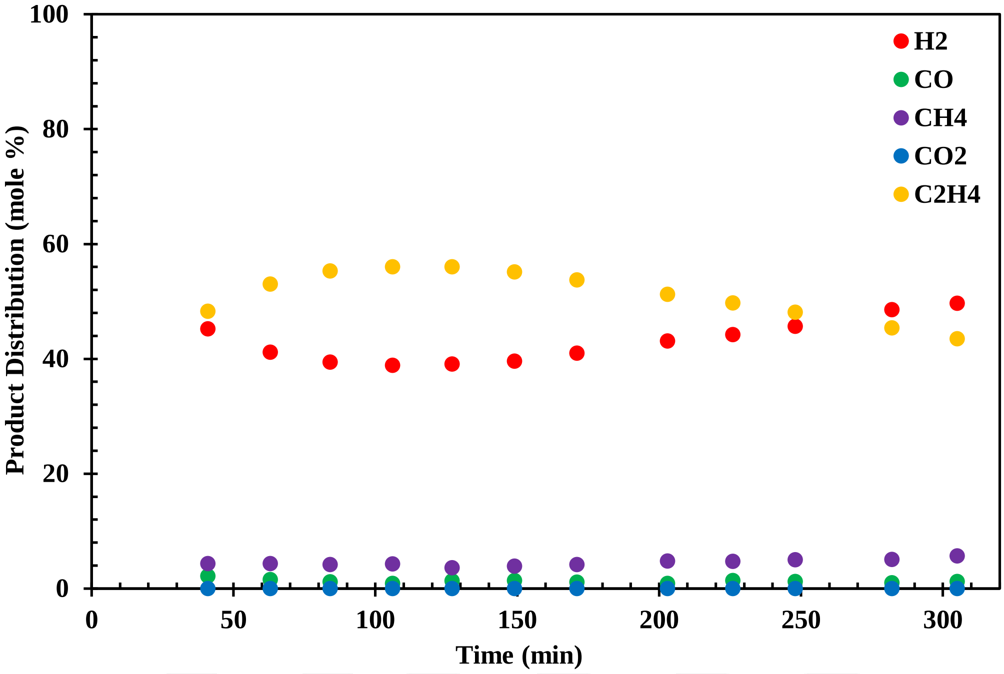

Figure 59: Product distribution at 600°C for the SRE reaction (Catalyst: MC)

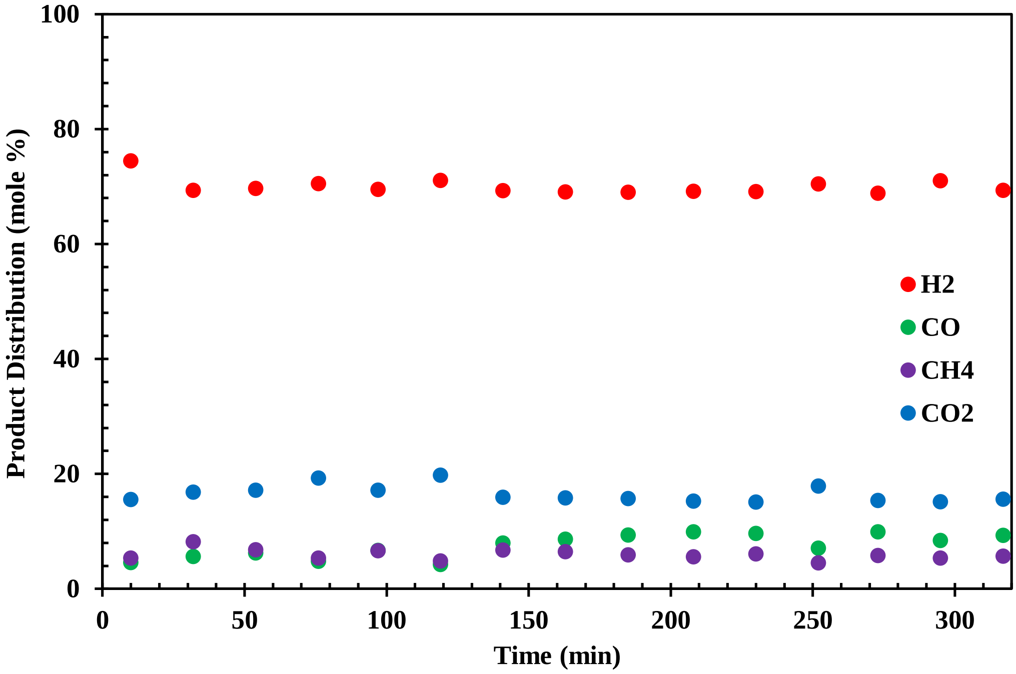

Figure 60: Product distribution at 600°C for the SRE reaction (Catalyst: 5Ni-MC)

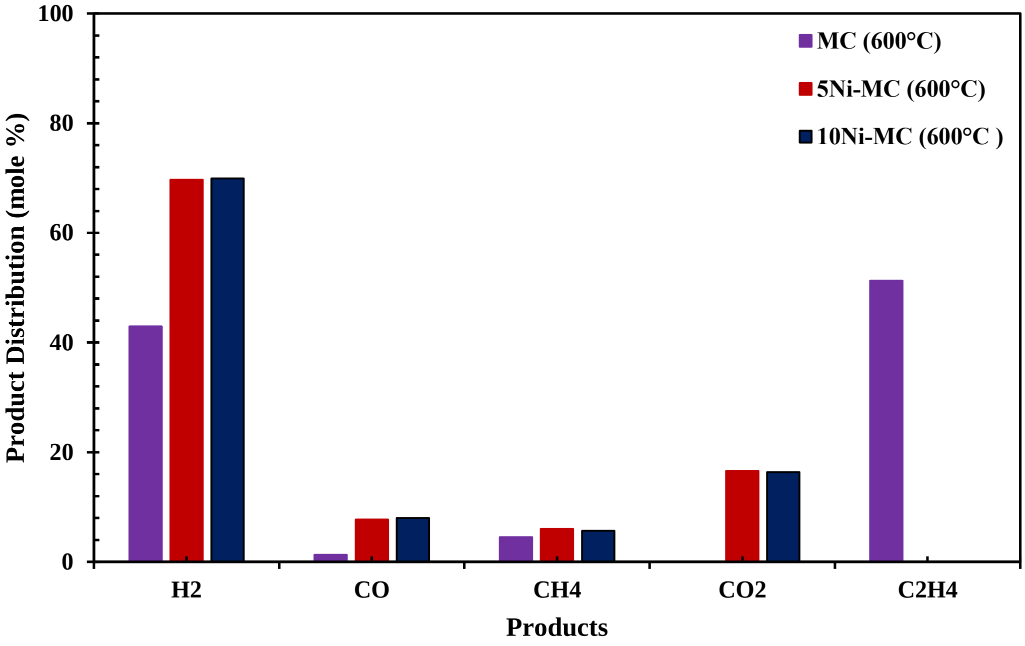

Figure 61: Effect of metal loading on hydrogen production for MC, 5Ni-MC and 10Ni-MC at 600°C (SRE reaction environment)

6.2.5.3 Effect of the Packing of Catalyst and Sorbent on Hydrogen Production

Whether the 10Ni-MC catalyst was proper candidate for the mixed-SESRE concept or not, different sorbent and catalyst configurations were also investigated for this catalyst. For the SESRE-M experiment at 600°C, the product distribution is shown in Figure 62. In the first 80 min, the purity of the hydrogen increased to 87 %. Moreover, in this period, there was nearly no carbon dioxide in the product gas stream. After the saturation period, the mole percentage of the hydrogen in the SESRE-M decreased to values below the SRE results. This might be associated with the activity loss of the catalyst. For this catalyst, the acidity was 0.209 mmol/g catalyst. Same situation faced with 10Ni-SBA-15 catalyst was also valid for this catalyst. In the mixed concept, catalyst lost their activity due to low acidity towards the basic nature of sorbent so the mole percentage of the hydrogen was lower than that of hydrogen in the SRE experiment after 180 min. Moreover, in the first 100 min, CO_2 was nearly not observed in the product stream due to the low CO_2 amount produced because ethanol decomposition reaction gave undesired CO and CH_4 products. The formation of the ethanol decomposition reaction suppressed the ethanol steam reforming reaction.

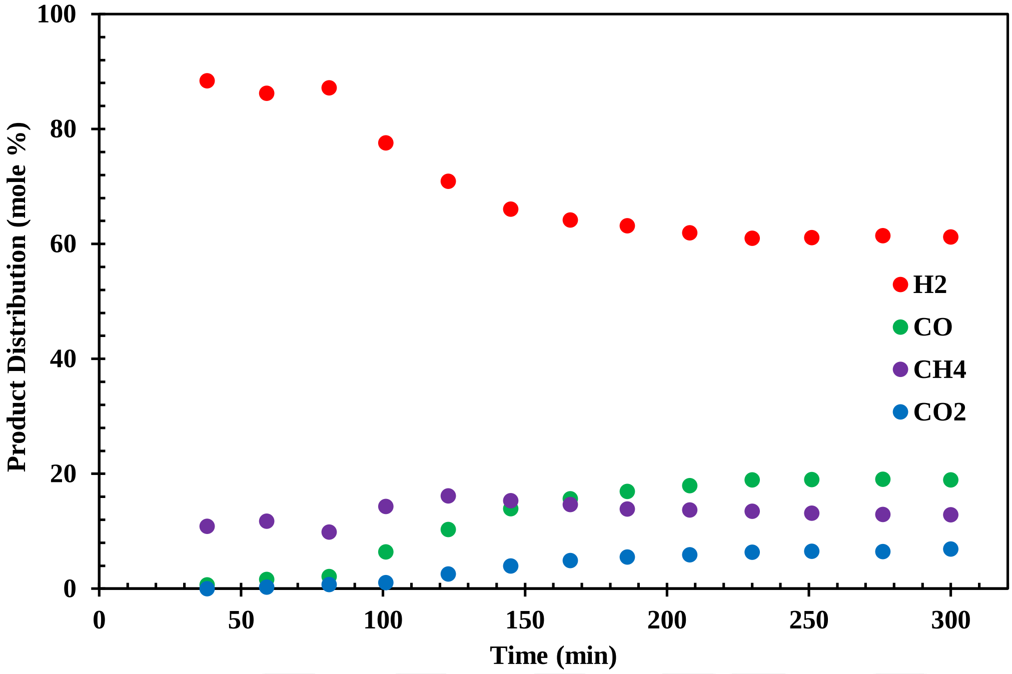

Figure 62: Product distribution at 600°C for the SESRE-M configuration (Catalyst: 10Ni-MC)

In order to minimize the contact between catalyst and sorbent, SESRE-1O and SESRE-3O experiments were investigated for this catalyst. For SESRE-1O experiment at 600°C, the product distribution is shown in Figure 63. For SESRE-3O experiment at 600°C, the product distribution is shown in Figure 64. In the SESRE-1O experiment, the hydrogen mole percentage reached to 90 % in the first 60 min. Then, it started to decrease with the saturation of CaO with carbon dioxide. Moreover, there was nearly no carbon CO and CO_2 in the product gas stream. The mole percentage of the carbon dioxide decreased from 16 % to nearly 0 % in the first 60 min compared to the SRE experiment. After the breakthrough period, the mole percentage of the hydrogen decreased and stayed constant at a value of 72 %. When the SESRE-M and SESRE-1O experiments were compared, the mole percentage of the methane in the SESRE-M test was 13 %; on the other hand, the mole percentage of the methane was only 4 % in the SESRE-1O. Moreover, after the breakthrough period of CO_2, the mole percentage of the carbon monoxide in the SESRE-M test was 19 %; on the other hand, the mole percentage of the carbon monoxide was only 8 % in the SESRE-1O. The decrease in the methane and carbon monoxide may be due to the suppressing the ethanol decomposition reaction with minimizing the contact between catalyst and CaO.

When the SESRE-1O and the SESRE-3O experiments were compared with each other, with an increase in the contact between catalyst and CaO with an increase in the ordering, the methane and carbon monoxide mole percentages slightly increased with the SESRE-3O experiment.

As a result, with the ordered configuration, the catalyst stayed active towards to the ethanol steam reforming reaction. With an increase in the ordering, the capture time of sorbent increased for the 10Ni-MC catalyst. The comparison graph for all configurations is represented in Figure 65. With the SESRE-3O concept, the mole percentage of the hydrogen is higher in the first 150 min compared to other configurations. Therefore, the best configuration considering the capture time and also the purity of the hydrogen was SESRE-3O.

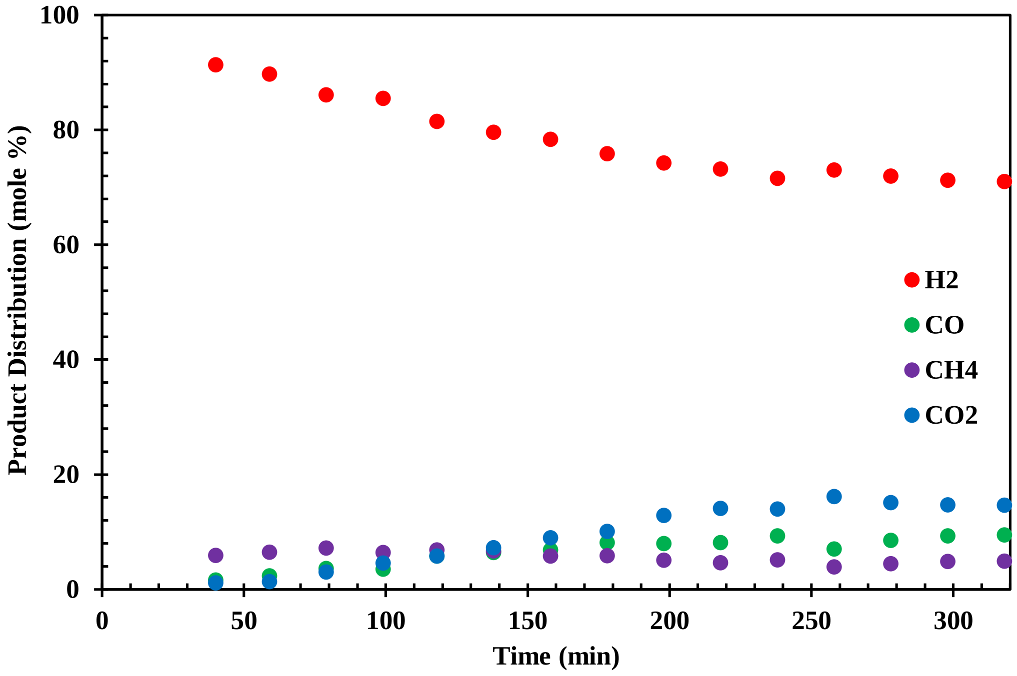

Figure 63: Product distribution with SESRE-1O configuration at 600°C (Catalyst: 10Ni-MC)

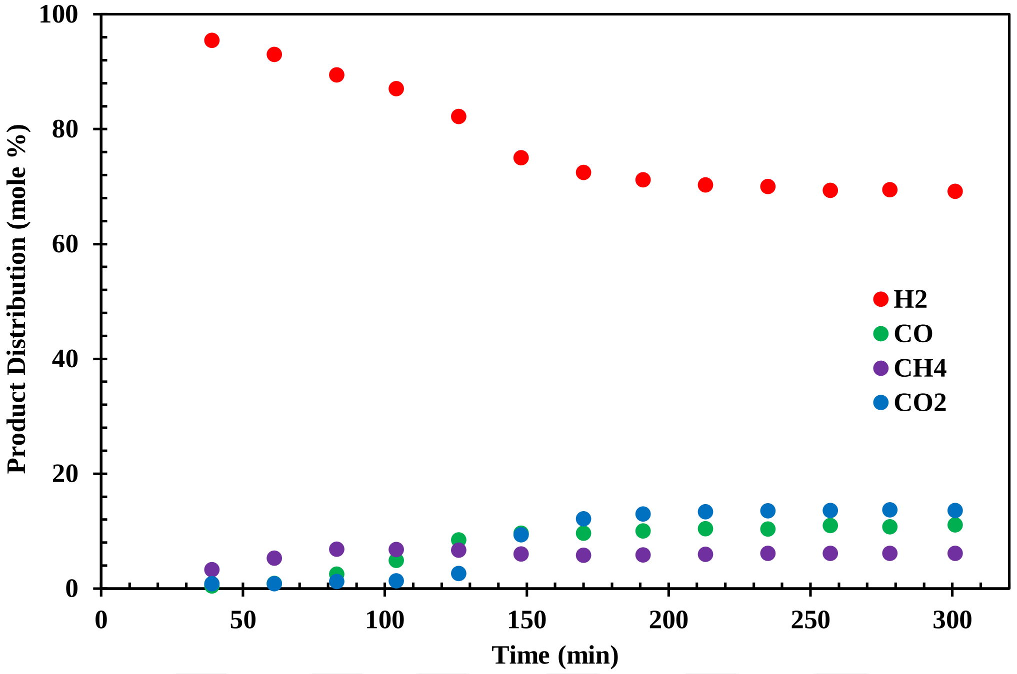

Figure 64: Product distribution with SESRE-3O configuration at 600°C (Catalyst: 10Ni-MC)

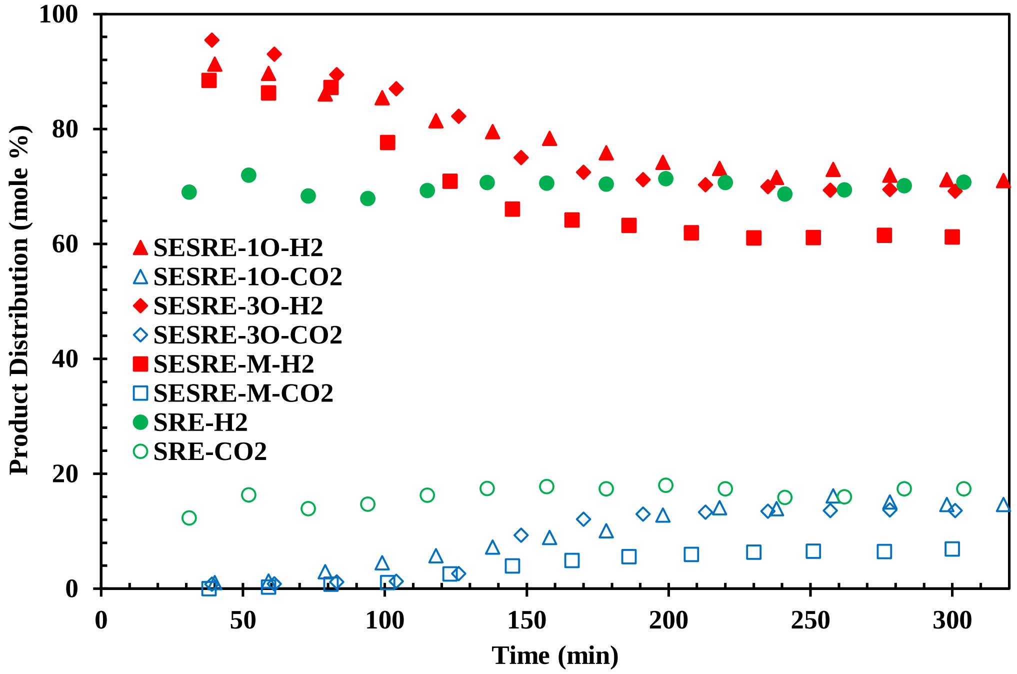

Figure 65: Comparison of mole percentages of H_2 and CO_2 for the SRE and SESRE reactions at 600°C (Catalyst: 10Ni-MC)

For the 5Ni-MC catalyst, SESRE-M product distribution is shown in Figure 66. The comparison graph for SRE and SESRE-M is also shown in Figure 67. The mole percentage of the hydrogen reached to only 80 % in the reaction time of 30 min and its started to decrease. In the first 70 min, there was nearly no carbon dioxide in the product stream. The increase in methane mole percentage in the first 100 min may be due to the reverse dry reforming of methane reaction. The catalyst did not stay active towards to CaO. It can be seen from the comparison graph that the mole percentage of the hydrogen after 190 min reached to 62 % which was below the result obtained in the SRE experiment.

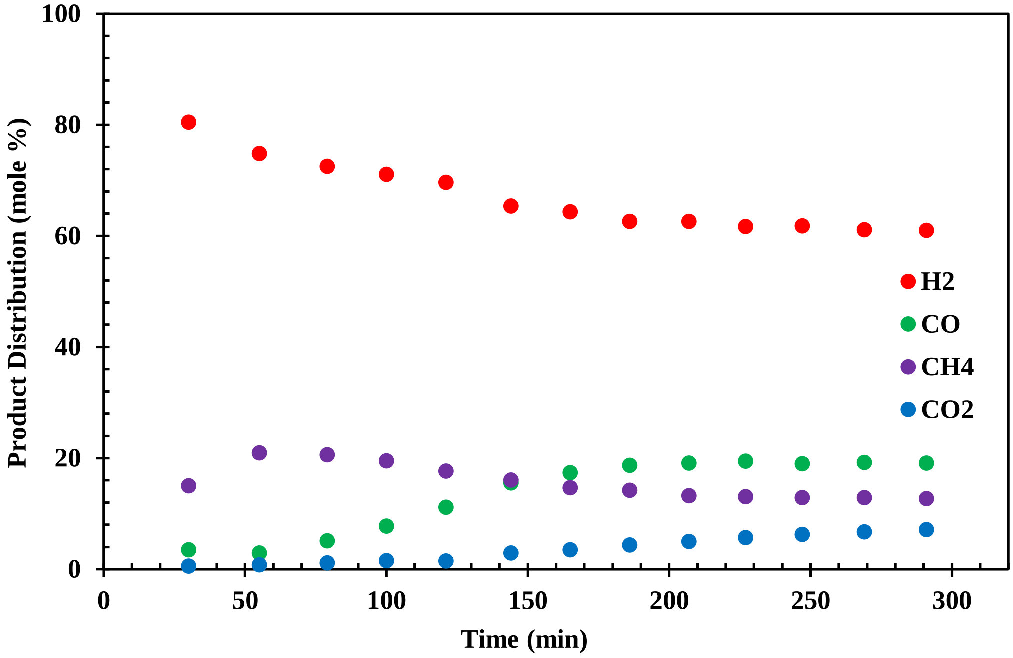

Figure 66: Product distribution at 600°C for the SESRE-M configuration (Catalyst: 5Ni-MC)

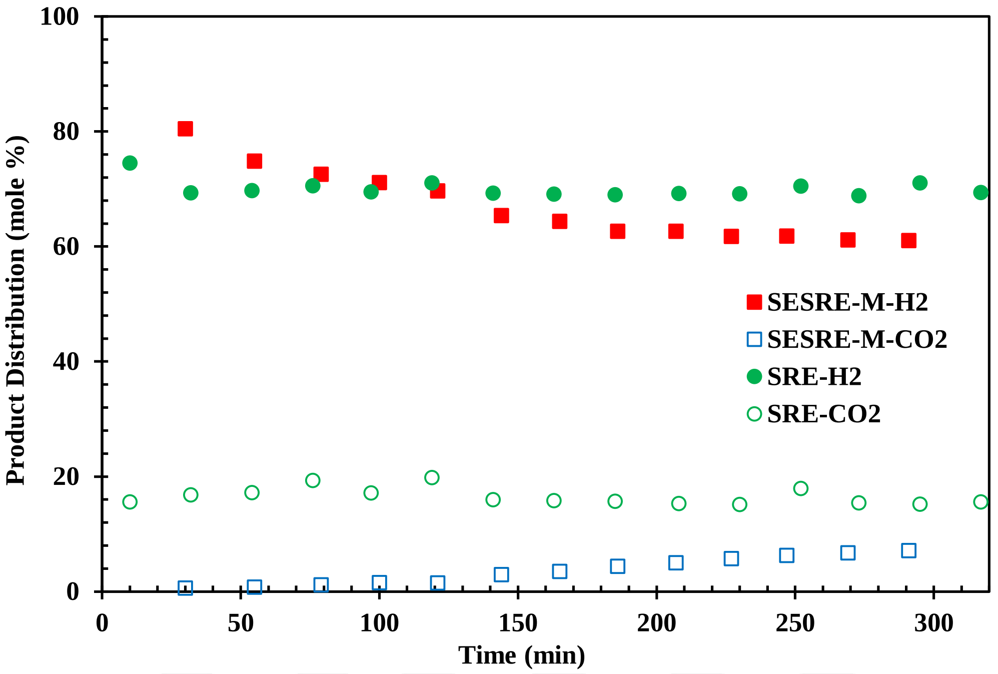

Figure 67: Comparison of mole percentages of H_2 and CO_2 for the SRE and the SESRE-M reactions at 600°C (Catalyst: 5Ni-MC)

6.2.6 TGA Results of the Spent Mesoporous Carbon Supported Catalysts

The TGA results for the unused 10Ni-MC catalyst and used 10Ni-MC catalyst in the reaction at 600°C are shown in Figure 68. The remaining part nearly 10 % for the unused catalyst was due to the nickel loading. On the other hand, for the spent catalysts after the reaction the remaining amount was only 6 %. This showed that due to the carbon formation, the nickel loading amount decreased from 10 % to 6 %. It was evident that the coke formation on the mesoporous carbon supported catalysts was observed. Moreover, the thermal stability of the spent catalyst was higher than that of unused catalyst. The thermal stability of the spent catalyst increased with a decrease in reaction temperature. This may also be explained by the structure of carbon deposited.

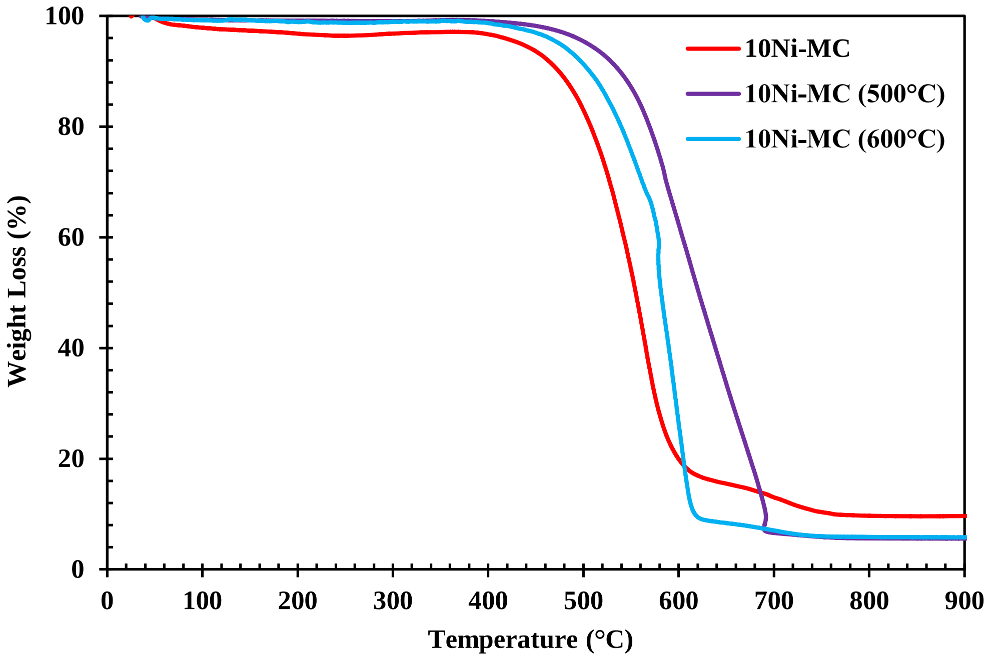

Figure 68: TGA results of the spent and fresh 10Ni-MC catalyst

6.3 Characterization and Activity Results of Silica Aerogel Supported Catalysts

6.3.1 X-Ray Diffraction Results of Silica Aerogel Supported Catalyst

XRD pattern of nickel impregnated silica aerogel (10Ni-SA) is shown in Figure 69. A broad diffraction peak at 22.5° was assigned to amorphous silica. It was evident that the catalyst showed the silica structure which is the nature of silica aerogel after nickel impregnation. The peaks at 2θ values of 44, 52 and 76° showed the presence of metallic nickel (JPDC-01-071-4653 given in Appendix B). Nickel crystallite size was calculated and tabulated in Table 12.

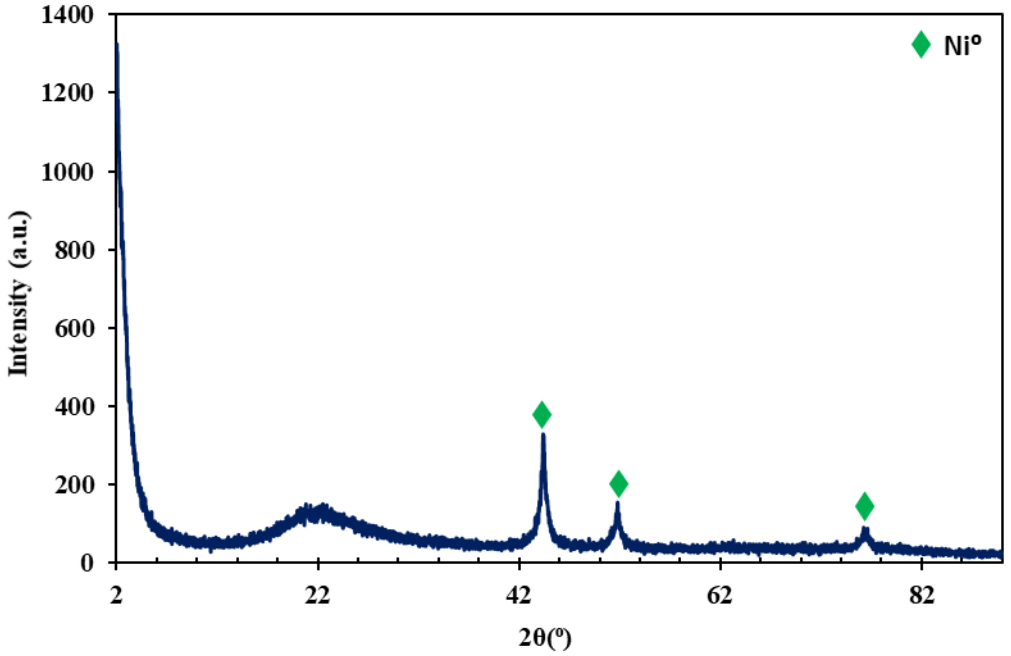

Figure 69: XRD pattern of the 10Ni-SA catalyst

Table 12: Crystallite size of the nickel loaded silica aerogel supported catalyst

Catalyst	**2θ (°)**	**$t_{crystallite\ size}$ (nm)**
10Ni-SA	44.42	18.9

6.3.2 N_2 Adsorption/Desorption Isotherms and Physical Properties of the Materials

The physical properties of the SA and 10Ni-SA catalysts are shown in Table 13. Nitrogen adsorption/desorption isotherms and pore size distributions for the SA and 10Ni-SA catalysts are given in Figures 70-71. After nickel impregnation, surface area, pore volume and pore diameter of the catalyst decreased due to the blockage of the pores with nickel particles. Moreover, silica aerogel had a wide range of pore diameter containing mesopores and macropores. With nickel loading, nickel particles located to the mesopores and macropores of the catalyst support which can be seen from the Figure 71. According to IUPAC classification, silica aerogel had Type IV isotherm with H3 hystheresis loop in the relative pressure range between 0.65 and 0.95. On the other hand, nickel impregnated silica aerogel had Type IV isotherm with H1 hystheresis loop in the relative pressure range of 0.74 and 0.98. With nickel loading, the hystheresis starting point shifted to larger value. This indicated that there was also a shift to the higher mesopores. Therefore, the isotherm and pore size distribution were consistent with each other.

Table 13: The physical properties of SA and 10Ni-SA

	Multipoint BET Surface Area (m^2/g)	BJH Desorption Pore Volume (cm^3/g)	BJH Desorption Average Pore Diameter (nm)	Microporosity (%)
SA	786	3.6	11.1	3.6
10Ni-SA	613	2.1	8.8	7.1

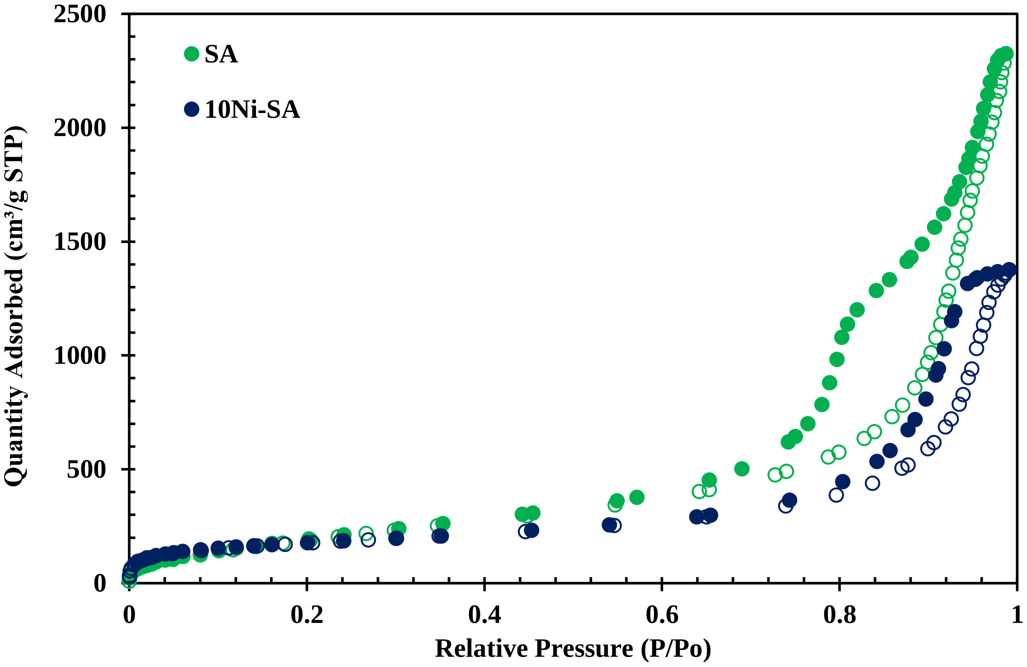

Figure 70: N_2 adsorption/desorption isotherms of the SA support and 10Ni-SA catalyst (Filled symbols: Desorption branch, Empty symbols: Adsorption Branch)

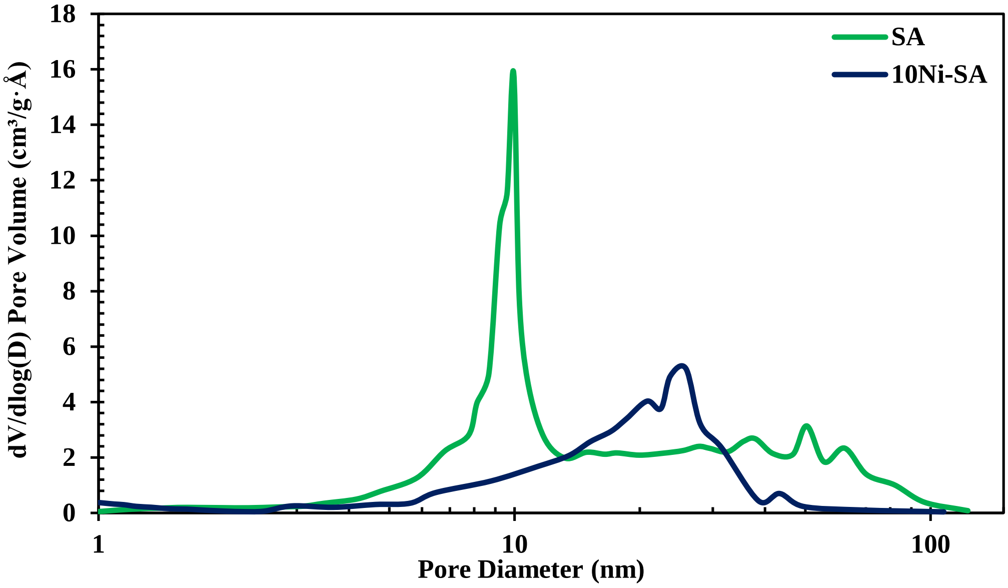

Figure 71: Pore size distributions of SA and 10Ni-SA

6.3.3 Temperature Programmed Ammonia Desorption (NH_3-TPD) Results

NH_3-TPD result of the synthesized material are shown in Figure 72. Two peaks at 333°C and 352°C were observed. Total acid capacity of the catalyst was calculated and found to be 0.6 mmol/g catalyst.

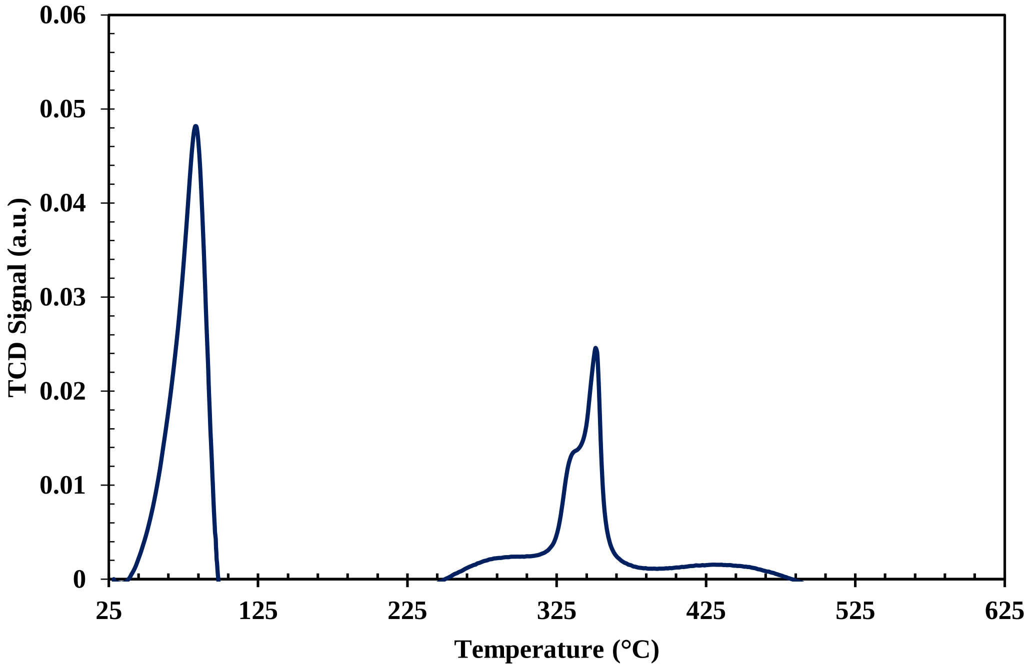

Figure 72: NH_3-TPD graph of the 10Ni-SA catalyst

6.3.4 Activity Results of Silica Aerogel Supported Catalysts on Hydrogen Production

6.3.4.1 The Effect of the Reaction Temperature

Nickel impregnated silica aerogel was also tested in the SRE and SESRE reactions in order to see the effect of this support on the reaction. With this aim, 10Ni-SA catalyst was tested in the SRE reaction at 500°C and 600°C and product distributions are given in Figures 73-74. Stable product distributions for both temperatures were obtained and the comparison of average product distributions is shown in Figure 75. The percentages of hydrogen yield value were 54 % at 500°C and 77 % at 600°C. Hydrogen yield enhancement was obtained with the increase in temperature. For both temperatures, complete conversion was achieved. With decreasing the effect of water gas shift reaction with an increase in temperature, carbon monoxide amount increased and carbon dioxide amount decreased.

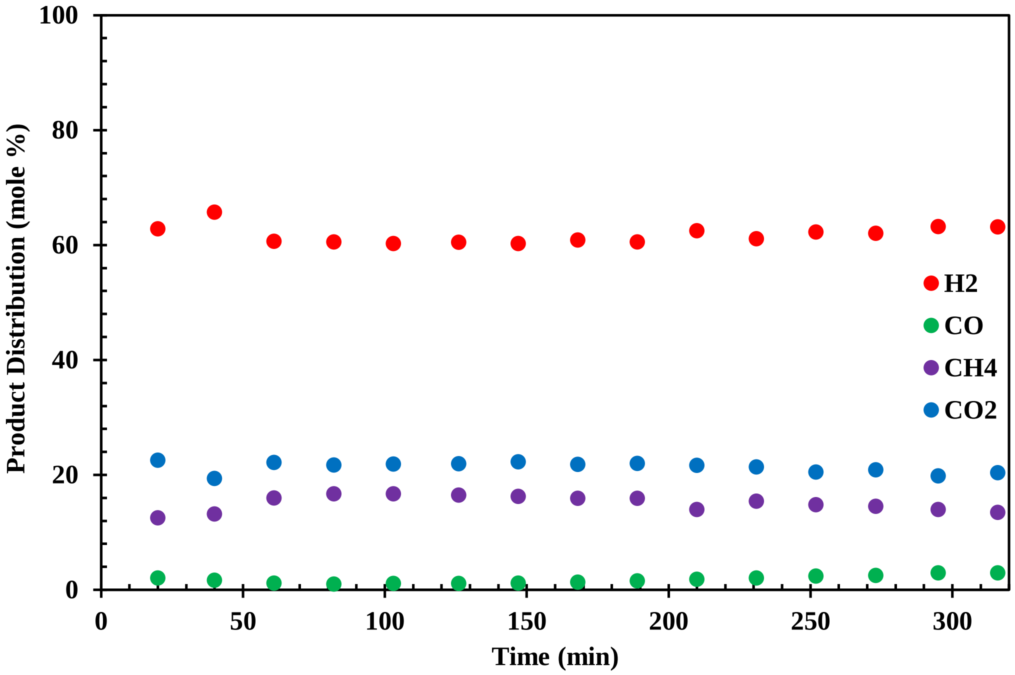

Figure 73: Product distribution of SRE at 500°C (Catalyst: 10Ni-SA)

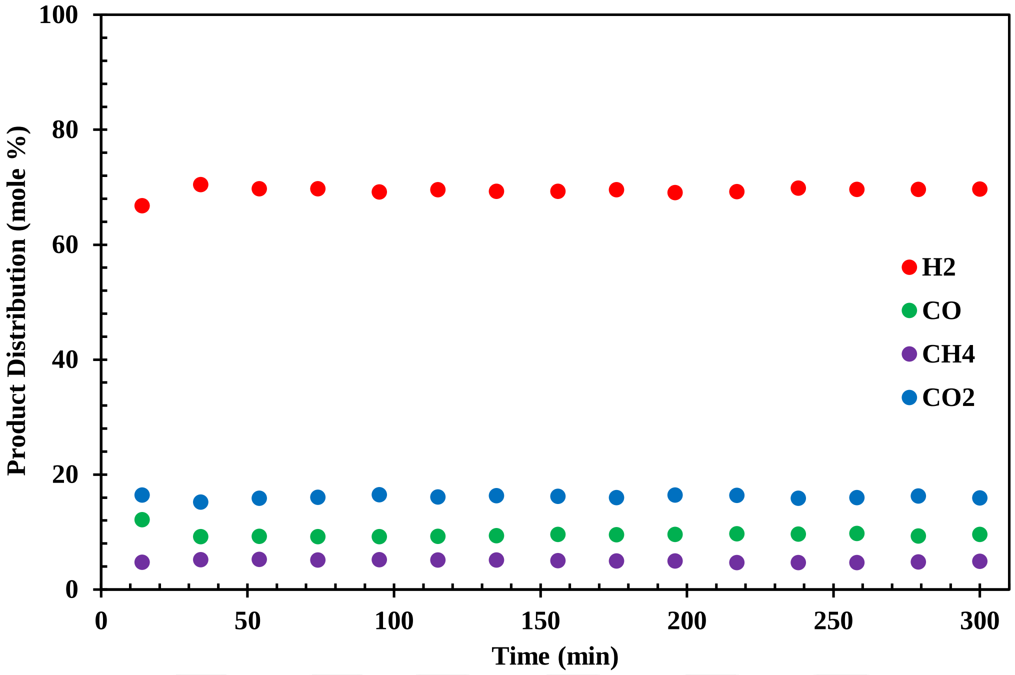

Figure 74: Product distribution of SRE at 600°C (Catalyst: 10Ni-SA)

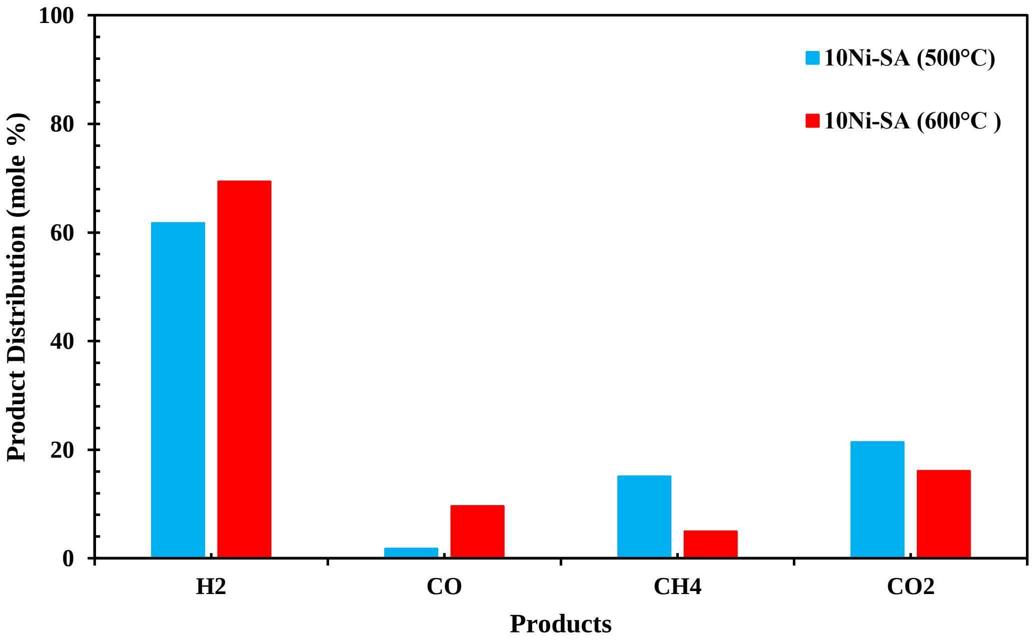

Figure 75: Effect of reaction temperature on the product distribution for the 10Ni-SA (SRE reaction environment)

6.3.4.2 Effect of the Packing of Catalyst and Sorbent on Hydrogen Production

The catalyst was also tested in the SESRE-M and SESRE-3O experiments at 500°C and 600°C. The product distributions at 600°C for the SESRE-M and SESRE-3O are represented in Figures 76-78. In the pre-breakthrough section, the mole percentages of carbon monoxide and carbon dioxide was nearly 1 %, whereas the mole percentage of the hydrogen enhanced and sustained at very high level, 93 %. This proved that adsorption of carbon dioxide through CaO was effectively achieved, improving water gas shift reaction. With the saturation of CaO, the sorption enhanced effect was diminished. In the breakthrough stage, the mole percentage of the carbon dioxide increased step by step. In the post-breakthrough stage, the sorbent was totally filled with carbon dioxide so the effect of the sorption enhance process totally disappeared. All the mole percentages reached the same values with the steam reforming process in the post-breakthrough stage.

Product distributions of mixed and ordered SESRE experiments were nearly same with each other. Mixed concept did not affect the catalytic activity of the 10Ni-SA catalyst. Acid capacity of the catalyst may be the reason of this. Compared to the 10Ni-SBA-15 catalyst, the acid capacity of the 10Ni-SA catalyst was higher. Total acid capacity of 10Ni-SA catalyst was 0.6 mmol/g. The higher the acid capacity was, the better the catalytic activity was towards to hydrogen production for the mixed SESRE experiments.

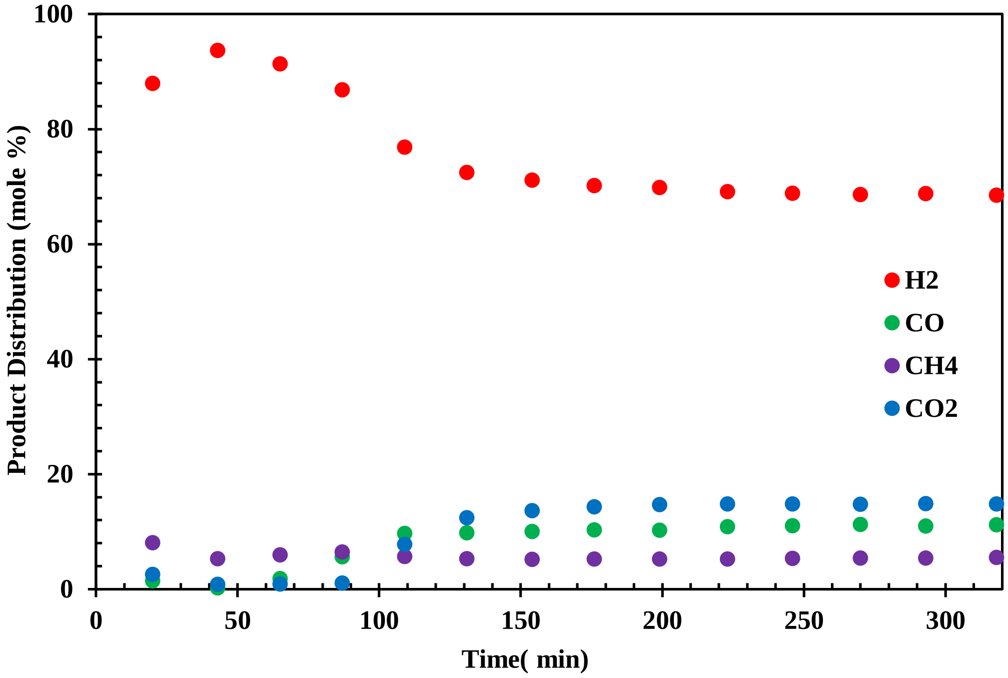

Figure 76: Product distribution of SESRE-M at 600°C (Catalyst: 10Ni-SA)

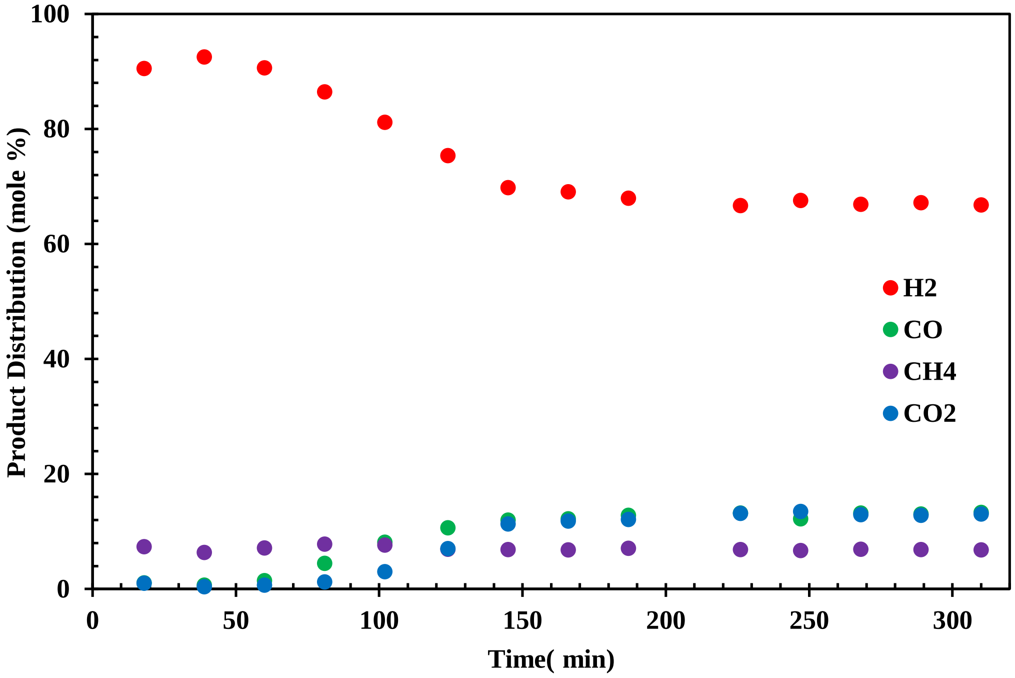

Figure 77: Product distribution of SESRE-3O at 600°C (Catalyst: 10Ni-SA)

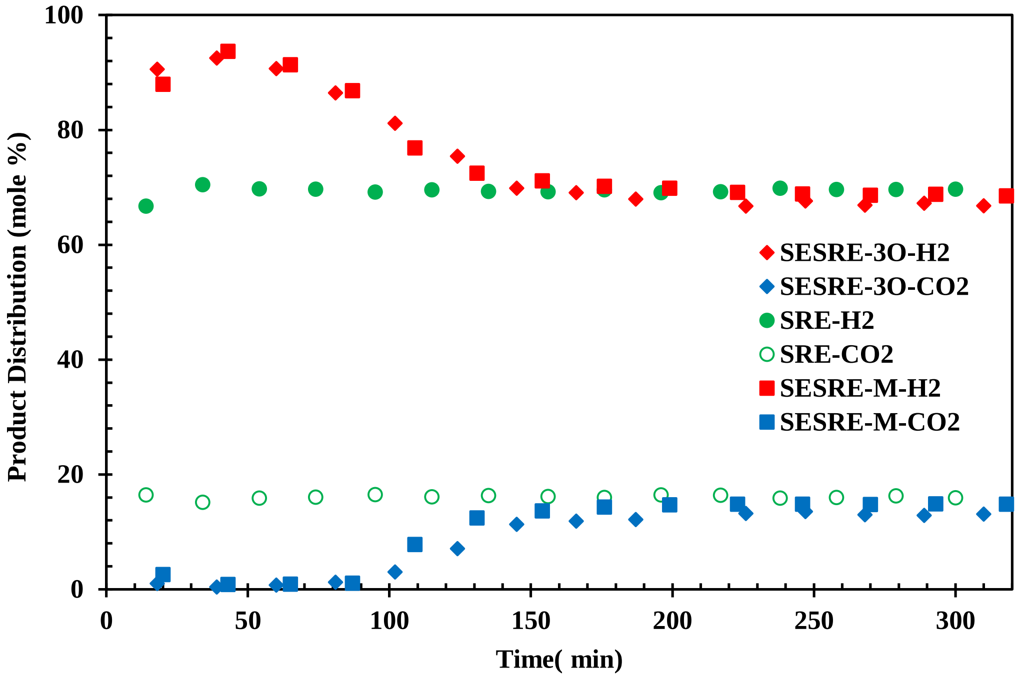

Figure 78: Comparison of mole percentages of H_2 and CO_2 for the SRE and SESRE reactions at 600°C (Catalyst: 10Ni-SA)

The catalyst was also investigated at 500°C in the SESRE-3O experiment and product distribution is given in Figure 79. The comparison graph for the SRE and SESRE-3O experiments is given in Figure 80. The mole percentage of the hydrogen reached to nearly 86 % in the first 60 min, giving no carbon dioxide and carbon monoxide. Enhancement in the hydrogen mole percentage was achieved in the first 150 min, then the product distribution was same with the SRE experiment at 500°C.

When the temperature effect on the sorption enhanced process was investigated, high temperatures favored the hydrogen purity in the pre-breakthrough stage. The highest hydrogen purity was achieved at 600°C.

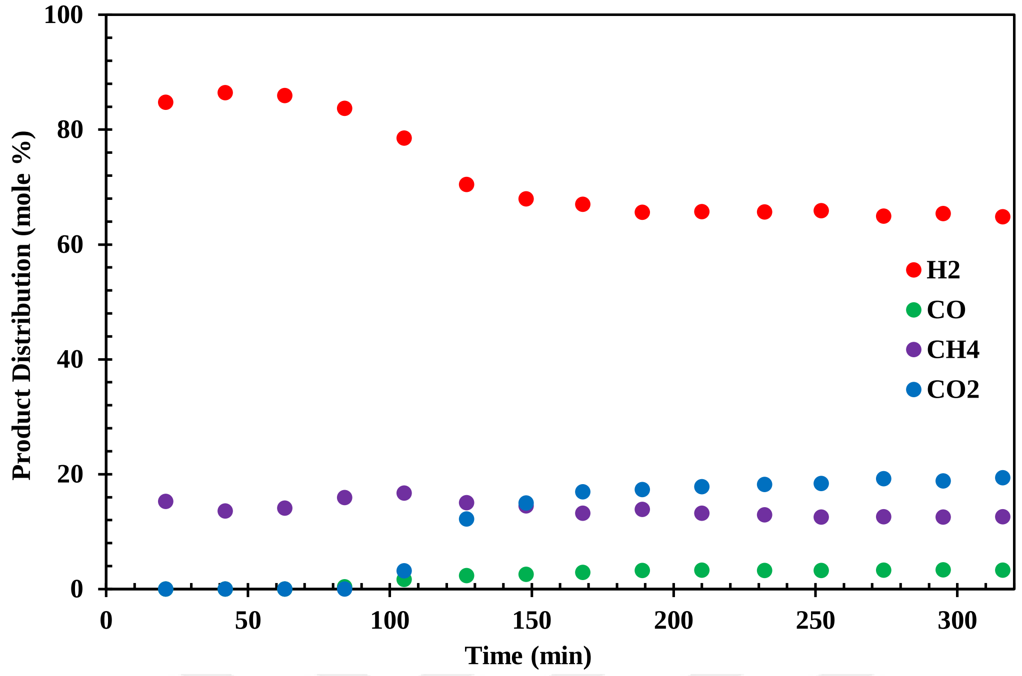

Figure 79: Product distribution of SESRE-3O at 500°C (Catalyst: 10Ni-SA)

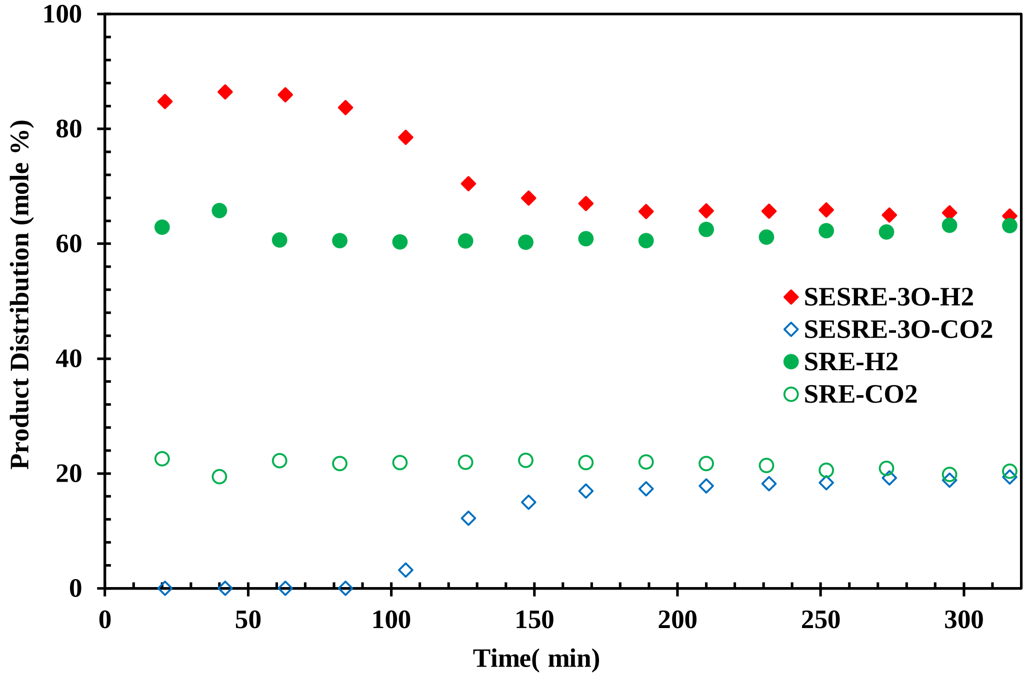

Figure 80: Comparison of mole percentages of H_2 and CO_2 for the SRE and SESRE reactions at 500°C (Catalyst: 10Ni-SA)

6.3.5 TGA Results

The TGA analysis results for the spent catalysts are given in Figure 81. The coke formation was 48 % at 500°C and only 12 % at 600°C. The reason of the high coke formation at 500°C compared to that of at 600°C may be due to the formation of cold-spots and the occurrence of Bouduard reaction in these cold spots.

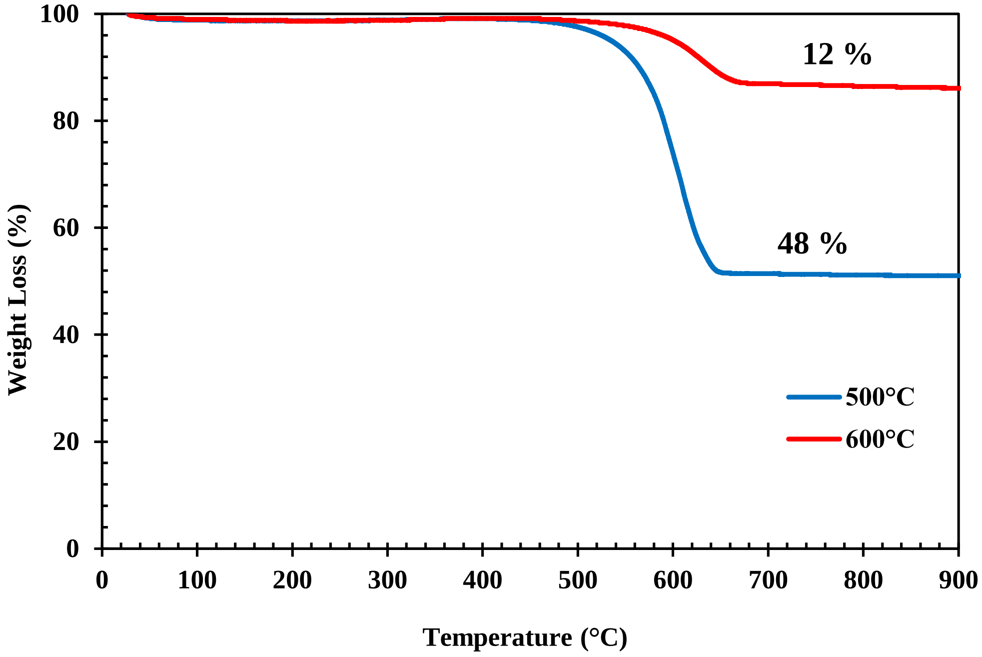

Figure 81: TGA results for the spent 10Ni-SA catalyst at different reaction temperatures

6.4 Characterization and Activity Results for Silica Aerogel Templated Carbon Material Supported Catalyst

Mesoporous carbon (MCMT) was synthesized using silica aerogel as a template. The effect of washing with HF or NaOH, adding silylating agent to silica aerogel in the synthesis, and calcination temperature of silica aerogel on the structure of the materials were investigated.

6.4.1 Characterization of Silica Aerogel Templates

6.4.1.1 Fourier Transform Infrared Spectroscopy (FTIR)

FTIR analysis was performed in order to determine whether the synthesized material was silica aerogel or not. The FTIR spectrum of silica aerogel (without calcination, SA-NC) is given in Figure 82. For SA-NC, the absorption peak at 800 cm^{-1} was due to the symmetric Si-O-Si stretching vibration. Moreover, the peaks at 844 cm^{-1} and at 1253 cm^{-1} showed the Si-C bonds in the silica aerogels. The peak at 960 cm^{-1} also indicated the Si-O-Si bonds in the silica template. Moreover, the band at 1060 cm^{-1} with a shoulder at 1152 cm^{-1} was refer to asymmetric Si-O-Si stretching vibrations. The peak at 2960 cm^{-1} showed the C-H bond. Silica aerogel with the characteristic peaks was successfully synthesized.

During the synthesis of the silica aerogels, in the chemical surface modification step by a silylating agent such as TMCS, silica aerogels gain the property of hydrophobicity. The main reason of hydrophobicity of aerogel is due to the presence of Si-C and C-H bonds in silica aerogel after the surface modification step. These groups result from the replacement of the surface H in Si-OH by $Si(CH_3)_3$ groups during the chemical surface modification step. The existing Si-OH groups are the main reason of the hydrophilicity of the aerogels before the chemical surface modification step. Moreover, with the calcination after the synthesis, Si-C and C-H bonds can be totally disappeared. As a result, hydrophobicity of the silica aerogel can be changed. The hydrophilicity of the silica aerogel is important point in the synthesis of the mesoporous carbon. In order to check whether the synthesized aerogels are hydrophilic or not, FTIR spectrum of calcined aerogels and the aerogels synthesized without TMCS was performed. FTIR spectra of the synthesized silica aerogels are shown in Figure 82. The peaks observed at different wavenumbers for all silica aerogel supports are shown in Table 14.

The absence of silylating agent did not affect the formation of silica template. The formation of all characteristic peaks for the silica was observed for the silica aerogel synthesized without TMCS. Only the peaks appeared after the surface modification step were not observed for these supports. Hydrophilic silica supports were successfully synthesized.

With the calcination at 450°C and 700°C under air atmosphere the peak showing C-H bond at 2960 cm^{-1} disappeared. For the uncalcined silica aerogel and the silica aerogel calcined at 450°C, the Si-C bond appeared, but its peak intensity decreased with the calcination at 450°C and totally disappeared with the calcination at 700°C. By calcination, at 450°C and 700°C under air, hydrophobic silica aerogels can be converted to hydrophilic aerogels. Characteristic peaks of silica supports were observed for all the silica aerogel samples. The characteristic peaks were preserved. Those silica aerogel supports were used for the synthesis of mesoporous carbon support.

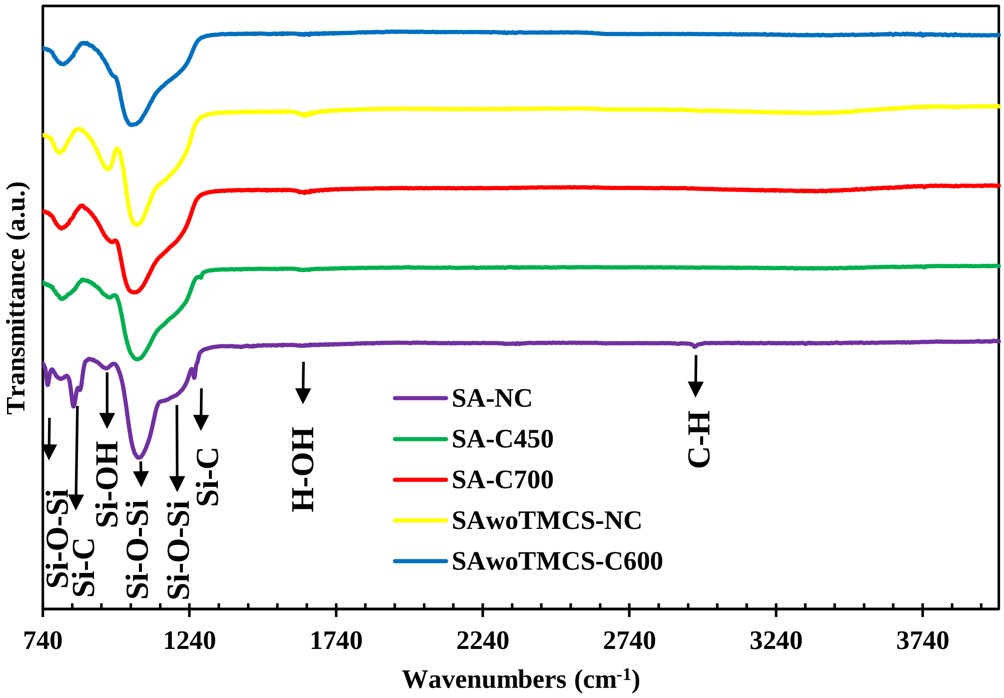

Figure 82: FTIR spectra for the silica aerogel support material

Table 14: Peak identification for all silica aerogel supports

Wavenumber (cm^{-1})	**SA-NC**	**SA-C450**	**SA-C700**	**SAwoTMCS-NC**	**SAwoTMCS-C600**
800	√	√	√	√	√
844	√	√	X	X	X
960	√	√	√	√	√
1060	√	√	√	√	√
1152	√	√	√	√	√
1253	√	√	X	X	X
2960	√	X	X	X	X

6.4.1.2 N_2 Adsorption/Desorption Isotherms and Physical Properties of the Silica Aerogel Materials

The physical properties of the uncalcined silica aerogel (SA-NC), silica aerogel calcined at 450°C (SA-C450) and 700°C (SA-C700) and silica aerogel without TMCS (SAwoTMCS-NC) and silica aerogel without TMCS and calcined at 600°C (SAwoTMCS-C600) are given in Table 15. As expected, all the synthesized silica aerogels had high surface area, pore volume and pore diameter. SAwoTMCS-NC and SAwoTMCS-C600 had lower pore volume and pore diameter than that of the SA, SA-C450, and SA-C700. The reason of the decrease in the pore volume and pore diameter was due to the elimination of chemical modification step in the synthesis. When the ambient pressure drying method was used in the synthesis of the aerogel, this method reduced the surface tension by chemical modification of hydrophilic gel surface. The functionalized gel can be dried without critical shrinkage due to the elimination of condensation reactions in the interior surface of the pores. For SAwoTMCS-NC and SAwoTMCS-C600, due to the shrinkage of the pores, the pore diameter and pore volume decreased (Zhang et al. 2017). Due to this, the microporosity of the template without TMCS was higher than that of the template containing TMCS. The microporosity values for the aerogels calcined at 450°C and 700°C were 7 % and 6 %, respectively. Moreover, the microporosity of SAwoTMCS-C600 was 17 %, which was same with the uncalcined template. Calcination did not affect the microporosity of the template.

Table 15: Physical properties of SA and SAwoTMCS templates

Template	Multipoint BET Surface Area (m^2/g)	BJH Desorption Pore Volume (cm^3/g)	BJH Desorption Average Pore Diameter (nm)	Microporosity (%)
SA-NC	823.3	3.0	8.5	4
SA-C450	852	3.8	11.7	6
SA-C700	836	3.4	10.4	7
SAwoTMCS-NC	857.6	1.1	3.5	17
SAwoTMCS-C600	844	1.1	3.3	17

For the synthesized silica aerogel templates, the N_2 adsorption/desorption isotherms are shown in Figure 83. Pore size distribution for all the silica aerogel templates are also shown in Figures 84-85. Pure aerogel showed Type IV isotherm with H3 hysteresis loop, which indicated the mesoporous structure of the silica aerogel. Considering the pore size distribution, the pure aerogel contained mesopores and macropores in the structure. With the calcination of pure aerogel at 450°C and 700°C, the isotherm type was preserved but the hysteresis became H1 hysteresis loops. The quantity of the adsorbed volume for the calcined aerogels increased compared to pure one. Looking at the pore size distribution, the calcined aerogels consisted of mainly mesopores. The isotherms of SA-C450 and SA-C700 shifted to the higher relative pressure values compared to that of SA-NC. This proved that the pore size distribution shifted to the higher mesopores.

Moreover, the silica aerogel synthesized without TMCS also showed Type IV isotherm with H3 hysteresis loop. Calcination of the aerogel without TMCS did not affect the isotherm. SAwoTMCS-NC and SAwoTMCS-C600 materials had nearly no macropores by looking at the pore size distribution. This can be the reason of high microporosity compared to SA-NC.

The pore size distribution of SAwoTMCS-NC and SAwoTMCS-C600 shifted to lower pore diameter values compared to SA-NC, SA-C450 and SA-C700. This showed that the pore diameter values of these materials were lower compared to pure and calcined aerogels. This result was in good agreement with the isotherm because the isotherms of SAwoTMCS-NC and SAwoTMCS-C600 shifted to the lower relative pressure values compared to that of SA-NC. This meant that the pore diameters of the SAwoTMCS-NC and SAwoTMCS-C600 materials were lower than that of SA-NC, SA-C450 and SA-C700 values.

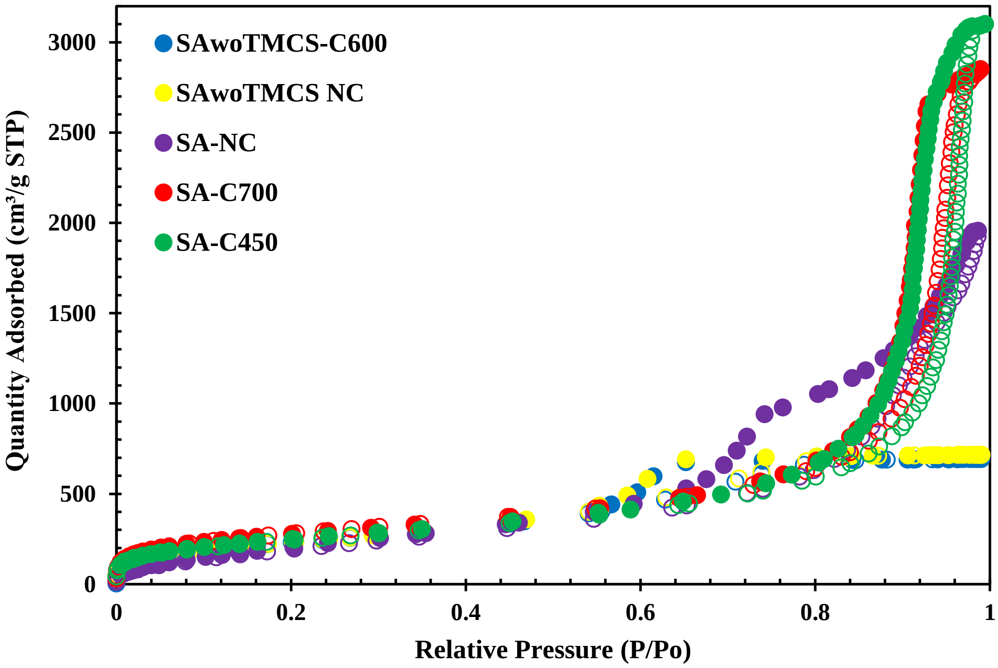

Figure 83: N_2 adsorption/desorption isotherms for the synthesized templates (Filled symbols: Desorption branch, Empty symbols: Adsorption Branch)

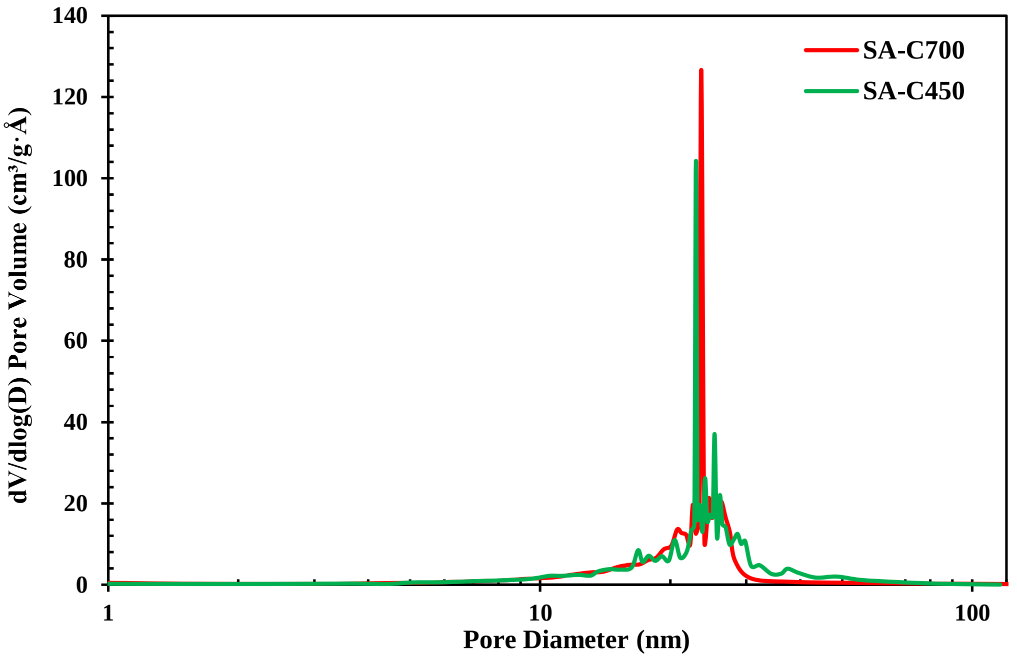

Figure 84: Pore size distributions for the SA-C450 and SA-C700

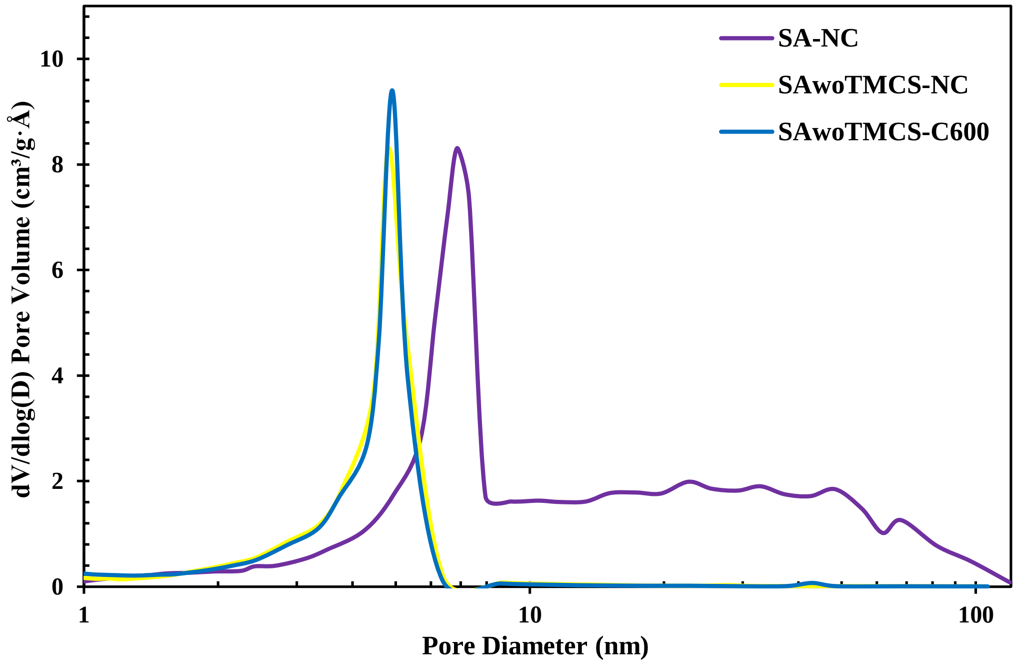

Figure 85: Pore size distributions of SA-NC, SAwoTMCS-NC and SAwoTMCS-C600

6.4.2 Characterization of Silica Aerogel Templated Carbon Materials

6.4.2.1 X-Ray Diffraction Results of Mesoporous Carbon Supports

The XRD patterns of the synthesized mesoporous carbon supports are shown in Figure 86. All MCMT materials showed two broad peaks at 22.4° and 43.5°. These peaks correspond to the (002) and (101) difraction peaks of graphite. The same peaks with CMK type materials were observed for MCMT-type materials (Lei et al. 2008).

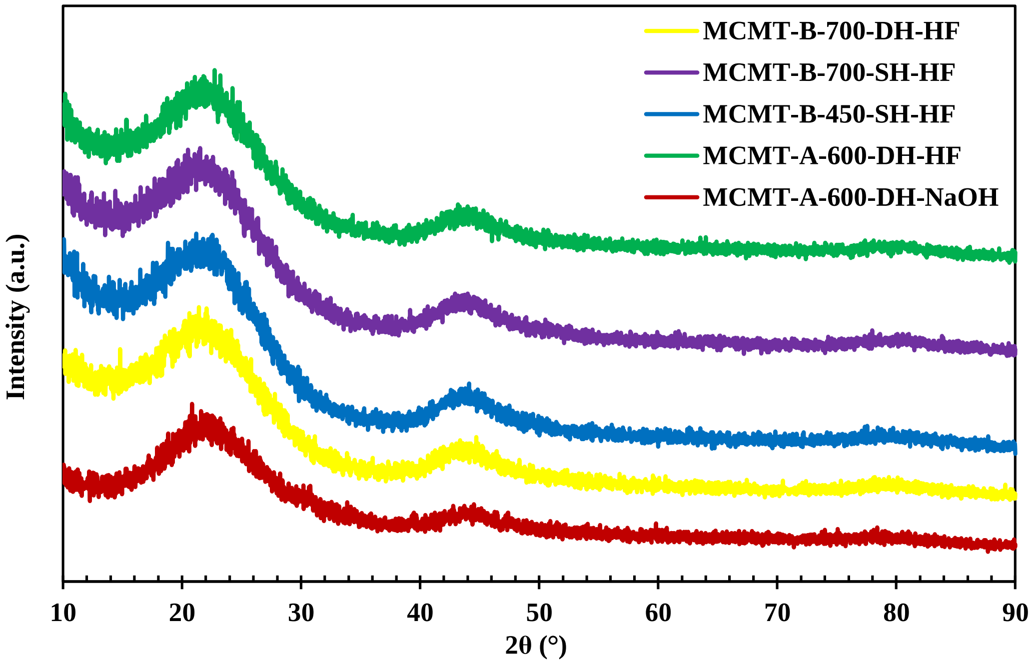

Figure 86: XRD patterns of mesoporous carbon supports

6.4.2.2 RAMAN Results

The Raman spectra for the MCMT-A-600-DH-HF, MCMT-A-600-DH-NaOH and MCMT-B-700-DH-HF materials are shown in Figure 87. The two main raman peaks were observed at 1335 and 1590 cm^{-1}. The first one at 1335 cm^{-1} represents the D band and this peak shows the disordered carbonaceous products and structural defects, on the other hand; the second one at 1590 cm^{-1} shows the G band and this peak generally appears in the Raman spectrum of the graphite. I_D/I_G band intensities are given in Table 16. Same graphitic domain size was achieved for all synthesized carbon materials. The Raman results were in agreement with XRD results.

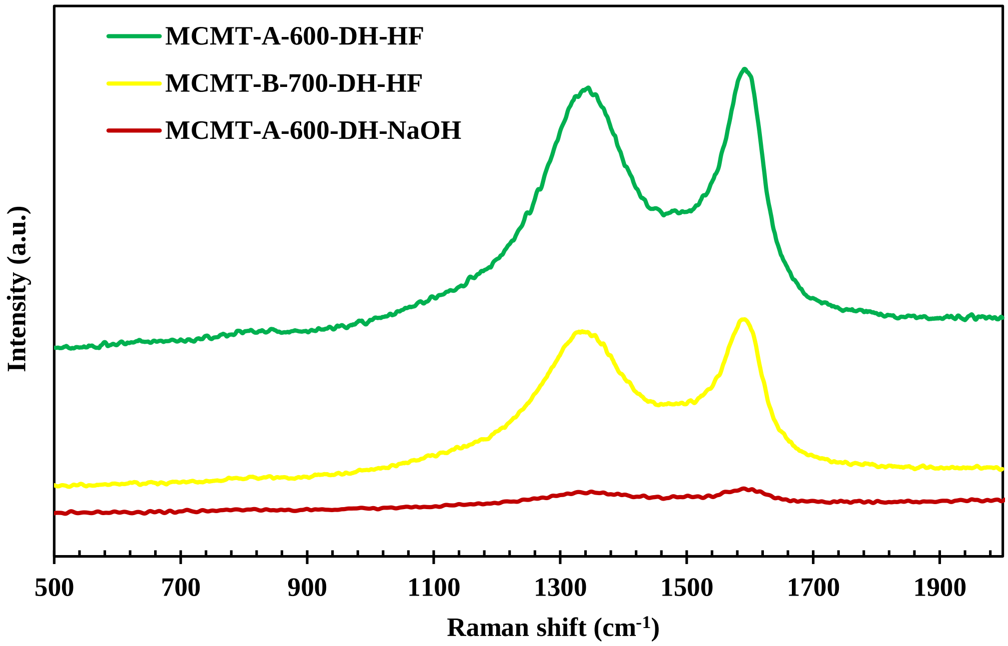

Figure 87: Raman spectra of the synthesized MCMT materials

Table 16: I_D/I_G band intensities obtained from Raman spectra

Carbon species	I_D/ I_G
MCMT-A-600-DH-HF	0.96
MCMT-A-600-DH-NaOH	0.96
MCMT-B-700-DH-HF	0.95

6.4.2.3 N_2 Adsorption/Desorption Isotherms and Physical Properties

The textural properties of the carbon materials synthesized from the aerogel templates are given in Table 17. Results showed that the calcination temperature of the silica aerogels did not affect significantly the surface area and pore diameter of the carbon materials. The carbon materials washed with HF gave higher surface areas compared to the materials washed with NaOH. It was evident that NaOH did not remove all silica in the materials. On the other hand, HF removed the silica template completely, giving the carbon materials with high surface area. When the silica aerogels which did not contain silylating agent were used as a template, the final carbon materials gave high pore volume and pore diameter. This may be due to the high porosity of the silica aerogel materials. The distance between the pores was smaller than pore diameter of the aerogels and this distance between pores was the pores of the produced carbon materials. On the other hand, silica aerogels without TMCS did not have high porosity due to the shrinkage of the pores and this may be the reason of high pore diameter values of the carbon materials.

The microporosity of the MCMT-A type materials was lower than that of the MCMT-B type materials. This result can be also consistent with the pore diameter values. MCMT-A type materials had bigger pore diameter values with low microporosity.

Table 17: Physical properties of silica aerogel templates and synthesized carbon materials

Template	Carbon Samples	BJH Desorption Average Pore Diameter (nm)	BJH Desorption Pore Volume (cm^3/g)	Multipoint BET Surface Area (m^2/g)	Microporosity (%)
SA-C700	MCMT-B-700-DH-NaOH	3	0.5	574	33
	MCMT-B-700-DH-HF	2.82	1.1	1263	34
	MCMT-B-700-SH-HF	2.76	1.09	1262	34
SA-C450	MCMT-B-450-DH-NaOH	2.8	0.37	422	33
	MCMT-B-450-DH-HF	2.81	1.07	1198	32
	MCMT-B-450-SH-HF	2.72	1.06	1253	35
SAwoTMCS-C600	MCMT-A-600-DH-NaOH	3.81	1.14	957	26
	MCMT-A-600-SH-NaOH	3.81	0.85	695	23
	MCMT-A-600-DH-HF	3.75	1.41	1179	25
	MCMT-A-600-SH-HF	3.57	1.34	1195	27

N_2 adsorption/desorption isotherms of MCMT-A and MCMT-B type materials washed with NaOH are given in Figure 88. MCMT-B materials showed Type IV isotherm with H2 hysteresis loop; on the other hand, MCMT-A materials showed Type IV isotherm with H1 hysteresis loop which showed narrow pore size distribution and H2 hysteresis loop which showed wide pore size distribution. The pore size distribution of MCMT-A and MCMT-B type materials washed with NaOH are given in Figure 89. The existence of the two hysteresis loops for MCMT-A materials was also consistent with the pore size distribution. MCMT-A-600-DH-NaOH and MCMT-A-600-SH-NaOH materials had bimodal pore size distributions with two peaks at nearly 3.5 nm and 16.4 nm and at nearly 3.5 nm and 11.4 nm, respectively. For the MCMT-B type materials, narrow pore size distribution was obtained which was consistent with isotherm. MCMT-B-450-DH-NaOH material had narrow pore size distribution with a peak at 3.6 nm. The intensities of the mesopore peaks of MCMT-B materials were lower than that of mesopore peaks for MCMT-A type materials. Moreover, MCMT-A type materials contained mesopores. In addition, double heating process improved the mesopores of the materials. The isotherms and pore size distributions for MCMT-B type materials were consistent with the literature (Lei et al. 2008)

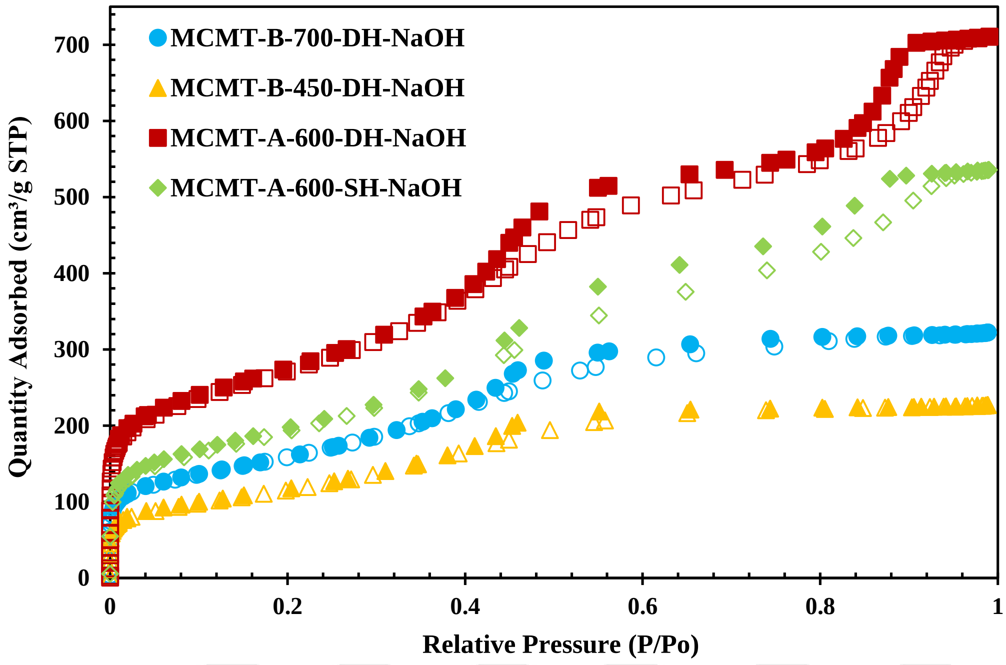

Figure 88: N_2 adsorption/desorption isotherms of the synthesized mesoporous carbons with NaOH treatment (Filled symbols: Desorption branch, Empty symbols: Adsorption Branch)

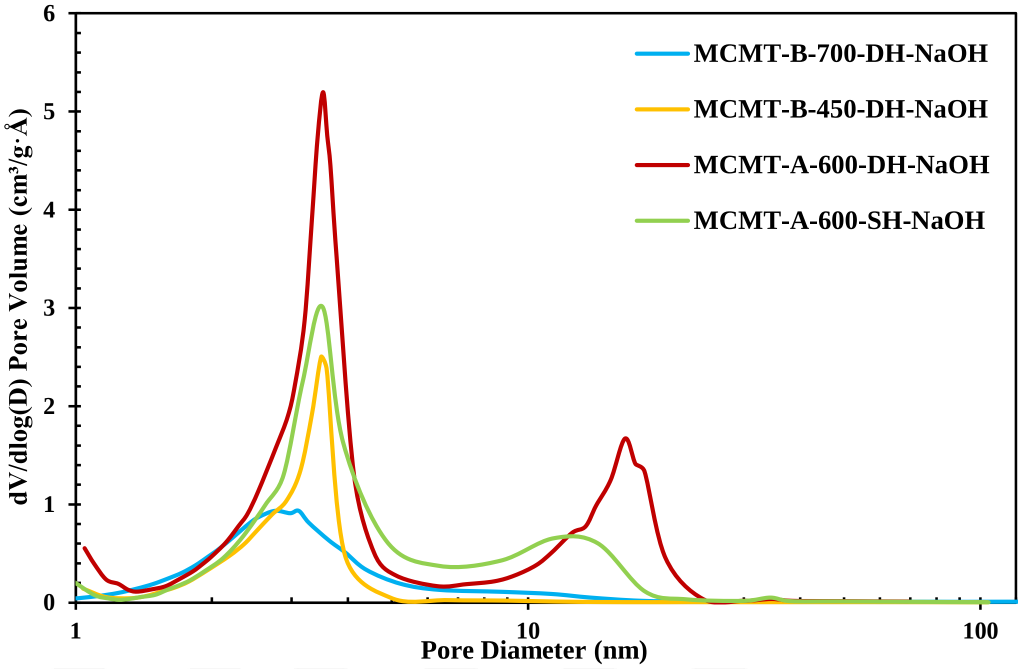

Figure 89: Pore size distributions of the synthesized mesoporous carbons with NaOH treatment

N_2 adsorption/desorption isotherms for MCMT-A and MCMT-B type materials washed with HF are given in Figure 90. MCMT-B materials showed Type IV isotherm with H2 hysteresis loop; on the other hand, MCMT-A materials showed Type IV isotherm with H1 and H2 hysteresis loops. Calcination temperature and heating procedure did not affect the isotherm. The only effect was the change in the silica aerogel support. With the use of the SAwoTMCS-C600 as a template, formation of two different hysteresis loops was observed. The pore size distributions of MCMT-A and MCMT-B type materials washed with HF are given in Figure 91. MCMT-A-600-DH-HF and MCMT-A-600-SH-HF materials had two different types of pores. The existence of the two hysteresis loops was also consistent with the pore size distribution. Calcination temperature and heating procedure did not affect the isotherms and pore size distributions of the synthesized materials. All MCMT-B type materials had narrow pore size distributions with a peak at 3.5 nm. The intensities of peak in mesoporous region were lower with the use of calcined silica aerogels as a template compared to SAwoTMCS-C600 as a template. Microporosity values of the

MCMT-A materials were lower than that of MCMT-A type materials due to the existence of the mesopores in the MCMT-A type materials.

The isotherm and pore size distribution obtained with MCMT-B type materials was consistent with the literature (Wang et al. 2016).

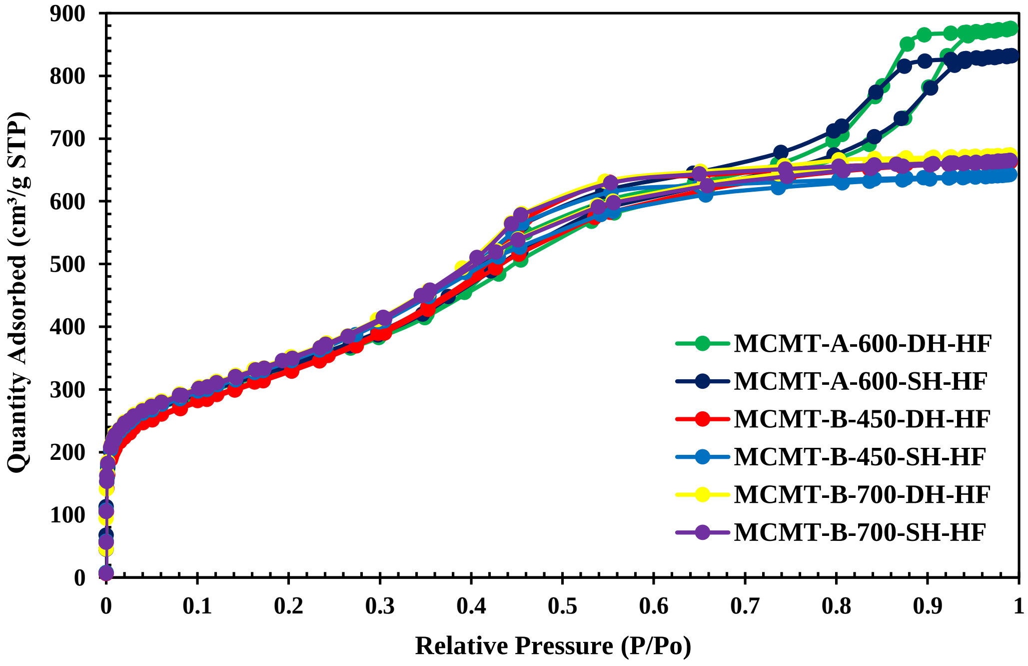

Figure 90: N_2 adsorption/desorption isotherms of the synthesized mesoporous carbons with HF treatment

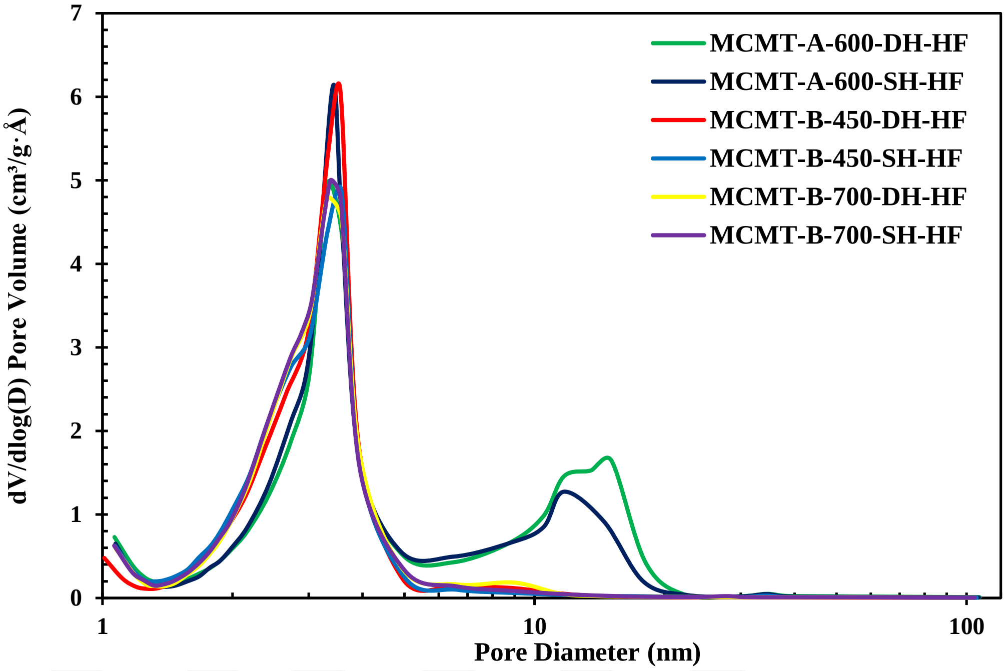

Figure 91: Pore size distributions of the synthesized mesoporous carbons with HF treatment

6.4.2.4 Thermal Gravimetric Analysis (TGA) Results

Thermal gravimetric analysis result for the silica templates under air is given in Figure 92. The first weight loss at a temperature range of 25°C and 100°C was due to the moisture content in the SA-C450 and SAwoTMCS-NC templates. The weight loss at nearly 370°C was due to removal of methyl groups from aerogel.

Thermal gravimetric analysis result for the silica templates under nitrogen is given in Figure 93. The weight loss between 25°C and 100°C was due to the moisture content in the SA-C450, SA-C700 and SAwoTMCS-NC templates. The weight loss at a temperature range of 370°C and 760°C was due to the breaking of C-H and Si-C bonds and removal of methyl group from the structure of the aerogel. SAwoTMCS-C600, SA-C450 and SA-C700 materials were thermally stable.

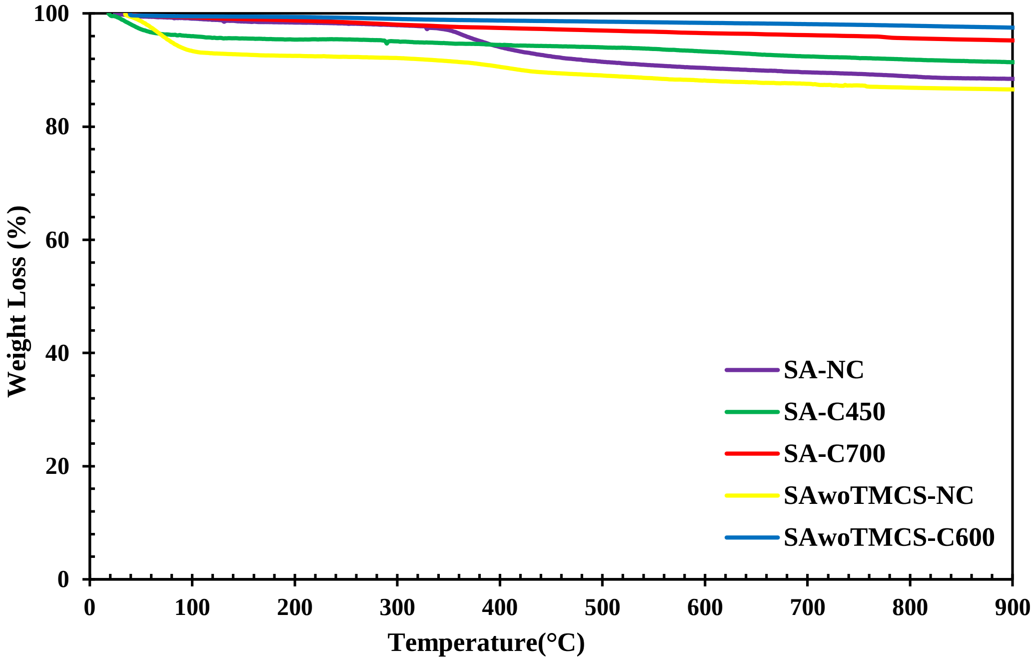

Figure 92: TGA graph of the synthesized silica aerogel templates under air flow

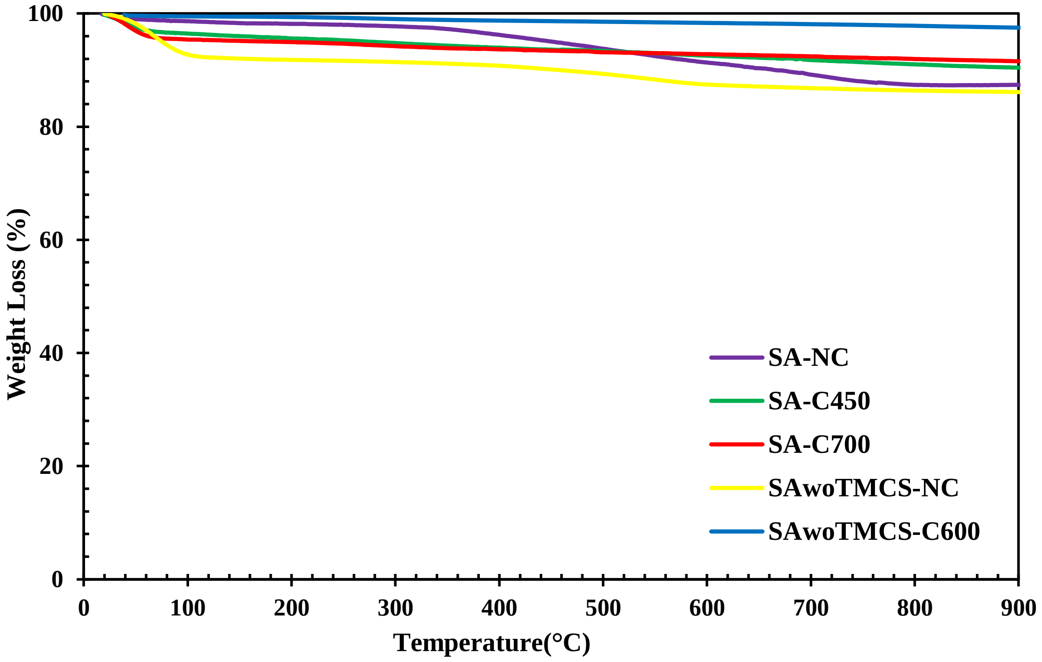

Figure 93: TGA graph of the synthesized silica templates under nitrogen flow

Thermal gravimetric analysis results for the MCMT type materials under air and nitrogen were given in Figures 94-95. The first weight loss at a temperature range of 25°C and 100°C was due to the moisture content. Thermal stability and thermal decomposition temperature of the MCMT-A-600-DH-NaOH material was lower compared to other materials. It can be said that all silica template was totally removed except for the MCMT-A-600-SH-HF material. There was 10 % silica remaining in this material. These results were consistent with the physical properties of the materials.

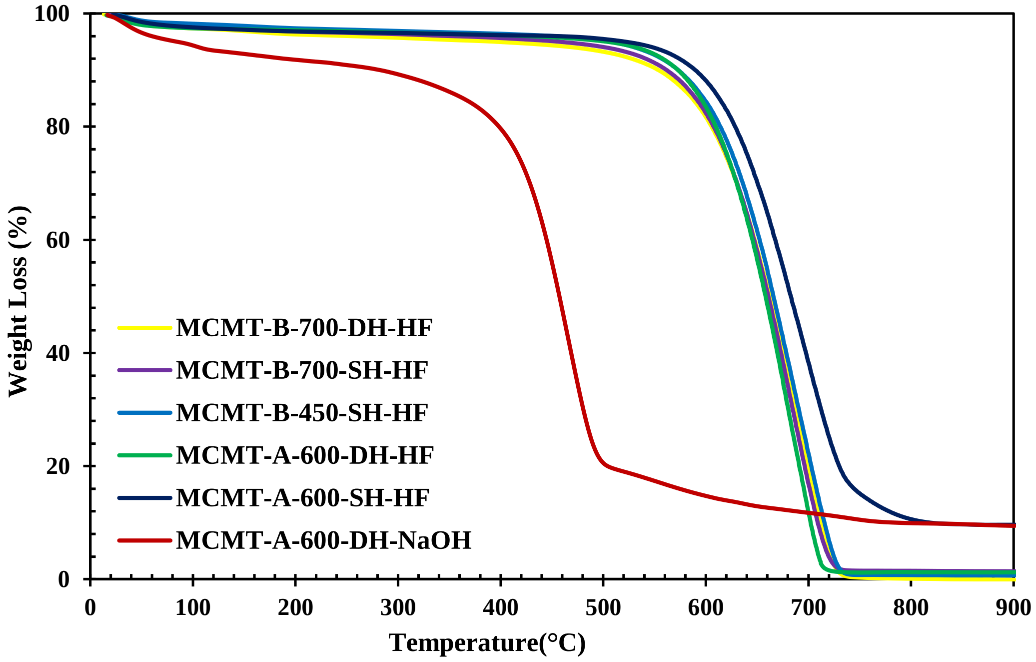

Figure 94: TGA graph of MCMT materials under air flow

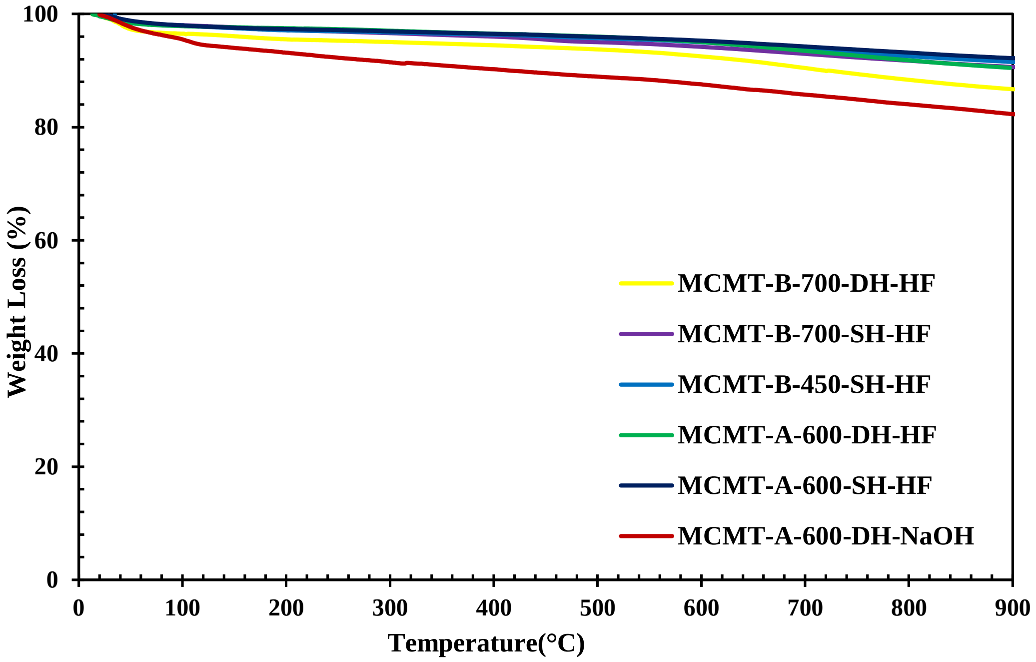

Figure 95: TGA graph of MCMT materials under nitrogen flow

6.4.2.5 Scanning Electron Microscopy (SEM) Results

SEM images for the MCMT-A-600-DH-NaOH material at different magnifications are presented in Figures 96-97. The formation of the pores at different sizes can be easily seen from the SEM images. The morphology of the MCMT-A-600-DH-NaOH was very similar with the silica aerogel. Unremoved NaOH which was represented in red frames in the form of fiber can be observed in SEM images (Figure 97). When EDX analysis can be performed for the overall view of the material (Figure 98), MCMT-A-600-DH-NaOH material consisted of nearly 93% C, 5 % O, 1.5 % Na and 0.5 % Si. However, the EDX result for Figure 96c, this material contained 81% C, 5.5 % O, 3 % Na and 10.5 % Si. These results showed that there was a nonhomogeneous distribution of carbon in the material. Unremoved silica template in the catalyst decreased the surface area and pore diameter of the supports. This result was consistent with the BET results.

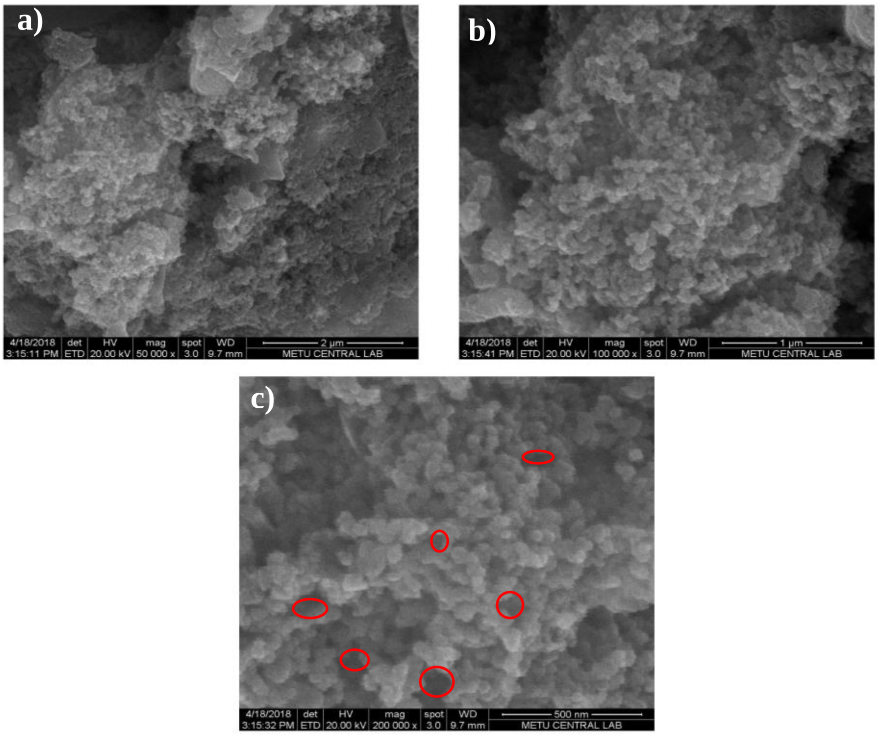

Figure 96: SEM images of MCMT-A-600-DH-NaOH at different magnifications: a) 50000X, b) 100000X, and c) 200000X

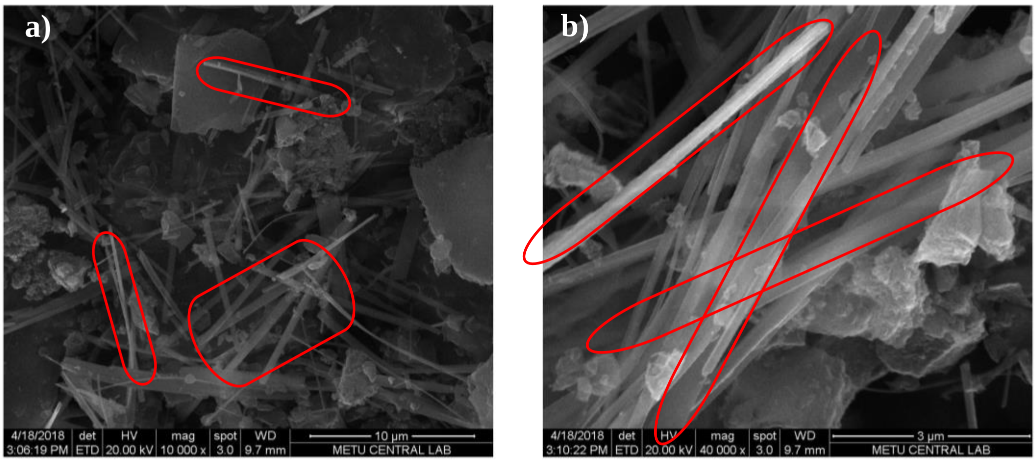

Figure 97: SEM images of MCMT-A-600-DH-NaOH at different magnifications: a) 10000X and b) 40000X

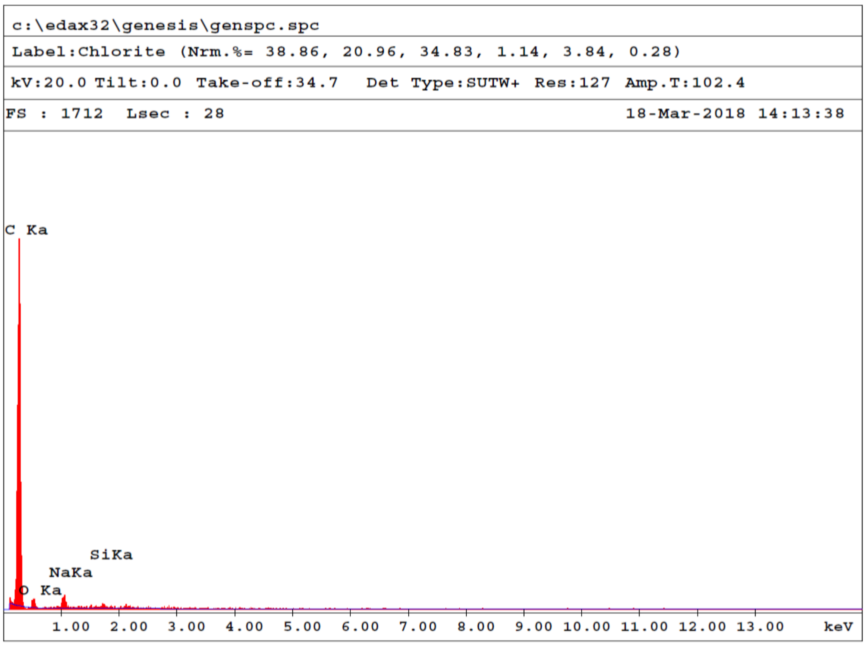

Figure 98: EDX spectrum of MCMT-A-600-DH-NaOH

SEM images for MCMT-A-600-DH-HF are shown in Figures 99-100. The EDX result for the Figure 100b is given in Figure 101. There was not any unremoved HF in the catalyst according to EDX spectrum. The material contained only 100 % carbon. The formation of pores at different sizes can be easily observed from the SEM images. The sponge structure was obtained in the MCMT-A-600-DH-HF material. Considering Figure 99, the morphology was similar to the silica aerogel structure. The porous material was obtained.

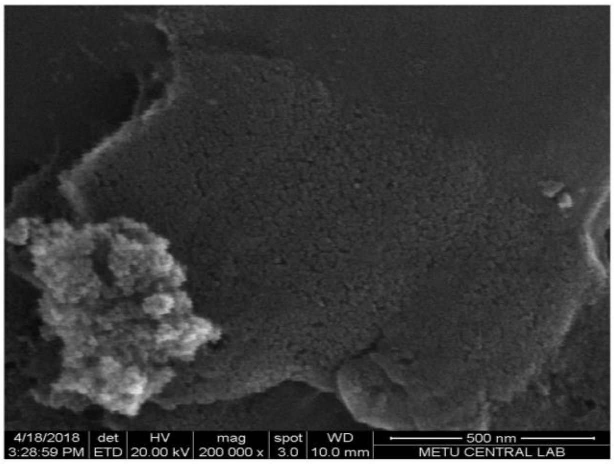

Figure 99: SEM image of MCMT-A-600-DH-HF at 200000X magnification

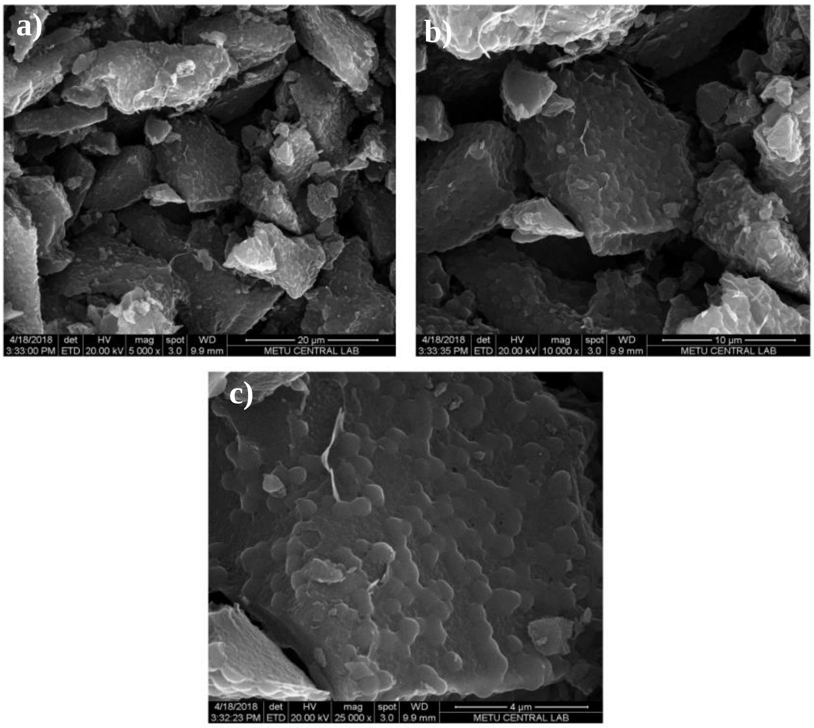

Figure 100: SEM images of MCMT-A-600-DH-HF at different magnifications: a) 5000X, b) 10000X, and c) 25000X

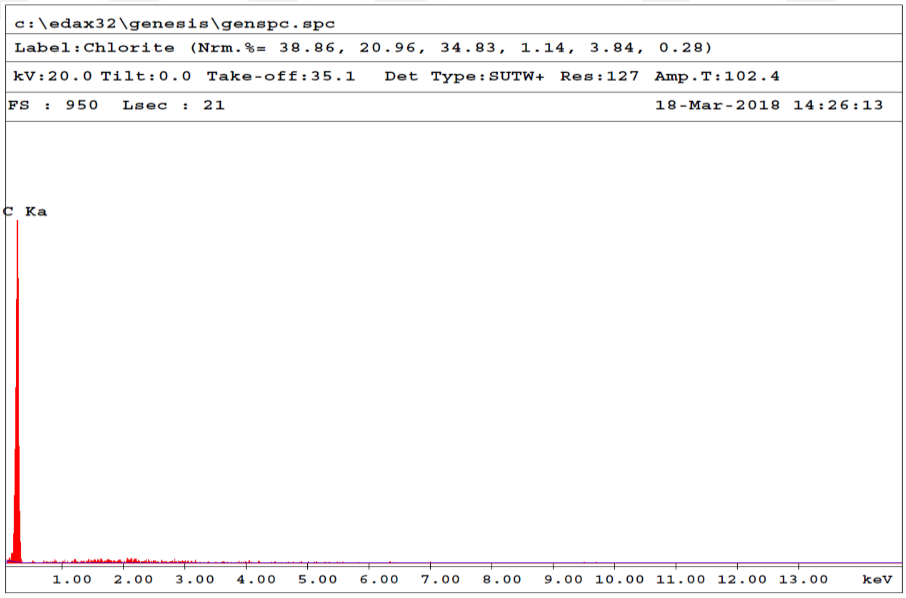

```
c:\edax32\genesis\genspc.spc
Label:Chlorite  (Nrm.%= 38.86, 20.96, 34.83, 1.14, 3.84, 0.28)
kV:20.0 Tilt:0.0  Take-off:35.1   Det  Type:SUTW+  Res:127  Amp.T:102.4
FS  :  950   Lsec  :  21                               18-Mar-2018 14:26:13
```

Figure 101: EDX spectrum of MCMT-A-600-DH-HF

SEM images for MCMT-B-450-DH-HF and MCMT-B-700-DH-HF are shown in Figure 102, and Figures 104-105, respectively. The EDX result for the Figure 102a is given in Figure 103. The EDX result for the Figure 104a is given in Figure 106. There was not any unremoved HF in the MCMT-B-450-DH-HF material according to EDX spectrum. Two different structures were obtained for this material. The first structure of the MCMT-B-450-DH-HF material was similar to the porous structure of the silica aerogel. The second structure resembled sponge structure. However, some unremoved silica template was observed for MCMT-B-700-DH-HF material. The formation of pores at different sizes can be easily observed from the SEM images.

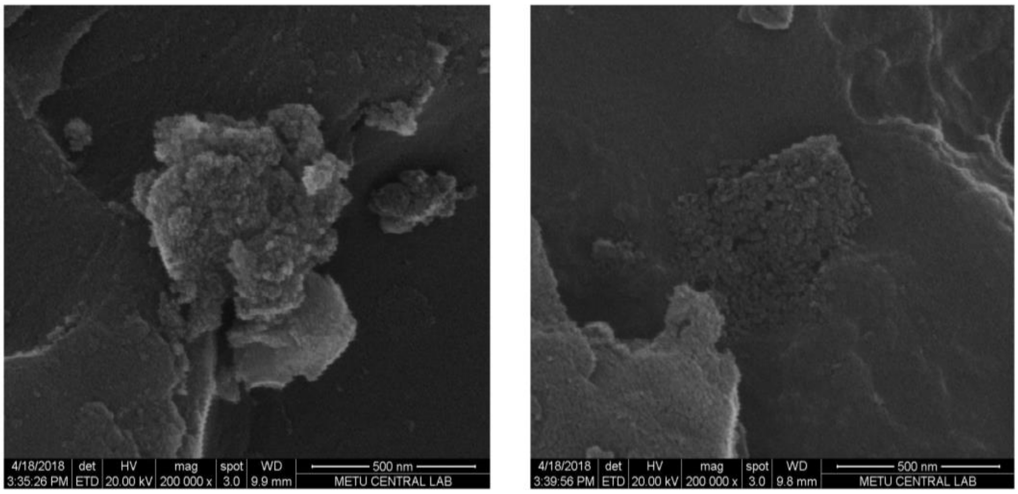

Figure 102: SEM images of MCMT-B-450-DH-HF at 200000X magnification

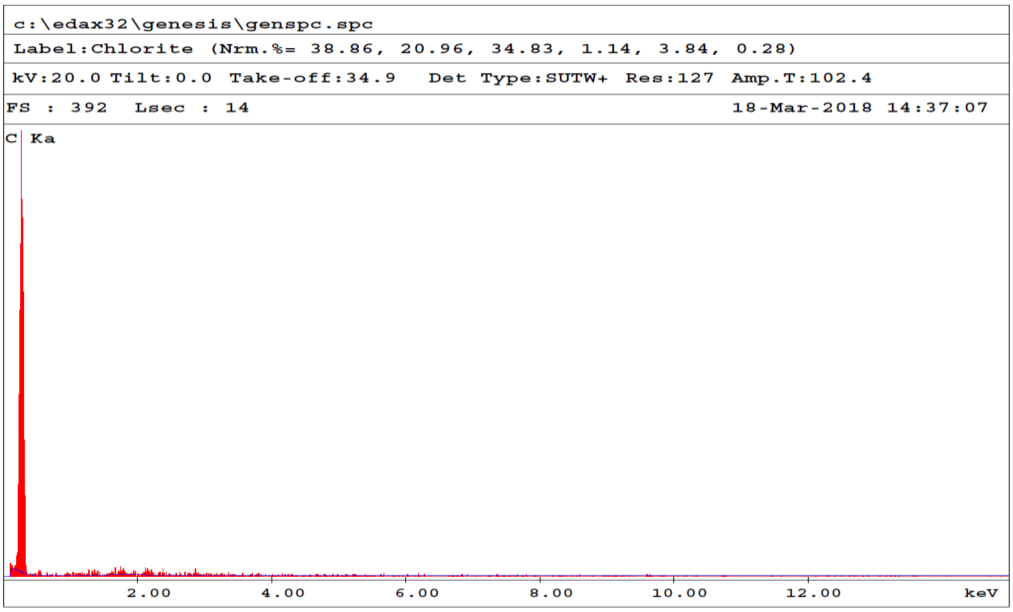

```
c:\edax32\genesis\genspc.spc
Label:Chlorite (Nrm.%= 38.86, 20.96, 34.83, 1.14, 3.84, 0.28)
kV:20.0 Tilt:0.0 Take-off:34.9  Det Type:SUTW+ Res:127 Amp.T:102.4
FS : 392  Lsec : 14                                18-Mar-2018 14:37:07
```

Figure 103: EDX spectrum of MCMT-B-450-DH-HF

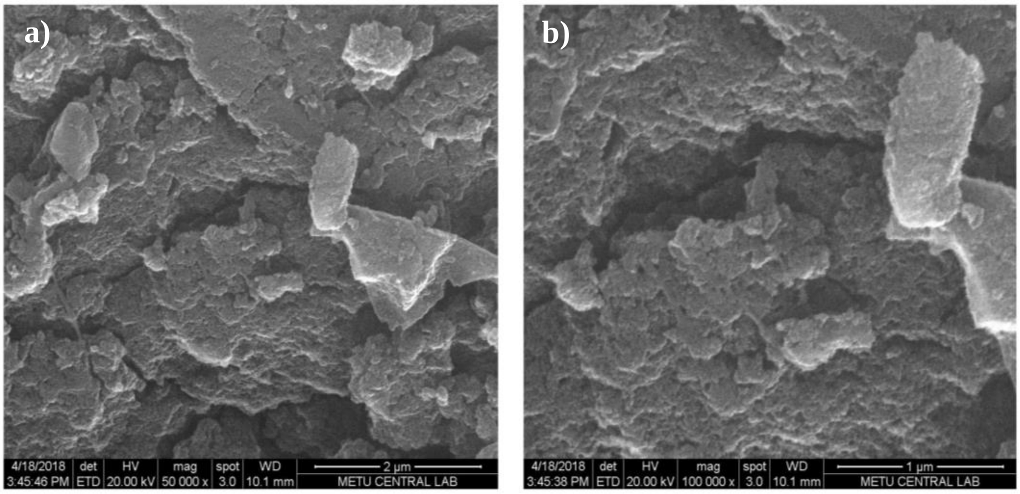

Figure 104: SEM images of MCMT-B-700-DH-HF at different magnifications: a) 50000X and b) 100000X

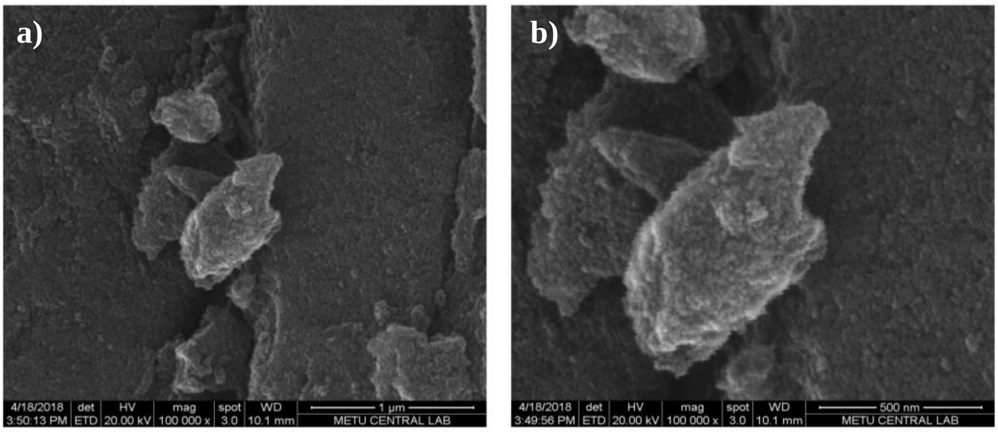

Figure 105: SEM images of MCMT-B-700-DH-HF at different magnifications: a) 100000X and b) 200000X

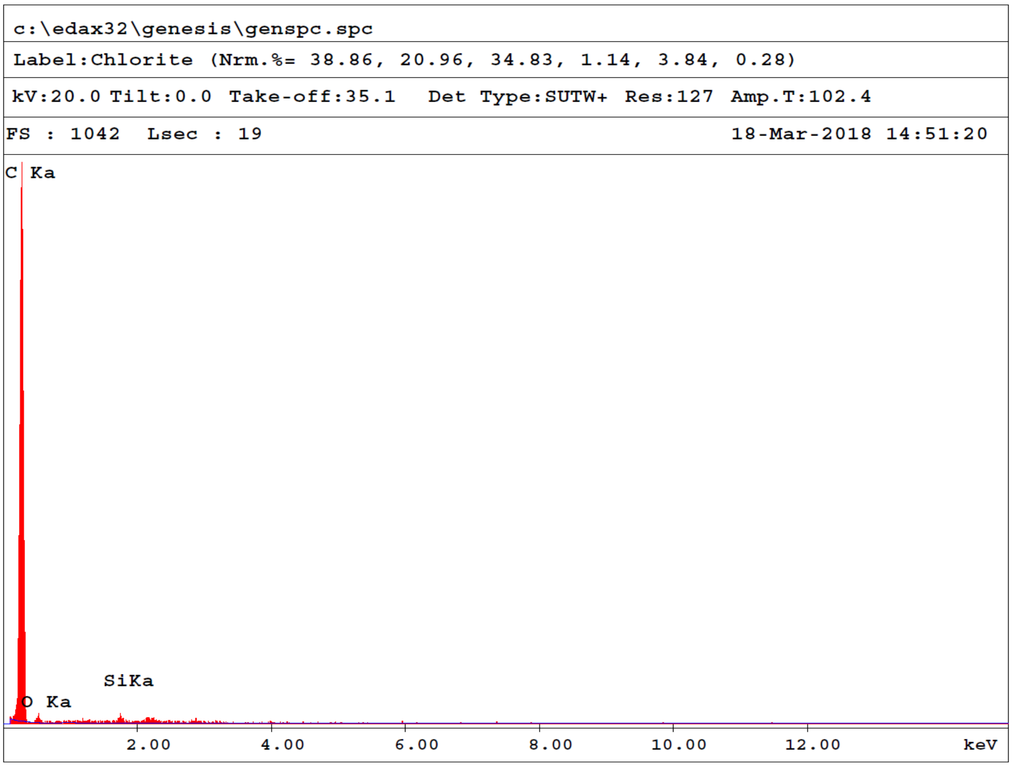

Figure 106: EDX spectrum of MCMT-B-700-DH-HF

6.4.3 Characterization of Nickel Impregnated MCMT Type Catalysts

The best catalyst support considering the pore diameter and volume and surface area was MCMT-A-600-DH-HF and MCMT-A-600-DH-NaOH. Therefore, nickel was impregnated to these catalyst supports and these catalysts were tested in the SRE and SESRE reactions.

6.4.3.1 X-Ray Diffraction Results

XRD patterns of nickel impregnated MCMT catalysts are shown in Figure 107. A broad diffraction peak at 22.5° was assigned to amorphous carbon. After impregnation of nickel to the catalyst support, the intensity of carbon peaks decreased due to incorporation of nickel to the catalyst support. It was evident that the catalyst preserved the carbon structure after nickel impregnation. For 10Ni-MCMT-A-600-DH-HF, the peaks at 2θ values of 44, 52 and 76° showed the presence of metallic nickel (JPDC-01-071-4653 given in Appendix B). On the other hand, for 10Ni-MCMT-A-600-DH-NaOH, some unreduced NiO peaks (JPDC-01-071-1179 given in

Appendix B) appeared in the XRD pattern in addition to metallic nickel. Nickel crystallite size was calculated and tabulated in Table 18. Higher crystallite sizes were obtained for both catalysts.

Table 18: Crystallite size of the nickel loaded MCMT supported catalysts

Catalyst	2θ (°)	$t_{Ni,crystallite\ size}$ (nm)
10Ni-MCMT-A-600-DH-NaOH	44.42	40.41
10Ni-MCMT-A-600-DH-HF	44.36	35.65

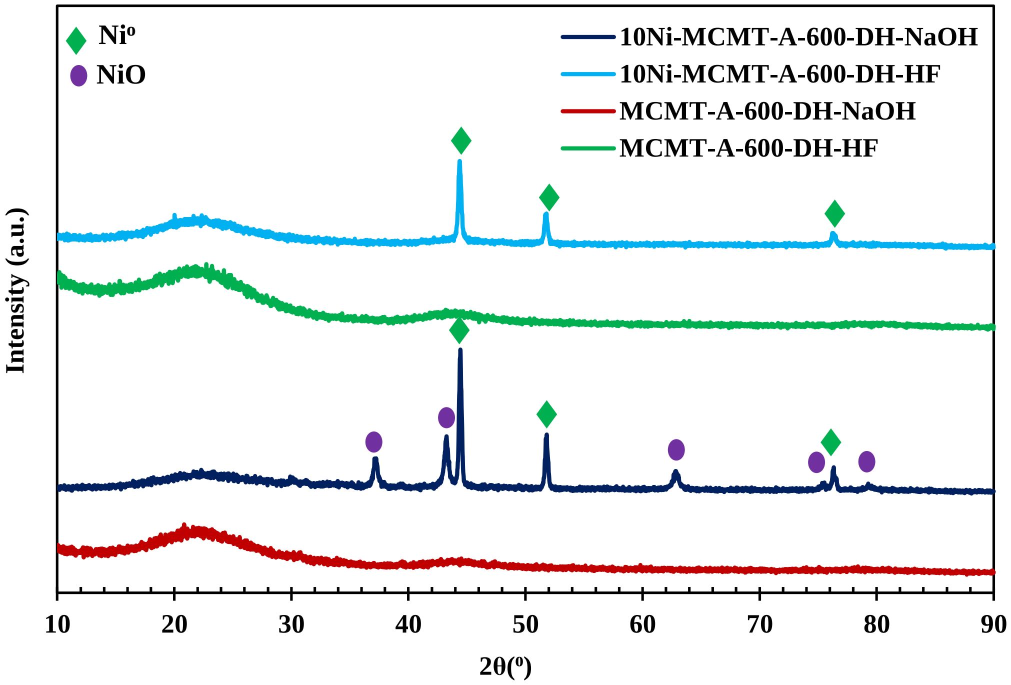

Figure 107: XRD patterns of 10Ni-MCMT-A-DH-NaOH and 10Ni-MCMT-A-DH-HF

6.4.3.2 N_2 Adsorption/Desorption Isotherms and Physical Properties of the Materials

The physical properties of the MCMT supported catalysts are shown in Table 19. After nickel impregnation, surface area and pore volume of the catalysts decreased as expected. Moreover, pore diameters of the both catalysts increased compared to the that of supports.

Table 19: The physical properties of MCMT type catalysts

Catalyst	Multipoint BET Surface Area (m^2/g)	BJH Desorption Pore Volume (cm^3/g)	BJH Desorption Average Pore Diameter (nm)	Microporosity (%)
MCMT-A-600-DH-NaOH	957	1.14	3.81	26
10Ni-MCMT-A-600-DH-NaOH	274	0.55	6.44	25
MCMT-A-600-DH-HF	1195	1.34	3.57	27
10Ni-MCMT-A-600-DH-HF	820	0.99	3.87	27

Nitrogen adsorption/desorption isotherms of MCMT supports and MCMT supported catalysts are given in Figures 108-109. 10Ni-MCMT-A-600-DH-NaOH showed Type IV isotherm with H3 hysteresis loop, 10Ni-MCMT-A-600-DH-HF indicated Type IV isotherm with H2 hysteresis loop which showed wide pore size distribution of non-uniform size and H3 hysteresis loop.

Pore size distributions of MCMT supports and MCMT supported catalysts are given in Figures 110-111. For 10Ni-MCMT-A-600-DH-NaOH catalyst, due to the location of nickel particles to the mesopores, the pore size distribution shifted to the macropore region. For 10Ni-MCMT-A-600-DH-HF catalyst, the location of nickel particles were mainly mesopores of the catalyst.

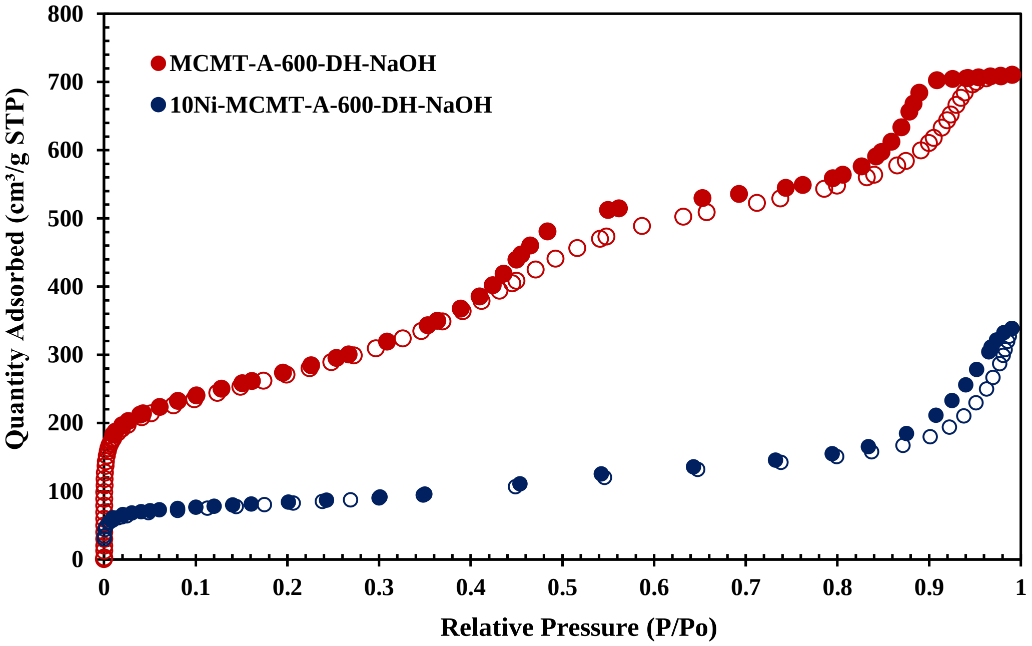

Figure 108: N_2 adsorption/desorption isotherms of the MCMT-A-600-DH-NaOH support and 10Ni-MCMT-A-600-DH-NaOH catalyst (Filled symbols: Desorption branch, Empty symbols: Adsorption Branch)

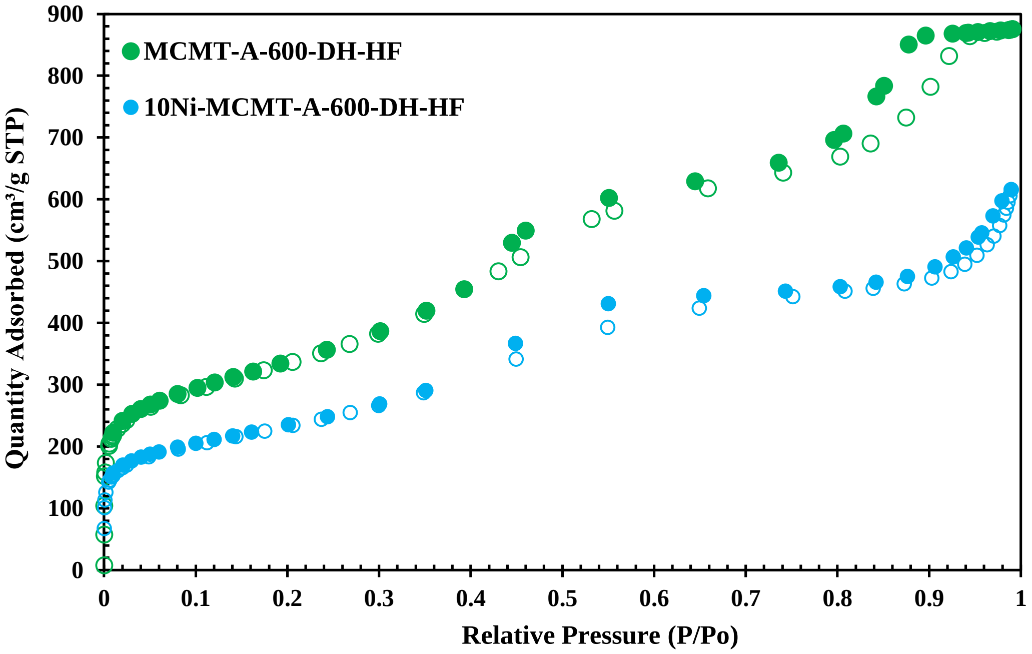

Figure 109: N_2 adsorption/desorption isotherms of the MCMT-A-600-DH-HF support and 10Ni-MCMT-A-600-DH-HF catalyst (Filled symbols: Desorption branch, Empty symbols: Adsorption Branch)

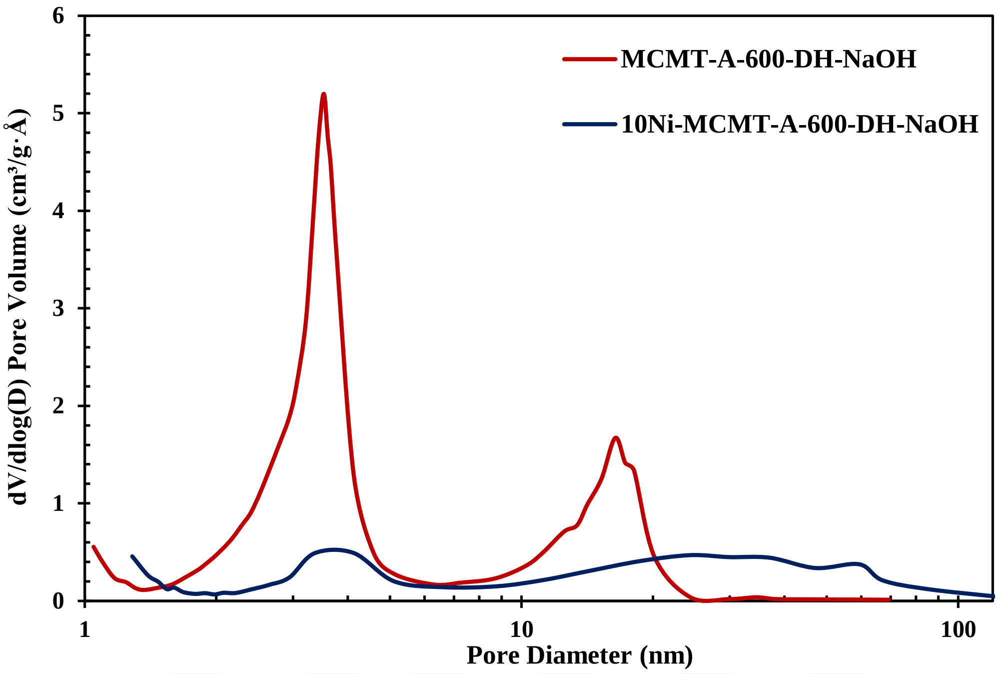

Figure 110: Pore size distributions of the MCMT-A-600-DH-NaOH support and 10Ni-MCMT-A-600-DH-NaOH catalyst

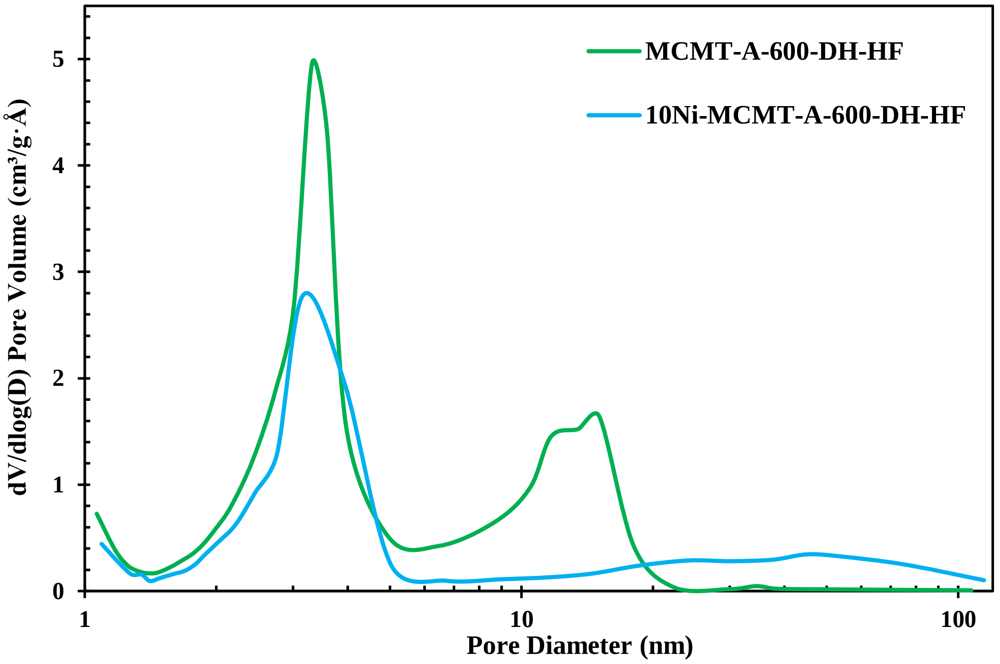

Figure 111: Pore size distributions of the MCMT-A-600-DH-HF support and 10Ni-MCMT-A-600-DH-HF catalyst

6.4.3.3 Temperature Programmed Ammonia Desorption (NH_3-TPD) Results

NH_3-TPD results of the MCMT supported catalysts are shown in Figure 112. Total acid capacity of the catalysts are tabulated in Table 20. Four peaks at 160°C, 330°C, 410°C and 510°C were observed for the 10Ni-MCMT-A-600-DH-NaOH catalyst; on the other hand, three peaks at 300°C, 390°C and 450°C were seen for the 10Ni-MCMT-A-600-DH-HF catalyst. The peak at 160°C was disappeared for the 10Ni-MCMT-A-600-DH-HF catalyst. The shift between the peak locations can be due to the location of the thermocouple. Acidity of the 10Ni-MCMT-A-600-DH-NaOH catalyst was higher than that of the 10Ni-MCMT-A-600-DH-HF catalyst in spite of the highly acidic synthesis route of the 10Ni-MCMT-A-600-DH-HF catalyst. This higher acidity may be due to the presence of silica in the 10Ni-MCMT-A-600-DH-HF.

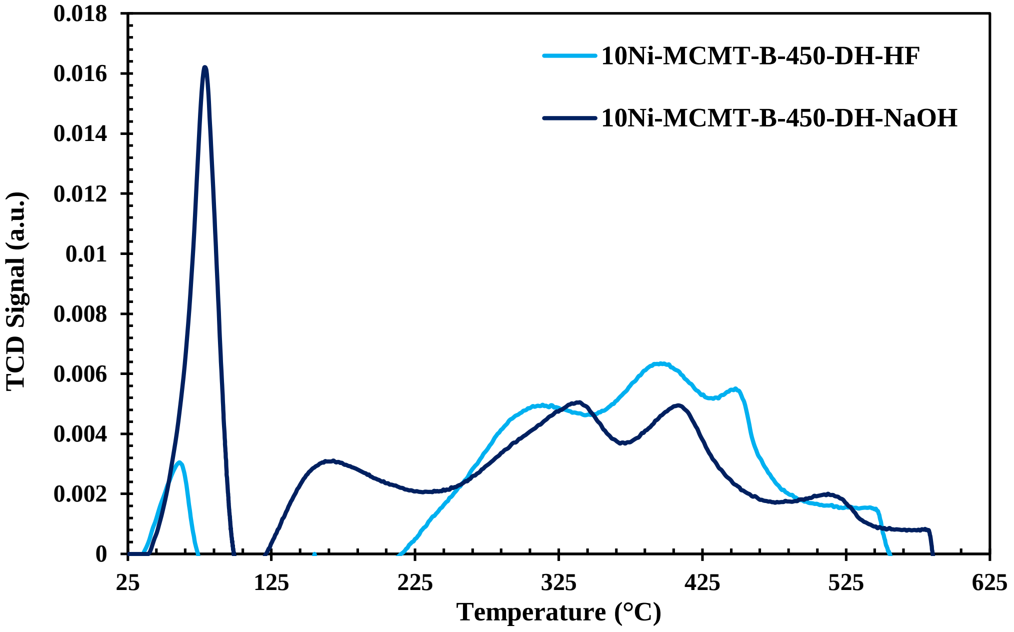

Figure 112: NH_3-TPD graphs of the Ni loaded MCMT catalysts

Table 20: Acid capacities of the Ni loaded catalysts

Catalyst	Total acid capacity (mmol/g)
10Ni-MCMT-A-600-DH-NaOH	0.30
10Ni-MCMT-A-600-DH-HF	0.19

6.4.4 Activity Results of the Synthesized Mesoporous Carbon Supported Catalysts

Product distribution for the 10Ni-MCMT-A-600-DH-HF catalyst is given in Figure 113. The average product distribution was 55.5 % H_2, 27.8 % CO, 14.7 % CH_4 and 2 % CO_2. The percentage of the hydrogen yield was 42 %. Complete conversion was achieved for the SRE reaction. The product distribution was not stable throughout the experiment. In the first 100 min, the mole percentage of the hydrogen decreased and then it increased. The carbon dioxide amount was nearly 2 %, indicating that the steam reforming reaction was not dominant for this catalyst. This may be due to the low acidity of the synthesized material considering TPD analysis. Due to ethanol decomposition reaction, the mole percentages of carbon monoxide and methane was high.

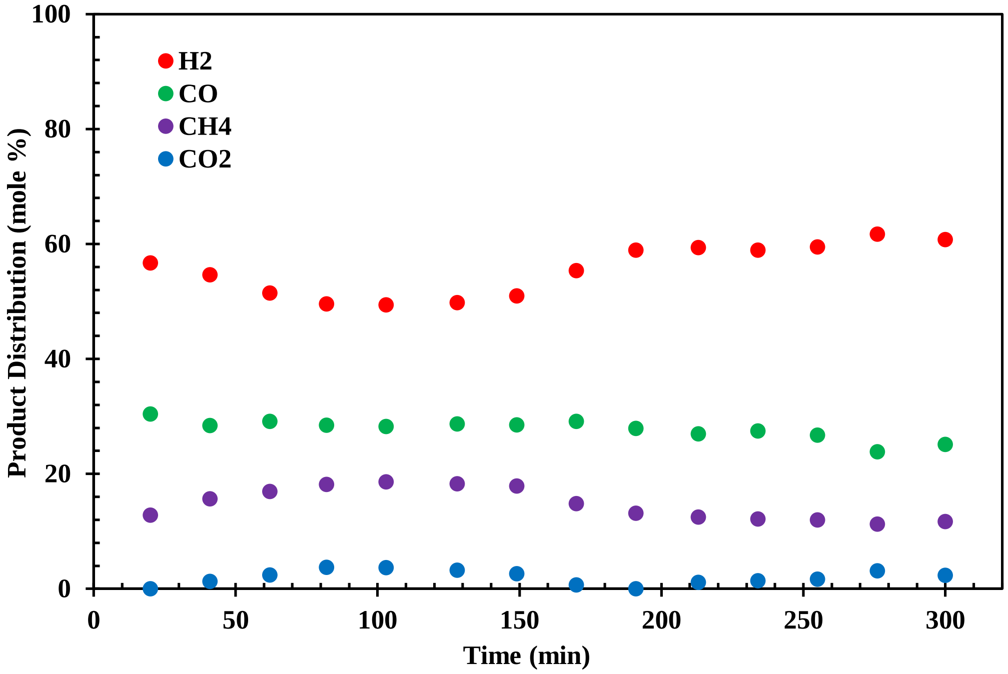

Figure 113: Product distribution at 600°C for the SRE reaction (Catalyst: 10Ni-MCMT-A-600-DH-HF)

The product distribution for the 10Ni-MCMT-A-600-DH-NaOH catalyst is given in Figure 114. Very stable product distribution was achieved with this catalyst. Hydrogen yield percentage was 65 % for this catalyst. The average product distribution was 66

% H_2, 15.7 % CO, 8.6 % CH_4 and 9.8 % CO_2. Compared to 10Ni-MCMT-A-600-DH-HF catalyst, significant hydrogen yield enhancement was achieved with this catalyst. Actually, the surface area of 10Ni-MCMT-A-600-DH-NaOH was lower than that of 10Ni-MCMT-A-600-DH-HF. However, the acidity of 10Ni-MCMT-A-600-DH-NaOH catalyst and its pore diameter were higher than that of 10Ni-MCMT-A-600-DH-HF catalyst. Acidity and higher pore diameter can be reason of the difference in hydrogen yield. Moreover, there was some unremoved silica template in the 10Ni-MCMT-A-600-DH-NaOH catalyst. The high activity compared to 10Ni-MCMT-A-600-DH-HF catalyst may be due to the presence of silica. Moreover, the presence of NaOH fiber rods in the catalyst may favor the steam reforming of ethanol reaction. Low hydrogen mole fraction in the 20th min was due to the presence of NiO particles in the catalyst, NiO was reduced with the produced hydrogen to metallic nickel so hydrogen was used in the 20th min.

The product distributions for the 10Ni-MCMT-A-600-DH-NaOH catalyst in the SESRE-M and SESRE-3O concepts are given in Figures 115-116. The comparison graph for this catalyst is shown in Figure 117. Mixed and ordered concepts gave nearly same product distribution for this catalyst. The mole percentage of the hydrogen increased from 66 % to 74 % in both SESRE experiments in the first 180 min with the capture of carbon dioxide. High methane mole percentage in the first 180 min may be due to the reverse dry reforming of methane reaction. After this period, with an increase in carbon dioxide amount, the importance of this reaction disappeared.

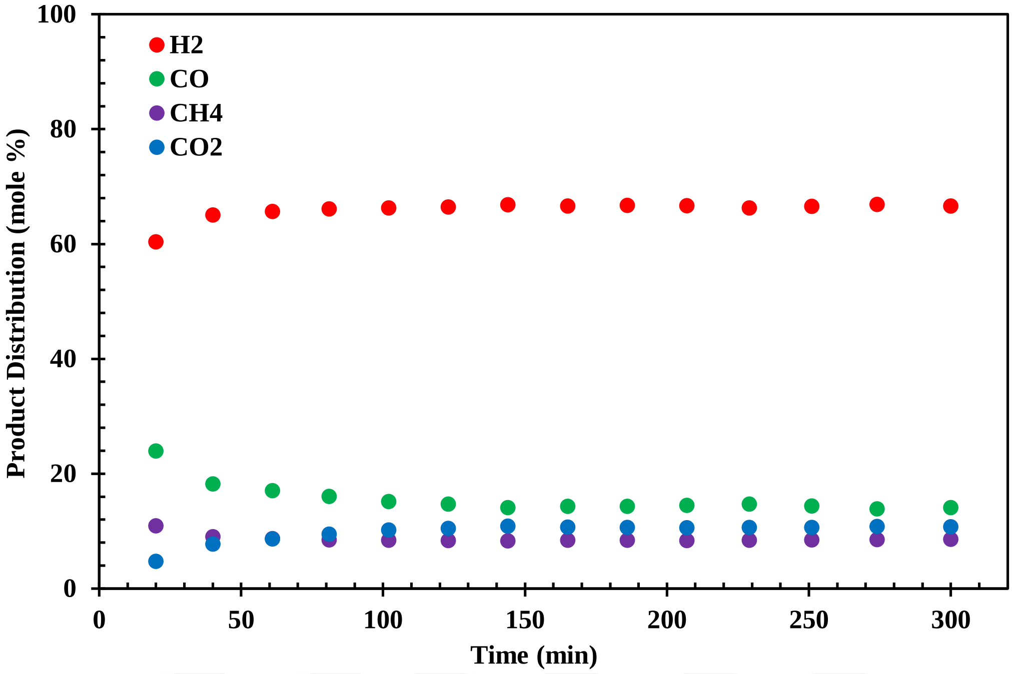

Figure 114: Product distribution at 600°C for the SRE reaction (Catalyst: 10Ni-MCMT-A-600-DH-NaOH)

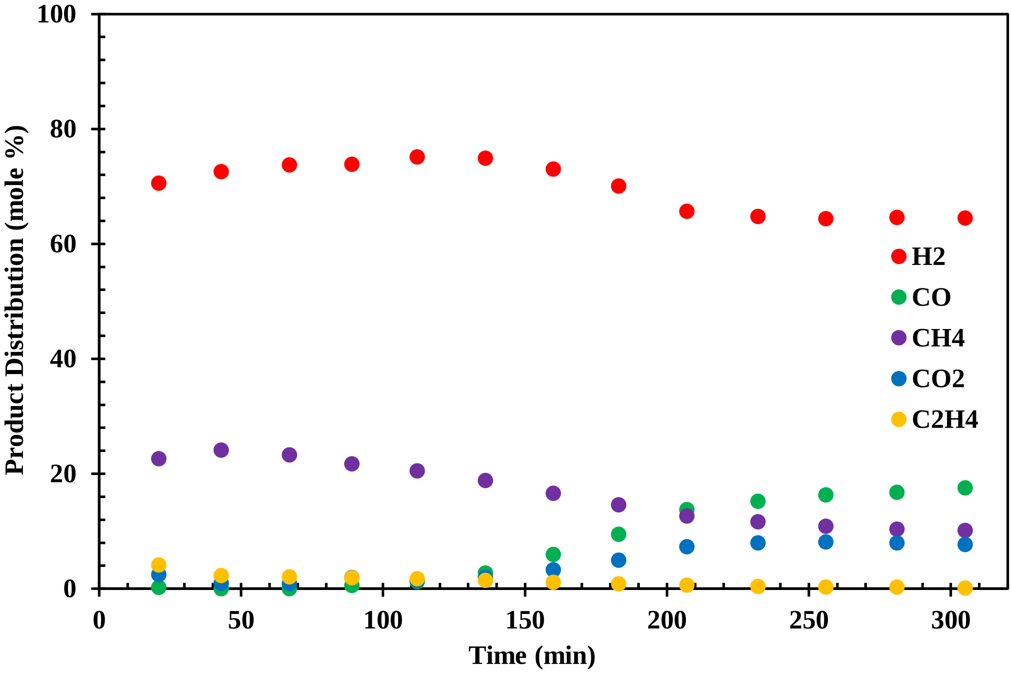

Figure 115: Product distribution with the SESRE-M configuration at 600°C (Catalyst: 10Ni-MCMT-A-600-DH-NaOH)

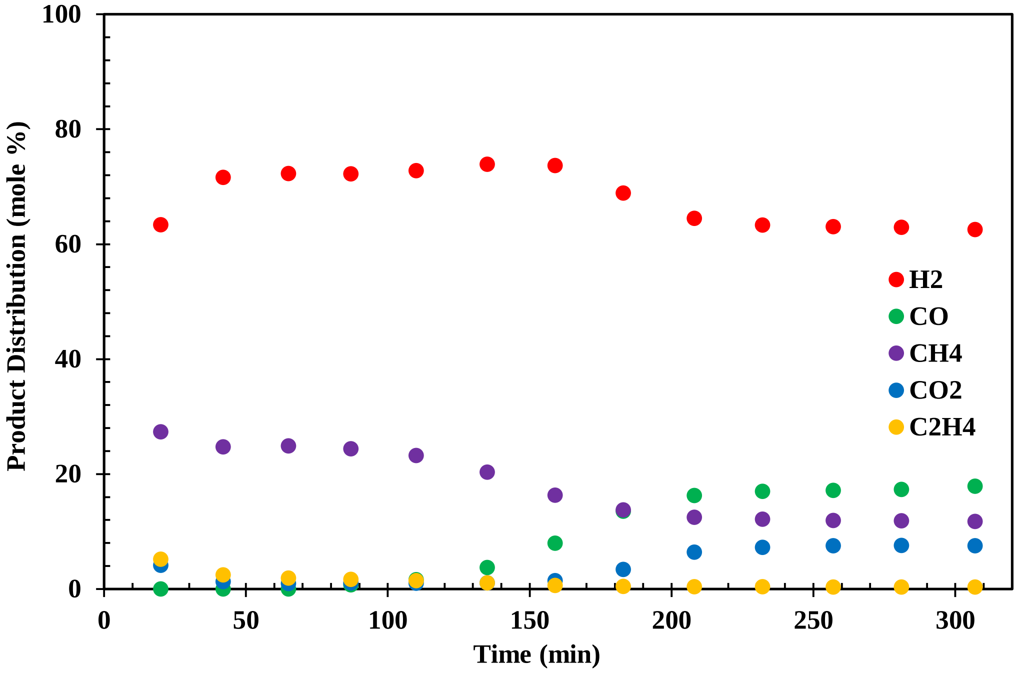

Figure 116: Product distribution with the SESRE-3O configuration at 600°C (Catalyst: 10Ni-MCMT-A-600-DH-NaOH)

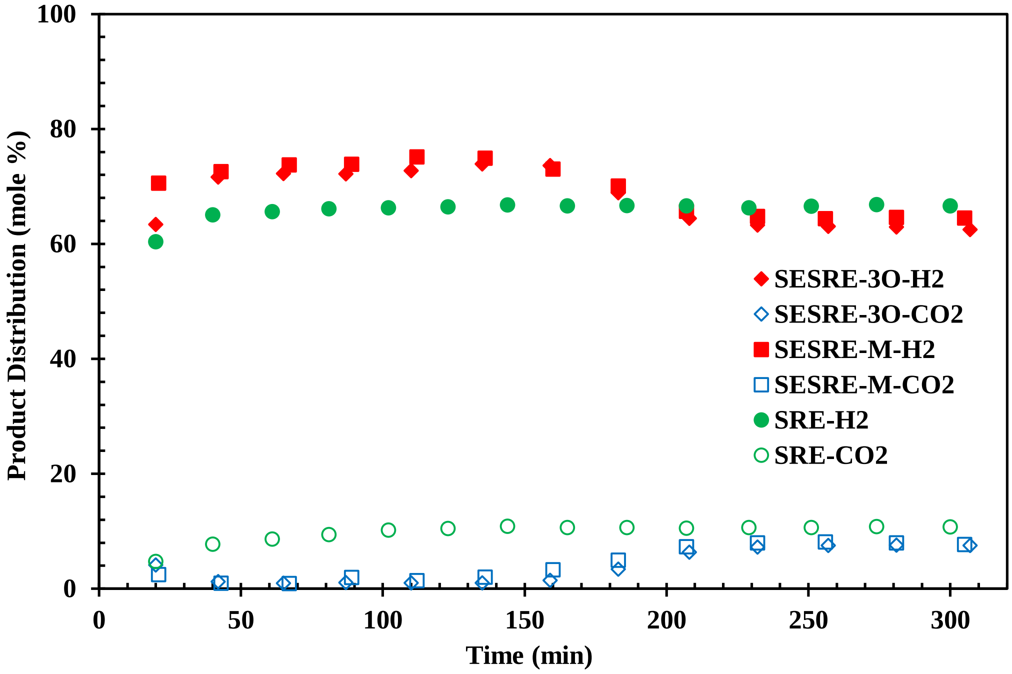

Figure 117: Comparison of mole percentages of H_2 and CO_2 for the SRE and the SESRE reactions at 600°C (Catalyst: 10Ni-MCMT-A-600-DH-NaOH)

6.5 Comparison of the Synthesized Catalysts

The average mole percentages of products for the SRE experiments at 600°C are given in Figure 118. The 10Ni-SBA-15, 10Ni-MC, and 10Ni-SA catalysts gave nearly same product distributions towards the SRE reaction environment.

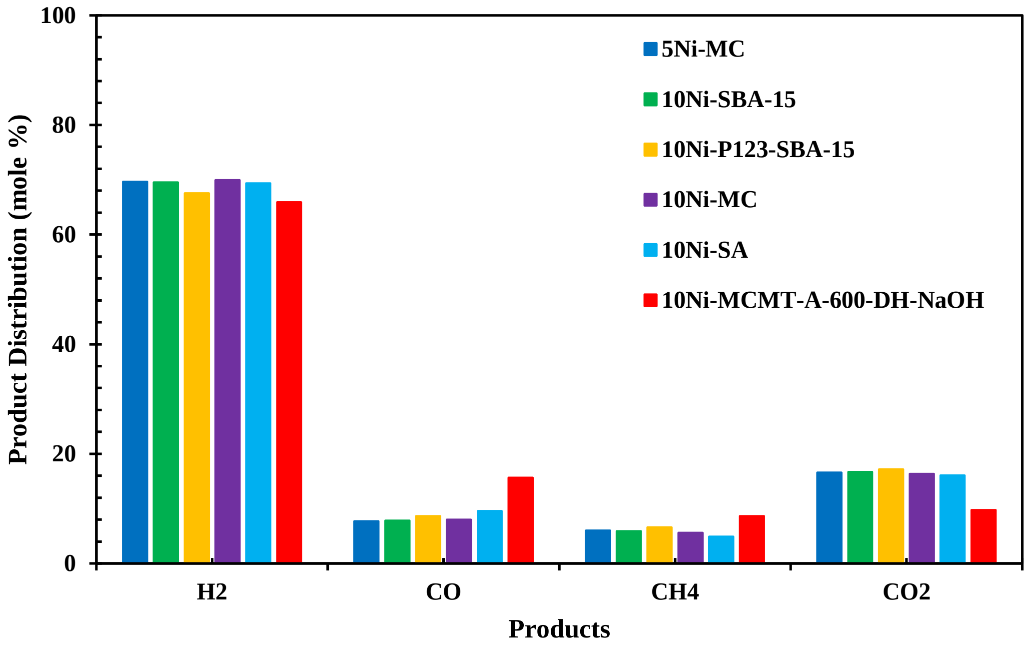

Figure 118: The average mole percentages of the products for all catalysts in SRE experiments at 600°C

The average hydrogen yield values for all catalysts in the SRE reaction are given in Figure 119. Nickel impregnated commercial mesoporous carbon was the best candidate among the carbon supported catalysts due to its physical and chemical properties.

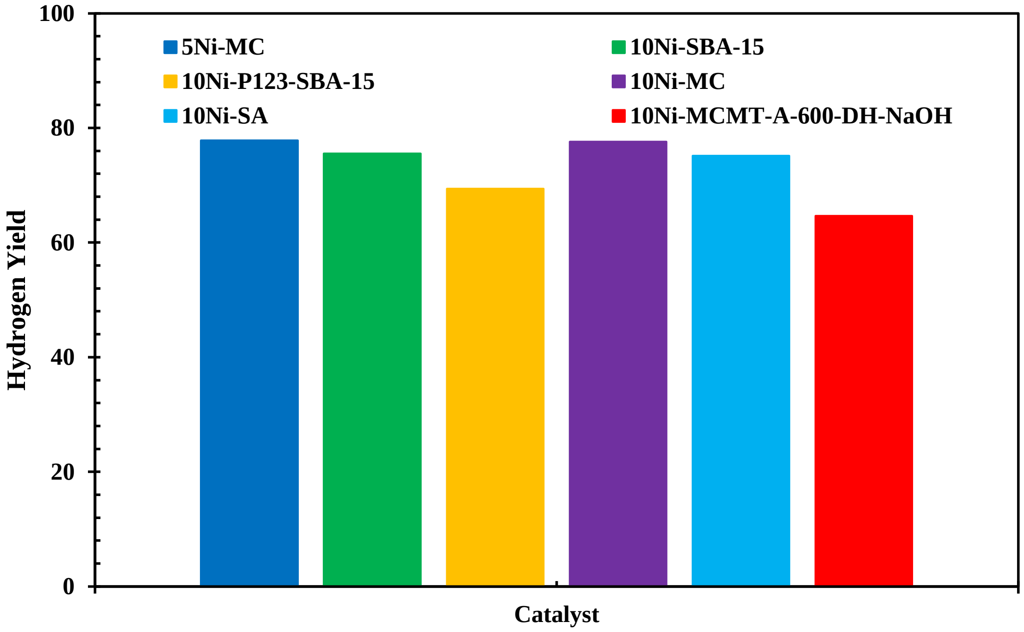

Figure 119: Hydrogen yield values for SRE experiments at 600°C

The mole percentages of the hydrogen at different reaction times for all the SESRE tests are presented in Figure 120. With an increase in the ordering in SESRE tests, the enhancement in the hydrogen mole percentages was achieved for all catalysts. Mixed concept only gave good results for the 10Ni-SA catalyst due to the high acidity of the catalyst compared to others. With the capture of carbon dioxide, the steam reforming of ethanol reaction shifted to the formation of more hydrogen and in this way, the mole percentage of the hydrogen achieved nearly 95 %. High purity hydrogen was achieved with a trace amount of carbon monoxide and carbon dioxide. With an increase in the reaction time, all CaO was saturated with carbon dioxide so the mole percentage of the hydrogen decreased.

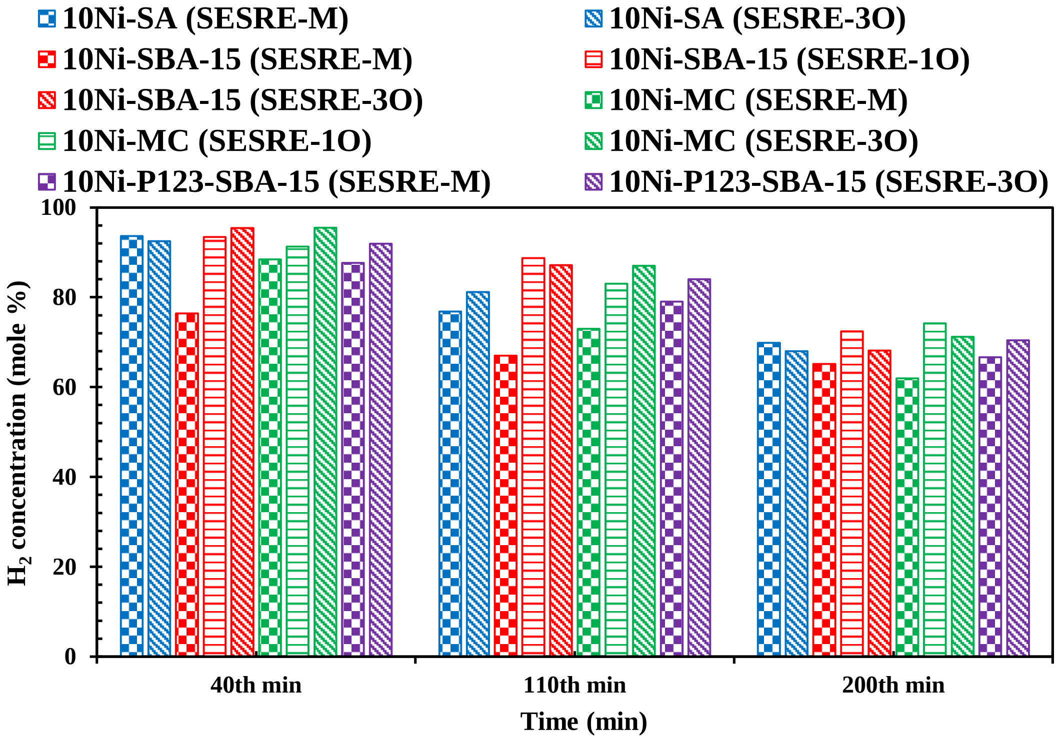

Figure 120: The mole percentages of H_2 for all catalysts in different sorbent-catalyst configurations in the SESRE reaction at 600°C

The mole percentages of the carbon monoxide at different reaction times for all the SESRE tests are presented in Figure 121. Capture of carbon dioxide also decreased the carbon monoxide amount considering the water gas shift reaction. Therefore, in the first 40 min, nearly no carbon monoxide was observed in the product distribution. For the mixed SESRE concept, ethanol decomposition reaction was important so at higher reaction times, the percentage of the carbon monoxide was higher compared to the ordered SESRE concepts.

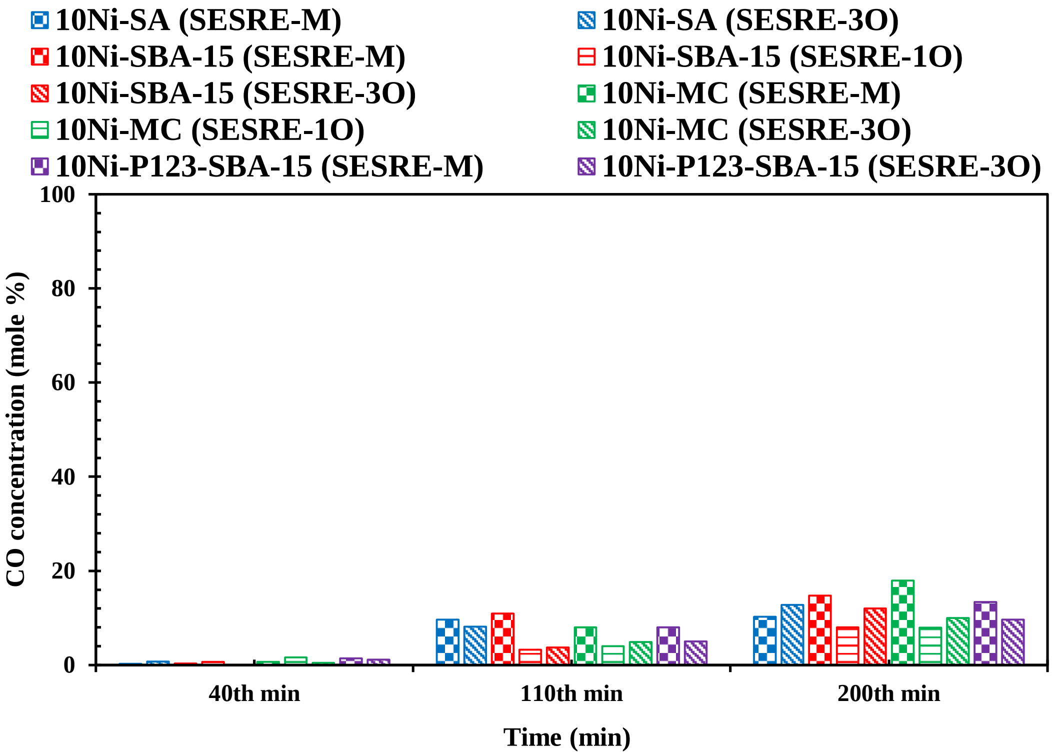

Figure 121: The mole percentages of CO for all catalysts in different sorbent-catalyst configurations in the SESRE reaction at 600°C

The mole percentages of the methane at different reaction times for all the SESRE tests are presented in Figure 122. As seen from the figure, the methane formation was higher in the SESRE-M configuration. This was also due to the ethanol decomposition reaction. Moreover, a decrease in the carbon dioxide may also favored the reverse dry reforming of methane reaction. Therefore, an increase in the methane mole percentages in the initial reaction times can be due to ethanol decomposition reaction.

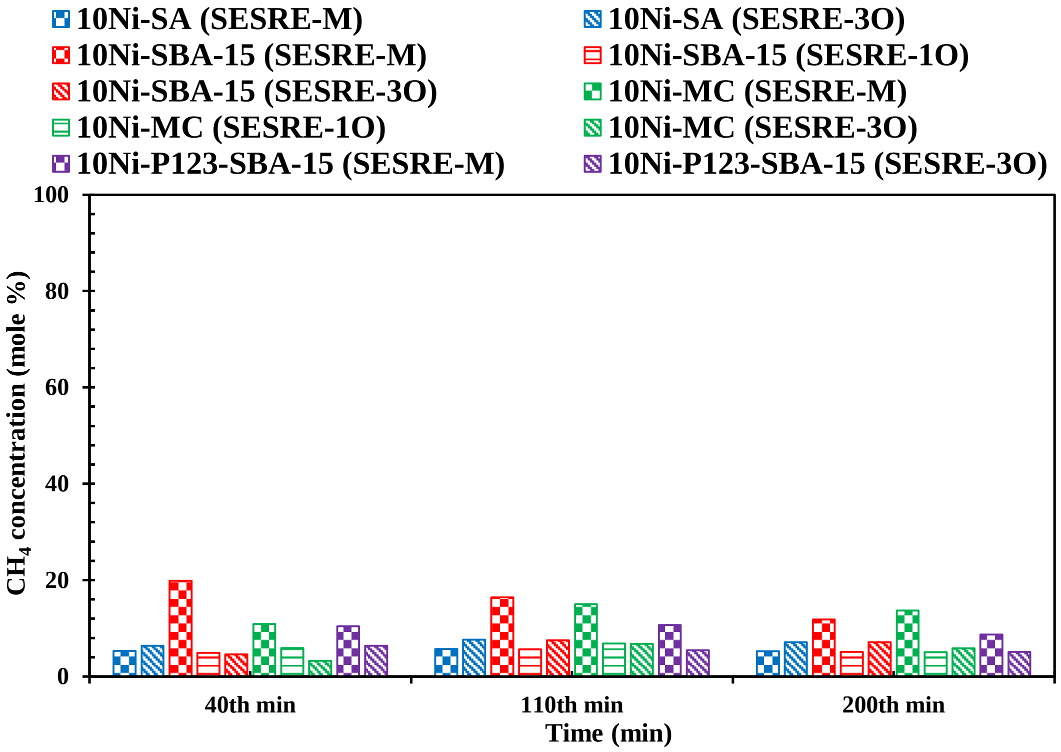

Figure 122: The mole percentages of CH_4 for all catalysts in different sorbent-catalyst configurations in the SESRE reaction at 600°C

The mole percentages of the carbon dioxide at different reaction times for all the SESRE tests are presented in Figure 123. In the first 40 min, there was nearly no carbon dioxide in the product distributions. With an increase in the reaction time, carbon dioxide amount increased due to the saturation of CaO with carbon dioxide.

Coke deposition amounts for all the catalyst at 500°C and 600°C are given in Table 21. At 600°C, the most stable catalyst was the 10Ni-SA catalyst. On the other hand, the catalyst had the highest thermal stability at 500°C was the 10Ni-P123-SBA-15 catalyst due to the small nickel crystallite size. For the 10Ni-SBA-15 and 10Ni-P123-SBA-15 catalysts, the highest coke deposition was observed at 600°C. However, for the 10Ni-SA catalyst, the coke formation was higher at 500°C.

Considering all the catalysts, the 10Ni-SA catalyst gave high activity towards SESRE-M experiment compared to other catalysts. Moreover, coke formation at 600°C is the lowest for this catalyst. On the other hand, with the 10Ni-MC and 10Ni-SBA-15 catalysts, the mole percentage of the hydrogen reached to nearly 95 % in the first 40 min.

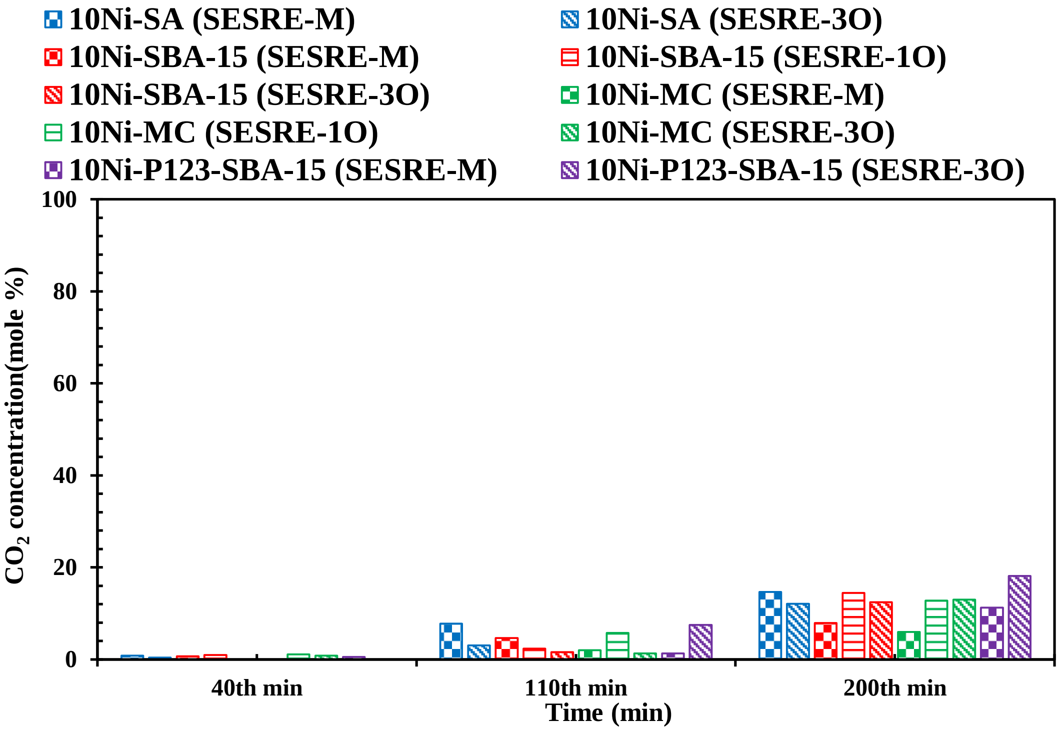

Figure 123: The mole percentages of CO_2 for all catalysts in different sorbent-catalyst configurations in SESRE experiments at 600°C

Table 21: Coke deposition for spent catalysts

Catalyst	Reaction Temperature(°C)	Coke Deposition (%)
10Ni-SBA-15	500	51
	600	56
10Ni-P123-SBA-15	500	5
	600	37
10Ni-SA	500	48
	600	12

6.6 Activity Results of Microwave Heated System for the 10Ni-SBA-15 Catalyst

The 10Ni@SBA-15 catalyst was also tested in the SRE and SESRE-M reactions in microwave heated reactor system at 600°C. The product distributions for the SRE and SESRE-M reactions are given in Figures 124-125. In activity tests performed at 600°C, complete conversion of ethanol was achieved in the SRE reaction in MWR system. The mole percentage of the hydrogen in the SRE reaction in both MWR and CHR systems was nearly 69 %. Comparison of CHR with MWR, the average mole percentage of carbon dioxide decreased from 16 % to 12 % and the average mole percentage of carbon monoxide increased from 8 % to 14 %. The main reason of an increase in the mole percentage of carbon monoxide and a decrease in the mole percentage of carbon dioxide was a decrease in the formation of cold spots in the microwave heated system. Due to the exothermic nature of the WGSR, the formation of cold spots in the catalyst bed favored this reaction. In other words, with minimizing the cold regions in MWR, the possibility of the formation of WGSR was reduced. Moreover, the mole percentage of methane reduced in the MWR compared to CHR in SRE tests. MWR enhanced the methane steam reforming reaction, occurring at the high temperatures with minimizing cold regions in the reactor bed. Same hydrogen yield value was achieved for both heating types. The percentage of the hydrogen yield value for the SRE reaction was 76 % in both CHR and MWR.

The comparison graph for the SRE and SESRE-M experiments in MWR is shown in Figure 126. In the first 40 min, the purity of the hydrogen reached to 90 % in SESRE reaction. The methane formation in SESRE test compared to SRE test increased due to the reverse dry methane reforming reaction with a decrease in the carbon dioxide. CO_2 was nearly not observed in the product stream until reaction time of 60 minutes, which meant that CaO adsorbed all CO_2 during this period. After pre-breakthrough period, CO_2 started to appear in the product stream, since most of CaO were saturated with CO_2. In the post-breakthrough period, the mole percentage of hydrogen and carbondioxide for the SRE and SESRE reached the same value.

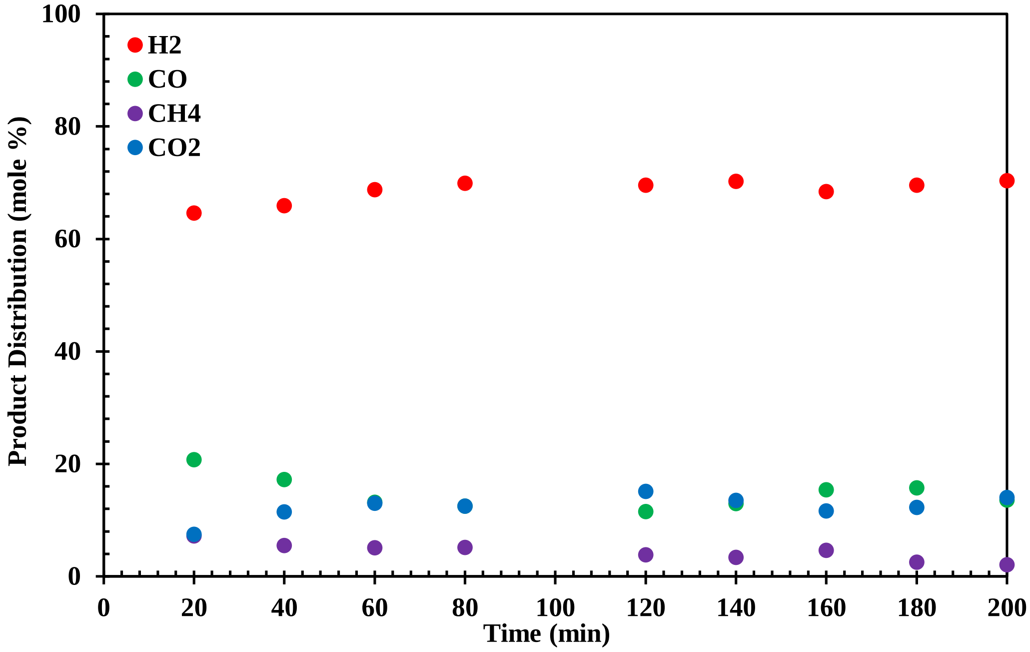

Figure 124: Product distribution at 600°C for the SRE reaction in MWR (Catalyst: 10Ni-SBA-15)

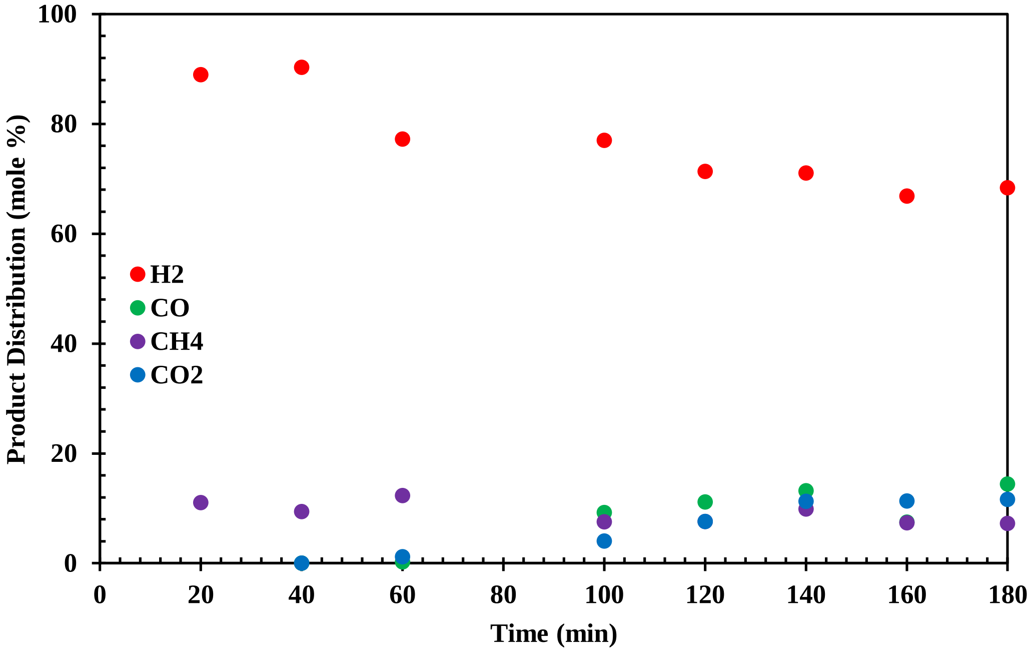

Figure 125: Product distribution at 600°C for the SESRE-M reaction in MWR (Catalyst: 10Ni-SBA-15)

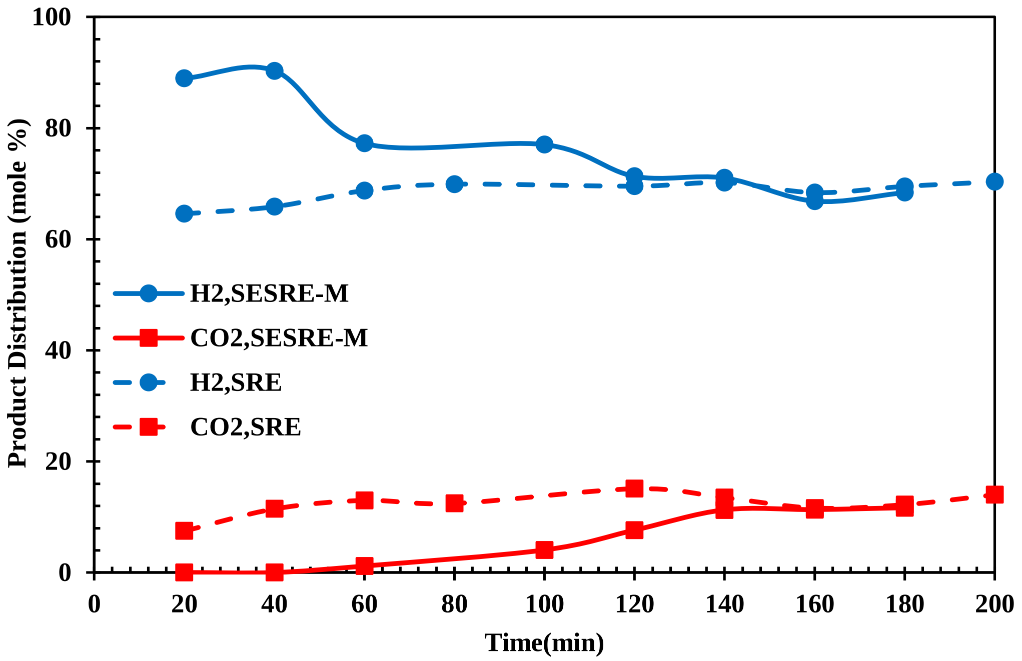

Figure 126: Comparison of H_2 and CO_2 compositions at 600°C for the SRE and SESRE in MWR

The comparison of reactor types and product distributions at different reaction times for SRE and SESRE-M tests are shown in Figures 127-128. Comparison of the product distributions observed during the first 20 minutes of SRE and SESRE tests performed in both conventionally heated and microwave heated reactors clearly showed significant enhancement of hydrogen yield in SESRE tests.The decrease in the mole percentage of the hydrogen for MWR system in the first 20 min was due to the fact that the system did not reach to stable conditions. In-situ removal of CO_2 also facilitated WGSR, decreasing the mole percentage of carbon monoxide. At reaction times higher than 120 min, a decrease in mole percentage of hydrogen and an increase in the mole percentage of carbon monoxide and carbon dioxide were observed, due to saturation of CaO with CO_2.

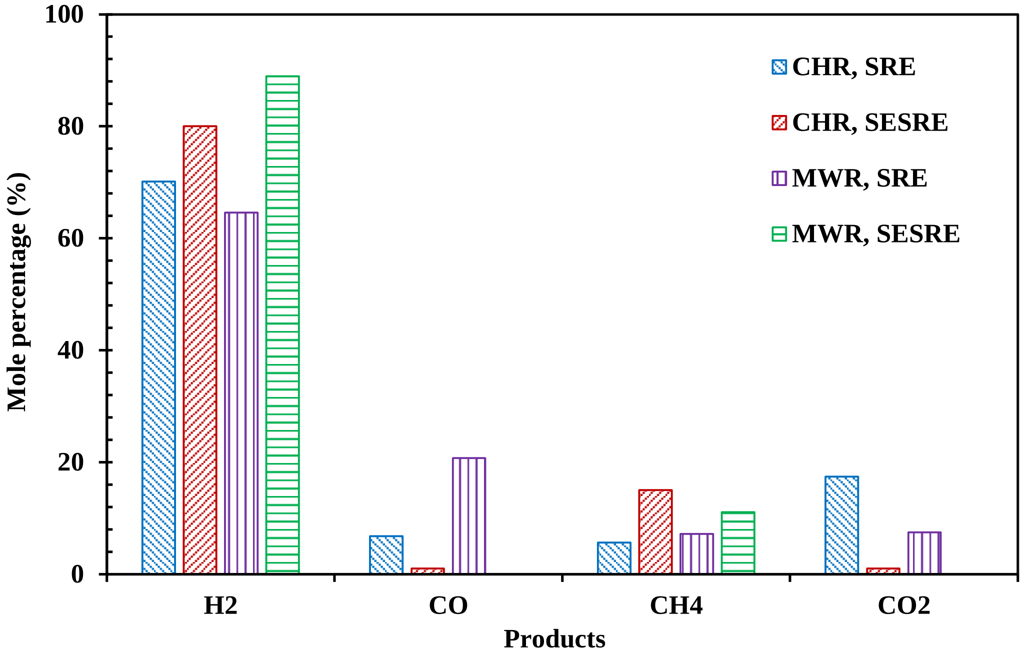

Figure 127: Comparison of product distributions for SRE and SESRE in conventionally and microwave heated reactors at 600 °C at the 20th minute of the reaction

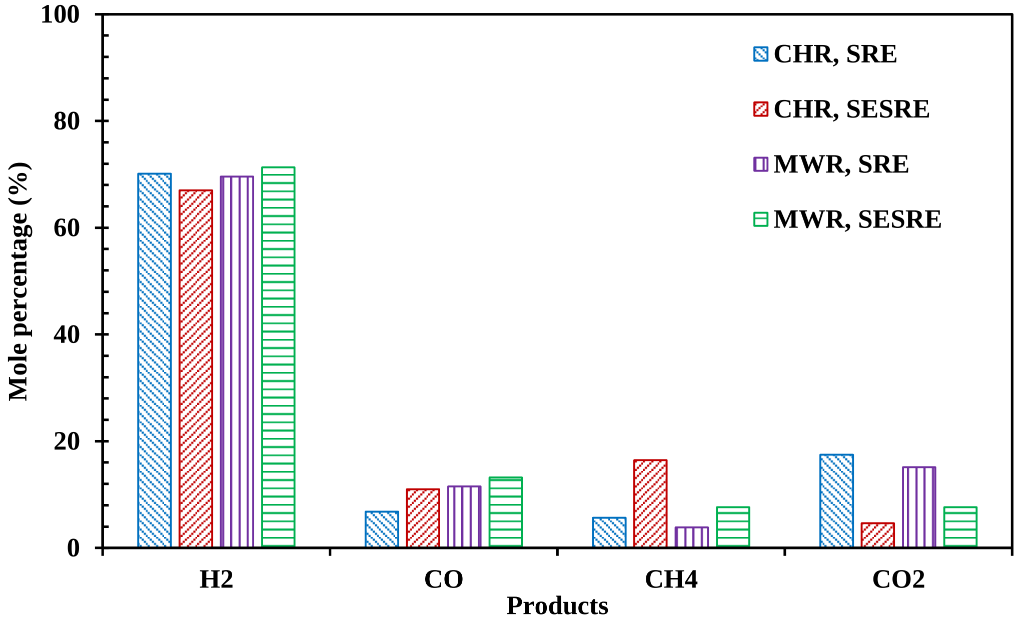

Figure 128: Comparison of product distributions for SRE and SESRE in conventionally and microwave heated reactors at 600 °C at the 120th min of the reaction

TGA analysis results for the spent catalysts for SRE tests are shown in Figure 129. While conventional heating caused 56% coke formation, the coke formation was only 3 % in microwave heated reactor. Focused microwave heating minimized the coke formation. Temperature uniformity in the radial direction and formation of hot spots within the catalyst bed minimized coke formation in the microwave heated reactor.

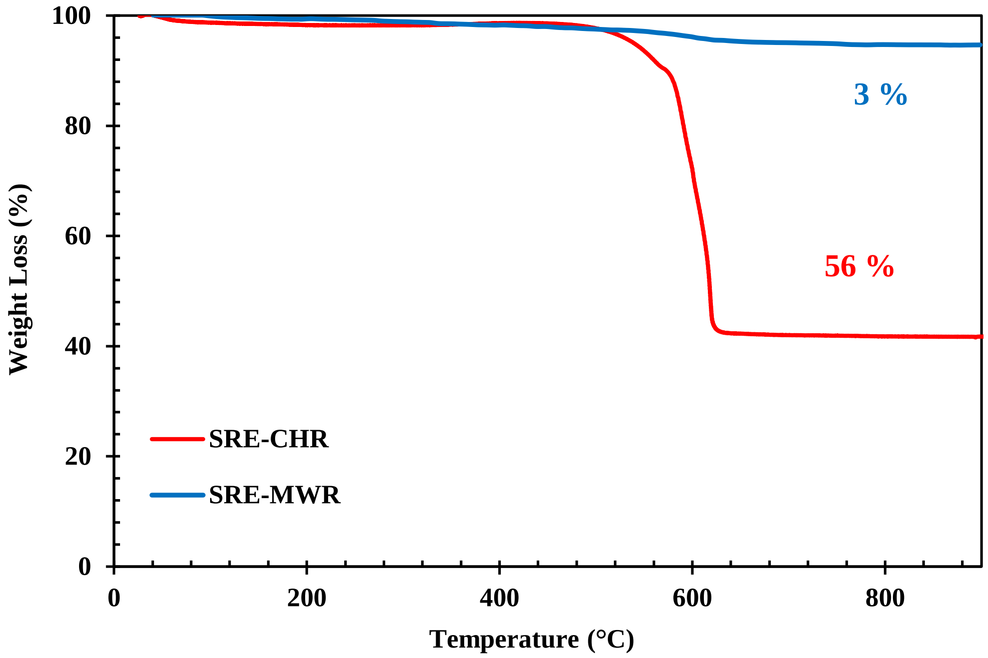

Figure 129: TGA analysis results for spent catalysts for the SRE in conventionally and microwave heated reactors

CHAPTER 7

CONCLUSIONS AND RECOMMENDATIONS

- Nickel impregnated SBA-15 was successfully synthesized with Type IV isotherm with H1 hysteresis. With the surfactant asisted method, the 10Ni-P123-SBA-15 catalyst was synthesized with the smallest nickel crytallite size compared to that of 10Ni-SBA-15 catalyst.

- In the SRE activity test results of SBA-15 type catalysts with an increase in the reaction temperature mole percentage of the hydrogen increased from 62 % to 68 %. Complete conversion was achieved. In the SESRE experiments of the SBA-15 catalyst, SESRE-1O gave the best product distribution compared to other packing concepts in terms of catalytic activity and purity of the hydrogen. For the 10Ni-P123-SBA-15 catalyst, nearly same product distribution was achieved with the 10Ni-SBA-15 catalyst. However, the coke formation decreased from 56 % to 38 % due to the smaller nickel crystals at 600°C. Moreover, the coke formation decreased from 37 % to 5 % at 500°C.

- With use of microwave heating system for the 10Ni-SBA-15 catalyst, the coke formation in the spent catalysts for the SRE was decreased from 56% to 3% compared to conventionally heated system. Same hydrogen yield value was achieved for the SRE reaction in both microwave heated and conventionally heated reactor systems.

- 5Ni-MC and 10Ni-MC catalysts showed Type IV isotherms with H2 hystheresis loop.

- In the SRE activity test results of MC type catalysts complete conversion was achieved. The percentage of the hydrogen yield was increased from 51 % to 78 % with an increase in the temperature. The best packing configuration was found to be SESRE-3O for this catalyst.

- Nickel impregnated silica aerogel were successfully synthesized with Type IV isotherm with H1 hysteresis.

- In SRE activity test results of silica aerogel type catalysts, highly stable product distribution was obtained at different temperatures. Hydrogen yield enhancement was achieved with increasing the reaction temperature. Moreover, with the 10Ni-SA catalyst, the ordered and mixed concepts gave nearly same product distribution The mole percentage of the hydrogen reached to nearly 93 % in the first 60 min, giving nearly no carbon dioxide and carbon monoxide in both SESRE-M and SESRE-3O experiments.

- MCMT-B materials showed Type IV isotherm with H2 hysteresis loop; on the other hand, MCMT-A materials showed Type IV isotherm with H1 and H2 hysteresis loops, indicating bimodal pore size distribution. The highest surface area, pore volume and pore diameter were achieved with the MCMT-A-600-DH-HF support, synthesized from the silica aerogel without TMCS calcined at 600°C and heated using the double heating step. MCMT-A-600-DH-HF support has a surface area of 1179 m^2/g, a pore volume of 1.41 cm^3/g and a pore diameter of 3.75 nm. Considering the TGA and SEM analyses, with NaOH washing, some unremoved silica structure remained in the MCMT materials. On the other hand, with HF washing step, all silica template removed from the material.

- The 10Ni-MCMT-A-600-DH-NaOH catalyst gave stable product distribution and compatible catalytic activity compared to silica based catalysts in the SRE reaction. Hydrogen yield percentage was 65 % for 10Ni-MCMT-A-600-DH-

NaOH catalyst. Two packing concepts SESRE-M & SESRE-3O gave nearly same product distribution, enhancing the mole percentage of the hydrogen in the pre-breakthrough ad breakthrough periods.

- The best catalyst was 10Ni-SA compared to others due to low coke formation. The average product distribution was found to be 69.3 % H_2, 9.6 % CO, 4.9 % CH_4 and 16.1 % CO_2 and the percentage of hydrogen yield value was 77 % at 600°C. The coke formation was 12 % at 600°C. In the SESRE-M and SESRE-3O tests, the mole percentage of the hydrogen reached to nearly 93 % in the first 60 min, giving a little amount of carbon dioxide and carbon monoxide at 600°C. Enhancement in the hydrogen mole percentage was achieved in the first 150 min, then the product distribution was same with the SRE experiment at 600°C.

- With the usage of CaO regeneration system, the continuous production of the high purity hydrogen can be achieved. Moreover, the packing concepts can be investigated in terms of increasing the number of sections or changing the amounts of CaO and catalyst in the sections. For example, firstly in the catalyst bed, a high amount of catalyst can be put with small amount of sorbent, and then, a high amount of CaO with a low amount of catalyst can be located to the catalyst bed. In this way, sorption capacity and purity of the hydrogen can be developed. In addition to this, in order to remove the coke formation on the catalyst, regeneration of catalyst can be performed under air atmosphere in order to improve the catalytic activity.

- The required hydrogen molar flow rate for Hyundai Tucson Fuel Cell vehicle with an electric motor power of 100 kW is 62.16 mole/min. In order to use hydrogen produced from steam reforming of ethanol in the presence of the 10Ni-SA catalyst in the fuel cell vehicle hydrogen production system must be scale-up and experimental parameters must be optimized.

- For MCMT type materials, the procedure can be revised in order to improve the catalytic activity of the catalyst such as aging time and aging temperature.

REFERENCES

Aceves Olivas, D.Y., Baray Guerrero M.R., Escobedo Bretado M.A., Marques da Silva Paula M., Salinas Gutierrez J., Guzman Velderrain V., Lopez Ortiz A., Collins-Martınez V., “Enhanced Ethanol Steam Reforming by CO_2 Absorption Using CaO, CaO*MgO or Na_2ZrO_3”, International Journal of Hydrogen Energy, 39, 16595-16607, 2014.

Alvarado, F., and Gracia, F., “Steam Reforming of Ethanol for Hydrogen Production : Thermodynamic Analysis Including Different Carbon Deposits Representation”, Chemical Engineering Journal, 165(2), 649–657, 2010.

Amiri, T. Y., and Moghaddas. J., “Cogeled Copperesilica Aerogel as a Catalyst in Hydrogen Production from Methanol Steam Reforming”, International Journal of Hydrogen Energy, 40(3), 2015.

Araiza, D. G., Gómez-Cortés, A. and Díaz. G. “Effect of Ceria Morphology on the Carbon Deposition during Steam Reforming of Ethanol over Ni/CeO_2 Catalysts.” Catalysis Today, 2018, doi: 10.1016/j.cattod.2018.03.016.

Cadwallader, L.C., and J.S. Herring, “Safety Issues with Hydrogen as a Vehicle Fuel” Idaho National Engineering, and Environmental Laboratory, 1999

Domínguez, A. et al. “Microwave-Assisted Catalytic Decomposition of Methane over Activated Carbon for CO_2-Free Hydrogen Production.” International Journal of Hydrogen Energy, 32(18), 4792–4799, 2007.

Domínguez, M., Fidalgo B., Fernandez Y., Pis J.J., Menendez J.A. “Co-SiO_2 aerogel-Coated Catalytic Walls for the Generation of Hydrogen.” Catalysis Today, 138(3-4), 193–197, 2008.

Durka, T., Gerven T. V., and Stankiewicz A., “Microwaves in Heterogeneous Gas-Phase Catalysis: Experimental and Numerical Approaches.” Chemical Engineering and Technology, 32(9), 1301–1312, 2009.

Durka, T., Stefanidis, G.D., Gerven T.V., Stankiewicz A.I., “Microwave-Activated Methanol Steam Reforming for Hydrogen Production.” International Journal of Hydrogen Energy, 36(20), 12843–12852, 2011.

Ezzeddine, Z., Batonneau-Gener I., Pouilloux Y., Hamad H., “Removal of Methylene Blue by Mesoporous CMK-3 : Kinetics, Isotherms and Thermodynamics.” Journal of Molecular Liquids, 223, 763–770, 2016.

Kleitz, F., Choi S. H. and Ryoo. R. “Cubic Ia3d Large Mesoporous Silica: Synthesis and Replication to Platinum Nanowires, Carbon Nanorods and Carbon Nanotubes.” Chemical communications, 17, 2136–2137, 2003.

Fidalgo, B., A. Domínguez, J. J. Pis, and J. A. Menéndez. “Microwave-Assisted Dry Reforming of Methane.” International Journal of Hydrogen Energy, 33(16), 4337–4344, 2008.

Fierro, V., Akdim O., Provendier H. and Mirodatos C. “Ethanol Oxidative Steam Reforming over Ni-Based Catalysts.” Journal of Power Sources, 145(2), 659–666, 2005.

FreedomCAR & Fuel Partnership, “Hydrogen Production- Overview of Technology Options.”, 2009, retrieved from https://www1.eere.energy.gov/hydrogenandfuelcells/pdfs/h2_tech_roadmap.pdf

Guler, M., Dogu T., and Varisli D., “Hydrogen Production over Molybdenum Loaded Mesoporous Carbon Catalysts in Microwave Heated Reactor System.” Applied Catalysis B: Environmental, 219, 173–182, 2017.

Gunduz, S., and Dogu. T.,“Sorption-Enhanced Reforming of Ethanol over Ni- and Co-Incorporated MCM-41 Type Catalysts.” Industrial and Engineering Chemistry Research, 51, 8796–8805, 2012.

Gündüz, S., and Dogu T., “Hydrogen by Steam Reforming of Ethanol over Co-Mg Incorporated Novel Mesoporous Alumina Catalysts in Tubular and Microwave Reactors.” Applied Catalysis B: Environmental, 168–169, 497–508, 2015.

Gurav, L., Jung I., Park H., Kang E. S., and Nadargi D. Y., “Silica Aerogel: Synthesis and Applications.” Journal of Nanomaterials, 2010, 1–11, 2010.

Hayes, B.L., “Microwave Synthesis: Chemistry at the Speed of Light”, CEM Publishing, Matthews, NC 2002.

He, S., Mei, Z., Liu N., Zhang L., Lu j., Li X., Wang J., He D., and Luo Y., “Ni/SBA-15 Catalysts for Hydrogen Production by Ethanol Steam Reforming: Effect of Nickel Precursor.” International Journal of Hydrogen Energy 42, 14429–14438, 2017.

He, S., He S., Zhang L., Li X., Wang J., He D., and Lu J., “Hydrogen Production by Ethanol Steam Reforming over Ni/SBA-15 Mesoporous Catalysts: Effect of Au Addition.” Catalysis Today 258, 162–168, 2015.

Joo, S. H., Choi J.S., Oh I., Kwak J., Liu Z., Terasaki O. And Ryoo R., “Ordered Nanoporous Arrays of Carbon Supporting High Dispersions of Platinum Nanoparticles.” Nature, 412, 169-172, 2001.

Jun, S., Sang H. J., Ryong R., and Michal K. “Synthesis of New , Nanoporous Carbon with Hexagonally Ordered Mesostructure.” American Chemical Society, 122, 10712–10713, 2000.

Kistler, S. S., “Coherent Expanded Aerogels and Jellies.” Nature, 127, 741, 1931.

Lee, C. H., and Ki B. L. "Application of One-Body Hybrid Solid Pellets to Sorption-Enhanced Water Gas Shift Reaction for High-Purity Hydrogen Production." International Journal of Hydrogen Energy, 39, 18128–18134, 2014.

Lee, C. H., Lee K.B., "Sorption-Enhanced Water Gas Shift Reaction for High-Purity Hydrogen Production: Application of a Na-Mg Double Salt-Based Sorbent and the Divided Section Packing Concept." Applied Energy, 205, 316–322, 2017.

Lei, Z., Bai S., Xiao Y., Dang L., An L., Zhang G., and Xu Q., "CMK-5 Mesoporous Carbon Synthesized via Chemical Vapor Deposition of Ferrocene as Catalyst Support for Methanol Oxidation.", The Journal of Physical Chemistry C, 112, 722–731, 2007.

Li, D., Zeng L., Li X., Wang X., Ma h., Assabumrungrat S., and Gong J., "Ceria-Promoted Ni/SBA-15 Catalysts for Ethanol Steam Reforming with Enhanced Activity and Resistance to Deactivation." Applied Catalysis B: Environmental, 176–177, 532–541, 2015.

Li, L., Tang D., Song Y., Jiag B., and Zhang Q.,"Hydrogen Production from Ethanol Steam Reforming on Ni-Ce/MMT Catalysts." Energy, 149, 937–943, 2018.

Li, X., Tuo Y., Li P., Duan X., Jiang H., and Zhou X., "Effects of Carbon Support on Microwave-Assisted Catalytic Dehydrogenation of Decalin." Carbon, 67, 775–83, 2014.

Lima da Silva, A. et al. "Thermodynamic Analysis of Ethanol Steam Reforming Using Gibbs Energy Minimization Method: A Detailed Study of the Conditions of Carbon Deposition." International Journal of Hydrogen Energy, 34(10), 4321–4330, 2009.

Liu, M., Yang D. , and Qu. Y. "Preparation of Super Hydrophobic Silica Aerogel and Study on Its Fractal Structure." Journal of Non-Crystalline Solids, 354(45–46), 4927–4931, 2008.

Maleki, H., Durães L., and Portugal. A., "An Overview on Silica Aerogels Synthesis and Different Mechanical Reinforcing Strategies." Journal of Non-Crystalline Solids, 385, 55–74, 2014.

Malfait, W., Zhao S., Verel R., Iswar S., Rentsch D., Fener R., Zhang Y., Milow B., and Koebel M., ."Surface Chemistry of Hydrophobic Silica Aerogels." Chemistry of Materials, 27(19), 6737–6745, 2015.

Mazloomi, K. and Gomes C., "Hydrogen as an Energy Carrier: Prospects and Challenges." Renewable and Sustainable Energy Reviews, 16(5), 3024–3033, 2012.

Menéndez, J. A., Arenillas A., Fidalgo B., Fernandez Y., Zubizzarreta L., Calvo E.G., and Bermudez J.M., "Microwave Heating Processes Involving Carbon Materials." Fuel Processing Technology, 91(1), 1–8, 2010.

Mishra, R. R., and Sharma, A. K., , "Microwave-Material Interaction Phenomena: Heating Mechanisms, Challenges and Opportunities in Material Processing." Composites Part A: Applied Science and Manufacturing, 81, 78–97, 2016.

Momirlan, M. and Veziroglu. T. N., "The Properties of Hydrogen as Fuel Tomorrow in Sustainable Energy System for a Cleaner Planet." International Journal of Hydrogen Energy, 30(7), 795–802, 2015.

Qi, T., Yang Y., Wu Y., Wang J., Li P., and Yu J., "Sorption-Enhanced Methanol Steam Reforming for Hydrogen Production by Combined Copper-Based Catalysts with Hydrotalcites." Chemical Engineering & Processing: Process Intensification, 127, 72–82, 2018.

Roggenbuck, J., Koch G., and Tiemann M., "Synthesis of Mesoporous Magnesium Oxide by CMK-3 Carbon Structure Replication." Chemistry of Materials, 18(17), 4151–4156, 2006.

Ryoo, R., Joo S. H., and Jun S., "Synthesis of Highly Ordered Carbon Molecular Sieves via Template-Mediated Structural." The Journal of Physical Chemistry B, 103(37), 7743-7746, 1999.

Nettelroth D., Schwarz H., Burblies N., Guschnski N., and Behrens P., "Catalytic Graphitization of Ordered Mesoporous Carbon CMK-3 with Iron Oxide Catalysts: Evaluation of Different Synthesis Pathways." Physica Status Solidi A, 213(6), 1395–1402, 2016.

Sinkó, K. "Influence of Chemical Conditions on the Nanoporous Structure of Silicate Aerogels." Materials, 3(1), 704–740, 2010.

Soleimani Dorcheh, A., and Abbasi M. H., "Silica Aerogel; Synthesis, Properties and Characterization." Journal of Materials Processing Technology, 199(1), 10–26, 2008.

Tao, M., Xin Z., Meng X., Bian Z., and Lv Y., "Highly Dispersed Nickel within Mesochannels of SBA-15 for CO Methanation with Enhanced Activity and Excellent Thermostability." Fuel, 188, 267–276, 2017.

Thapliyal, P. C., and Singh K., "Aerogels as Promising Thermal Insulating Materials: An Overview." Journal of Materials, 2014, 1–10, 2014.

U.S. Department of Energy "Hydrogen and Fuel Cell Technologies Program: Storage." Energy Efficiency and Renewable Energy, 2011, retrieved from https://www1.eere.energy.gov/hydrogenandfuelcells/pdfs/doe_h2_storage.pdf

Varisli, D., Korkusuz C., and Dogu T., “Microwave-Assisted Ammonia Decomposition Reaction over Iron Incorporated Mesoporous Carbon Catalysts.” Applied Catalysis B: Environmental, 201, 370–380, 2017.

Vizcaino, A., J., Carrero A., and Calles J. A., “Hydrogen Production by Ethanol Steam Reforming over Cu–Ni Supported Catalysts.” International Journal of Hydrogen Energy, 32(10–11), 1450–1461, 2007.

Wang, X., Wu S., Li Z., Yang X., Su H., Hu J., Huo Q., Guan J., and Kan Q., “Microporous and Mesoporous Materials Cu (II), Co (II), Fe (III) or VO (II) Schiff Base Complexes Immobilized onto CMK-3 for Styrene Epoxidation.” Microporous and Mesoporous Materials, 221, 58–66, 2016.

Will, H., Scholz P., and Ondruschka B., “Microwave-Assisted Heterogeneous Gas-Phase Catalysis.” Chemical Engineering and Technology, 27(2), 113–122, 2004.

Wu, G., Yu Y., Cheng X., and Zhang Y., “Preparation and Surface Modification Mechanism of Silica Aerogels via Ambient Pressure Drying.” Materials Chemistry and Physics, 129(1–2), 308–314, 2011.

Wang, W. and Wang, Y. Q. “Thermodynamic Analysis of Steam Reforming of Ethanol for Hydrogen Generation”, International Journal of Energy Research, 32, 1432–1443, 2008.

Xia, K., Gao Q., Wu C., Song S., and Ruan M., “Activation, Characterization and Hydrogen Storage Properties of the Mesoporous Carbon CMK-3” Carbon, 45(10), 1989–1996, 2007.

Yang, W., Liu H., Li Y., Wu H., and He D., “CO_2 reforming of Methane to Syngas over Highly-Stable Ni/SBA-15 Catalysts Prepared by P123-Assisted Method.” International Journal of Hydrogen Energy, 41, 1513–1523, 2016.

Zhang, C., Dai C., Zhang H., Peng S., Wei X., and Hu Y., “Regeneration of Mesoporous Silica Aerogel for Hydrocarbon Adsorption and Recovery” Marine Pollution Bulletin, 122, 129–138, 2017.

Zhang, X., Rajagopalan K., Lei H., Ruan R., and Sharma B., “An Overview of a Novel Concept in Biomass Pyrolysis: Microwave Irradiation” Sustainable Energy Fuels, 1, 1664–1699, 2017.

Zhou, J., Su W., Deng S., and Wang X., “Enhanced CO_2 Sorption on Ordered Mesoporous Carbon CMK-3 in the Presence of Water”, Journal of Chemical & Engineering Data, 61, 1348-1352, 2016.

APPENDIX A

CALCULATION OF METAL LOADING AMOUNT TO CATALYST

Nickel was impregnated to all the catalyst support (10 % by weight). For 1 g SBA-15 catalyst, 10 weight % nickel was impregnated to the catalyst support. The required nickel amount was 0.1 g. The nickel source was $Ni(NO_3)_2.6H_2O$.

$\mathrm{MW}_{\mathrm{Ni(NO_3)_2.6H_2O}} = 290.81\ g/mole$

$\mathrm{MW}_{\mathrm{Ni}} = 58\ g/mole$

$$\mathrm{m}_{\mathrm{Ni(NO_3)_2.6H_2O}} = \frac{0.1 \times \mathrm{MW}_{\mathrm{Ni(NO_3)_2.6H_2O}}}{\mathrm{MW}_{\mathrm{Ni}}} = \frac{0.1 \times 290.81\ g/mole}{58\ g/mole} = 0.514\ g$$

APPENDIX B

XRD DATA OF NICKEL, NICKEL OXIDE AND CARBON

XRD data of nickel, nickel oxide and carbon are given in Tables B.1-B.3

Table B.1 XRD Data of Nickel

Formula: Ni **PDF Card No:** 01-071-4653 **Radiation:** CuKα_1 **Wavelength:** 1.54060 Å			
2θ (°)	**d spacing (Å)**	**Intensity (%)**	**h k l**
44.48	2.035	100	1 1 1
51.83	1.763	41.9	2 0 0
76.35	1.246	16.1	2 2 0

Table B.2 XRD Data of Nickel Oxide

Formula: NiO **PDF Card No:** 01-071-1179 **Radiation:** CuKα_1 **Wavelength:** 1.54060 Å			
2θ (°)	**d spacing (Å)**	**Intensity (%)**	**h k l**
37.24	2.412	68.0	1 1 1
43.27	2.089	100	2 0 0
62.86	1.477	46.5	2 2 0
75.39	1.260	16.5	3 1 1
79.38	1.206	11.8	2 2 2
95.03	1.044	4.5	4 0 0
106.96	0.958	5.1	3 3 1
111.08	0.934	12.0	4 2 0
129.17	0.853	9.6	4 2 2
146.67	0.804	4.4	5 1 1

Table B.3 XRD Data of Carbon

Formula: C **PDF Card No:** 00-041-1487 **Radiation:** CuKα_1 **Wavelength:** 1.54060 Å			
2θ (°)	**d spacing (Å)**	**Intensity (%)**	**h k l**
26.38	3.376	100	0 0 2
42.22	2.139	2.0	1 0 0
44.39	2.039	6.0	1 0 1
50.45	1.807	1.0	1 0 2
54.54	1.681	4.0	0 0 4
59.69	1.548	1.0	1 0 3
77.24	1.234	3.0	1 1 0
83.18	1.160	3.0	1 1 2
86.82	1.121	1.0	0 0 6
93.59	1.057	1.0	2 0 1

APPENDIX C

CALCULATION OF CRYSTALLITE SIZE OF METAL

Crystallite size of the nickel is calculated from the Scherrer equation with the help of XRD data for 10Ni@SBA-15. Its XRD data is shown in Table C.1.

Table C.1 XRD Data for 10Ni-SBA-15

2-theta(deg)	d (A)	Int. I(cps deg)	FWHM(deg)
21.6(4)	4.11(7)	8035(4929)	7.8(13)
44.434(6)	**2.0371(2)**	**1015(9)**	**0.457(5)**
51.784(13)	1.7639(4)	416(7)	0.499(11)
76.312(16)	1.2468(2)	189(4)	0.54(4)

Scherrer equation is shown in equation C.1.

$$t_{crystallite\ size} = \frac{C \times \lambda}{B \times \cos(\frac{2\theta}{2})} \qquad \text{C.1}$$

C: crystal shape factor (0.89)

λ: Wavelength (0.154 nm for copper)

B: Full width at half max

2θ: Peak angle

The peak at 44.43° which has the highest intensity is used for the calculation of nickel crystallite size.

$$B = FWHM_{Ni} \times \frac{3.14}{180} = 0.457 \times \frac{3.14}{180} = 7.972 \times 10^{-3}\ radians$$

$$t_{crystallite\ size} = \frac{0.89 \times 0.154}{7.972 \times 10^{-3} \times \cos(\frac{44.43}{2})} = 18.57\ nm$$

APPENDIX D

CALCULATION OF TOTAL ACID CAPACITY OF CATALYSTS

Calculation of the total acidity was performed using the area under the TCD Signal versus temperature graph. For the 10Ni-SBA-15 catalyst, the total area under the curve was equal to 0.19385. Then, total acid capacity was calculated from the D.1, which based on the calibration curve of ammonia gas.

$$Total\ Acid\ Capacity\ (ml\ NH_3) = Area \times 3.3108 + 0.0053 \qquad \text{D.1}$$

$$Total\ Acid\ Capacity = 0.19385 \times 3.3108 + 0.0053 = 0.652\ ml\ NH_3$$

Then, using the ideal gas equation (D.2),

$$N_{NH_3} = \frac{V_{NH_3} \times P}{R \times T} \qquad \text{D.2}$$

$$N_{NH_3} = \frac{0.652 \times 10^{-3}(L) \times 1\ (atm)}{0.082(\frac{L.atm}{mole.K}) \times 293(K)} = 2.7 \times 10^{-5}\ mole\ NH_3$$

The sample weight was 0.1 g. Therefore, acidity can be calculated:

$$Total\ acidity = \frac{2.7 \times 10^{-2}\ mmole\ NH_3}{0.1\ g} = 0.27 \frac{mmole}{g} catalyst$$

APPENDIX E

BETA FACTOR CALCULATION OF GASES

Calibration factors were calculated using the standard gas mixture containing 1 % H_2, 1 % CO, 1 % CH_4, 1 % CO_2, 1 % C_2H_4 in Argon by volume. The beta factor of carbon dioxide was taken as 1 and the others were calculated using equation E.1. Calibration factors are given in Table E.1.

$$\frac{N_{CO_2}}{N_i} = \frac{A_{CO_2}\beta_{CO_2}}{A_i\beta_i} \qquad \text{E.1}$$

Table E.1 Calibration factors for gas compounds

Compound	**Mole Fractions**	**Retention Time (min)**	**β Factor**
H_2	0.0092	1.65	0.0998
CO	0.0097	1.89	1.536
CH_4	0.0099	2.50	0.281
CO_2	0.0100	4.61	1.00
C_2H_4	0.0084	5.69	0.313

For the liquid calibration factors, the beta factor of the ethanol was taken as 1 and beta factor for water was calculated. Equation E.1 was also used for the calculation of liquid beta factors. For the beta factor calculation of the water, the sample with the known volume (Water/Ethanol=5 by volume (nearly similar ratio with the liquid sample after the reaction)) was prepared and injected to the gas chromatography at least three times until the similar areas were observed for the water and ethanol, separately.

Assuming 1000 ml water and 200 ml ethanol in the mixture,

$$\rho_{water} = 1\frac{g}{ml} \; ; \; \rho_{ethanol} = 0.789\frac{g}{ml}$$

$$N_{ethanol} = V_i \rho_i \frac{1}{MW_i} \tag{E.2}$$

Moles of the ethanol can be calculated using equation E.2:

$$N_{ethanol} = 200ml \times 0.789 \frac{g}{ml} \times \frac{1\,mole}{46\,g} = 3.43\,mole$$

Moles of the water can be calculated using E.2:

$$N_{water} = 1000ml \times 1 \frac{g}{ml} \times \frac{1\,mole}{18\,g} = 55.56\,mole$$

Then, using equation E.1, the beta factor for water can be calculated.

$$\frac{N_{water}}{N_{ethanol}} = \frac{A_{water}\beta_{water}}{A_{ethanol}\beta_{ethanol}}$$

The average of the areas under the curves in gas chromatography spectra was taken and put into the equation E.1.

$$\frac{55.56\,mole}{3.43\,mole} = \frac{215225 \times \beta_{water}}{15150 \times 1} \qquad \beta_{water} = 0.98$$

Calibration factors for liquid compounds are given in Table E.2.

Table E.2 Calibration factors for liquid compounds

Compound	Retention Time (min)	β Factor
H_2O	8.67	0.98
C_2H_5OH	11.5	1.00

APPENDIX F

PRODUCT MOLE PERCENTAGES, PERCENTAGE OF HYDROGEN YIELD AND CONVERSION CALCULATIONS

- **Calculation of Product Mole Percentages in the Gas Effluent Stream**

The areas for each gas compound were taken from the gas chromatography and they were multiplied with the calibration factors. Then, product distributions in the mole percentages, ethanol conversion and hydrogel yield were calculated.

Sample calculation was given for the SRE reaction, the 10Ni-SA catalyst at 600°C in the 34th min.

$$N_A = Area_A \times \beta_A \qquad \text{F.1}$$

$$N_{Total} = N_{H2} + N_{CO} + N_{CH4} + N_{CO2} \qquad \text{F.2}$$

$N_{H_2} = 26394 \times 0.0998 = 2634.12$

$N_{CO} = 223.5 \times 1.536 = 343.296$

$N_{CH_4} = 690.1 \times 0.281 = 193.92$

$N_{CO_2} = 567.1 \times 1 = 567.1$

$N_{Total} = 2634.12 + 343.296 + 193.92 + 567.1 = 3738.44$

Then, the percentage of each product in gas stream was calculated from F.3.

$$y_A(\%) = \frac{N_A}{N_{total}} \times 100 \qquad \text{F.3}$$

$$y_{H_2}(\%) = \frac{2634.12}{3738.44} \times 100 = 70.4\ \%$$

$$y_{CO}\ (\%) = \frac{343.296}{3738.44} \times 100 = 9.18\ \%$$

$$y_{CH_4}(\%) = \frac{193.92}{3738.44} \times 100 = 5.19\ \%$$

$$y_{CO_2}(\%) = \frac{567.1}{3738.44} \times 100 = 15.17\ \%$$

The percentage of each gas product was calculated and product distribution graph was plotted for the SRE and SESRE experiments.

- **Ethanol conversion and Hydrogen Yield Calculation**

The volumetric flow rate of the product gas stream was measured at every run by a soap bubble flow meter. The average of the volumetric flow rate throughout the experiment was 50.84 ml/min. The volumetric flow rate of the argon was 30 ml/min. The total flow rate of the gaseous products was found from Equation F.4.

$$Q_{Gas\ Products} = Q_{Total} - Q_{Argon} \qquad \text{F.4}$$

Then, for each gas species, the volumetric flow rate was calculated using Equation F.5.

$$Q_A = Q_{Gas\ Products} \times y_A \qquad \text{F.5}$$

$$Q_{H_2} = (50.84 - 30) \times 0.704 = 14.797\ ml/min$$

$$Q_{CO} = (50.84 - 30) \times 0.0918 = 1.928\ ml/min$$

$$Q_{CH_4} = (50.84 - 30) \times 0.0514 = 1.089\ ml/min$$

$$Q_{CO_2} = (50.84 - 30) \times 0.15 = 3.186\ ml/min$$

Density values for each species were calculated from Equation F.6.

$$\rho_A = \frac{P \times M_A}{R \times T_{room}} \qquad \text{F.6}$$

$$\rho_{H_2} = \frac{P \times M_{H_2}}{R \times T_{room}} = \frac{1\ atm \times 2\ g/mol}{82.05\ (\frac{ml.atm}{mol.K}) \times 293\ K} = 0.0000832\ g/ml$$

$$\rho_{CO} = \frac{P \times M_{CO}}{R \times T_{room}} = \frac{1\ atm \times 28\ g/mol}{82.05\ (\frac{ml.atm}{mol.K}) \times 293\ K} = 0.0011647\ g/ml$$

$$\rho_{CH_4} = \frac{P \times M_{CH_4}}{R \times T_{room}} = \frac{1\ atm \times 16\ g/mol}{82.05\ (\frac{ml.atm}{mol.K}) \times 293\ K} = 0.0006655\ g/ml$$

$$\rho_{CO_2} = \frac{P \times M_{CO_2}}{R \times T_{room}} = \frac{1\ atm \times 44\ g/mol}{82.05\ (\frac{ml.atm}{mol.K}) \times 293\ K} = 0.0018302\ g/ml$$

Molar flow rate of each species can be calculated from Equation F.7.

$$F_A = Q_A \times \frac{\rho_A}{M_A} \tag{F.7}$$

$$F_{H_2} = Q_{H_2} \times \frac{\rho_{H_2}}{M_{H_2}} = 14.797\frac{ml}{min} \times \frac{0.0000832\frac{g}{ml}}{2\frac{g}{mol}} = 0.000615\ mol/min$$

$$F_{CO} = Q_{CO} \times \frac{\rho_{CO}}{M_{CO}} = 1.928\frac{ml}{min} \times \frac{0.0011647\frac{g}{ml}}{28\frac{g}{mol}} = 0.0000802\ mol/min$$

$$F_{CH_4} = Q_{CH_4} \times \frac{\rho_{CH_4}}{M_{CH_4}} = 1.089\frac{ml}{min} \times \frac{0.0006655\frac{g}{ml}}{16\frac{g}{mol}} = 4.53 \times 10^{-5}\ mol/min$$

$$F_{CO_2} = Q_{CO_2} \times \frac{\rho_{CO_2}}{M_{CO_2}} = 3.186\frac{ml}{min} \times \frac{0.0018302\frac{g}{ml}}{44\frac{g}{mol}} = 0.000133 mol/min$$

The amount of the liquid product obtained from the condenser throughout the experiment was 0.8456 g. Mole fractions of compounds in the liquid mixture is given in Table F.1.

Table F.1 Mole fractions of compounds in the liquid mixture

Liquid component	Areas	Moles	Mole fractions
H_2O	206909	206909	0.995
C_2H_5OH	1103	1103	0.005

Total reaction time was 321 min. Then, the mass flow rate of the liquid products was calculated as 0.8456/321= 0.00263 g/min.

Then molar flow rate of the liquid ethanol was calculated from Equation F.8.

$$F^{f}_{ETOH,liquid} = X_{ETOH,L}\frac{m_{liquid}}{(M_{ETOH} \times x_{ETOH,L} + M_{H2O} \times x_{H2O,L})} \qquad \text{F.8}$$

$$F^{f}_{ETOH,liquid} = 0.005\frac{0.00263}{(46 \times 0.005 + 18 \times 0.995)} = 7.25 \times 10^{-7} mol/min$$

From the carbon balance, the molar flow rate of the ethanol fed to the reactor can be calculated using Equation F.9.

$$F_{ETOH}{}^{o} = \frac{F_{CO}}{2} + \frac{F_{CH_4}}{2} + \frac{F_{CO_2}}{2} + F^{f}_{ETOH,liquid} \qquad \text{F.9}$$

$$F_{ETOH}{}^{o} = \frac{0.000106}{2} + \frac{4.11 \times 10^{-5}}{2} + \frac{0.000143}{2} + 7.25 \times 10^{-7} = 0.0001297$$

Then, the ethanol conversion can be calculated using the Equation F.10.

$$X_{ETOH} = \frac{F^{o}_{ETOH} - F^{f}_{ETOH,liquid}}{F^{o}_{ETOH}} \qquad \text{F.10}$$

$$X_{ETOH} = \frac{0.0001297 - 7.25 \times 10^{-7}}{0.0001297} = 0.994$$

Then, hydrogen yield can be calculated from equation.F.11.

$$H_2\ yield = \frac{F_{H_2}}{F^{o}_{C2H5OH}} \qquad \text{F.11}$$

$$H_2\ yield = \frac{0.000615}{0.0001297} = 4.74$$

The percentage of the hydrogen yield can be calculated from Equation F.12.

$$The\ percentage\ of\ H_2\ yield = \frac{H_2\ yield}{6} \times 100 \tag{F.12}$$

$$The\ percentage\ of\ H_2\ yield = \frac{4.74}{6} \times 100 = 79\ \%$$